System Level Approach towards Intelligent Healthcare Environment

Dragan Avirovik

Dissertation submitted to the faculty of the Virginia Polytechnic Institute and State University in partial fulfillment of the requirements for the degree of

Doctor of Philosophy

In

Mechanical Engineering

Shashank Priya, Chair

Andrew J. Kurdila

Muhammad R. Hajj

John J. Socha

Digant P. Davé

05/27/2014

Blacksburg, VA

Keywords: actuators, medical, piezoelectric, shape memory alloy, wireless capsule endoscopy

System Level Approach towards Intelligent Healthcare Environment

Dragan Avirovik

Abstract

Surgical procedures conducted without proper guidance and dynamic feedback mechanism could lead to unintended consequences. In-vivo diagnostics and imaging (the Gastro-Intestinal tract) has shown to be inconvenient for the patients using traditional endoscopic instruments and often these conventional methods are limited in terms of their access to various organs (e.g. small intestines). Embedding sensors inside the living body is complex and further the communication with the implanted sensors is challenging using the current RF technology. Additionally, continuous replacement and/or batteries recharging for wireless sensors networks both in-vivo and ex-vivo adds towards the complexity. Advances in diagnostics and prognostics techniques require development at multiple levels through systems approach, guided by the futuristic intelligent decision making environment that reduces the human interference. The demands are not only at the component level, but also at the connectivity of the components such that secure, sustainable, self-reliant, and intelligent environment can be realized. This thesis provides important breakthroughs required to achieve the vision of intelligent healthcare environment. The research contributions of this thesis provide foundation for developing a new architecture for continuous medical diagnostic and monitoring. The chapters in this thesis cover four fundamental technologies covering the in-vivo imaging, ex-vivo imaging, energy for sensors, and acoustic communication. These technologies are: locomotion mechanism for wireless capsule endoscope (WCE), multifunctional image guided surgical (MIGS) platform, shape memory alloy (SMA) thermal energy harvester and thermo-acoustic sonar using carbon nanotube (CNT) sheets.

First, two types of locomotion mechanisms were developed, the first one inspired by millipede legged type mechanism and the second one based on the traveling waves that were induced onto the walls of the WCEs through vibration.

Both mechanisms utilize piezoelectric actuators and couple their dynamics and actuation capability in order to achieve propulsion. This controlled locomotion will provide WCE advantage in terms of conducting localized diagnostics. Next, in order to conduct ex-vivo surgical procedures using the OCT such as removing the unwanted tissue and tumors short distance beneath the skin, MIGS platform was developed. The MIGS platform is composed of three key elements: optical coherence tomography (OCT) probe, laser scalpel and high precision miniature scanning and positioning stage. The focus in this dissertation was on design and development of the programmable scanning and positioning stage. The combination of in-vivo tool such as WCE and ex-vivo tool such as MIGS will provide opportunity to conduct many non-invasive procedures which will save time and cost. In order to power the feedback sensors that assist in remote operation of surgical procedures and automation of the diagnostic algorithms, an energy harvester technology based on the SMA thermal engine was designed, fabricated, and characterized. A mechano-thermal model for the overall SMA engine was developed and experimentally validated. Finally, the thermo-acoustic sound generation mechanism using CNT sheets was investigated with the goal of developing techniques for acoustic localization of WCE and customized sound generation devices. CNT thermo-acoustic projectors were modeled and experimentally characterized to quantify the dynamics of the system under varying drive conditions.

The overall vision of this thesis is to lay down the foundation for intelligent healthcare environment that provides the ability to conduct automated diagnostics, prognostics, and non-invasive surgical procedures. In accomplishing this vision, the thesis has addressed several key fundamental aspects of various technologies that will be required for implementing the automation algorithms.

Acknowledgements

Financial Support –I would like to gratefully acknowledge the financial support from the following agencies:

- National Institute of Health
- National Energy Management Institute Committee
- Office of Naval Research
- National Science Foundation

As I am writing this section I stop and reflect…

I reflect not only on my many years spent at Virginia Tech and Blacksburg, but also on the time spent in my native Macedonia. It has been quite a journey reaching to a point in my life where I obtain a Ph.D. in Mechanical Engineering. It feels very surreal. Nevertheless, it is the reality and what better place, but the beginning of probably one of the most important documents in my life to take the time and thank everyone that has taken a part of this journey with me. There have been many that have directly or indirectly contributed towards my successes and my greatest fear and upset is that I will not be able to include everyone. As a result I would like to say thank you to all of you and to apologize from the bottom of my heart that I have not listed your name.

I would like to begin by thanking my advisor, Prof. Shashank Priya primarily for giving me the opportunity to join his lab and his group of highly dedicated, very intelligent and supportive students. Thank you for your support and guidance. Thank you for challenging me and at the same time giving me the freedom to pursue my ideas. You have always given me the utmost respect, and have entrusted numerous projects and tasks even when I did not trust myself to deliver. There have been so many instances when I would feel de-motivated because of a problem I have faced in my research, but after talking to you it would always feel so much better. In fact, one reason why I have been able to achieve as much as I have is that every time I would leave your office, I would get boost of motivation, to create something new, to get inspired and invent the future. I sincerely hope that I will get the chance to work with you in future again and to collaborate on projects that will most certainly make a positive impact to society.

Along with Prof. Priya, I would like to thank my committee members, for their guidance and support. Prof. Kurdila, thank you so much for your help in the various problems I have faced throughout my graduate studies. You were always available to share your ideas, and provide direction in my work. I am thankful that I had the opportunity to sit in your classes and learn

from you. Prof. Hajj, thank you for being there not only as a professor with whom I have discussed research, but also personal matters as well. Prof. Dave, thank you for your time and opportunity to work alongside with you on my first research project as a graduate student. I gained a lot of experience and knowledge which helped me grow as a researcher in the area of engineering with medical field applications. Finally, Prof. Socha, thank you for agreeing to be a part of my committee and to share your professional guidance and provide me with comments and suggestions.

Besides my committee members, I would like to thank Prof. Tarazaga for all the help, guidance and opportunities that has given me. It has been a real joy working in a lab where your expertise, character and personality is present. It has been of enormous help, learning from you, about: vibration, research, life as an academic, positive attitude towards life and so much more.

I would also like to thank Beth Howell, whose help around the lab and offices, had made my research experience so much easier, and if it wasn't for her, my time spent as a PhD student would have been a lot longer. Of course, I would also like to thank, Lauren Mills, Yara Haddad and Erin Singleton for helping with everything else in the office.

Both Justin Farmer and Bryan Joyce have led the CIMSS and CEHMS lab during my years spent as a PhD student. I am very grateful for your help and dedication in making everything run smoothly.

It goes without saying that the presence of colleagues and friends in the lab made my work so much more enjoyable. Every single one of you guys was always very supportive, always available to help, and many times very glad and open to collaborate on projects which made a difference. I thank all of you CIMianSS and CEHMianSS for sharing small parts of your lives with me.

Dr. Amin Karami, Dr. Mana Afshari, Dr. Andy Sarles and Dr. Lei Yu, during the beginning of my Ph.D. you were those I would turn to with any questions I would have. You have represented an inspiration when I would see you work and tackle difficult research challenges. Dr. Karami, thank you for collaborating with me on the L-Shape motors, your knowledge and experience in the field of vibration and smart materials has made a great impact in my research area.

I would also like to acknowledge my collaborators, Sriram Malladi, Dr. Chee-Sung Park, Dr. Ali Aliev, Scott Bressers ,Ravi Kishore, Dushan Vuckovic and Dr. Ashok Kumar, who

assisted me in some of the work presented in this dissertation and at the same time shared their knowledge and experiences with me.

I am also very grateful to our mechanical engineering coordinator and advisor Mrs. Cathy Hill, for always being there to help and guide me through the mechanical engineering graduate program.

A special thanks to my colleague and friend Sriram. I have learned so much from you in the fields of smart materials and vibration. We accomplished much in a very short time on the work on traveling waves. One thing I will miss the most will be working with you. Therefore I am setting a goal with hopes that in near future our paths will once again cross and that we will get to work on things that are truly revolutionary.

Besides my acknowledgements to people tied to the lab, there is still those that have been a part of my life outside the lab as well. These are my friends and family while in the United States and the time before crossing the Atlantic.

I would first like to thank my best friend Aziz (Dr. Mahama Aziz Traore). We have started our endeavors at Virginia Tech in 2005 and we have been side by side together since then. It has been a great joy and privilege to know such a great person with whom I could share anything. Aziz you have been the person that I could go to and talk to at anytime and anywhere. Even though our career paths might take us to different direction and places, my friendship with you will never fade. That is my promise to you.

My very good friends Preston Pinto, Milisav Danilovic, Joseph Najem, Iva Sokolic, Oxana Brenes, Dragan Trifunovic, thank you for being you. You have always been full of life, excitements and ideas. It has been a pleasure just being around you since you have always emitted love and positive attitude. Knowing people like you has changed my life. I could not ask for better friends, with such pure sole and character. Thank you for having to deal with me all of these years.

I would also like to thank my girlfriend Pamela Flausino. I am so happy that I have been blessed to meet such a wonderful person. The past year I have been with you, has definitely given my life a different direction.. Thank you for always listening to me and being the person I can talk to when things are difficult, but also when things are good and pleasant. Thank you for sharing parts of your life with me.

I would also like to thank my host family from Oklahoma: Papa, Naomi, Shauna, Hall and Brandy for allowing both my sister and myself to stay in their home. I had a wonderful time and experience great things while being a part of your family.

From my time before coming to the United States and really from the very beginnings I would like to thank my best friends Marija Kalevska and Darko Stojanovski and my oldest friend Ilco Petrovski. Even with the distance between, our friendship has still remained very strong. You were always there for me back then and I know you are here for me now as well, regardless of the distance between us.

Besides my colleagues and friends, my gratitude goes to my family without whom, none of this would have been possible. First, my grandparents: Dragica and Dragan Avirovik and Borislavka and Dimitar Mitrovski. I cannot imagine life without knowing you and sharing my life with you. You always felt proud, always believed that I can achieve great things. You believed that I could succeed in anything I put my mind to. I miss you all so much and life will never be the same without you. If you can hear me, please know that you will always be in my heart and memories and that I love you very much.

I would also like to thank my dearest sister Dragana Avirovik. Having you here with me and knowing that you are always close by, has always kept me feeling secure and safe. I had to mature and grow as a person away from my parents, and it was definitely not an easy task, but the mere fact that my little sister was always next to me, helped me stay on the right path. We have been through so much together and I believe we have done well so far. You have represented my support all these years and I am very grateful for that. Love you sis!

Last but not least, I would like to acknowledge and thank my lovely parents Gordana and Mladen Avirovik. I am truly proud to call you mom and dad. It is the two of you that made all of this possible. It was your dedication from very early on, to send me to the United States to pursue my education and dreams in hopes for a better future. Your sacrifice to send your children away at the ages of 15 and 17, deserves the utmost respect. I know how it felt for me and Dragana living oceans apart, but I cannot even gauge how you might have felt. You did all of this because you wanted the best future for us. There are no words or means that I can do to repay what you have done for me. The only thing I can do is say thank you. Thank you for allowing me to come to Virginia Tech, thank you for supporting me throughout these years, thank you for helping me reach the title of Philosphiae Doctor, Ph.D. in Mechanical Engineering. As a small symbol of my

appreciation for all that you have done for me so far, I would like to dedicate my Doctoral dissertation presented in this document to the both of you.

LOVE YOU MOM AND DAD!

Table of Content

Chapter 1 – Introduction 1

1.1 Problem Statement 1

1.2 Background 2

1.3 Previous Work 7

1.3.1 Background of Endoscopy 8

1.3.2 Locomotion Mechanisms 13

1.3.2.1 Internal Locomotion Mechanisms Review 14

1.4 Dissertation Structure 18

Chapter 2 – Piezoelectric Actuators: Concept and Theory 21

2.1 Introduction 21

2.2 Concept Design and Principle of Operation 24

2.2.1 L-Shape and U-Shape Piezoelectric Motor 24

2.3 Theoretical Modeling 27

2.3.1 Finite Element Analysis 28

2.3.2 Analytical Modeling of L-Shape Piezoelectric Actuator 31

2.3.2.1 Mechanical Model 32

2.3.2.2 Electro-Mechanical Modeling 45

2.3.2.3 Results and Summary 47

2.3.3 Parametric Study 51

2.4 Conclusion 55

Chapter 3 – Experimental Characterization of Piezoelectric Motors and Development of Locomotion Mechanisms 56

3.1 Introduction 56

3.2 L-Shape Motor Experimental Study 57

3.2.1 L-Shape Motor Characterization 63

3.2.2 Crawling inspired robot utilizing L-Shape Piezoelectric Actuators 67

3.2.2.1 Experimental Characterization 70

3.3 U-Shape Motor Experimental Study 72

3.3.1 U-Shape Motor Characterization 74

3.3.2 Crawling Inspired Robot 76

3.3.2.1 Modeling the kinematics of the robot 78
3.4 Conclusion 80
Chapter 4 – Controlled Locomotion of Wireless Capsule Endoscopes through Traveling Wave Phenomenon 81
4.1 Introduction 81
4.2 Traveling Waves Formation 83
4.3 Theoretical modeling 85
4.4 Experimental Characterization 89
4.5 Mechanical Wave Characterization 93
4.6 Conclusion 102
Chapter 5 – Complementary Technology for the Intelligent Healthcare Environment 103
5.1 Multifunctional Image Guided Surgical Platform (MIGS) 104
5.1.1 Introduction 104
5.1.2 Design and Development 105
5.1.3 Three-axis positioning and scanning stage design using only two actuators 107
5.1.3.1 Dynamics of stage 109
5.1.3.2 Kinematic study 111
5.1.3.3 Control System 114
5.1.3.4 Experimental Analysis 117
5.1.4 Comparative research study 121
5.1.5 Applications of three-axis positioning and scanning platform 125
5.1.5.1 Laser based micro-machining 126
5.1.5.2 Mask-less lithography 128
5.1.6 Conclusion 129
5.2 Miniature Shape Memory Alloy Heat Engine for Powering Wireless Sensor Nodes 130
5.2.1 Introduction 130
5.2.2 Experimental Setup and Principle of Operation 132
5.2.3 Experimental Characterization of Device 134
5.2.4 Demonstration study 136
5.2.5 Discussion 137
5.2.6 Conclusion 139

5.3 Carbon Nanotube Thermo-Acoustic Projector 139
5.3.1 Introduction 140
5.3.2 Modeling 142
5.3.3 Results and Discussion 145
5.3.4 Conclusion 151
Chapter 6 –Conclusions and Future Studies 152
6.1 Summary and Conclusion 152
6.2 Future Studies 153
Appendix A. Remote light energy harvesting and actuation using shape memory alloy – piezoelectric hybrid transducer 161
A.1 Introduction 161
A.2 Design concept and experimental setup 162
A.3 Hybrid system characterization study 163
A.4 Material analysis and optical properties of SMA wire 167
A.5 Conclusion 169
Publications that have resulted from this dissertation 170
References 171

List of Figures

Figure 1.1 Most common medical errors 2
Figure 1.2 Projected technological components that will be required for an intelligent hospital room 6
Figure 1.3 Intelligent hospital room representation 7
Figure 1.4 Key functionalities that complement the wireless capsule endoscopes 9
Figure 2.1 1st Mode Shape of a Piezoelectric Bimorph with Clamped – Free Boundary Conditions 24
Figure 2.2 Piezoelectric motor structure and 3D orientation: (a) L-Shape piezoelectric motor, (b) U –Shape piezoelectric motor 25
Figure 2.3 Principle of Operation: (a) Motion of the L-Shape Piezoelectric Motor; (b) Sinusoidal Voltage Signals Delivered to the Base and Wing. 27
Figure 2.4 ATILA Model of the L-Shape Piezoelectric Motor 28
Figure 2.5 FEM Impedance - Frequency Relationship for Base and Wing, (a) Base Length = 9mm, Wing Length = 27mm, (b) Base Length = 11mm, Wing Length = 27mm. 30
Figure 2.6 Simulation of the L-shaped Piezoelectric Motor using ATILA 31
Figure 2.7 Piezoelectric motor structure and 3D orientation. 33
Figure 2.8 Determinant vs. frequency relationship for base and wing: (a) Base length =9mm, Wing length=27mm, (b) Base length=11mm, Wing length=27mm. 39
Figure 2.9 Natural Frequencies for the L-Shape Piezoelectric Motor. 41
Figure 2.10 Mode Shapes of the L-Shape Structure: (a)1st Bending Mode of Wing, (b) 1st Bending Mode of Base, (c) 2nd Bending Mode of Wing, (d) 2nd Bending Mode of Base, (e) 3rd Bending Mode of Wing, (f) 3rd Bending Mode of Base. 43
Figure 2.11 First natural frequency as a function of the length of base. 45
Figure 2.12 Transfer Function for displacement at motor's tip. 49
Figure 2.13 3-D tip motion as a function of frequency. 50
Figure 2.14 3-D Tip motion as a function of voltage. 51
Figure 2.15 Relationship between the natural frequency of the motor and its size 52
Figure 2.16 Simulated tip motion as a function of size and natural frequency of L-Shape motor. 53
Figure 3.1 L-Shape Piezoelectric Motor Prototype 58
Figure 3.2 Experimental Impedance - Frequency Relationship for Base and Wing, (a) Base Length =9mm, Wing Length=27mm, (b) Base Length=11mm, Wing Length=27mm 58
Figure 3.3 Experimental Setup for Measuring Elliptical Motion at Tip. 59
Figure 3.4 Laser vibrometer readings at the tip of the L-Shape motor 60
Figure 3.5 Principle of operation – analytical, (a) static equilibrium, (b) Base Voltage = Max, Wing Voltage = 0, (c) Base Voltage = 0, Wing Voltage = Max, (d) Base Voltage = Min, Wing Voltage = 0, (e) Base Voltage = 0, Wing Voltage = Min, and (f) Same as Motion in (b). 61
Figure 3.6 Motion at the tip of the L-Shape Piezoelectric Motor. Comparison between experimental Model, FEM Model and analytical model. 62

Figure 3.7 Experimental setup for actuating linear stage. 63
Figure 3.8 Velocity data of linear stage with different surface materials. 64
Figure 3.9 Experimental setup for measuring rotational velocity, torque and efficiency. 65
Figure 3.10 Displacement and velocity curves of the L-Shape piezoelectric motor. 66
Figure 3.11 Load characteristics of L-Shape piezoelectric motor. 67
Figure 3.12 L-Shaped piezoelectric motor. 68
Figure 3.13 Crawling robot principle of operation: a) Actuation setup of piezoelectric motors, b) Schematic diagram representing the gait of the robot 69
Figure 3.14 Forces produced by robot: a) Forces in x, y and z direction as the robot moves, and b) Pull force exhibited by the robot 71
Figure 3.15 Motion of the tip of the legs: a) motion of the legs in the x-direction, b) motion of the legs in the y-direction, c) elliptical motion generated at the tip of each leg 72
Figure 3.16 Principle of operation of U-shaped piezoelectric motor and its vibrational characteristics 74
Figure 3.17 Performance characterization curves of U-Shape piezoelectric motor: (a) Angular velocity and angular displacement as a function of time, (b) Mechanical power as a function of angular velocity, (c) Angular velocity and efficiency of motor as a function of torque. 76
Figure 3.18 Millibot: (a) Millipede inspired mobile robot utilizing U-Shaped piezoelectric motor, (b) Experimental setup, and (c) Gait of millibot 77
Figure 3.19 Locomotion characterization of the millibot: (a) Four distinct time steps demonstrating the motion of the robotic legs, (b) Elliptical motion generated at the tip of the motor in the x-y plane 78
Figure 3.20 Circle reference and variables of the path that the legs trace. 79
Figure 4.1 Concept of traveling wave based wireless capsule endoscope 82
Figure 4.2 Schematic description of the approach used for the analysis of locomotion mechanism inspired by the traveling wave phenomenon 83
Figure 4.3 Concept description for formation of the traveling waves through finite medium. 85
Figure 4.4 Schematic diagram of the beam structure. 86
Figure 4.5 Experimental analysis of traveling waves generated on a free-free beam. (a) Experimental Setup, (b) Modal Analysis, (c) Traveling wave through free-free beam 89
Figure 4.6 3D representation of traveling waves obtained (a) theoretically and (b) experimentally. 91
Figure 4.7 Complete analysis of the traveling waves through finite medium and their behavior on a free-free beam 92
Figure 4.8 Traveling wave envelope obtained experimentally and theoretically. Actuation was conducted at a frequency between two mode shapes with phase difference of 90° and frequency of 241Hz. 93
Figure 4.9 Conceptual illustration of standing, traveling and hybrid waves and the different methods of their classification 96

Figure 4.10 Comparison of mechanical waves obtained experimentally and theoretically at 243Hz and phase difference of 90° between the two excitation signals: (a) traveling wave waveform, (b) response of the wave according to the Hilbert's approach, (c) response of the wave according to the Fourier's method 97
Figure 4.11 Parametric study and cost function analysis Red color – wave travels from right to left, blue color – wave travels from left to right. 98
Figure 4.12 Theoretical and experimental results of the cost function between the 2nd and 3rd mode shape. (a) Cost Function window between the two mode shapes, (b) Theoretical and experimental results of the CF as a function of frequency and phase angle 90°, (c) Theoretical and experimental results of the minimal CF 100
Figure 4.13 Comparison between the Hilbert's and Fourier's approach at 243Hz (a-c) and 720Hz (c-d) : (a and d) Hybrid wave waveform, (b and e) CF as a function of points taken across the structure, Points corresponding to the maxima, minima and arbitrary in between the two are presented. Fourier's approach, (c and f) CF as a function of points taken across the structure, Hilbert's approach 101
Figure 5.1 (a) Linear stage using lead screw mechanism, (b) Free body diagram (FBD) of translational motion using lead screw mechanism 106
Figure 5.2 Three axis scanning and positioning stage: (a) CAD design, (b) Prototype 107
Figure 5.3 (a) Z-axis mechanism, (b) Diagram of translational mechanism in the z-axis example problem) 109
Figure 5.4 (a) Workspace representation of the three-axis scanning and positioning stage, (b) Diagram describing the Cartesian manipulator composed of prismatic joints and links 112
Figure 5.5 Diagram of the control system for the three-axis positioning and scanning stage 115
Figure 5.6 (a) Experimental setup diagram, (b) Experimental setup 117
Figure 5.7 Velocity measurements in the X and Y direction 118
Figure 5.8 Rigid motion study: (a) x-axis out of the page, (b) x-axis into the page, (c) y-axis out of the page, (d) y-axis into the page. 1, 2, 3 are the sections representing the x-axis and 4, 5, 6 the sections representing the y-axis. Each section is defined by 28 individual points. The symbols before each number: " – ", " --- " and " + ", represent motion in the negative direction, mid position and motion in the positive direction respectively 119
Figure 5.9 Complex geometrical patterns written using the 3-axis stage: (a) Maze, (b) Raster Scan, (c) Virginia Tech logo 121
Figure 5.10 Actuator comparison chart 122
Figure 5.11 Three axis motorized stage comparison chart 124
Figure 5.12 Setup for a laser-based micromachining 127
Figure 5.13 MEMS Fabrication procedure. (a) Conventional vs. Proposed, (b) mask-less photolithography setup in the clean room 129
Figure 5.14 Measurement technique: (A) Illustrative diagram of experimental setup, (B) Experimental setup used for characterization 133
Figure 5.15 Angular speed of the generator as a function of temperature 134

Figure 5.16 Mechanical characterization of SMA turbine: (A) Angular velocity and Torque curves, (B) Mechanical power as a function of angular speed 135
Figure 5.17 Electrical characterization of SMA turbine: (A) Output voltage as a function of resistance, (B) Electrical power as a function of resistance..... 136
Figure 5.18 Block diagram of the wireless node 137
Figure 5.19 Conceptual illustrations for implementation of miniature SMA heat energy harvester 138
Figure 5.20 Thermo-acoustic sound projectors inside the human body 140
Figure 5.21 Experimental setup for characterizing MWCNT sheets..... 142
Figure 5.22 Lumped element mechanical model representation of the CNT projector..... 142
Figure 5.23 Displacement and Velocity as a function of time..... 144
Figure 5.24 (a) Natural frequency as a function of stiffness, (b) Amplitude of vibration as a function of natural frequency..... 145
Figure 5.25 Free-Free boundary conditions for vibrational characterization of variable MWNT sheets TA device: a) Soft mat, b) stiff mat, c) table top, d) hanging, e) suspended 146
Figure 5.26 Vibration characterization study: a) Frequency response spectrum of TA device based on different free-free boundary conditions, b) 1st Mode Shape, c) 2nd Mode Shape, and d) 3rd Mode Shape. 146
Figure 5.27 Velocities and displacement of TA devices at 1st natural frequency: a) Velocity through the centerline in x direction, b) Velocity through the centerline in y direction, c) Displacement through the centerline in x direction, and b) Displacement through the centerline in y direction. 147
Figure 5.28 (a) Schematic diagram of the TA projector comprising free-standing MWNT sheet suspended between two soda-lime glass plates (1x50x75 cm3 Corning microscope slides). (b) The typical image of the plate displacement at first harmonic taken by scanning laser vibrometer Polytec PSV400. (c) The sound pressure spectra of several TA projector comprising single MWNT sheet suspended between two glass plates. The spectra were taken in the near field (r=3 cm) in air. 148
Figure 5.29 Vibration summary results of TA device with different compliance: (a) velocity profile in x direction, (b) velocity profile in y direction (c) displacement profile in x - direction, (d) displacement profile in y direction, (e) 3-D profile for different compliance designs. (C-C-C-C corresponds to clamped conditions around the four edges, S-S-S-S corresponds to simply supported conditions around the four edges)..... 149
Figure 5.30 Temperature profile of TA device with three different sections, three layers, two layers and single layer of CNT sheets..... 150
Figure 5.31 Experimental results on the thermal characteristics of TA device: a) Temperature profile through the center line over TA device for different power levels at 60sec time interval, b) Temperature profile through the center line of TA device as a function of time at 3.7W power input, and c) Cooling profile of TA device..... 151
Figure 6.1 Suction mechanism: (a) Initial state, (b) Suction 154

Figure 6.2 Design of a L-Shape actuator driven capsule with a suction mechanism 155
Figure 6.3 Prototypes of traveling wave inspired locomotion mechanisms: (a) free-free beam, (b) wireless capsule endoscope..... 156
Figure 6.4 Alternative concept of the one presented in Figure 4.2, Chapter 4. 157
Figure 6.5 Altering the properties of SMA in order to change the dynamics of the system 159
Figure A.1 Schematic representation of system: (a) Piezoelectric bimorph in a cantilever beam configuration in non-deformed and deformed shape as a result of SMA wire actuation, (b) Hysteresis loop of SMA, (c) Voltage generated by the piezoelectric bimorph and tip deflection of cantilever beam. 162
Figure A.2 Experimental setup used in this study 163
Figure A.3 (a) Experimentally obtained hysteresis loops of SMA wire, (b) Experimental and numerical model of temperature as a function of time to determine heat transfer coefficient, (c) Outputs of the system as a function of time..... 165
Figure A.4 Power generated by the piezoelectric bimorph as a function of frequency for different preloads and SMA attachment locations..... 166
Figure A.5 Actuation characteristics of system: (a) Tip displacement as a function of different preloads, (b) Tip displacement as a function of load at different frequencies of excitation..... 167
Figure A.6 (a) X-ray diffraction pattern, (b) absorbance, and (c) and (d) Raman spectra of the SMA..... 169

List of Tables

Table 2.3-1Geometrical Properties of the Piezoelectric Bimorph Used in the ATILA Analysis. 29
Table 2.3-2 PZT-5X45 Properties Used in the ATILA Model 29
Table 2.3-3 Other Materials Used in the ATILA Model 29
Table 3.2-1 Comparison of Results 62
Table 4-1 Experimental and theoretical results for the natural frequency of free-free beam 90
Table 5.1-1 Three-axis positioning and scanning stage specifications 111
Table 5.1-2 D-H Parameters for three-axis positioning and scanning stage 113
Table 5.1-3 Actuator specifications 123
Table 5.1-4 Three axis motorized stage specifications 125

Chapter 1 – Introduction

1.1 Problem Statement

Misdiagnosis is a very common mistake that occurs in the medical field with alarming 40% of the total cases often resulting in consequences of severe magnitudes due to wrong or missed treatment. As a consequence, missed diagnostics have been responsible for $38.8 billion in spending between 1986 and 2010, [1] and this has been the cause for injuries for 80000-160000 patients yearly. Even though medical practitioners are trained to provide careful and systematic diagnostics, these are not 100% accurate. It is therefore necessary to understand that misdiagnosis occurs primarily due to the lack of information doctors acquire from their patients. Often the reason for this is that current technology does not provide conclusive analysis of the causes for specific diseases. There are many possibilities for the symptoms exhibited by the patient and unfortunately a correct diagnosis requires multiple tests. This could be both time consuming and also source for error. What is needed is automation and continuous monitoring techniques that are able to utilize data analytic techniques to predict the right diseased state.

Unlike misdiagnosis, there are also medical errors that can result in deterioration of the sickness. According to the study conducted for CNN Health, [2], quarter million causalities and several million injuries in United States occur due to the errors such as the ones listed in Figure 1.1. Patient falls due to the negligence costs the US healthcare system $1billion annually, [3]. Moreover, infectious diseases inside the Emergency Rooms (ER), waiting areas, procedure rooms and hallways represent a serious problem in hospitals. There have been recorded 1.7 million healthcare infectious diseases in U.S. hospitals [4], and around 100000 deaths each year from such infections. Mistakes are inevitable in any institution and unfortunately they will continue to exist. The biggest distraught is that many of these errors can be avoided by proper support from technology. Integration of sensors networks inside hospitals will be able to provide information that could assist in continuously acquiring information which will provide resources to tackle the errors. However, distributed sensor networks require a power source that will allow their continuous unrestrained operation. The dominant sources for power are batteries, but they need to be periodically replaced and/or recharged which imposes maintenance issues. In case, the sensors are embedded in the structure then replacement or recharging would not be feasible. Thus, other sources for powering the sensor nodes have to be developed.

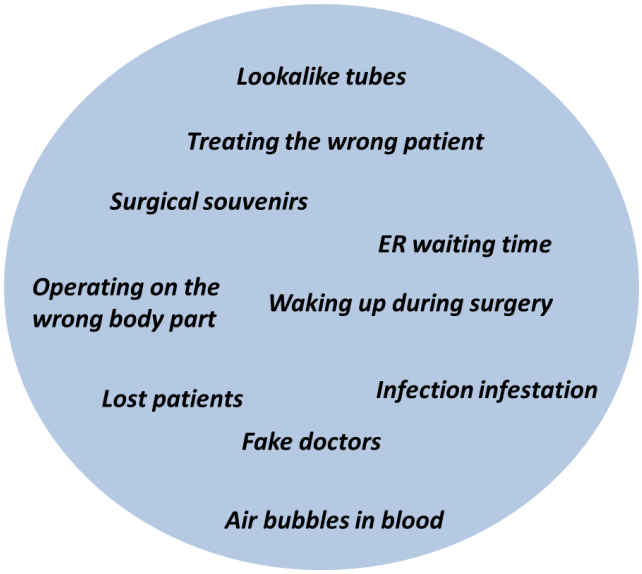

Figure 1.1 Most common medical errors

1.2 Background

Developing a futuristic high-tech hospital establishment requires the merger of many technologies and their integration. This dissertation focusses on some novel technologies that will pave the pathway for better diagnostics, error-free hospital environments and comfortable experience for the patients.

Determining the disease that a patient is facing can be established by identifying all the symptoms and then properly correlating them with the known disease conditions. One way to achieve this is through the development of equipment, sensors and instruments which will be able to diagnose, treat and communicate between each other in order to form a closed loop system. This system will be able to acquire and analyze the collected data and correspondingly produce an appropriate response such as: alerting of medical staff, repeating diagnostics or conducting alternative one, and/or executing treatment protocol.

From a diagnostic point of view, some of the most commonly used technologies in hospitals are imaging instruments: Magnetic Resonance Imaging (MRI), X-Ray, photo acoustic imaging, thermography, ultrasound, endoscopes, and etc.

With its roots going back to the 1st half of the 20th century, the MRI has come long way and has become one of the most essential tools in the field of diagnostics. [5]. MRI works on the principle of imaging the protons which are abundant in the human body. When resonance frequency (Larmor resonance frequency) is applied, the protons align with the magnetic field;

they absorb the energy and then relax back to the original state. During relaxation they produce a voltage spike which is detected by the radio antenna. Based on the strength of the signal and its density, the MRI machine is able to create an image of the interior part of the human body. MRI has been used in detecting neoplastic meningitis with limited use in leukemia and lymphoma, [6], breast cancer detection[7], multiskeletal system, [8], detection of brain tumor, [9] and etc.

X-Ray or computed tomography [10] is another widely used tool for scanning the abnormalities in body. It uses electromagnetic radiation at frequencies in the range 30 petaherz-30exahertz. As the patient is exposed to the X-rays, some of the rays are absorbed by the bones due to their high calcium content. As such they do not reach the detector and consequently makes them visible on the radiograph generating contrast in the images.

Photo-acoustic imaging [11] works on the principle of generating acoustic waves through light. For this imaging technique, non-ionized laser pulses are sent to biological tissues. The energy which is absorbed is converted into heat and leads towards thermoelastic expansion, which can be deteced by ultrasonic transducers. In this case, optical scattering increases with the depth of penetration. For these reasons, they are mainly used for imaging at distances of 1mm below the skin. Some of the key imaging function for photo-acoustic imaging is cancer detection.

Similar to the photo-acoustics, another technology that uses optics for imaging is optical coherence tomography (OCT) [12, 13]. This imaging technique uses near infrared light to penetrate the skin with depths below 1mm. It is similar to ultrasound however instead of sound it uses light to obtain a cross-sectional image of the tissue. Unlike other methods, this technique obtains very high quality image of the tissue topography and can be used to detect skin cancer and tumors in the skin.

Another imaging approach is thermography, [14] which was established on the principle of detecting the heat radiation and physiology of thermoregulation of the human body. One application of this technique is for breast cancer detection since the tumor requires increased supply of nutrients which increases circulation and causes temperature increase.

Another acoustic method for diagnostics is ultrasound [15]. Medical sonograph is used to capture the size and image of the muscles, tendons, including many internal organs. A high frequency sound 2-18MHz is produced and directed towards the human body. By measuring the time delay between the generated sound and the reflected one which is received by the receiver,

it causes a transducer to generate electrical signals. These signals are then processed and digital images are constructed.

Endoscopy represents the less-invasive procedure unlike the non-invasive procedures previously discussed. Endoscopes are equipped with cameras and are mainly used for inspecting the gastrointestinal (GI) tract of the human body but can also be used for inspecting the respiratory tract, the ear, the urinary tract and the reproductive systems.

Besides imaging tools, other sensors in hospitals can be of significance if they can be used for collecting relevant information unobtrusively. One type of sensor is radio frequency identification (RFID) that has the potential to play important role in hospitals. Through proper integration, these sensors can assist in eliminating or at least drastically reducing some of the medical errors presented in Figure 1.1, [16]. The RFID system is composed of two key elements, RFID tag and RFID scanner. The RFID tags contain information which is electronically stored and can be integrated on tools, equipment, patients, doctors etc. RFID tags can be scanned while in motion without the need to be in the direct line of sight. These tags are composed of antennas and electronic chip which are responsible for transmitting data signals. Tags can use batteries or collect energy from the electromagnetic field produced by the RF scanner. The active RFID tags send out periodic signals to a reader and the passive ones only transmit the information when illuminated by an RFID scanner. The RFID can also be active if it reads signals from a passive tag or be passive if it reads a signal from an active tag. A computer or smart phone can control the scanner and can also acquire and analyze the data. The integration of such technology can provide important information on identification and localization of staff and patients and localization of medical equipment within the hospital. In addition this technology can serve as access key to different rooms, patient files, medical drugs and etc. In a Smart Hospital, every patient, doctor, administrative staff or hospital staff will have an RFID tag. This tag will allow the medical staff to know whether the patient is in the hallway, the restroom, at a rehabilitation site or is undergoing a surgery. In a scenario where the RFID tag belongs to a medical staff, as soon as the nurse or doctor enters patient's room, a snap shot of the patients' vital signs and sensory interpretation will be automatically displayed on a screen. Based on their clearance level, they will be able to get access to the patient's medical history and daily treatments and accordingly admit the proper medication.

The General Electric (GE) Company is a major player in the area of a Smart hospital. One of the initiatives of GE is developing technology which will mitigate medical errors through the integration of intelligent real-time monitoring system, [3]. Monitoring hand hygiene compliance, clinical rounding adherence and patient falls are some of the tasks being pursued. It uses RFID technology and system visualization algorithm that is able to track the patients' face and detect whether patients are in need of assistance or not. In a scenario where a patient is crying or is in pain, the system detects it and consequently alerts the medical staff for attendance. But RFID are not the only sensors that can find use in hospitals. Temperature, humidity, occupancy, motion, heat, acceleration and other sensors will be used as well. The downside is that all these sensors need some type of power source, which currently is dominated by batteries. Batteries though, unfortunately follow the slowest progression trend in mobile computing. They often need to be recharged or replaced, they have limited life span and there is also the issue with their disposal.

Because of these reasons it is essential that alternative power solutions are discovered and matured. Energy harvesting is a research area which explores this issue. This research topic is challenging and is even more complex in the indoor environments. In nature, energy sources that can be found in abundance are: solar, wind, geothermal, hydro and vibration. Only few of them can find applications in indoor environment and the most promising among them are thermal and vibration. *Since vibration can mainly be obtained from operating machines and the source of vibration needs to produce very high amplitudes for significant power harvesting, the focus in this dissertation was mainly towards thermal sources such as hot water/steam pipes*.

Another initiative by GE is developing a more attractive imaging diagnostic room for kids. The Adventure Series ^{TM} is an experience which makes imaging technologies such as Magnetic Resonance Imaging (MRI), X-Ray, and Computed Tomography (CT) more inviting. Instead of conventional hospital paint and design, the GE Adventure Series ^{TM} has redesigned them into different colorful experiences that young children find very amusing, such as: Pirate island, Coral city, Space adventure, Jungle adventure and etc., [17].

Comfort in hospital environment is an essential ingredient towards expediting the healing process. Besides the integration of electronic devices such as video game consoles, TV and internet, aesthetics and acoustics can be adjusted to provide additional support through sound therapy. It has be shown that sound therapy can enhance the relaxation and reduce the stress

levels [18]. In addition, sound can also aid in the relief of many pathologies. Stress is a common problem, but it is very often present in patients which have or will undergo medical surgical procedures. Since stress can potentially enhance other side effects [19] it can have adverse effect on the medical procedure that is about to be performed and therefore lead to complications. Medical therapy through sound can be used to activate the Nitric Oxide (NO) molecule that offers protection against microbes and physiological disorders such as hypertension. In addition it can diminish the immune and endothelial activation. *In this thesis, a novel sound generating device is introduced that has two purpose (1) provide a source for acoustic localization in the wireless capsule endoscope WCE module, and (2) provide a source for customized sound therapy through flexible speakers.*

The development of SMART futuristic hospital has several practical challenges that need to be addressed by developing multifunctional technological components. Figure 1.2 describes a set of tools that can assist with the transformation of an ordinary hospital room into an intelligent environment. Some of these elements are: sensors, simulation equipment, diagnostic tools and various electronic components that help in creating a safe and relaxing environment while providing the state-of-the-art automated diagnostics and prognostics.

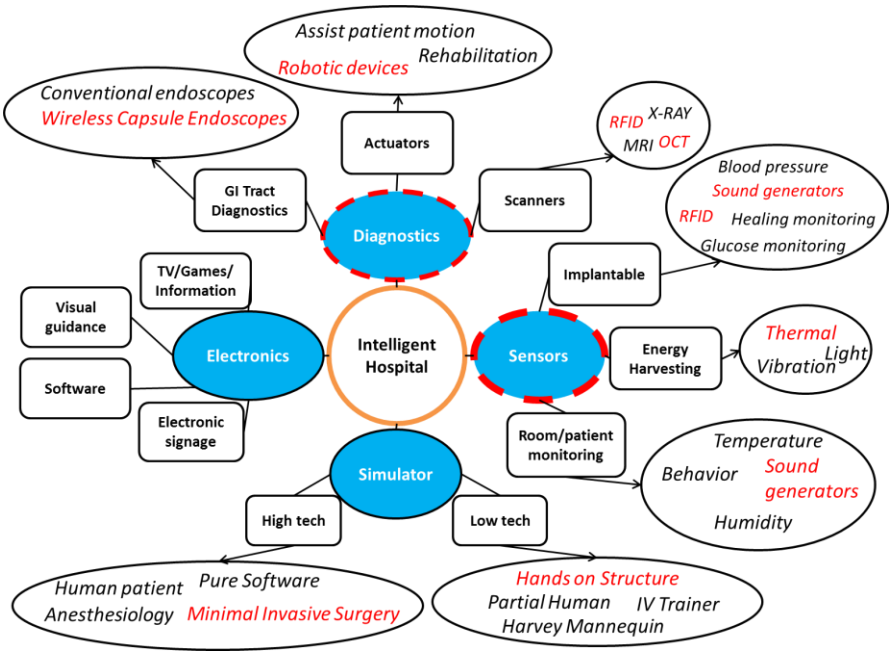

Figure 1.2 Projected technological components that will be required for an intelligent hospital room

This dissertation focuses on a subset of technological advancements required for intelligent healthcare environment. The integration of these devices/technologies into a smart hospital room, Figure 1.3 will provide the rapid advancement required to achieve the vision of automated healthcare that is cheap, reliable and fast. The numbers in this figure correspond to the four focus areas in this thesis.

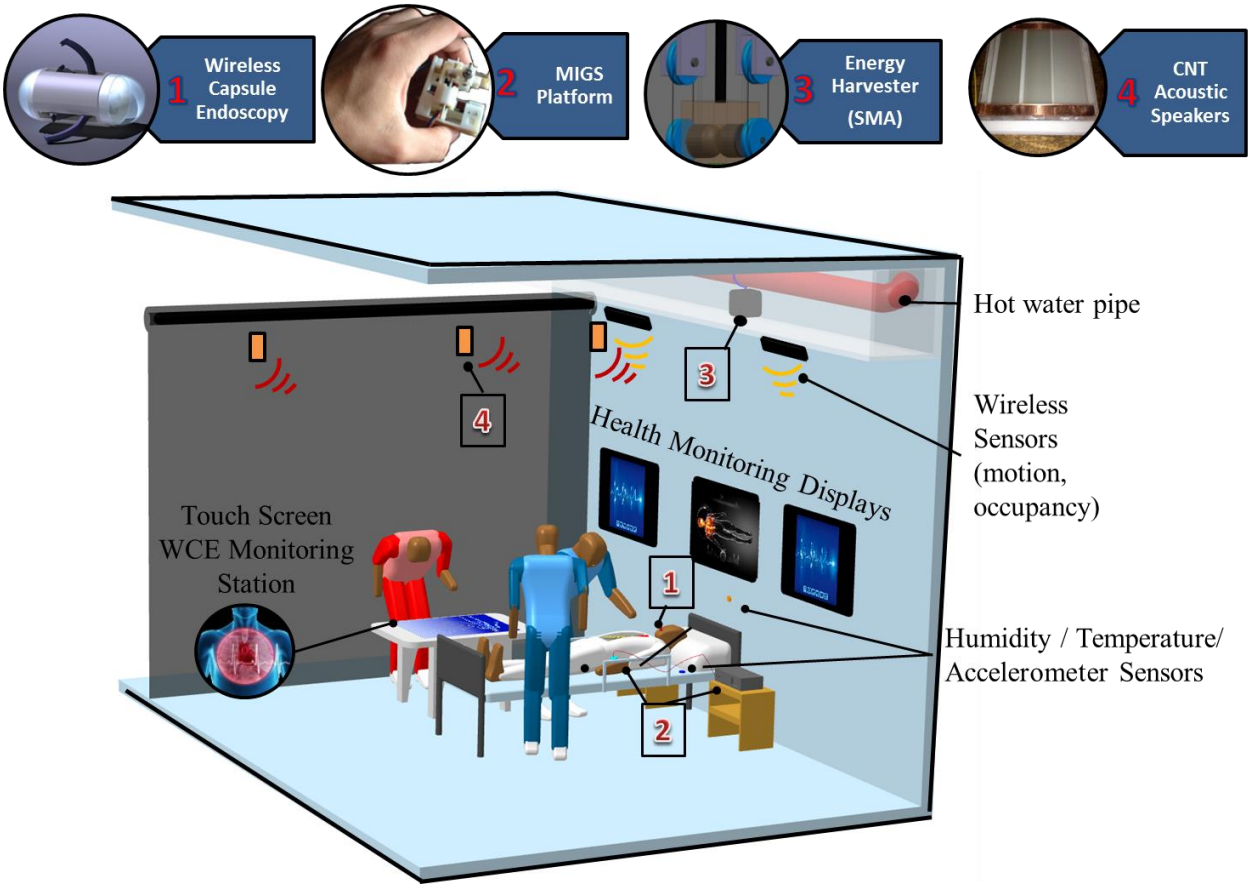

Figure 1.3 Intelligent hospital room representation

1.3 Previous Work

As described by Figure 1.3, there are four key technologies that are addressed in this dissertation. The main emphasis was towards the development of active locomotion mechanism for wireless capsule endoscopes, represented as "1". First, in order to introduce the current state of the research in these areas and define the problem statement for wireless capsule endoscopy, a detailed literature review is provided.

1.3.1 Background of Endoscopy

Endoscopy of the upper and lower Gastro Intestinal (GI) tract is considered to be a routine diagnostic and therapeutic outpatient procedure. It is a procedure for closer and noninvasive examination of the GI tract, conducted by insertion of endoscopes through the human esophagus or rectum. These medical instruments are defined by long flexible tubes that contain illumination component, lens/camera visual system, and additional tube that enables introduction of medical instruments or manipulators. Accordingly, they provide diagnosis and therapy of a wide variety of pathologies that originate in the epithelial tissue. Moreover, upper and lower GI endoscopies are considered to be powerful tools in diagnosis of gastrointestinal inflammatory disease (gastritis, esophagitis, Chrons disease, Inflammatory bowel disease)[20], cancer [21], varicose venous structures [22]. The same procedure can be utilized for minor therapeutic procedures such as foreign body removal[23], sclerosis/ banding of esophageal varices[24], esophageal stenting[25], and removal of GI polyps[26]. Advances in fiber optics and imaging technology have greatly improved the visualization capabilities of conventional endoscopes. Nevertheless, the reach and maneuverability of tethered endoscopes is limited. Comprehensive endoscopy of the organs in the digestive system such as esophagus, stomach, small and large intestines is very difficult, if not impossible.

It was in the earlier part of the last decade when the wireless capsule endoscopes (WCEs) were introduced, which leveraged the advances in telemetry, telemetry (Pillcam, Given Imaging Ltd.), miniature optics and microelectronics. Respectively, these achievements are responsible for a paradigm shift in visualization of the GI tract for clinical diagnosis. Currently WCEs are approved by the FDA for the diagnosis of Crohn's disease, intestinal bleeding and inflammatory bowel syndrome. Due to the size and less invasive functionality when compared to conventional endoscopes, patients are far more receptive to undergo a WCE procedure. Nonetheless, WCEs come with major disadvantage over conventional endoscopes because of their passive nature. They cannot be controlled or conduct biopsy, and targeting specific areas of interest inside the GI tract is simply inconceivable. Consequently, the results of the WCE's operation as it moves along the GI tract are images acquired at random locations and orientations. These images are wirelessly transmitted to a recorder worn by the patient around the waist or are saved onto a chip inside the WCE and then uploaded to a computer once removed from the GI tract. Once acquired, these images aid towards a coarse medical diagnosis.

In view of the current state of the art research accomplishments in endoscopy, the intention of the work in this dissertation is to contribute towards advancing this technology by transitioning the behavior of existing WCEs from passive to active. Likewise, it is one of the key objectives of the research vision previously described, to develop a controllable pill-size medical which will aid towards more sophisticated medical diagnostics.

Designing a swallowable device that can replace conventional endoscopes is a challenging task and requires interdisciplinary research approach with focus on finding solutions for the following key functionalities presented in Figure 1.4 and discussed in more details in, [27]: locomotion, diagnostics, localization, power, anchoring, telemetry, tissue manipulation and vision. Accordingly, in the past decade considerable research has been conducted towards resolving some of the fundamental challenges associated with WCE. Out of all the research areas covered in Figure 1.4, perhaps one of the most influential for the future of medical robotics is the locomotion mechanism. It is in fact, this functionality that has one of the largest impacts in WCE technology and what has represented an inspiration behind the research focus contained in this proposal.

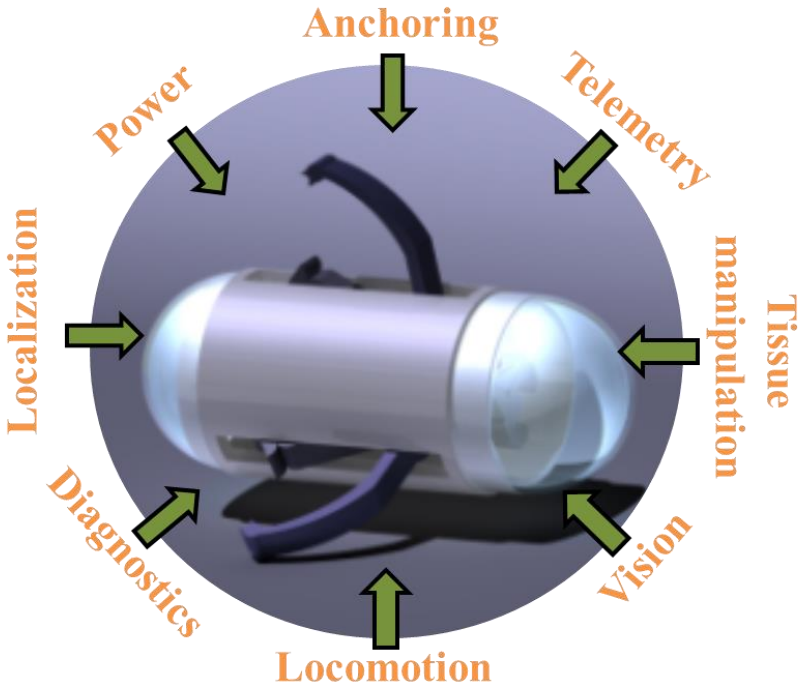

Figure 1.4 Key functionalities that complement the wireless capsule endoscopes

Vision: Acquiring and transferring images obtained from the GI tract over to a platform outside the human body is one objective that WCEs need to accomplish. The images need to be of high definition and should be transmitted at around 24 frames per second in order to appear as a video. This will provide better control over the device and will improve the diagnostic capabilities. The images/video can either be stored on a small hard drive integrated onto the capsule, or the images can be viewed as they are being acquired. The latter is the more appropriate research initiative since real time feed is necessary in cases when biopsy or intervention is required.

The vision system requires on board hardware composed of: vision sensor, lens, illumination source, image compression chip and optimal sensor (which is composed of charged couple devices). Nevertheless, current image sensors capture 2 frames per second and collect around 55000 images from the very beginning to the end of the operation inside the GI tract [28]. Since the data transfer between the capsule and the outside platform is rather slow, image compression is also essential. The challenge lies in the data transfer when the power is limited and the size requirement is critical. For future robotic capsules the estimate is 20 or more compression ratio [29]. Besides the ability to transfer images at high rate from the capsule, other great challenge is the quality of the images acquired. A comparison between the capsule vision system and traditional endoscopes has been presented in [30]. It has been determined that capsule endoscopes are safe method of visualizing the mucosa through colons fluids, however the sensitivity of detecting colonic polyps, advanced adenomas and colorectal cancer is very low. In order to obtain better quality images a much more extensive bowel preparation regime on patients is required. In addition, a great potential is the ability to visualize the entire intestine environment. Even if the streaming obtained is 24 frames/sec, it does not guarantee that specific areas are going to be captured. For these reasons, it is highly desired that a 360° angle of view vision system is available, [31] in order to make a safe decision on the diagnosis.

Localization: Inside the GI tract, the capsule travels from esophagus through the stomach to the small and large intestines. As seen from the PillCam capabilities, images of the tract can be obtained via the integrated camera, however, the exact location of the capsule inside the body remains a mystery. In order to be able to locate where the images of specific lesions are taken, an accurate tracking of the bio-robot capsule is required. This will improve the accuracy of the diagnosis and it will be able to use this location as a reference for future treatments. So far,

four methods of tracking the capsule have been explored: radio frequency (RF) triangulation, magnetic tracking, computer vision and ultrasound, [32]. For both the RF triangulation and magnetic triangulation, array of sensors outside the body are used to measure the signal coming from the capsule. Using magnetic theory for the latter one and a permanent magnet inside the capsule, an estimate of the location of the capsule can be found. An estimate instead of exact location can be obtained due to the fact that the signals from the body go through different mediums, therefore, delays in acquiring the data is obtained. Due to noise in the signals the experimental error can reach 37 mm using RF and around 5 mm using magnetic tracking. RF signals do not propagate efficiently through water environment and due to the fact that the body is 65% water, RF is not the most accurate localization approach. Ultrasonic pulses emitted outside the body and echoed from the capsule can also present a way of tracking the capsule along with tracking of the radioactive material placed inside the capsule which will emit signals that are strong enough to be detected using radiation cameras, but weak enough to avoid adverse effect to the patient's health [32]. There are two methods which can be proposed for tracking the capsule inside the GI tract. One of these localization method consists of two parts. A permanent magnet is placed inside the wireless capsule which is located at x, y, z location inside the human GI tract with respect to a reference frame. Since the permanent magnet emits a magnetic field, the same can be measured using magnetic sensor such as the 3-axis magnetic sensor with microtesla sensitivity, HMC1043 (Honeywell). This array of magnetic sensors can be integrated on a vest which the patient can wear while the endoscopic procedure is under way. An external power supply can be used to power the magnetic detection sensors which can also be integrated with the vest. Once the signal is detected, it is amplified, ran through a control circuit, and the data is acquired. Using triangulation algorithm an accurate positioning and orientation of the magnet, i.e. the capsule can be obtained. The focus would be to utilize this existing technology and improve it by providing a visual representation of the position and orientation of the WCE on a display screen, such as laptop. This approach has not yet been tested but it is expected to provide an *estimated* visual representation of the movement of the capsule inside the digestive tract. Before the diagnosis begins, a scan of the human body can be obtained using any regular high resolution technique such as MRI. This will provide the information of the size and shape of the digestive tract specific to the patient's body. This image file can then be saved as an STL file and opened by computer aided design (CAD) software such as NX Unigraphics or Solid Works,

which will provide 3-D representation of the GI tract. Once this is accomplished, an interface of the 3-D image obtained from the CAD software with NI Labview can be obtained. Combining the 3-D image, with the data acquired from the magnetic sensor a virtual graphical representation of the capsule moving through the patient's body can be created.

An alternative to this method would be acoustic wave triangulation and communication with either implantable sensors or sensors placed outside the patient's body. This approach coincides with some of the research efforts pursued in this dissertation and accordingly is presented in Chapter 5.3.

Telemetry: Wireless communication is what makes WCEs the state of the art medical device. The Pillcam uses unidirectional communication. It acquires images from the GI tract and then transfers them to a receiver outside the body. For future WCEs, however, the communication has to occur in both directions. In one direction, the acquired images are sent to the receiver and in the other direction commands from an external controller are sent to the actuators required to propel the robotic endoscope. Wired endoscopes can obtain HD quality 1920 x 1080 pixels per frame at 30 frames per second. Due to the limitations of the current technology, this is a very ambitious goal for WCEs. Instead, research effort should put more emphasis on the power efficiency and data rate. For wireless control of the motors the ZigBee technology seems to most promising with 250Kbps. On the other hand, for image transmission and data transfer, an innovative new method known as electric – field propagation which uses the human body as a conductive medium could potentially be used. This method has demonstrated the capability to transmit data at rates of 10 megabits per second [33].

Power: Piezoelectric motors are characterized with high force, fast response, low power requirements and miniaturization capability which makes them favorable over other actuators such as: shape memory alloys, electromagnetics motors, electro active polymers etc. As a reference, the Squiggle motor (New Scale Technologies), is the smallest commercial motor with power requirements of <300mW. Thus, use of piezoelectric is quite positive for developing locomotion mechanisms using piezoelectric actuators. Current designs such as the PillCam and the Olympus wireless capsules use watch batteries with 3V at 55mA-hr and can deliver 20mW of power. Other researchers have used Lithium Metal Oxide battery TLM-1030 batteries, which can provide enough power required for both DC brushless motors rated at 430 mW and the real time

vision system which requires 180 mW. With this battery the 12 legged capsules, [34] can complete a 30 minute colon transit.

In order to reduce power consumption, the design of the WCEs can be such that the robot can be activated only at the area of interest. At any time before the desired section of the GI tract has been reached, the capsule can take advantage of the peristalsis and therefore save energy. Besides, having an on and off switch, alternative solutions such as wireless power transmission and energy harvesting are worth investigating as well. Wireless power transmission can be created using inductive coupling. This concept is presented by Carta et.al [35], where power can be derived from a magnetic field established by an external solenoid coil. The system employs a set of orthogonal ferrite (3D) coils, embedded in the capsule, and an external unit driven by a class E amplifier. The system delivers 300 mW of power from the base station to the capsule.

Diagnostics and Tissue Manipulation: The invention of the Pillcam has revolutionized endoscopy because of the ability to wirelessly obtain images from the GI tract. The application continues to gain attention from researchers and many new concepts are being pursued for this medical imaging device. In fact, besides the ability to diagnose the patients by only visually identifying the abnormalities inside the digestive tract, the research today focuses towards integration of on-board diagnostic system. Sensors that will measure the pH level, pressure, oxygen concentration, blood chemistry, temperature etc. are just few examples that have been proposed [36]. For example, by measuring the pH level and pressure, [37] diagnosis of the gastroesophageal reflux disease can be obtained.

Moreover, besides sensing, biopsy is probably the most desired functionality for future WCEs. By collecting a sample from a tissue present in the digestive tract, medical doctors can provide much more confident diagnosis for any disease. Conducting biopsy in the GI tract requires that $1mm^3$ of tissue sample is obtained and then analyzed within 1-2 hour of extraction, [38]. Some biopsy tools that have been developed for WCEs are discussed in [39, 40].

1.3.2 Locomotion Mechanisms

Multiple factors aid towards the efficacy of swallowable robots among which the locomotion component has one of the largest impact. Still in their infancy, the WCE robots have long way to go before they can be used inside human patients for diagnostics. Current locomotion mechanisms can be categorized in two groups: external and internal to the body.

External systems do not require actuation mechanism rather only a magnet enclosed inside the capsule. A corresponding external magnetic field in this case is used to control the motion of the capsule inside the body through controlled attraction and repulsion. On the other hand internal to the body locomotion mechanism enclose the entire system which includes: actuators, linkages, legs, batteries, and on board electronics. Both types of mechanisms have advantages and disadvantages. Some of the more obvious ones are that the external locomotion does not need additional power or onboard electronics to propel the capsule, while it can still provide large forces and torques that assists the motion through GI tract. The disadvantage is the large size and complexity of the system that is outside the patient's body and it is responsible for controlling the capsule. The internal locomotion system even though requires complex system of elements stored inside the capsule as well as additional power storage to drive the mechanism; it does have a very valuable advantage. It can provide more accurate locomotion and the patient will not be limited to a hospital environment, instead he/she can swallow the pill and go along with his/her normal day, while the WCE scans the GI tract. This is significant as far as the patient adoption of the technology is concerned and thus internal system represent the future of this technology i. In next section, literature review on some of the most popular internal locomotion mechanisms is presented.

1.3.2.1 Internal Locomotion Mechanisms Review

Several locomotion mechanisms have been reported in literature that has certainly increased the interest in the field of wireless capsule endoscopy. This section will provide an insight in to the state-of-the-art, covering some of the notable advancements. First, an introduction to various actuation mechanisms that are relevant towards the design of WCEs is provided. These actuators are: electro-magnetic, piezoelectric, shape memory alloys, pneumatic and electro-active polymers.

- **Electromagnetic** actuators are the most traditional actuators and a wide variety of designs is commercially available. They can be obtained in different sizes and shapes and with varying output capabilities: rotational and linear. Their efficiency goes down as the size of the motor reduces but they are able to retain torque, velocity and other performance characteristics enough to meet the requirement for various platforms. Their miniaturization is much more complex and sometimes even not feasible when compared

to other actuators. Many drivers/controllers are easily available for controlling the electromagnetic actuators. Moreover, since size is a limitation, in WCEs they are only used in the rotational mode. This means that their integration requires gearing and additional mechanical assembly that will convert the rotational motion of the motor in to a desired motion required to propel the WCE. Electromagnetics are very affordable and are the most common actuators used in the design of locomotion mechanism for WCEs.

- **Piezoelectric** actuators are commonly used in high precision applications where high sensitivity and fast time response is required. Unlike electromagnetic motors, piezoelectric motors have higher efficiency at lower size. They can be developed even on the MEMS scale. They can be used to create both rotational and linear motion while their size remains small. Nevertheless they usually need high voltage input, which makes the driver/controller more complex than the electromagnetic motors. Additional advantages are that they are completely non-magnetic and are non-flammable. Because of their high precision, small scale design, vibration characteristics and low power requirements, these actuators were selected for the locomotion mechanism presented in this dissertation.
- **Shape memory alloy actuators** are the most traditional muscle-type actuators on the market. They usually come in a wire shape, which makes them attractive when size is of great importance. Unlike piezoelectric they have a slow response time since they are actuated electrically by joule heating. Usually, they are operated at frequencies below 1 Hz, since it takes time for the SMA to heat up and then cool down to its reference temperature before it achieves one full cycle. SMAs are characterized with a hysteresis, which makes control more difficult when compared to piezoelectric and electromagnetic. They also require more power to operate them when compared to the previous actuators discussed. They however can produce large force and can also be integrated in many bio-inspired designs due to their muscle type actuation capability.
- **Electro-active polymer actuators** are soft type actuators which are dominantly used for the development of artificial muscles. They are stimulated by electric field and their main advantage is large strains and large forces. There are various types of electroactive polymers: dielectric, ferroelectric, ionic, electrorheological, liquid crystalline etc. Most commonly used in the WCE application are the dielectric ones, which usually require high voltage but low electrical power consumption.

- **Pneumatic actuators** convert the energy from a compressed air into a mechanical motion. They are classified with high strength and also good response time. A great disadvantage in the WCE design is that lines of air need to be attached to the capsule in order to produce propulsion. This consequently eliminates the wireless part of wireless capsule endoscopes. In addition, control and leakage of the pneumatic actuators can also represent a significant problem.

According to the published literature on WCEs, the internal locomotion mechanisms can be categorized in the following three groups: legged type, inchworm/earthworm type and other innovative concepts. It is important to mention that some of the most impressive work on WCE locomotion mechanisms has mainly been conducted (Dario et al.) on legged type mechanisms and (Kim et al.) on inchworm or earthworm type mechanisms.

Probably one of the most influential design in terms of operation and small scale manufacturing capabilities that had gone into the development is the 12 legged capsule [41, 42]. This robotic capsule has most of the required endoscopic functionalities such as: vision system, power and telemetry while maintaining a capsule size of 11mm in diameter and length of 25mm. The legs are fabricated from Nitinol, which due to the high elastic properties creates a gentle interaction with the walls of the intestines. It uses electromagnetic motors coupled with lead screw and gear train which converts the rotational motion into a specific gait that the legs use to propel the capsule. The total power for this design has been reported to be 430mW and the speed, 50mm/min.

Another legged type mechanism that also uses electro-magnetic actuator and has attracted attention in the media and research community is presented in [43, 44]. The novelty behind this mechanism is the use micro pillar adhesives on the legs of the capsule (manufactured using lithographic techniques) in order to assist with propulsion as well as anchoring. The inspiration behind the micro pillars was drawn from gecko feet and beetle foot hairs. Unlike the 12 legged robot, the legs used in this design do not use hooks to grab onto the walls, but instead adhesive patch which drastically lowers the risk of injuries that can occur onto the intestine wall. The presence of the adhesives increases the friction as much as 200%. The total power requirement for this WCE robot is 450mW and can reach speeds up to 13mm/min. The total size of this capsule is 33mm x 15mm.

Besides the legged mechanisms, the earthworm-like locomotive mechanism have also been developed and one such design is presented in[45]. This mechanism is operated by impact type piezoelectric actuator which can achieve strokes up to 11mm. In order to generate enough traction with the walls of the intestines, clamping device mimicking claws of an insect were fabricated. The speed of the capsule was 2.23mm/s as tested on dead porcine intestines. The total size of the robot was 15mm in diameter while 30mm under retraction stage and 41mm under elongation.

Similarly robots have also been developed by (Kim et.al),[46, 47]. These robots also use micro-hooks as a clamping device, but unlike a piezoelectric actuator, they use two-way linear shape memory alloy (SMA) spring actuators. For the one presented in [47], microhooks with diameter of 180μm were used to develop the bio-mimetic clamping element in the WCE. The total size of the capsule was 13mm in diameter and 33mm in length. The speed of the robot was measured as 14.7mm/min while 300mA of current was used to actuate the SMA springs.

A novel locomotion principle was developed and presented in [48] using SMA actuator. The inspiration behind this design is from the movement of mucus-cilia system. The locomotion is achieved by number of steps which correspond to opening and closing of the hind cilium in different order. The size of this capsule was similar to the other one, 11mmx35mm and the speed was as high as 24mm/min. Similarly to the other ones, this one as well underwent test in dead porcine intestines.

Besides the endoscopes that belong either to the legged or earthworm/inchworm type, other types such as paddling, [49] and screw type, [50] endoscopic mechanisms exist as well. Both are very simple in design and the more effective in terms of propulsion has demonstrated to be the paddling one. This design had demonstrated speeds 198-375mm/min while requiring <1W of power.

All of the summarized state of the art WCE robots share similar dimensions (length and diameter) and pill-like resembling design. Additionally, their mechanism is mainly based on actuators such as: electromagnetic, piezoelectric and shape memory alloys (in the order of most-least popular), all of which affect the speed, torque and power requirements differently. Nevertheless, the most important outcome of the literature review is identifying that besides the ability to produce locomotion; these designs also possess many disadvantages. Some encompass sophisticated mechanisms which provide effective locomotion characteristics, while being

associated with highly complex designs, which lead towards large space requirements and high manufacturing costs. Similarly, addition of mass (elements that compose the locomotion mechanism) to the system will drastically affect the efficiency and power requirement, which is already a significant challenge in WCEs. Moreover, none of the existent concepts has steering capability and many can just propel in one direction (either forward or reverse). As a result of these missing functionalities, this technology has not yet reached readiness level for medical use, therefore leaving the door open for other research discoveries.

Because some of these reasons, an attempt has been made in this dissertation to develop novel solutions to these existent problems. Accordingly a legged type and body propelled, both using traveling wave phenomenon have been investigated. As it will be seen, the idea behind the legged type has been inspired by the locomotion capabilities of millipedes and/or centipedes. As a result emphasis has been on the development of actuators that will directly represent the leg of the capsule and therefore avoiding any additional linkages and gear trains inside the capsule. Even more promising solution that is presented in Chapter 4 is propulsion achieved through the generation of traveling waves on the surface of the capsule, while freeing the entire space inside the capsule for power storage, on board electronics and vision system.

1.4 Dissertation Structure

The dissertation is organized according to the vision shown in Figure 1.3 Intelligent hospital room representation. The device represented by 1 in this figure is thoroughly discussed in Chapters 2, 3 and 4 under the theme of a wireless capsule endoscope with active locomotion system. This study is an attempt towards developing a locomotion mechanism for current Pillcam type of devices which function as a passive wireless capsule endoscope for inspection and diagnostics of the gastrointestinal GI Tract. The overall objective of a robotic WCE is to be equipped with not only a vision system (current Pillcam) but also a diagnostic lab on a chip module, biopsy instruments, and a locomotion mechanism. Using this advanced WCE, one can perform delicate surgical procedures or regular diagnostics through automated control functions available on the mobile or other computing devices. Chapter 2 discusses the concepts and theory behind the development of piezoelectric actuators that were fully characterized and then implemented onto a locomotion mechanism described in Chapter 3. Chapter 4 presents a novel mechanism based on the combination of piezoelectric actuation and traveling wave phenomenon

through solid structures. The study demonstrates the capability and potential of this mechanism to be used as propulsion for WCEs.

The device represented as “2” in the Figure 1.3 (and discussed in Chapter 5) is another device which not only can be used as a diagnostic tool but also as a surgical tool. The device is a multifunctional image guided (MIGS) platform composed of three elements: optical coherence tomography (OCT) probe, laser scalpel and a scanning positioning stage. By utilizing this device as a non-invasive medical tool, the surgeon can perform delicate and intricate procedures on patients at limited depths. The OCT probe is used as a visual guidance and the positioning stage is used to conduct a scan of the desired area which results in a 3-D image of the tissue topography underneath the skin. These images guide the surgeon as to where the abnormalities are present and then position the laser scalpel to that area to create an incision without affecting the nerves. The study was conducted in collaboration with a team of biomedical engineers with focus of this thesis on the development of the scanning and positioning stage.

The device represented as “3” in Figure 1.3 is described in Chapter 5.2. This device is a shape memory alloy based thermal energy harvester that recovers the waste heat from hot water/steam pipes in the hospitals. The objective for the energy harvester is to the power the many RFID and other type of sensors that will have a role in the monitoring of the environment and patient related physiological factors. The harvester proposed in this study can be easily attached to any hot source and generate enough energy to power the distributed wireless sensor network. The shape memory based advantages has several advantages over the conventional thermoelectric generators as described in Chapter 5.2 and the results demonstrated that this architecture could find much wider usage besides buildings.

The device represented as “4” in the Figure 1.3 is discussed in Chapter 5.3. This device represents a carbon nanotube (CNT) based thermo acoustic speaker which can find use for both acoustic localization and sound therapy. Some of the advantages of CNT based sound generation devices are their dimensions and non-magnetic nature which makes them promising candidates for integration with wide variety of equipment’s and tools. They are flexible and transparent which makes them suitable for wearable and decorative components. The sound generation component can be integrated inside the human body for data transmission and communication. The advantage of using acoustic waves over RF ones inside the human body is related to the fact

that water composes 65% of the human body. Because acoustic waves outperform the RF waves under water, it makes sound a promising modality for communication.

Lastly, Chapter 6 summarizes the work conducted in this thesis and provides future direction for the technologies investigated here.

Chapter 2 – Piezoelectric Actuators: Concept and Theory[1]

Before designing a locomotion mechanism for capsule endoscopes used in examination of the gastrointestinal tract, which otherwise is difficult to accomplished with traditional endoscopes (such as examination of the small intestines), it is important to begin at the fundamental level. As a result, this chapter focuses on the development of the actuator behind the propulsion mechanism of a legged type WCE. Accordingly, the focus of this chapter is to present two piezoelectric actuators developed using bending mode excitation principle. The two actuators presented are L-Shape piezoelectric actuator and U-Shape piezoelectric actuator. Their concept and principle of operation is presented first, followed by a theoretical analysis which was developed in order to predict the response of the system and for parameterization and optimization studies. The analysis encompasses two models, finite element piezoelectric model and distributed parameter piezoelectric model. The theory developed and presented is for the L-Shape piezoelectric motor, since the modeling approach for the U-Shape piezoelectric motor would follow the identical steps.

2.1 Introduction

In order to develop a locomotion mechanism for wireless capsule endoscopes WCEs piezoelectric actuators were selected. This chapter focuses on the development and design of two novel piezoelectric type actuators which represent the fundamental element of a legged WCE locomotion mechanism. The reason behind using piezoelectric actuators comes from their unique characteristics: reasonable combination of torque and speed, quick response, no backlash, simplistic design, miniaturization capabilities and high efficiencies at miniature dimensions. There are many types of piezoelectric motor that have been developed and presented in literature and several commercial products are available. Even though they all have a unique design, they can be classified in two categories as either Quasi-static and/or Ultrasonic motors [51]. The Quasi-static motors can either follow a stepping or inertial principle. Motors following the stepping principle are called clamping –type motors, where one set of actuators clamp to the

[1] Some of the work discussed in this chapter was published in IEEE UFFC. The following are the citations:

- Avirovik D., Priya S., "L-shaped piezoelectric motor-Part I: Design and experimental analysis", Ultrasonics, Ferroelectrics and Frequency Control, IEEE Transactions on;59:98-107,(2012)
- Avirovik D., Karami M.A., Inman D., Priya S., "L-shaped piezoelectric motor-part II: Analytical modeling", Ultrasonics, Ferroelectrics and Frequency Control, IEEE Transactions on;59:108-20,(2012)

rotor, while another set is unclamped and moves towards a new clamping location, in the process creating forward or backward movement. The inertial–type motors [52] use their inertia and difference between the static and dynamic friction to create the motion.

Ultrasonic piezoelectric motors on the other side can be classified into five categories based upon the shape of the stator [53]: longitudinal vibration [54], composite mode of longitudinal-bending vibration [55], composite mode of longitudinal-torsional vibration [56] [57], bending vibration [58] and in-plane vibration [59]. Exciting at least two orthogonal resonance modes of the stator vibrator, results in generation of an elliptical motion on the stator surface. The stators of these types of motors may have some additional elastic part, which is called a vibration coupler or a concentrator. Single mode vibrations on the piezoelectric element are converted into a multi-mode vibration at the tip of the concentrator. Either exciting two different electrode groups one at a time, or tuning the driving frequency of the vibrator to a different orthogonal frequency pair, controls the rotation or direction of the linear motion. If multi-vibrators are used, either the vibration or orientation of the vibrators needs to be orthogonal. In this type of motor, superimposing two orthogonal single mode vibrations with a phase shift generates elliptical motion.

Multiple commercially available piezoelectric motors were initially investigated as potential candidates in the drive train of the wireless endoscope including New Scale Technology's Squiggle motor [60], Nanomotion's HR series [61] and Micromo's PiezoLEGS [62]. The HR series motors and PiezoLegs motor from Micromo can achieve velocities up to 150mm/s and 12mm/s, respectively. They can meet the torque and resolution criterion; however their size is too big to be considered for WCEs. On the other hand the Squiggle motor was identified as a good candidate with impressively small size and satisfying torque and velocity of 10mm/s. However, the cost of all of these motors is extremely high and any further scaling increases the cost even more, thus limiting their application. This is one of the main reasons why an initiative was taken to develop novel cost-effective piezoelectric motors such as the L-shape and U-Shape actuators.

As it will be seen later in this thesis, additional advantages of the L-Shape and U-Shape piezoelectric actuators over the previously mentioned motors are evident due to their simple design, low manufacturing cost, ease of maintenance, inexpensive scaling and direct integration onto a locomotion mechanism as it will be seen in Chapter 3.

Piezoelectric elements are highly capacitive and their power requirements can be expressed as [63]:

$$p(t) = \frac{1}{2} CV^2 \omega \sin 2\omega t \qquad (2.1.1)$$

where the power is dependent on the applied voltage, capacitance and frequency. From this relationship it can be established that the power consumption is directly proportional to frequency. Therefore another advantage of the L-Shape and U-shape piezoelectric motor over the ultrasonic motors is precisely due to this relationship since operation will be in a region much below the ultrasonic one. Having operating frequency in the ultrasonic range does not disrupt the human hearing and therefore it has that advantage over the low frequency motors. However, the L-Shape motor was designed such that its optimal frequency of operation is below 300Hz and in the WCE application the frequency will be even lower <20Hz which will have a negligible effect on the human ear. In addition, it is safer to operate at lower frequencies to reduce the electrical fatigue. In any structure, whether it is homogeneous or a composite, defects are more likely to originate at higher frequency of vibration especially at the bonding interfaces. Further, miniaturization of piezoelectric motor is also a very important factor. This can be achieved if the structure and driving circuit of these motors are simplified so that they can be manufactured at low cost. One of the most suitable structures for miniaturization of piezoelectric motors is the multi (or mixed) mode excitation type which has been the pursuit in this work. Finally, designing a driving circuit for low frequency is simpler then designing one for the high frequency operation.

As shown in this chapter, both the L-shape and U-Shape piezoelectric motor utilize bending modes of two bimorph actuators. Since the structure and poling configuration of the active piezoelectric bimorph elements used are simple, this motor's structure is very suitable for miniaturization. The work presented in this chapter encompasses the concept design and principle of operation of the two actuators followed by the theoretical analysis. The theory uses finite element model (FEM) and distributed parameter model approach towards predicting the response of the motors. The theory presented in this dissertation only focuses on the L-Shape piezoelectric motor, since the modeling approach follows the same steps for the U-Shape motor as well. In Chapter 3, characterization of the two actuators as well as their integration onto a locomotion platform will be covered.

2.2 Concept Design and Principle of Operation

There have been limited studies on the bending - bending type piezoelectric / ultrasonic motors. In this category, Squiggle motor has shown promise due to its small compact size [60]. It utilizes two bending modes which are created using orthogonal piezoelectric plates bonded to the outside of a metal cylinder. Another example of bending type ultrasonic motor [64], uses the first bending vibration mode. It consists of a cylindrical stator, Ti, onto which PZT thin film is deposited. Four electrodes were attached around the circumference of the cylinder, which once excited with phase difference of 90º with respect to each other result in a wobbling motion. Kurosawa [58], designed a bar type traveling wave type ultrasonic motor with dual rotors. A piezoceramic was divided into four areas to excite two orthogonal bending modes, and therefore generate an elliptical motion. All of these motors share similar concept in the design and operation principle. Unlike most bending type motors, the L-Shape motor has a unique design, which makes it less complex, novel in its operation and rather intriguing.

For piezoelectric motors, highest torque, displacements and speeds are achieved by operating in the vicinity of resonance. In the motor design, two piezoelectric bimorphs mounted as cantilever beams form the foundation of the structure. The two bimorph elements were excited at their 1st natural frequency. Figure 2.1 shows an illustration of the 1st mode shape of a piezoelectric bimorph cantilever where voltage is the forcing function. During this excitation, the free end of the bimorph exhibits highest deflection.

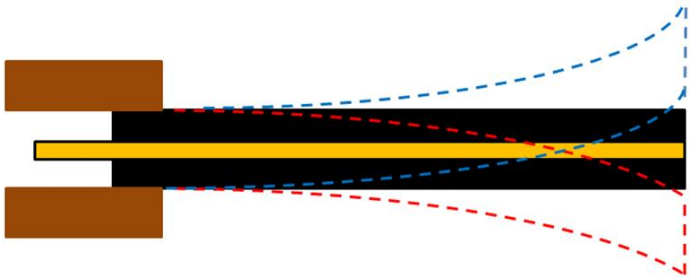

Figure 2.1 1st Mode Shape of a Piezoelectric Bimorph with Clamped – Free Boundary Conditions

2.2.1 L-Shape and U-Shape Piezoelectric Motor

In order to implement the two mode excitation principle, two piezoelectric bimorphs were attached normal to each other in an L-Shape and U-Shape formation as shown in Figure

2.2. The bimorph standing vertically is termed as the **base** of the motor and the bimorph mounted horizontally is the **wing** as shown in Figure 2.2 **(a).** Similarly, the top bimorph is the base and the bimorph below is referred to as the wing in the U-Shape motor as shown in Figure 2.2 (b). The boundary conditions for the motor can be described in the following way. The base is clamped at one end and it is free on the other one. At the free end, the base is connected to the wing via a coupler. Besides acting as an off-centered tip mass to the base, the wing is an important part of the motor, where one end is attached to the free end of the base through the coupler and the other end is free to oscillate. This motor generates motion in X, Y and Z direction. Even though the motion of the motor is in three directions the analysis and the theory will focus on characterizing the motion at the tip of the wing in the X and Y direction for the L-Shape motor and in the X and Z direction for the U-Shape motor. This is because largest deflections are present in the XY and XZ plane for the L-Shape motor and U-Shape motor, respectively, and this motion is large enough to illustrate the functionality of the motor.

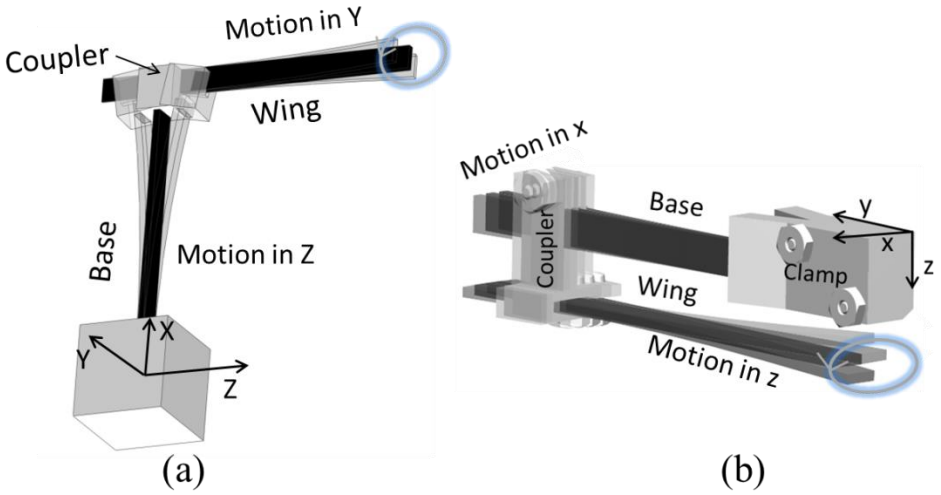

Figure 2.2 Piezoelectric motor structure and 3D orientation: (a) L-Shape piezoelectric motor, (b) U –Shape piezoelectric motor

Since both actuators shared the same dynamics in both the motors (L-shape and U-shape) and the difference was mainly in the geometry and the orientation of the piezoelectric bimorphs, thus theoretical analysis was conducted on one of the designs (L-Shape motor) and it is expected that the analysis can be easily extended to the other design. This is because it is safe to assume that both motors will achieve similar dynamics and responses as the interest is in generation of elliptical motion at the tip of the wing.

The principle of operation of the L-Shape piezoelectric actuator is shown in Figure 2.3. The elliptical motion generated at the tip of the motor is represented by six different steps corresponding to six different time intervals, shown in the image in Figure 2.3(a). The first signal is responsible for actuating the base and the second signal for the wing. The frequency for both signals was the same corresponding to the 1st natural bending mode frequency of the base and wing. The image in Figure 2.3(b) shows two sinusoidal voltage signals 90^{o} out of phase with respect to each other. The actuation begins with initial conditions set to zero. The initial conditions of the motor correspond to step 0, where at t=0, no power is being supplied to the motor and therefore the motor remains in static equilibrium. In step 1, voltage signal (red solid line) is delivered only to the base. This results in exciting the base at the 1st bending mode. In step 2, a sinusoidal signal 90^{o} out-of-phase (blue dotted line) is applied to the wing, therefore actuating the wing at its first resonance. During this step, no voltage is applied at the base which brings it back to its initial unstrained form, while the wing is the only element being actuated. In step 3, the voltage applied to the base is negative and the voltage applied to the wing is zero. This results in actuation of the base in the opposite direction to that obtained in step 1, while the wing returns back to its initial state of zero strain. In step 4, the base is actuated back to its initial position and the wing is actuated in the negative direction due to the negative voltage input. In step 5, a single elliptical motion is created. The steps continue to repeat, and the motor continues to deform as long as the above sequence is implemented.

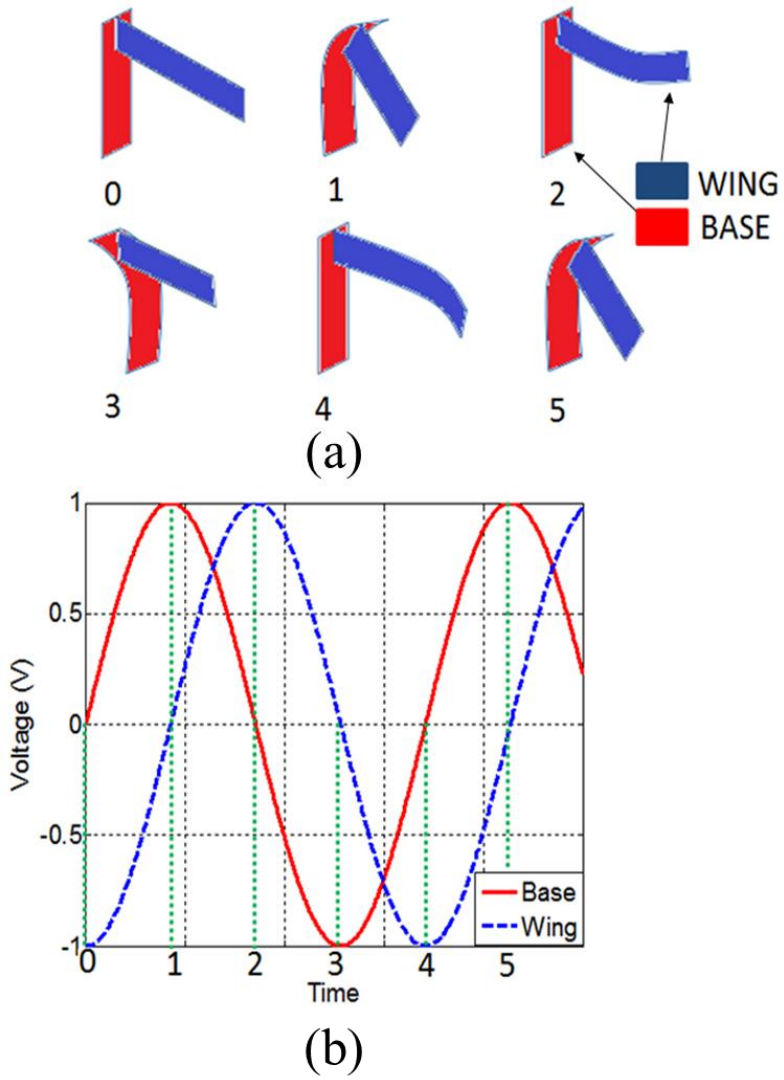

Figure 2.3 Principle of Operation: (a) Motion of the L-Shape Piezoelectric Motor; (b) Sinusoidal Voltage Signals Delivered to the Base and Wing.

2.3 Theoretical Modeling

In order to better understand the dynamics of the piezoelectric actuators presented in Section 2.2, two different theoretical models were presented and established: finite element model (FEM), Section 2.3.1 and distributed parameter model section 2.3.2. Once again, the theoretical models included in this dissertation are focused towards the L-Shape piezoelectric motor, since the dynamics is very similar and the only difference is the geometry. One can use the models presented in this work and expand it to the U-Shape piezoelectric motor on any other configuration of the piezoelectric bimorphs.

2.3.1 Finite Element Analysis

For L-shape motor, the two bimorphs should be actuated at their 1st bending mode resonance frequencies, which should be in the vicinity to each other. In this motor, the base acts as a cantilever beam with a tip mass equal to the weight of the wing. On the other side, the wing acts as a beam constrained by the base at one end and free on the other without any tip mass. In a cantilever beam structure, the relationship between the resonance frequency and tip mass is inversely proportional. This means that, as the mass of the tip increases, the natural frequency decreases. Also, if the width and thickness of the beam are kept the same, but the length of the beam changes, a similar relationship between the length and natural frequency can be obtained. The increase of length in the beam causes the resonance frequency to go down. Following these implications a FEM of the piezoelectric motor was developed. ATILA [65] was used to model the motor in order to obtain optimal geometry as shown in Figure 2.4.

In the FEA a hexahedral mesh was used for the structure, driving voltage was kept at $2V_{p\text{-}p}$ and the boundary conditions were based on the concept design shown in Figure 2.2. The geometry of the bimorphs is defined in Table 2.3-1 and the appropriate parameters for the piezoelectric material along with the material properties of the bimorphs are listed in Table 2.3-2 and Table 2.3-3 correspondingly.

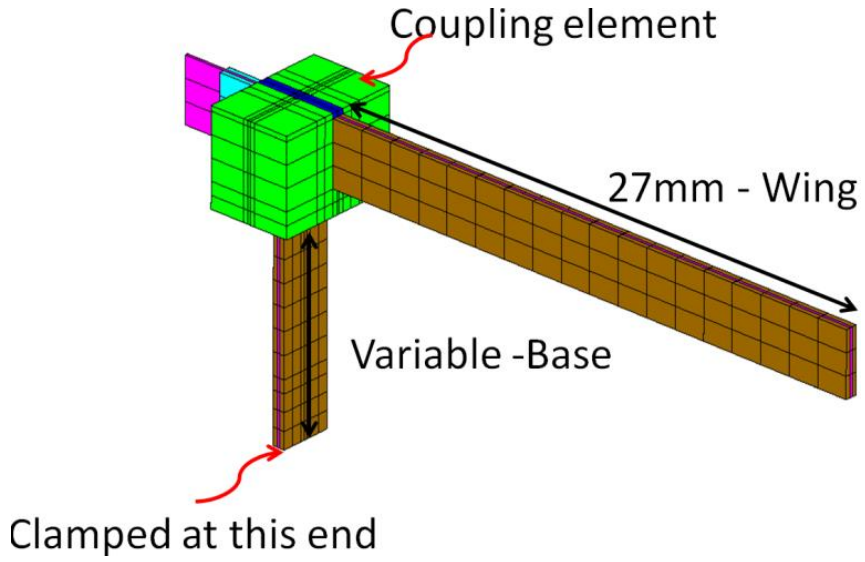

Figure 2.4 ATILA Model of the L-Shape Piezoelectric Motor

Table 2.3-1 Geometrical Properties of the Piezoelectric Bimorph Used in the ATILA Analysis

Dimensions (mm)			Free
Long	Wide	Thick	Length (mm)
35	2.5	0.6	28

Table 2.3-2 PZT-5X45 Properties Used in the ATILA Model

Mechanical Compliance $(\frac{m^2}{N})$		Piezoelectric Coupling $(\frac{C}{N})$		Relative Permittivity $\varepsilon_0 = 8.854 * 10^{-12}\frac{F}{m}$	
S_{11E}	16.5E-12	d_{15E}	741E-12	$\varepsilon_{11T}/\varepsilon_0$	3130
S_{12E}	-14.78E-12	d_{31E}	-320E-12	$\varepsilon_{33T}/\varepsilon_0$	4500
S_{13E}	-8.45E-12	d_{33E}	750E-12		
S_{33E}	20.7E-12				
S_{44E}	43.5E-12				

Table 2.3-3 Other Materials Used in the ATILA Model

	Carbon Fiber	APC Plastic	PZT-5X45
Young's Modulus (Pa)	210E9	4.1E9	N/A
Poisson's Ration	0.74	0.4	N/A
Density (kg/m^3)	1800	1400	7600

A harmonic FEA of the piezoelectric motor for a range of frequencies between 0 and 500Hz was conducted for three different scenarios, where, by manipulating the geometry of the motor a common frequency was found. In the first scenario only the base was actuated while the wing was treated as tip mass without any piezoelectric properties. In the second case, the wing

was actuated, while the base was modeled as a support for the wing. In both cases, the length of the base was modified until the natural frequencies for both elements matched. Once an acceptable length of the base was obtained, a complete model of the motor was developed. In order to show how the base affects the resonant frequency, two models of the piezoelectric motor were generated. In both models the bimorphs share the same properties and parameters for the piezoelectric material except for the length of the base. In the first model, the free length of the base was 9mm and the free length of the wing was 27mm. In the second model, the free length of the base was 11mm and the length of the wing was 27mm. The impedance vs. frequency curves for both cases are shown in Figure 2.5. As noticed in Fig. 5(a), the resonance frequency between the base and wing is slightly different, 263Hz and 288Hz respectively, however in Fig. 5 (b) it is identical, 243Hz.

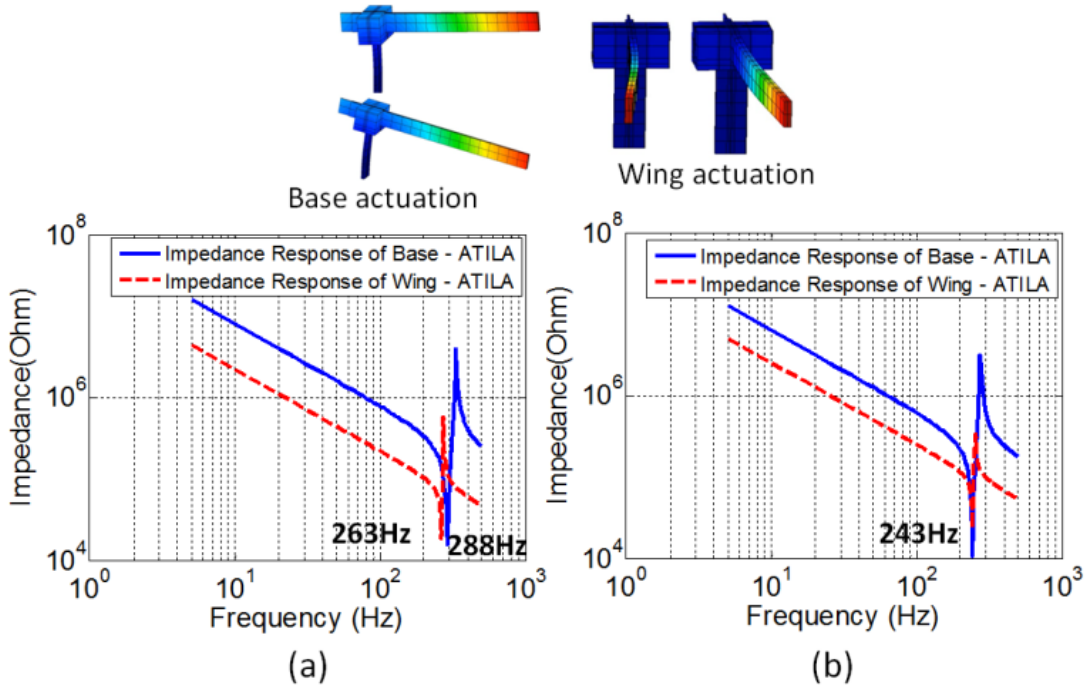

Figure 2.5 FEM Impedance - Frequency Relationship for Base and Wing, (a) Base Length = 9mm, Wing Length = 27mm, (b) Base Length = 11mm, Wing Length = 27mm.

The geometry from Fig. 5(b) was then used to create a complete model of the motor where both the wing and base were actuated by sinusoidal signals 90º out-of-phase and having amplitudes of 1V. A representation of the motion generated in the Y2 – Z2 plane is shown in Figure 2.6.

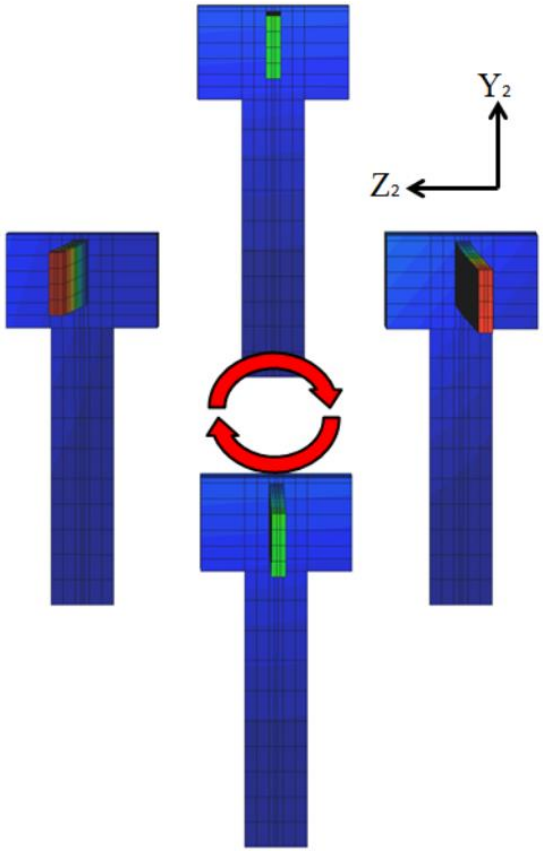

Figure 2.6 Simulation of the L-shaped Piezoelectric Motor using ATILA

2.3.2 Analytical Modeling of L-Shape Piezoelectric Actuator

The work presented in this section discusses the development of an analytical model for the L-shaped piezoelectric motor through distributed parameter approach. The emphasis is on the development of a precise analytical model which can predict the dynamical behavior of the motor based on its geometry. The motor was first modeled mechanically to identify the natural frequencies and mode shapes of the structure. Next, electromechanical model of the motor was developed to take into account the piezoelectric effect and the dynamics of L-Shape piezoelectric motor were obtained as a function of voltage and frequency. Finally, the analytical model was validated by comparing it to both experimental and FEM.

Some of the advantages of this model over a FEM and experimental model are the fast and accurate analyses, which consequently makes the modeling more user friendly. The analytical

model allows parameterization and optimization of the L-Shape motor as well as opportunity for scaling the prototype. In addition, by varying the parameters of the motor, the model can predict the dynamics at the tip that can be used to analyze as to how the motion will affect actuation of the WCEs.

It should be noticed that this study does not include a stator/rotor contact model and it is limited to analytical model of a free stator behavior. The contact between the stator and rotor is highly dependent on the friction between them. Thus, additional analysis is required to determine the criterion for optimum contact surface. The motion between the tip of the motor and the mechanical load is discontinuous and non-linear; consequently it requires intensive modeling technique. The assumption is that the response of the stator is not affected by the mechanical load, as long as the mass of the load is smaller than the piezoelectric motor itself.

2.3.2.1 Mechanical Model

The procedure for developing an analytical model of a complex structure such as the L-Shape piezoelectric motor is to break it up in smaller elements, approach each element individually and combine them at the end to obtain a complete model. The foundation of the analytical model was the mechanical system (first step), which was modeled following Hamilton's principle [4]. Using this approach, boundary conditions (BC) and equations of motion (EOM) are derived that allow obtaining natural frequencies and mode shapes for the system. The electromechanical model (second step) takes into account the piezoelectric elements and uses voltage as a forcing function. In the final stage of this paper, a comparison between the analytical, finite element and experimental model is presented.

The necessary factor before the Hamilton's principle can be implemented is the knowledge of the kinetic and potential energy of the system. Various other studies have used the Hamilton's approach in modeling piezoelectric motors including traveling wave ultrasonic motor, [66], bimodal ultrasonic motors [67], and ultrasonic rotary motor [68].

A schematic diagram of the 3D orientation of the motor is presented in Figure 2.7. It can be identified from this figure that the actuation of the base results in W_1 displacement in the Z_1 direction. As a result of the deflection of the base, a motion of the wing will occur in the X_2, Y_2 plane even if the wing is assumed to have no actuation properties. As such, the wing can exhibit

axial (U_2) displacement and rotational motion around Y_1. On the other side, when the wing is being actuated via input voltage, it bends in the Z_2 direction by W_2 distance. In addition the bending of the wing is responsible for creating a torsional vibration onto the base. The angle representing the torsion in the base is identified as β. This coupling occurring between the base and wing results in three axes motion of the motor's tip, in the X_2, Y_2, Z_2 direction.

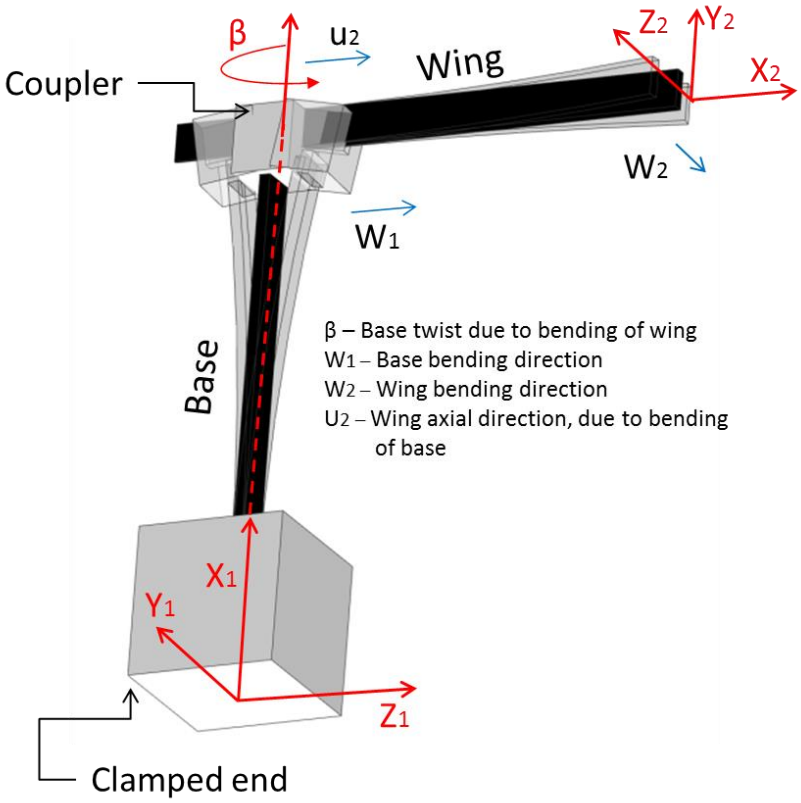

Figure 2.7 Piezoelectric motor structure and 3D orientation.

Understanding the dynamics of the motor was the single most important factor in defining the energy terms of the two members open frame structure. The kinetic and potential energy for the base and wing are defined by Eq. (2.3.1), (2.3.3) and (2.3.6), (2.3.8) respectively.

$$T_1 = \frac{1}{2}\int_0^{l_1} m_1 \dot{w}_1^2 dx_1 + \frac{1}{2}\int_0^{l_1} \rho_1 I_{p1} \dot{\beta}_1^2 dx_1 + \frac{1}{2} M_t \dot{w}_1 |_{x_1=l_1} \tag{2.3.1}$$

where the first term is the translational kinetic energy due to bending, the second term is rotational kinetic energy due to torsion (as a result of the bending vibration of the wing), and the

third term is kinetic energy of the tip mass (the mass of the wing together with the mass of the coupling element). Both the first and second term are integrated over the entire length of the base, l_1. The polar moment of inertia, I_p, for piezoelectric bimorph can be described as:

$$I_p = \frac{1}{12}\rho_s b h_s^{\,3} + 2\rho_p \left(\frac{1}{12} b h_p^{\,3} + b h_p \left(\frac{h_s + h_p}{2} \right)^2 \right) \tag{2.3.2}$$

The potential energy for the base is defined as:

$$V_1 = \frac{1}{2}\int_0^{l_1} Y_1 I_1 \left(\frac{\partial^2 w_1}{\partial x_1^{\,2}} \right)^2 + \frac{1}{2}\int_0^{l_1} GJ \left(\frac{\partial \beta}{\partial x_1} \right)^2 \tag{2.3.3}$$

where the first term is the potential energy due to bending and the second term is potential energy due to torsion. The bending stiffness for a piezoelectric bimorph, YI, is given as [69]:

$$YI = \left(\frac{2b}{3} \right) \left(\frac{Y_s h_s^{\,3}}{8} + \frac{1}{s_{11}} \left(\left(h_p + \frac{h_s}{2} \right)^3 - \frac{h_s^{\,3}}{8} \right) \right) \tag{2.3.4}$$

The torsional stiffness, GJ, is rather difficult to calculate analytically for a three-layer composite beam structure. This *GJ* was determined from an ATILA FEM static load model. Piezoelectric bimorph with the same properties as that used in the analytical model was modeled as a cantilever beam. At the free end, torque was applied across the width of the beam and the torsional stiffness was calculated to be 0.0028N/m:

$$GJ = \frac{\tau L}{\theta} \tag{2.3.5}$$

where τ is the torque applied, L is the length of the beam and θ the angle of twist.

For the wing, the kinetic and potential energies are given as:

$$T_2 = \frac{1}{2} l m_2 \dot{u}_2^{\,2} + \frac{1}{2}\int_0^{l_2} m_2 \dot{w}_2^{\,2} dx_2 + \frac{1}{2}\frac{d}{dt}\left(\frac{\partial w_1}{\partial x_1}(l_{1,t}) \right) I_z \tag{2.3.6}$$

where the first term is the translational kinetic energy of the wing, second term is the kinetic energy due to bending, integrated over the entire length of the wing, l_2, and the third term is the rotational kinetic energy about Z_2 which appears in the equation as a result of the moment created by the wing. The moment of inertia I_z was approximated by the following expression:

$$I_z = \frac{1}{3} m_2 \left(l_2 + e\right)(l_2 + e)^2 + \frac{1}{12} m_2 \left(l_2 + e\right) b^2 \tag{2.3.7}$$

where e is 2mm and it is included in Eq. (2.3.7) to provide a closer approximation of the moment of inertia. It is the section of the wing which is located inside the coupling element. The potential energy of the wing comes only from bending as seen below:

$$V_2 = \frac{1}{2} \int_0^{l_2} Y_2 I_2 \left(\frac{\partial^2 w_2}{\partial x_2} \right)^2 dx_2 \tag{2.3.8}$$

With the kinetic and potential energy for the system defined, the Hamilton's principle was applied to derive the EOM and BC. Three EOM and ten BC were obtained from the energy method. Equation (2.3.9) – (11) describe the EOM for the base due to bending, EOM for the base due to torsion and EOM for the wing due to bending.

$$m_1 \ddot{w}_1 + Y_1 I_1 w_1^{(4)} = 0 \tag{2.3.9}$$

$$\rho_1 I_p \ddot{\beta}_1 - GJ \beta_1^{(2)} = 0 \tag{2.3.10}$$

$$m_2 \ddot{w}_2 + Y_2 I_2 w_2^{(4)} = 0 \tag{2.3.11}$$

The BC of the piezoelectric motor obtained from the Hamilton's principle can be grouped into four categories: essential conditions at $x_1 = 0$ given by Eq. (2.3.12)-(2.3.14), natural conditions (forces) at $x_2 = l_2$ given by Eq. (2.3.15)-(2.3.16), kinetic conditions (equilibrium) at $x_1 = l_1$ and $x_2 = 0$ given by Eq.(2.3.17)-(2.3.19) and continuity at , $x_1 = l_1$ and $x_2 = 0$ given by Eq. (2.3.20)-(2.3.21). Explanation of each BC is provided below:

$$w_1(0,t) = 0 \tag{2.3.12}$$

where no displacement is present due to the clamping conditions,

$$w_1^{(1)}(0,t) = 0 \tag{2.3.13}$$

where no strain is present due to the clamping conditions,

$$\beta_1(0,t) = 0 \tag{2.3.14}$$

where the angle of twist is zero because of the clamping conditions,

$$Y_2 I_2 w_2^{(3)}(l_2,t) = 0 \tag{2.3.15}$$

where the shear force is zero at the free end of the wing,

$$Y_2 I_2 w_2^{(2)}(l_2,t) = 0 \tag{2.3.16}$$

where the moment at the free end of the wing is zero,

$$Y_1 I_1 w_1^{(2)}(l_1,t) - I_z \ddot{w}_1^{(1)}(l_1,t) = 0 \tag{2.3.17}$$

where balance of moments appears at the coupling element,

$$Y_1 I_1 w_1^{(3)}(l_1,t) - l_2 m_2 \ddot{w}_1(l_1,t) - M_t \ddot{w}_1(l_1,t) = 0 \tag{2.3.18}$$

where balance of forces appears at the coupling element

$$GJ\beta_1^{(1)}(l_1,t) - Y_2 I_2 w_2^{(2)}(0,t) = 0 \tag{2.3.19}$$

where the twist at the end of the base equals the bending moment of the wing

$$w_2(0,t) = 0 \tag{2.3.20}$$

where no displacement appears at the coupling element in the w_2 direction,

$$w_2^{(1)}(0,t) = -\beta_1(l_1,t) \tag{2.3.21}$$

where the strain of the wing at the coupling element equals the torsional angle at the end of the base.

The solution for the EOM presented in Eq. (2.3.9), (2.3.10) and (2.3.11), subjected to ten BC proceed the separation of variables solution of the form [70]:

$$w(x,t) = X(x)T(t) \tag{2.3.22}$$

where the displacement depends on two functions, one based on x and the other one based on t. Below are described the steps for solving the EOM. To begin, Eq. (2.3.22) is substituted in Eq. (2.3.9), (2.3.10) and (2.3.11) to yield:

$$\frac{Y_1 I_1}{m_1}\frac{X_1(x)^{(4)}}{X_1(x)} = -\frac{\ddot{T}(t)}{T(t)} = \omega^2 \tag{2.3.23}$$

$$\frac{GJ}{\rho_1 I_p}\frac{B(x)^{(2)}}{B(x)} = -\frac{\ddot{T}(t)}{T(t)} = \omega^2 \tag{2.3.24}$$

$$\frac{Y_2 I_2}{m_2}\frac{X_2(x)^{(4)}}{X_2(x)} = -\frac{\ddot{T}(t)}{T(t)} = \omega^2 \tag{2.3.25}$$

As it can be noticed that two equations, one temporal and one spatial can be obtained from Eq. (2.3.23), (2.3.24) and (2.3.25). The solutions for the corresponding spatial equations are given by Eq. (2.3.26), (2.3.27) and (2.3.28):

$$X_1(t) = a_1 \sin\beta x_1 + a_2 \cos\beta x_1 + a_3 \sinh\beta x_1 + a_4 \cosh\beta x_1 \tag{2.3.26}$$

$$X_2(t) = a_5 \sin\alpha x_1 + a_6 \cos\alpha x_1 \tag{2.3.27}$$

$$X_3(t) = a_7 \sin\gamma x_2 + a_8 \cos\gamma x_2 + a_9 \sinh\gamma x_2 + a_{10} \cosh\gamma x_2 \tag{2.3.28}$$

where β is $\left(\frac{\omega^2 m_1}{Y_1 I_1}\right)^{\frac{1}{4}}$, α is $\left(\frac{\rho_1 I_p \omega^2}{GJ}\right)^{\frac{1}{2}}$, γ is $\left(\frac{\omega^2 m_2}{Y_2 I_2}\right)^{\frac{1}{4}}$ and ω is the natural frequency for the system. These constants along with the constants of integration a_1 - a_{10} will be determined from the ten BC. The ten BC previously derived, yield ten equations and ten unknown constants of integration which can be written as a single matrix given by Eq.(2.3.30) . The matrix is composed of ten vectors given through Eq.(2.3.29). Notice that the vectors are in order corresponding to the EOM. EOM given by Eq.(2.3.9) goes with BC given by Eq.'s (2.3.12),

(2.3.13), (2.3.17) and (2.3.18). EOM given by Eq.(2.3.10) goes with BC given by Eq. (2.3.14) and (2.3.21). Finally, EOM given by Eq.(2.3.11) goes with the remaining BC.

$$
\begin{aligned}
M_1 &= [0,1,0,1,0,0,0,0,0,0] \\
M_2 &= [1,0,1,0,0,0,0,0,0,0] \\
M_3 &= [-E_1I_1\beta^2 \sin\beta l_1 + I_{z0}\omega^2\beta\cos\beta l_1, -E_1I_1\beta^2\cos\beta l - I_{z0}\omega^2\beta\sin\beta l_1, E_1I_1\beta^2\sinh\beta l + I_{z0}\omega^2\beta\cosh\beta l_1, \\
&\quad , E_1I_1\beta^2\cosh\beta l + I_{z0}\omega^2\beta\sinh\beta l_1, 0,0,0,0,0,0] \\
M_4 &= [-E_1I_1\beta^3\cos\beta l_1 + (M_t\omega^2 + l_2m_2\omega^2)(\sin\beta l), E_1I_1\beta^3\sin\beta l_1 + (M_t\omega^2 + l_2m_2\omega^2)(\cos\beta l), \\
&\quad , E_1I_1\beta^3\cosh\beta l_1 + (M_t\omega^2 + l_2m_2\omega^2)(\sinh\beta l), E_1I_1\beta^3\sinh\beta l_1 + (M_t\omega^2 + l_2m_2\omega^2)(\cosh\beta l), \\
&\quad ,0,0,0,0,0,0] \\
M_5 &= [0,0,0,0,0,1,0,0,0,0] \\
M_6 &= [0,0,0,0,\sin\alpha l_1, \cos\alpha l_1, \gamma, 0, \gamma, 0] \\
M_7 &= [0,0,0,0, GJ\alpha\cos\alpha l_1, -GJ\alpha\sin\alpha l_1, 0, -E_2I_2\gamma^2, 0, E_2I_2\gamma^2] \\
M_8 &= [0,0,0,0,0,0,0,1,0,1] \\
M_9 &= [[0,0,0,0,0,0,-\sin\gamma l_2, -\cos\gamma l_2, \sinh\gamma l_2, \cosh\gamma l_2] \\
M_{10} &= [0,0,0,0,0,0,-\cos\gamma l_2, \sin\gamma l_2, \cosh\gamma l_2, \sinh\gamma l_2]
\end{aligned}
\tag{2.3.29}
$$

$$
\begin{bmatrix}
M_{1,1} & M_{1,2} & \cdot & \cdot & \cdot & \cdot & \cdot & \cdot & \cdot & M_{1,10} \\
M_{2,1} & \cdot & & & & & & & & \cdot \\
\cdot & & \cdot & & & & & & & \cdot \\
\cdot & & & \cdot & & & & & & \cdot \\
\cdot & & & & \cdot & & & & & \cdot \\
\cdot & & & & & \cdot & & & & \cdot \\
\cdot & & & & & & \cdot & & & \cdot \\
\cdot & & & & & & & \cdot & & \cdot \\
\cdot & & & & & & & & \cdot & \cdot \\
M_{10,1} & & & & & & & & & M_{10,10}
\end{bmatrix}
\begin{bmatrix} a_1 \\ a_2 \\ a_3 \\ a_4 \\ a_5 \\ a_6 \\ a_7 \\ a_8 \\ a_9 \\ a_{10} \end{bmatrix}
=
\begin{bmatrix} 0 \\ 0 \\ 0 \\ 0 \\ 0 \\ 0 \\ 0 \\ 0 \\ 0 \\ 0 \end{bmatrix}
\tag{2.3.30}
$$

The vector equation (2.3.30) can have a non-zero solution for the constants of integrations $a = [a_1, a_2, ...a_{10}]$, only if the determinant of matrix M is singular. Matrix M is composed of equations which are a function of only one unknown, ω, the natural frequency and other constant parameters that are based on material properties and geometry. By setting the

determinant of the matrix to zero, numerically, the natural frequency of the L-shape structure can be obtained. A range of frequencies from 0 – 10 kHz, was used to calculate the determinant of matrix M. Figure 2.8 shows the relationship between the determinant and frequency for two different geometries of the L-Shape piezoelectric motor. In the first case the free length of the base is 9mm and in the second case it is 11mm. In both cases, the free length of the wing is kept at 27mm. In this study, the two geometries selected for the piezoelectric motor were the same geometries as that used in the FEM analysis, Part I [1]. Before the motor was optimized, the FEM model had 9mm long base and 27mm long wing. This was the first configuration which was used to simulate the motion of the motor and determine its characteristics. With additional analyses, it was determined that the optimal geometry for the motor had base length of 11mm and wing length of 27mm.

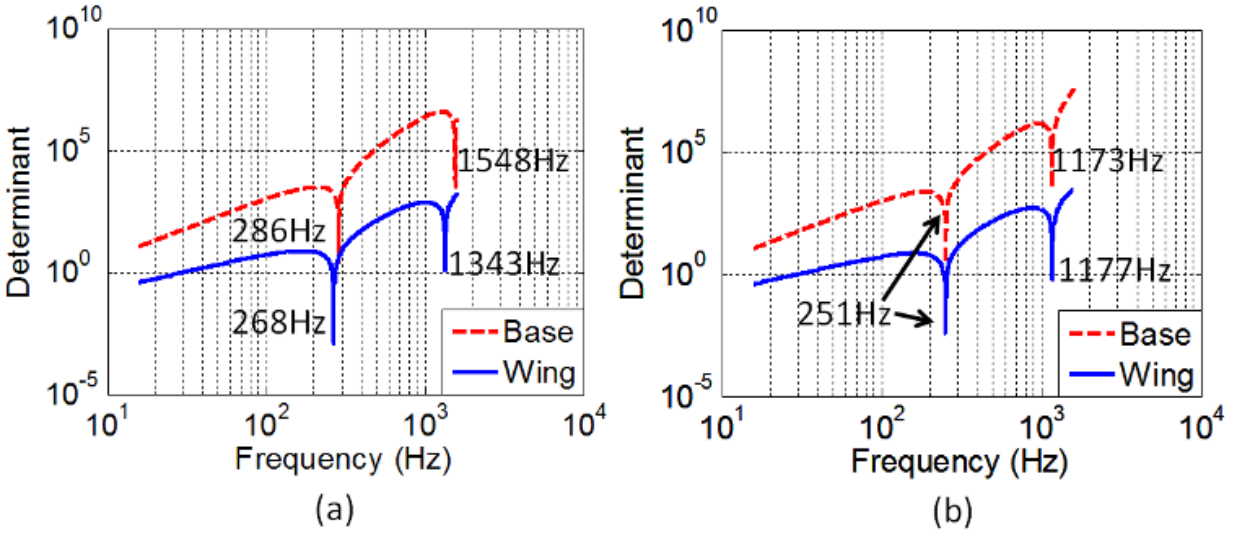

Figure 2.8 Determinant vs. frequency relationship for base and wing: (a) Base length =9mm, Wing length=27mm, (b) Base length=11mm, Wing length=27mm.

To compare the results with FEM models shown in Section 2.3.1, the same geometries for the experimental model shown in Chapter 3 and also for the analytical model here are used. It should be noted that the natural frequencies for the wing and base correspond to the frequencies at which the determinant of matrix M approaches zero. The first two natural frequencies for each element are shown in Figure 2.8. In the first case the determinant approaches zero for frequencies of 268Hz and 1343Hz, and 286Hz and 1548Hz for the wing and base respectively. In

the second case, the determinant approaches zero for frequencies of 251 Hz and 1.177 kHz and 251 Hz and 1.173 kHz for the wing and base respectively.

Before the mode shapes of the L-Shape motor can be obtained, constants of integrations $a=[a_1, a_{2,}...a_{10}]$ have to be obtained. There can be infinite solutions for the coefficients in a, however a unique solution can be obtained by setting one of the coefficients to 1. In this analysis a_{10} is set to 1 and the remaining coefficients $[a_1...a_9]$ can be calculated numerically, following the procedure shown below:

$$\begin{bmatrix} \overline{|M_{1,1}} & \dots & \overline{M_{1,9}|} & M_{1,10} \\ \vdots & M^* & & \vdots \\ \underline{|M_{9,1}} & & \underline{M_{9,9}|} & \vdots \\ M_{10,1} & \dots & & M_{10,10} \end{bmatrix} \begin{bmatrix} a_1 \\ \vdots \\ a_9 \\ a_{10} \end{bmatrix} = \begin{bmatrix} 0 \\ \vdots \\ 0 \\ 0 \end{bmatrix} \tag{2.3.31}$$

where,

$$M^* \begin{bmatrix} a_1 \\ \vdots \\ a_8 \\ a_9 \end{bmatrix} + a_{10} \begin{bmatrix} M_{1,10} \\ \vdots \\ M_{8,10} \\ M_{9,10} \end{bmatrix} = 0, \text{ results with } \begin{bmatrix} a_1 \\ \vdots \\ a_8 \\ a_9 \end{bmatrix} = -a_{10} \cdot (M^*)^{-1} \cdot \begin{bmatrix} M_{1,10} \\ \vdots \\ M_{8,9} \\ M_{9,10} \end{bmatrix}$$

Similarly if a_1 is set to 1, then coefficients $[a_2,..a_{10}]$ can be calculated numerically following:

$$\begin{bmatrix} M_{1,1} & M_{1,2} & & M_{1,10} \\ M_{2,1} & \overline{|M_{2,2}} & & \overline{M_{2,10}|} \\ \vdots & \vdots & M^* & \vdots \\ M_{10,1} & \underline{|M_{10,2}} & & \underline{M_{10,10}|} \end{bmatrix} \begin{bmatrix} a_1 \\ \vdots \\ a_9 \\ a_{10} \end{bmatrix} = \begin{bmatrix} 0 \\ \vdots \\ 0 \\ 0 \end{bmatrix} \tag{2.3.32}$$

$$M^* \begin{bmatrix} a_2 \\ \vdots \\ a_9 \\ a_{10} \end{bmatrix} + a_1 \begin{bmatrix} M_{2,1} \\ \vdots \\ M_{9,1} \\ M_{10,1} \end{bmatrix} = 0, \text{ results with } \begin{bmatrix} a_2 \\ \vdots \\ a_9 \\ a_{10} \end{bmatrix} = -a_1 \cdot (M^*)^{-1} \cdot \begin{bmatrix} M_{2,1} \\ \vdots \\ M_{9,1} \\ M_{10,1} \end{bmatrix}$$

It should be noted that either Eq. (2.3.31) or (2.3.32) can be used in the analysis for obtaining mode shapes as long as the determinant of M^* does not equal zero.

Depending on the geometry of the L-Shape structure, the natural frequency of the system corresponds to the natural frequency of the wing or the base. If the 1st natural frequency of the system corresponds to the 1st natural frequency of the base, then coefficients $[a_1,..a_4]$ have non-zero values while coefficients $[a_5,..a_{10}]$ equal zero. In the case where natural frequency of the system corresponds to the natural frequency of the wing, it is other way around. The reason behind this is because $[a_1,..a_4]$ correspond to the constants of integration in the spatial equation for the base Eq. (2.3.26), and coefficients $[a_5,..a_{10}]$ for the wing Eq.(2.3.27) and (2.3.28).

In the analytical analysis, the resonance of the system depends on the resonance of the base and the resonance of the wing. For the following geometry of the motor, base=9mm and wing=27mm, the 1st four natural frequencies are shown in Figure 2.9. The 1st natural frequency, 268Hz, corresponds to the 1st natural frequency of the wing, and the second natural frequency, 286Hz, corresponds to the 1st natural frequency of the base. Similarly the 3rd and fourth natural frequency, 1.343 kHz and 1.548 kHz, correspond to the 2nd natural frequency for the wing and base respectively. Knowing how the natural frequency of the individual element affect the natural frequency of the motor, mode shapes for the L-Shape structure can be obtained as well. Each mode shape of the motor is directly related to the mode shape of either the wing or the base.

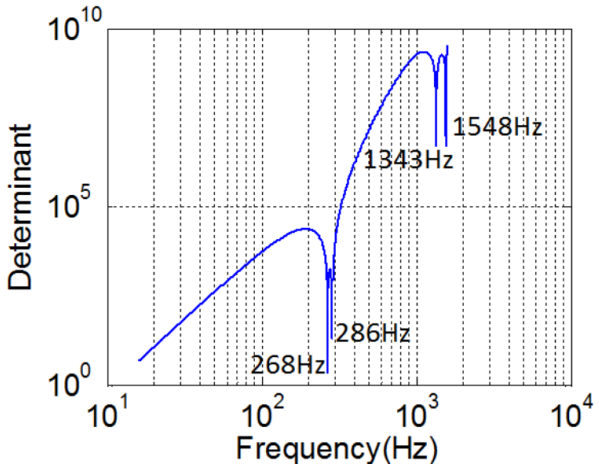

Figure 2.9 Natural Frequencies for the L-Shape Piezoelectric Motor.

In order to describe the procedure for obtaining the mode shapes of the motor, geometry was chosen where the free length of the base was 9 mm and the wing length was 27 mm. The 1st natural frequency as shown in Figure 2.9, 268Hz, was also the 1st natural frequency of the wing. For this frequency, the constants of integration $[a_{5,}..a_{10}]$ which can be calculated using the procedure shown in Eq. (2.3.31) or (2.3.32) are substituted into Eq. (2.3.27) and (2.3.28), resulting with an expression for the mode shape. Following the same steps, the 2nd mode shape of the motor which is based on the 1st natural frequency for the base, 286Hz, was used to calculate $[a_{1,}..a_{4}]$ which are then substituted into Eq. (2.3.26). This approach was used to obtain the 1st six mode shape of the piezoelectric motor based on bending vibration as shown in Figure 2.10. It should be noted that the 1st four natural frequencies of the system correspond to the 1st two bending modes of the wing and base, however the 3rd bending mode of the base and wing do not correspond to the 5th and 6th natural frequencies of the motor. The reason for this is related to the fact that at frequencies higher than 1.5 kHz torsional vibration modes dominate and the 3rd bending modes appear at much higher frequencies.

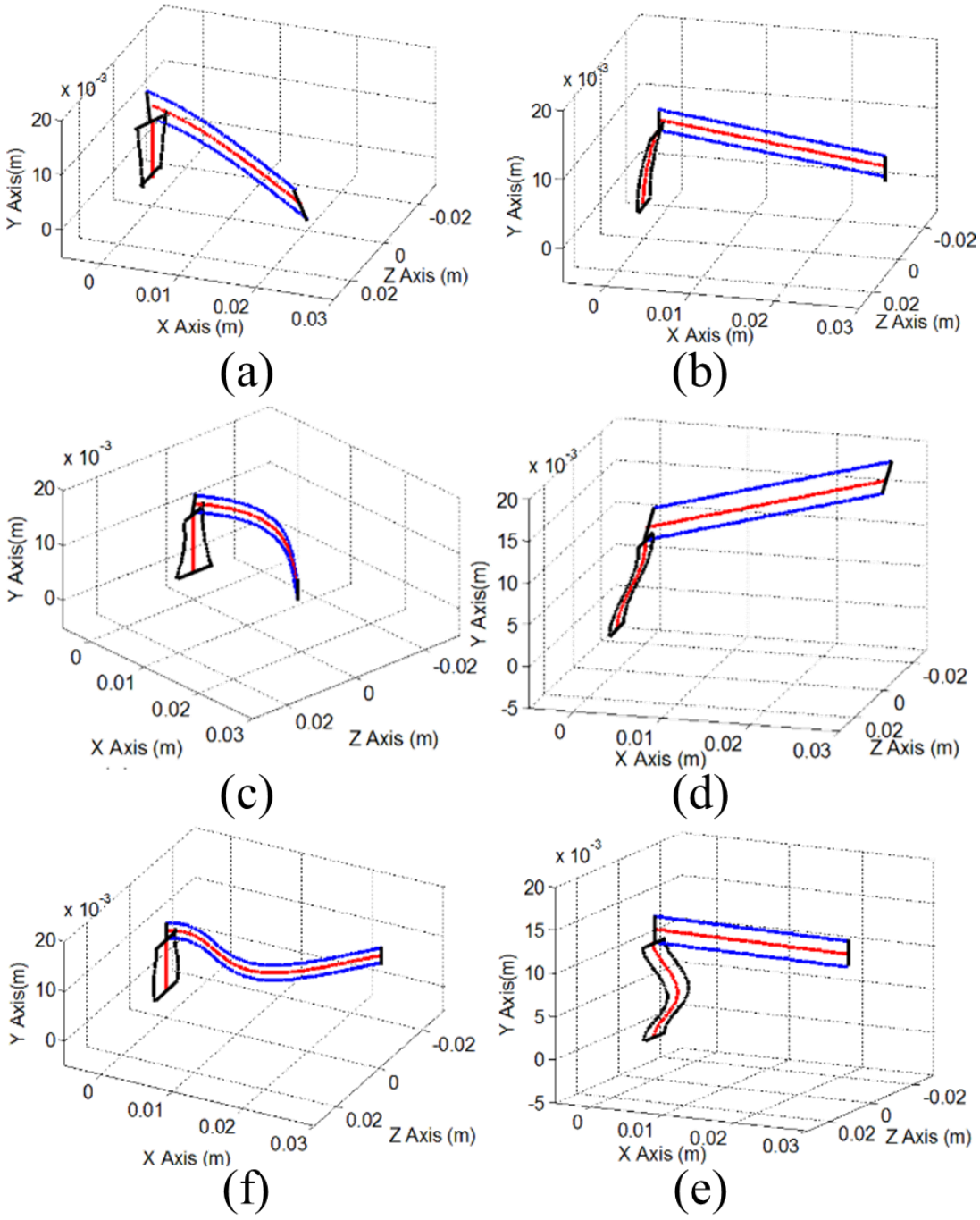

Figure 2.10 Mode Shapes of the L-Shape Structure: (a)1st Bending Mode of Wing, (b) 1st Bending Mode of Base, (c) 2nd Bending Mode of Wing, (d) 2nd Bending Mode of Base, (e) 3rd Bending Mode of Wing, (f) 3rd Bending Mode of Base.

Besides obtaining mode shapes and natural frequencies, the mechanical model was also used to define an optimal geometry of the L-Shape piezoelectric motor for piezoelectric bimorphs which were obtained from APC International (Catalog No. 40-1055 (350/025/0.60-SA), with dimensions shown in Table 2.3-1. The properties of the piezoelectric motor and ABS plastic coupler are shown in Table 2.3-2 and Table 2.3-3. The analysis was done by keeping the free-length of the wing at 27mm and varying the free-length of the base. The free-length of the base (clamp 1 – clamp 2) can be easily varied by adjusting the position of clamp 1. This implies that position of clamp 1 will not have significant influence on the robustness of the L-shape configuration of the motor. On the other hand, if the free length of the wing was decreased (clamp 2 – the right free end), the configuration of the motor would change from "L-shape" to a "T – shape". The T-shape orientation drastically alters the dynamics of the piezoelectric motor and this is why the length of the wing in this study was kept constant at 27mm. The graph shown in Figure 2.11 describes how the first natural frequency for the base and wing changes as a function of the free length of the base. From this plot it can be identified that the optimal geometry of the motor was obtained when the length of the wing was 27 mm and the free-length of the base was 11mm resulting with matching frequency of 252Hz. The goal of generating an elliptical motion at the tip is only possible if coupling between the bending vibration modes is acquired. The closer the natural frequencies for the two piezoelectric bimorph the more defined is the elliptical motion. This was validated with an FEM model in ATILA where the resonance frequency was also matched between the two elements at 242Hz.

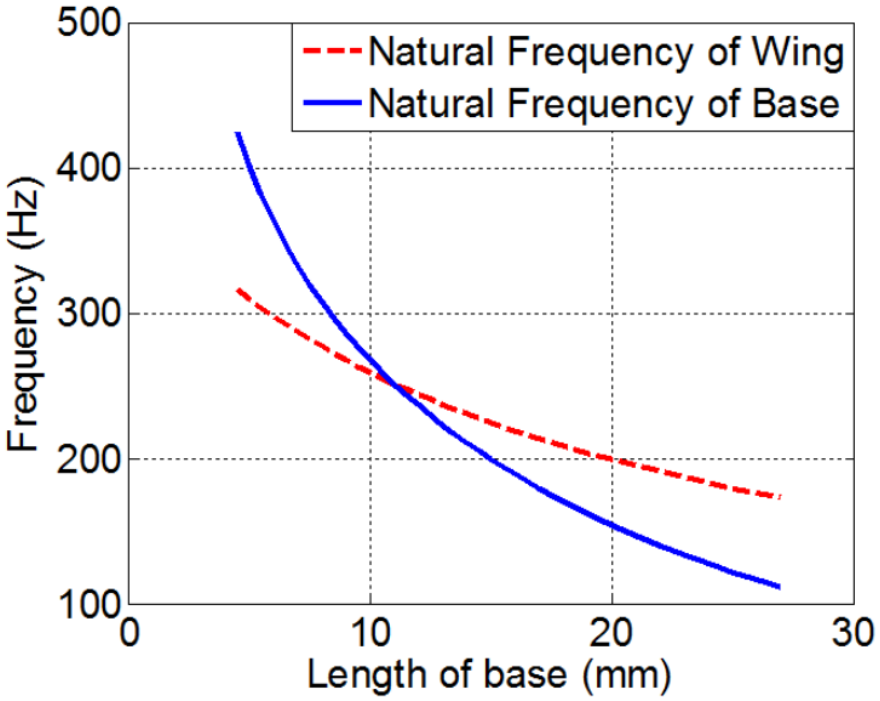

Figure 2.11 First natural frequency as a function of the length of base.

2.3.2.2 Electro-Mechanical Modeling

Once the free vibration model was completed, the analysis proceeded with an electromechanical model of the L-Shape piezoelectric motor. The fundamental elements of the motor are two piezoelectric bimorphs which analytically follow the Euler –Bernoulli model. Equation (33) represents the governing equations for bending vibration of a piezoelectric beam [71]:

$$YI\frac{\partial^{(4)}w_1(x,t)}{\partial x^{(4)}}+\rho A\frac{\partial^2 w_1(x,t)}{\partial t^2}=-\alpha\left[\frac{d\delta(x)}{dx}-\frac{d\delta(x-L)}{dx}\right]v(t) \tag{2.3.33}$$

where $v(t)$ is the voltage applied to the bimorphs, $\delta(x)$ is the Dirac delta function and α is the figure of merit at the average distance from the neutral axis of the piezoelectric bimorph:

$$\alpha=\frac{1}{2}Y_p d_{31} b(h_s+h_p)/2 \tag{2.3.34}$$

The electromechanical model follows modal analysis. A separation of variable solution was used to solve for the governing equation. Substituting, Eq.(2.3.33) in the equation below:

$$w(x,t)=\sum_{n=1}^{\infty}W_n(x)T_n(t) \tag{2.3.35}$$

where both W_n and T_n are dependent on n number of modes, resulting in the expression:

$$\sum_{n=1}^{\infty}\rho AW_n{\omega_n}^2T_n+\rho A\sum_{n=1}^{\infty}W_n\ddot{T}_n=-(\alpha)v(t)\left[\frac{d\delta(x)}{dx}-\frac{d\delta(x-l)}{dx}\right] \tag{2.3.36}$$

Next, Eq. (2.3.36) was multiplied by W_m and integrated over the entire length of the L-Shape structure $\int_0^{l_2}$. The orthogonality of the mode shape results:

$$(M_m)(\ddot{T}m+2\zeta mw_m\dot{T}_m+{\omega_m}^2T_m)=-\Psi_m \tag{2.3.37}$$

where M_m is defined in Eq.(2.3.38) as the mass term obtained from orthogonality and it was used to normalize the mode shapes of the system:

$$\begin{aligned}M_m=\rho_1A_1\int_0^{l_1}{W_{1m}}^2(x)dx+M_t{W_{1m}}^2(l)+\rho_1I_p\int_0^{l_1}{B_m}^2(x)dx+\\+\rho_2A_2\int_0^{l_2}{W_{2m}}^2(x)dx+I_z\left(\frac{dW_{1m}}{dx}(l_1)\right)^2+l_2m_2W_{1m}(l_1,t)\end{aligned} \tag{2.3.38}$$

Notice in Eq.(2.3.37) a damping term is added to the EOM, ζ . The reason for adding damping is to improve the analytical model so that it can closely match the real L-Shape piezoelectric motor. The damping ratio ζ was measured experimentally following the quadrature peak picking method for lightly damped systems [70]. The experiment was done by conducting FRF analysis on the L-Shape motor. The value calculated was 0.0053.

The term on the right side of the equal sign in Eq. (2.3.37) is defined as:

$$\Psi=v_1(t)\alpha_1\left(\tilde{W}_{1m}{}^{(1)}(l_1)-\tilde{W}_{1m}{}^{(1)}(0)\right)+v_2(t)\alpha_2\left(\tilde{W}_{2m}{}^{(1)}(l_2)-\tilde{W}_{2m}{}^{(1)}(0)\right) \tag{2.3.39}$$

where $\alpha_1=\alpha_2=\alpha$, due to identical piezoelectric and geometrical properties of the base and wing, $v_1(t)$ and $v_2(t)$ are the voltages applied to the base and wing respectively and $\tilde{W}_{1m},\tilde{W}_{2m}$ represent the normalized mode shapes of the system. In Eq.(2.3.39), $\tilde{W}_{(1m)(l_1)}$ and $\tilde{W}_{(1m)(0)}$ are the normalized mode shapes of the base defined in Eq.(2.3.40) being evaluated at l_1 and $l_1=0$ respectively. In addition, $\tilde{W}_{(2m)(l_2)}$ is the normalized mode shape of the wing defined in (2.3.41), evaluated at l_2. Finally, $\tilde{W}_{(2m)}{}^{(1)}(0)$ is the normalized mode shape of the wing evaluated at $l_2=0$, which is actually $\left(-\tilde{B}_1(l_1)\right)$ given by Eq.(2.3.42). This indicates that the mode shape of the wing

at $l_2 = 0$ corresponds to the torsional vibration mode shape of the base evaluated at l_1. The relationship is represented by the BC shown in Eq.(2.3.21).

$$\tilde{W}_{1m} = \frac{W_{1m}}{\sqrt{M_m}} \tag{2.3.40}$$

$$\tilde{W}_{(2m)} = \frac{W_{2m}}{\sqrt{M_m}} \tag{2.3.41}$$

$$\tilde{B}_{(1m)} = \frac{B_{1m}}{\sqrt{M_m}} \tag{2.3.42}$$

where W_{1m}, W_{2m}, B_{1m} are the mode shapes obtained from equations (2.3.26), (2.3.28) and (2.3.27) and $\sqrt{M_m}$ is defined in Eq.(2.3.38).

2.3.2.3 Results and Summary

It can be inferred that two elements, the base and the wing even though are being coupled together were actuated independently. Voltage 1 was applied to the base and Voltage 2 was applied to the wing. What this means is that two modes used in the analysis, which correspond to the first bending mode of vibration for the wing and base are independent of each other. Each bimorph oscillates at its own natural frequency. Therefore the first mode corresponds to the first natural frequency of the wing and the second mode to the first natural frequency of the base or vise-versa depending on the geometry of the motor.

Equation (2.3.37) can be written in the frequency domain by taking the Fourier transform of both sides.

$$-\omega^2 \eta_m(\omega) + 2\zeta\omega_n j\omega\eta_m(\omega) + \eta_m(\omega){\omega_m}^2 = \psi_m V(\omega) \tag{2.3.43}$$

where, $\eta_m(\omega)$ and $v(t)$ are Fourier transform of T_m(t) and $v(t)$ correspondingly. Equation (2.3.43) can be rewritten as:

$$\eta_m(\omega) = V(\omega)\frac{\Psi_m}{-\omega^2 + 2\zeta\omega_m j\omega + {\omega_m}^2} \tag{2.3.44}$$

The transfer function between displacement at motor's tip $W(tip,\omega)=\sum_{m=1}^{2}W_m(x)\eta(\omega)$ and voltage can be represented by three equations corresponding to X_2, Y_2 and Z_2 direction, Eq. (2.3.45), (2.3.46) and (2.3.47) respectively:

$$\frac{X_2(tip,\omega)}{V(\omega)}=\sum_{m=1}^{2}W_{1,m=1}(l_1)\frac{\Psi_m}{-\omega^2+2\zeta\omega_m j\omega+{\omega_m}^2} \tag{2.3.45}$$

$$\frac{Y_2(tip,\omega)}{V(\omega)}=-l_2\sum_{m=1}^{2}W_{1,}{}^{(1)}{}_{m=1}(l_1)\frac{\Psi_m}{-\omega^2+2\zeta\omega_m j\omega+{\omega_m}^2} \tag{2.3.46}$$

$$\frac{Z_2(tip,\omega)}{V(\omega)}=\sum_{m=1}^{2}W_{2,m=2}(l_2)\frac{\Psi_m}{-\omega^2+2\zeta\omega_m j\omega+{\omega_m}^2} \tag{2.3.47}$$

where motion in X_2 is dependent on the bending displacement at the tip of the base; motion in Y_2 depends on the bending angle at the tip of the base and Z_2 is the motion achieved at the tip of the wing when bending.

Figure 2.12 shows the relationship between the displacements in all three directions of the tip of the motor for a frequency range that covers the 1st two natural frequencies. As shown in Figure 2.12, the largest displacements in all three directions appear at the same natural frequency. The figure was obtained for the L-shape piezoelectric motor with optimal geometry, where free length of base and wing are 11 mm and 27 mm respectively.

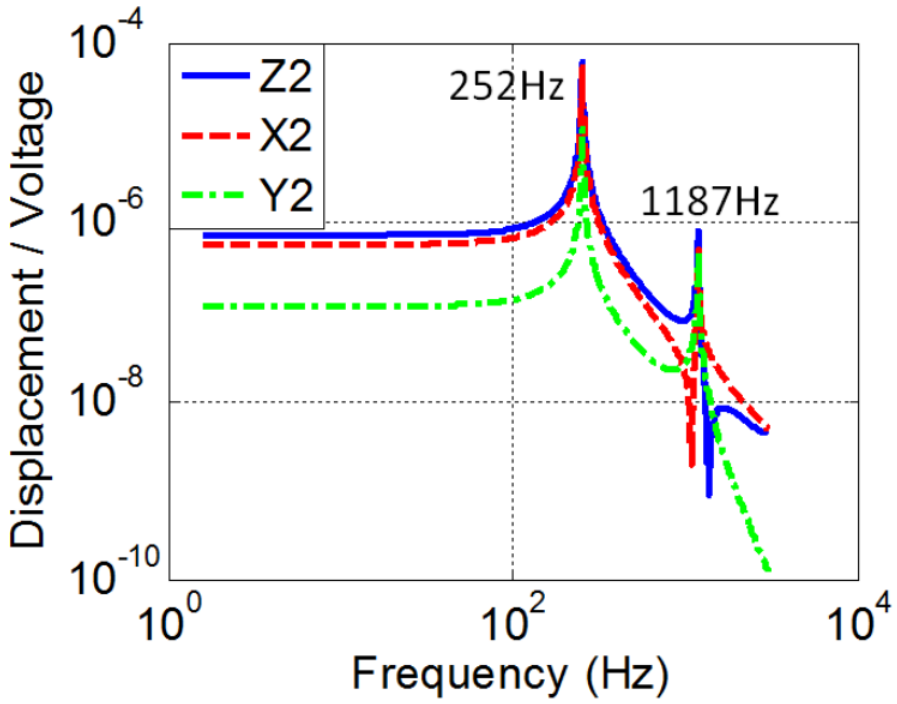

Figure 2.12 Transfer Function for displacement at motor's tip.

In order to describe the elliptical motion which is obtained at the tip of the motor, Eq. (2.3.44) was written in the time domain. This way, the motion can be presented for a specific frequency with respect to time, $W(tip,t)=\sum_{m=1}^{2}W_m(x)T_m(t)$. η_m is a complex value and when written in the time domain it is composed of a two parts, magnitude, Mag and phase value, ϕ,

$$T_m(t)=Mag\cdot\sin(\omega t+\phi) \tag{2.3.48}$$

The voltage signal responsible for actuating the bimorphs is represented as:

$$V(t)=a\sin(\omega t) \tag{2.3.49}$$

The magnitude is shown in Eq. (2.3.50) and the phase in Eq. (2.3.51):

$$Mag=a\left|\frac{\Psi_m}{-\omega^2+2\zeta w_m j\omega+\omega_m{}^2}\right| \tag{2.3.50}$$

$$\phi=\angle\left(\frac{\Psi_m}{-\omega^2+2\zeta\omega_m j\omega+\omega_m{}^2}\right) \tag{2.3.51}$$

Where $\angle$ (complex number) is just $\tan^{-1}(\frac{imag}{real})$.

With the equation represented in the time domain, the dynamics of the motor's tip can be expressed by X_2, Y_2 and Z_2

$$X_2(tip,t) = \sum_{m=1}^{2} W_{1,m=1}(l_1) \cdot T_m(t) \tag{2.3.52}$$

$$Y_2(tip,t) = \sum_{m=1}^{2} W_{2,m=2}(l_2) \cdot T_m(t) \tag{2.3.53}$$

$$Z_2(tip,t) = -l_2 \sum_{m=1}^{2} W_{1,}^{(1)}{}_{m=1}(l_1) \cdot T_m(t) \tag{2.3.54}$$

Using Eq. (2.3.52), (2.3.53) and (2.3.54), shown above, an elliptical motion at the tip of the motor can be obtained as long as the base and wing are actuated 90º out of phase. In the piezoelectric motor, the efficiency and working principle is highly dependent on the frequency of oscillation. Therefore an analysis on the motor with optimized geometry was developed, where the input voltage was 100 V and the frequency of excitation varied. Figure 2.13 shows the results obtained from the test. As seen in this figure, elliptical motion was generated at each frequency however the largest motion was obtained at 252.7Hz which is the same as the frequency reported in Figure 2.11.

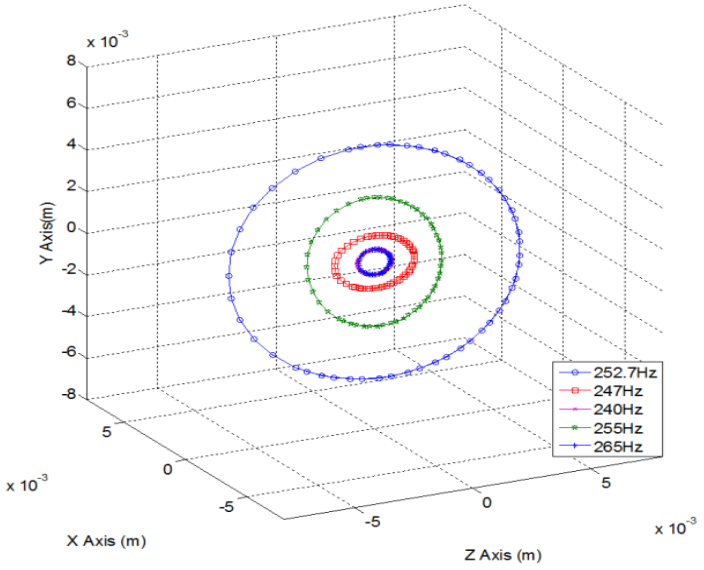

Figure 2.13 3-D tip motion as a function of frequency.

As mentioned before, if the piezoelectric bimorphs are actuated at resonance and if their 1st natural frequencies were close, than highest deflections, velocities and torques can be

expected. This plot confirm that hypothesis and demonstrates the fact that elliptical motion will be created at any frequency below the resonance and slightly above. The reason behind this is that the mode shape at the first resonance dominates over any frequencies below and frequencies above which are in close proximity. Additional analysis using the analytical model was also conducted. In this analysis the frequency was kept constant at 252.7Hz and the voltage varied. The motion generated by the tip is presented in Figure 2.14. It can be noticed from this figure that the deflection and voltage are directly proportional. The deflection of the motor's tip increases as the voltage amplitude increases.

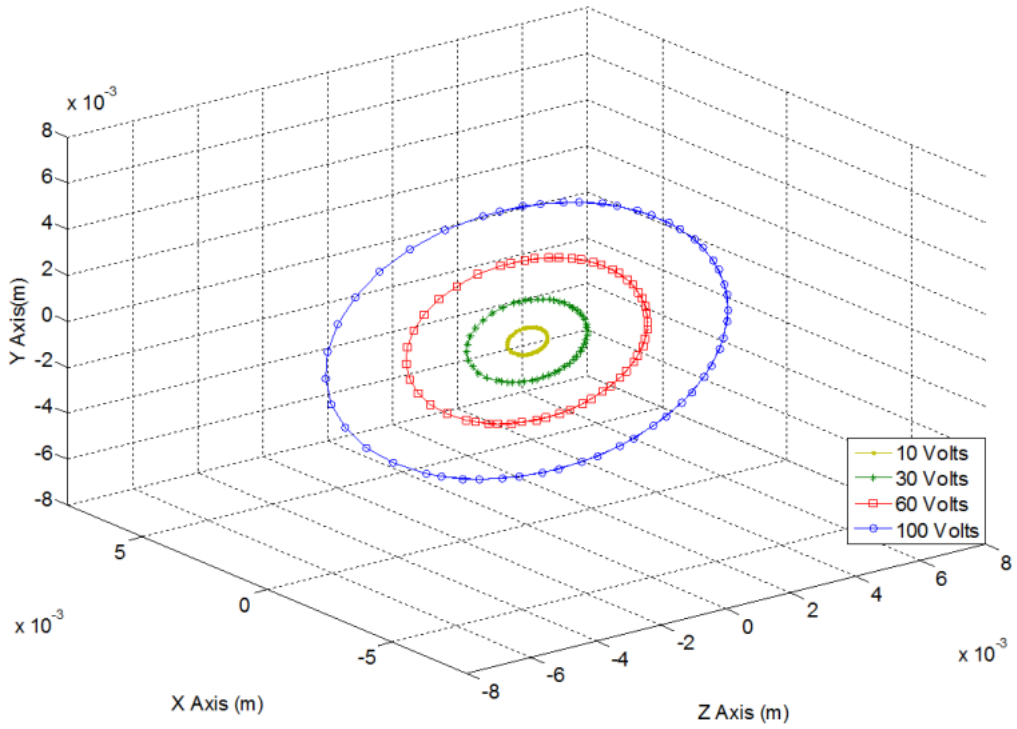

Figure 2.14 3-D Tip motion as a function of voltage.

2.3.3 Parametric Study

The advantage of the analytical model over the FEM model developed for the L-Shape motor was the fact that additional studies could be conducted, in a more convenient and inexpensive way. As such, parameterization study was conducted and the behavior of the motor as a function of its size was observed. Since the main objective is having the swallowable robot presented in this dissertation to operate inside the human body it is essential that its size resembles that of a pill. The parameterization study is presented in Figure 2.15 where for

selected motor sizes the variation in natural frequency is determined. The natural frequency of the motor is obtained when the natural frequency of the base and the natural frequency of the wing match or are very close to each other. As the total length of Base and Wing decreased, so did the natural frequency of the L-shape motor. It is essential to note that in order for the piezoelectric motor to work efficiently and produce largest deflection at its tip, it needs to operate at its natural frequency. The exact length of the base and wing and the corresponding natural frequency can be calculated by using the values shown on both Y axes.

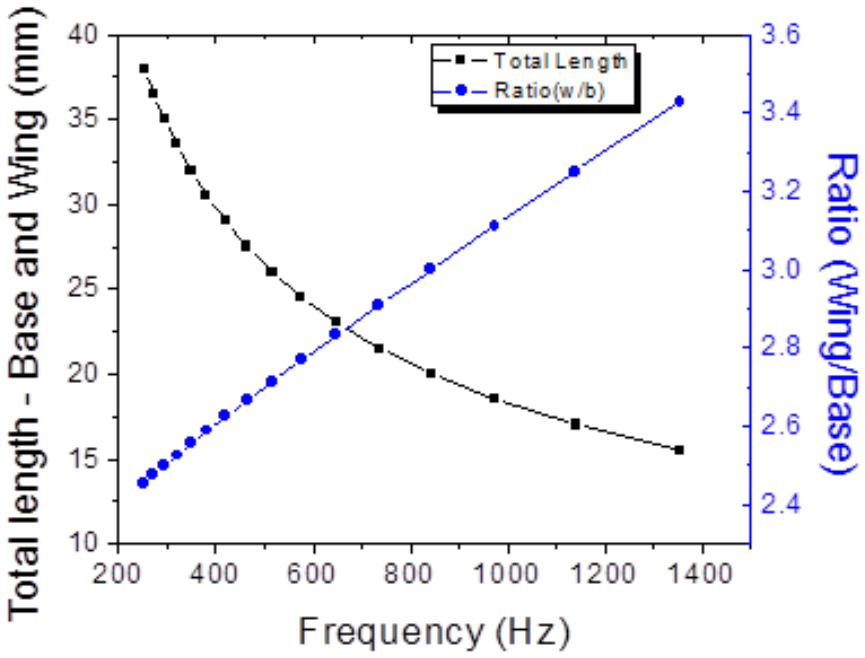

Figure 2.15 Relationship between the natural frequency of the motor and its size

Once the natural frequency for different size of the motor was calculated, it was possible to model the tip motion of the motor under no load. Shown in Figure 2.16 is the motion generated in all three directions X, Y and Z. As expected, the elliptical motion reduced as the size of the motor decreased. This study can also be expanded to any other frequency of oscillation below the first natural frequency. By computing the motion at the tip of the motor, a model for the motion of the entire robot can be achieved.

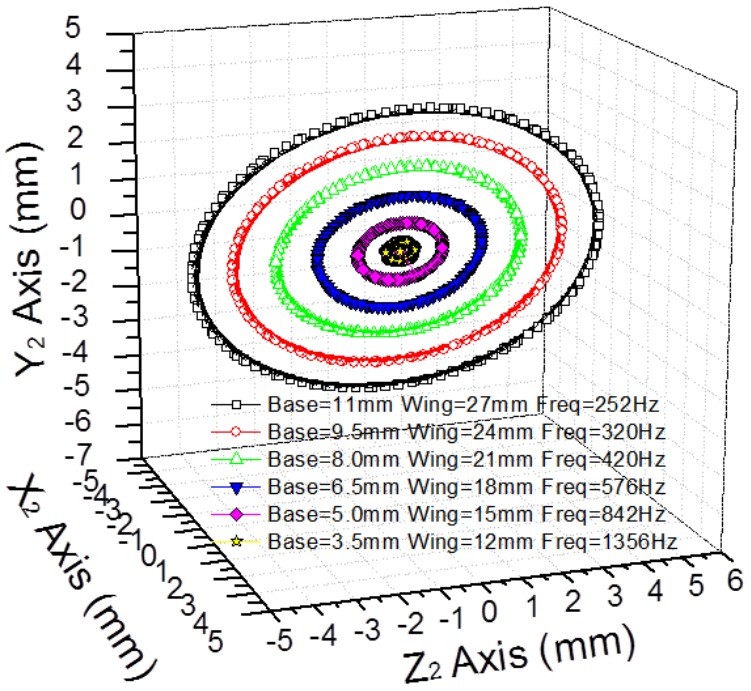

Figure 2.16 Simulated tip motion as a function of size and natural frequency of L-Shape motor.

Nomenclature

$\dot{a}$ – time derivative
$a^{(\ )}$ – spatial derivative
$_1$ –subscript corresponding to base
$_2$ –subscript corresponding to wing

m_1 – mass per unit lenght of base
m_2 – mass per unit length of wing
M_t – mass of wing and mass of coupling element
w_1 – deflection caused by actuation of base
w_2 – deflection caused by actuation of wing
u_2 – deflection of wing in X_2 due to base actuation
x_1 – base coordinate
x_2 – wing cooridnate
β_1 – twist angle of base
I_p – polar moment of inertia
b – width of piezoelectric bimorph
h_s – thickness of substrate
h_p – thickness of piezoelectric layer
ρ_s – density of substrate
ρ_p – density of piezoelectric layer
ρ_1 – density of bimorph
l_1 – free length of base
l_2 – free length og wing
Y_p – Young's modulus of elasticity for the piezoelectric layer
$Y_1 I_1$ – Bending stiffness of Base
$Y_2 I_2$ – Bending stiffness of Wing, same as Base
GJ – torsional stiffness
I_z – moment of inertia
t – time
A – cross sectional area of piezoelectric bimorph
s_{11} – elastic compliance at constant electric field

d_{31} – piezoelectric constant
ζ – damping ratio
α – coupling figure of merit
ω – natural frequency
j – unit imaginery number

2.4 Conclusion

In this study two piezoelectric motor concepts were presented, L-Shape and U-Shape, which define the fundamental work of the legged type locomotion mechanism discussed in Chapter 3. As a result first the principle of operation was presented followed by theoretical models. The theoretical models were used to predict the dynamics and the response of the motors as well as to provide insight to the geometry required for constructing the motors. Both FEM and distributed parameter electro-mechanical models using piezoelectric elements were used to represent the dynamics of the L-Shape motor. Finally, the study was able to not only predict the response of the motor in terms of the elliptical motion generated at the tip, but was also used in simulating parametric study. Accordingly, optimal geometry for different bimorph size was found and the corresponding response at the tip of the motor was presented. As a result of the theoretical models, further miniaturization of the WCEs, which are presented in Chapter 3 can be achieved, and prediction of their kinematics and response can be obtained.

Chapter 3 – Experimental Characterization of Piezoelectric Motors and Development of Locomotion Mechanisms[2]

3.1 Introduction

The drive train determines the size of the capsule and the power requirements consequently making the locomotion mechanism a fundamental part of future wireless endoscopes. It is also the key motivation behind the research presented in this dissertation. As discussed in the Chapter 1, this dissertation focuses on two types of locomotion mechanisms, legged and non-legged locomotion mechanism based on traveling waves induced on walls of WCEs (Chapter 4). Both designs utilize the phenomenon of traveling waves (T.W.) induced through the vibration of piezoelectric elements. Nevertheless, there is a significant difference between the two as it will be seen in the following sections.

This chapter focuses on the experimental characterization and demonstration of the L-shape and U-shape piezoelectric motors to be used as tentacles of legged driven wireless capsule endoscopes (WCE). First, a detailed characterization of the L-Shape and U-Shape piezoelectric motor is conducted, in order to determine the torque, velocity and efficiency curves. The details of the experimental setup and the steps are presented in this chapter. Following this, integration of the actuators onto a mobile platform is presented, where inspiration has mainly been drawn from the myriapoda subclass of arthropods. This group contains: millipedes, centipedes, symphulans and etc. where the profile of the legs in motion is represented by a propagating wave.

In order to develop a highly efficient and optimized solution, inspiration from biology was drawn. Nature has perfected its solution over millions of years and thus provides excellent guidance towards designing engineered systems. Previous research on developing miniature crawling inspired terrestrial robots has been conducted, [72-75]. The one most similar to the

[2] Some of the work discussed in this chapter was published in IEEE/ASME International conference, IEEE UFFC and IOP Smart Materials and Structures. The following are the citations:

- Avirovik, D., Priya, S., "Crawling-inspired robot utilized L-Shape Piezoelectric actuators," IEEE/ASME International Conference on Advanced Intelligent Mechatronics, Wollongong, Australia, (2013).
- Avirovik D., Priya S., "L-shaped piezoelectric motor-Part I: Design and experimental analysis", Ultrasonics, Ferroelectrics and Frequency Control, IEEE Transactions on;59:98-107,(2012)
- Avirovik D., Karami M.A., Inman D., Priya S., "L-shaped piezoelectric motor-part II: Analytical modeling", Ultrasonics, Ferroelectrics and Frequency Control, IEEE Transactions on;59:108-20,(2012)
- Avirovik, D., Butenhoff, B., Priya, S., "Millipede-inspired Locomotion through Novel U-Shaped Piezoelectric Motors", Smart Materials and Structures, 23 (2014)

work presented in this dissertation has been developed by the Harvard Microrobotics lab, which has been inspired by centipedes [74]. The microrobot utilizes a four-bar mechanism composed of piezoelectric actuators that convert the bending motion of piezoelectric beams into propulsive force. Correspondingly, proper actuation of multiple segments of these piezoelectric actuators results with locomotion of the mobile structure. Unlike this particular mechanism, the ones presented in this chapter directly utilize the L-Shape and U-Shape piezoelectric actuators without the need of four-bar mechanism or other linkages. The motion conducted at the tip of these actuators as previously presented traces a circle/ellipse. This is precisely what individual legs of centipedes and millipedes trace as well, [76]. As a result, by placing multiple actuators next to each other in a row, and actuating them accordingly, a propagating traveling wave can be generated which will result with propulsion. Because of the dynamics and structure of the L-Shape and U-Shape piezoelectric actuators, locomotion mechanisms have been developed.

The emphasis of this Chapter is on the integration of individual L-Shape or U-Shape piezoelectric motors in a row and their appropriate actuation. In accordance to this, first the L-Shape and U-Shape piezoelectric motors were experimentally validated and characterized and then integrated onto locomotion platforms. As a result, very simple, highly affordable crawling robots, utilizing low power piezoelectric bimorph actuators were developed and accordingly presented here.

3.2 L-Shape Motor Experimental Study

Following the theoretical approaches discussed in Chapter 2, FEA and distributed parameter, the optimized geometry of piezoelectric L-shape motor was identified and an actual prototype was constructed as shown in Figure 3.1 The bimorphs were obtained from APC International (Catalog No. 40-1055 (350/025/0.60-SA) and the clamps were built using a Rapid Prototyping Machine (DREAMS Lab, Virginia Tech). Initially, multiple tests were conducted to verify the theoretical model. First, the impedance of the base and wing was measured using an Impedance Analyzer (Hewlett Packard/Agilent 4194A) in the frequency range of 100 – 400Hz.

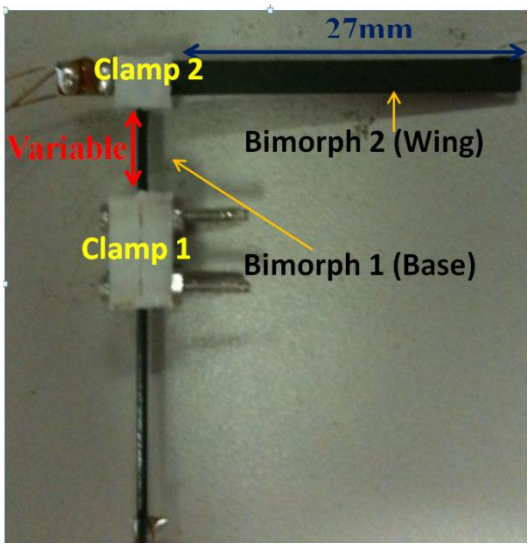

Figure 3.1 L-Shape Piezoelectric Motor Prototype

The measurements were conducted for two different cases as shown in Figure 3.2. In the first case the length of base was kept at 9mm and in the second case it was kept at 11mm. In both these cases, the wing length was kept at 27mm. The results in Figure 3.2 show excellent matching with the Finite Element Method (FEM) model results.

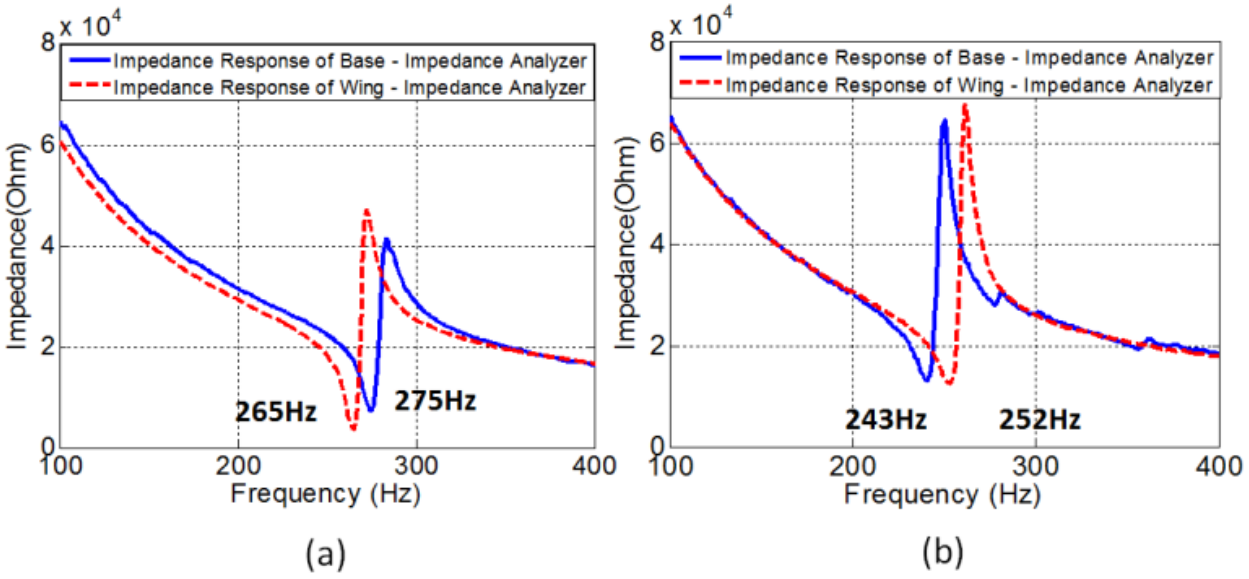

Figure 3.2 Experimental Impedance - Frequency Relationship for Base and Wing, (a) Base Length =9mm, Wing Length=27mm, (b) Base Length=11mm, Wing Length=27mm

Next, the elliptical motion generated at the tip of the motor was measured using the experimental setup shown in Figure 3.3. The setup consisted of a function generator (Wavetek

model 650) which was used to generate two sinusoidal waves 90º out-of-phase with respect to each other. The signals were then amplified using two high power amplifiers (HAS 4052). The second part of the diagram in Figure 3.3 illustrates the measurement procedure. Two laser vibrometers (Polytec PDV100 and Polytec OFV 055) were used to measure the tip velocity as indicated in the image. The signals from laser vibrometers were acquired by a data acquisition system SIGLAB, and Matlab was used to analyze and integrate the data in order to obtain displacements in Y_2 and Z_2 (see Figure 2.7). Using this experimental setup, multiple measurements were taken at the tip in the following range of frequencies, 190 - 270Hz. Since the bending resonance of the base and wing was kept at 243 and 251 Hz, the resonance of the combined structure was found to be 246Hz. To note, in mechanical vibration, the mode shape of a beam is the same at any frequency below the 1st natural frequency and slightly above it.

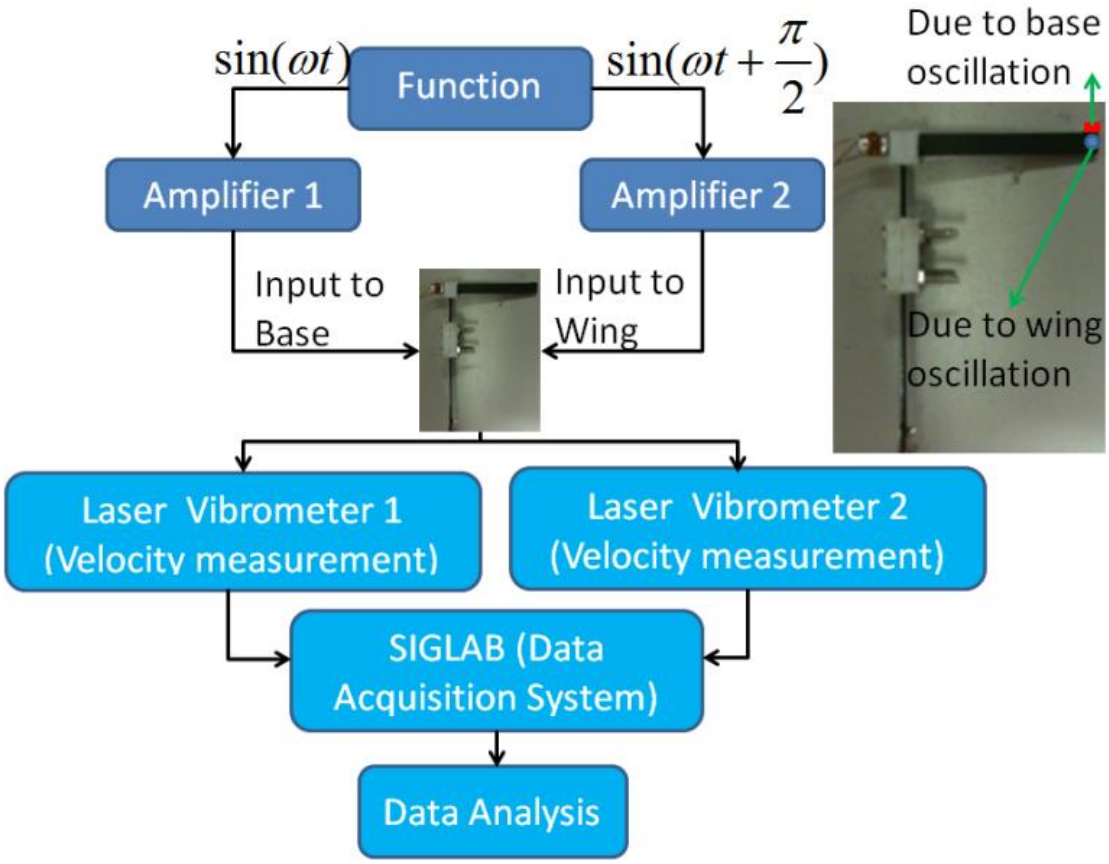

Figure 3.3 Experimental Setup for Measuring Elliptical Motion at Tip.

In this study, both the beam and wing experience the same mode shape for a cantilever beam, however, the deflection at the tip for each beam becomes greater as the oscillating

frequency approaches the 1st natural frequency. Since their individual natural frequencies are very close to each other it is safe to say that their joint natural frequency is in between the individual frequencies. Therefore at 246 Hz, both the base and wing experience the first bending mode and highest deflection at the tip.

Measured velocities from the two laser vibrometers are shown in Figure 3.4. The two signals correspond to the velocity measured due to the bending of the wing in the Z_2 direction and the bending of the base in the X_2 direction which translates to a deflection of the wing's tip in the Y_2 direction. The velocity signals were obtained at actuation frequency of 246Hz.

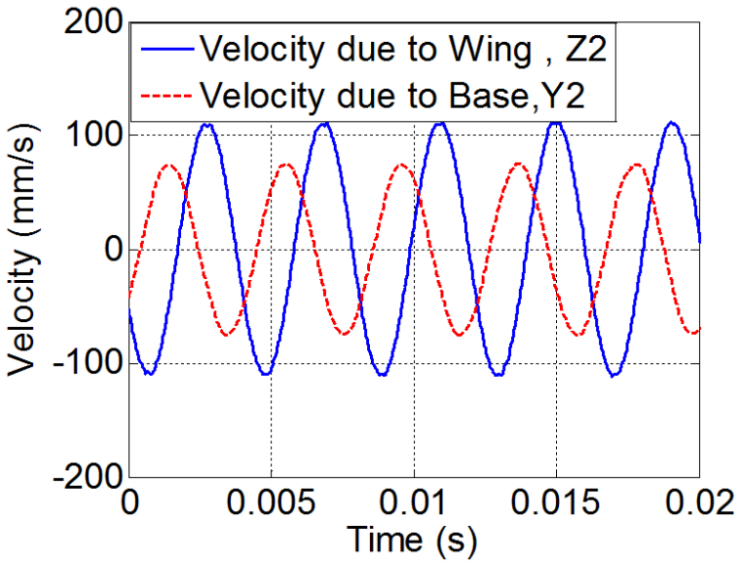

Figure 3.4 Laser vibrometer readings at the tip of the L-Shape motor

The experimental results were then compared to the analytical model (distributed parameter) and FEM which are discussed in Chapter 2. First, the principle of operation of the piezoelectric motor described in Figure 2.3 was compared with the steps of actuation obtained analytically in Figure 3.5. It can be seen from these figures that there was an excellent match between the expectation and calculations. Besides the principle of operation, the elliptical motion generated at the tip of the motor was compared between the three models as well. The analysis was conducted at resonance frequency of the L-Shape piezoelectric motor, where the forcing input was 1 V.

An image of the elliptical motion generated in the Z_2, X_2 direction is presented in Figure 3.6 As seen in the plot, the motion at the tip obtained analytically was very close to the motion obtained experimentally and through a FEM model.

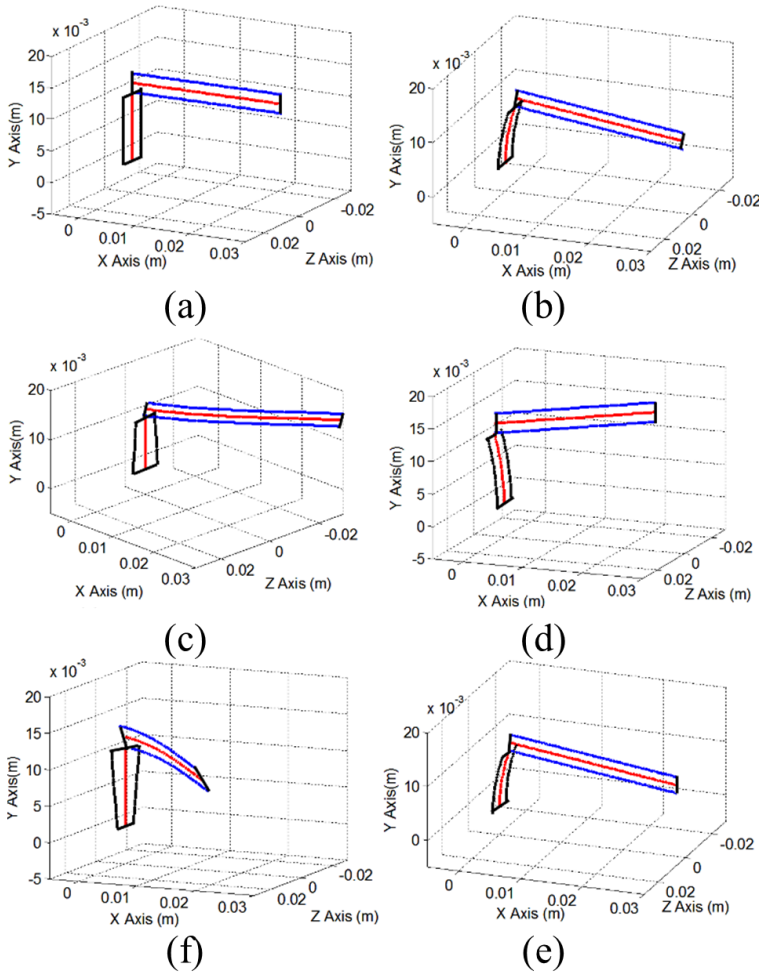

Figure 3.5 Principle of operation – analytical, (a) static equilibrium, (b) Base Voltage = Max, Wing Voltage = 0, (c) Base Voltage = 0, Wing Voltage = Max, (d) Base Voltage = Min, Wing Voltage = 0, (e) Base Voltage = 0, Wing Voltage = Min, and (f) Same as Motion in (b).

As observed, the resonance frequencies are very close to each other along with the displacement values in the Z_2, X_2. The results obtained analytically, experimentally and through FEM are in close proximity to each other.

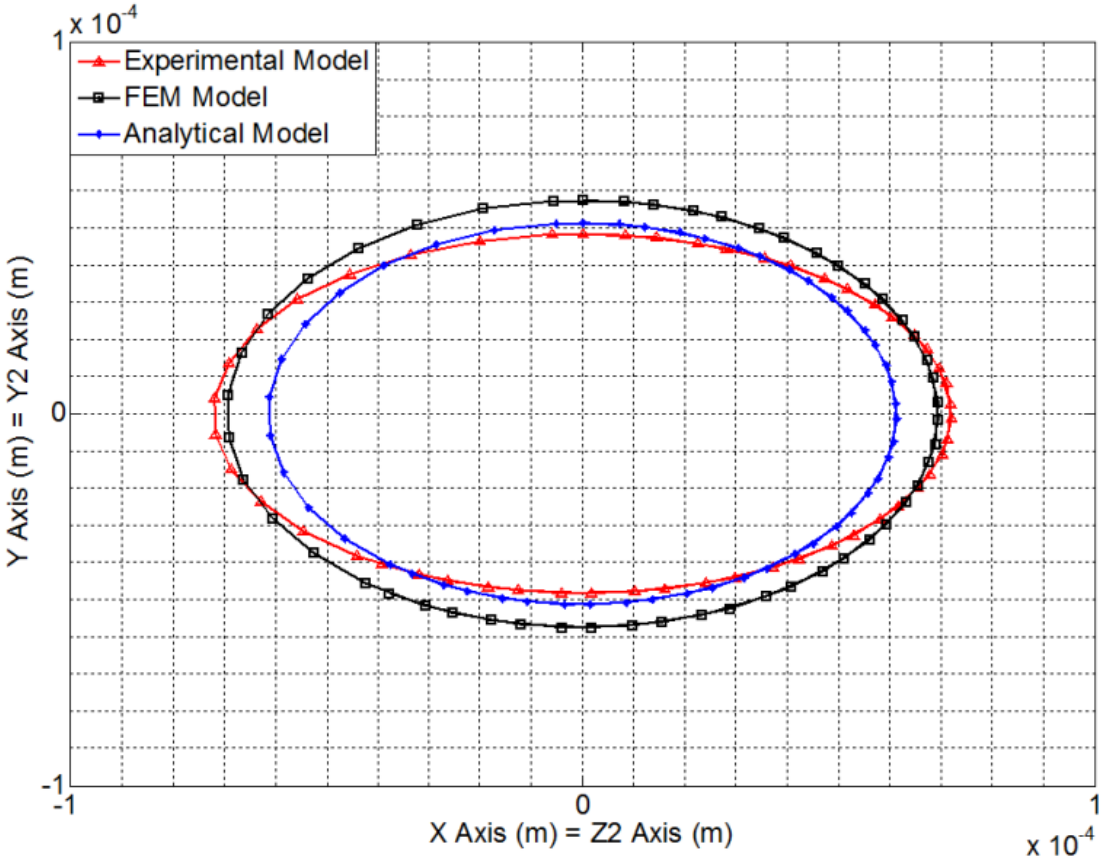

Figure 3.6 Motion at the tip of the L-Shape Piezoelectric Motor. Comparison between experimental Model, FEM Model and analytical model.

Finally, comparison between the three models relating the natural frequencies for the wing and base at two different geometries is shown in Table 3.2-1 and as indicated, a close match between the three can be observed.

Table 3.2-1 Comparison of Results

	Experimental		FEM (ATILA)		Analytical (D.P.)	
	Base	Wing	Base	Wing	Base	Wing
1st resonance Base=9mm Wing=27mm	275Hz	265Hz	288Hz	263Hz	286Hz	267Hz
1st resonance Base=11mm Wing=27mm	243Hz	252Hz	243Hz	243Hz	252Hz	252Hz
Elliptical motion (1volt)	X=±6.9E-5m Y=±5.2E-5m		X=±7.0E-5m Y=±5.7E-5m		X=±6.15E-5m Y=±5.15E-5m	

3.2.1 L-Shape Motor Characterization

Once the vibrational characteristics were obtained and the excitation frequencies were determined, the piezoelectric motor was characterized by actuating two stages: linear and rotational. In the first case, a linear stage fabricated by using a rapid prototyping machine was actuated by the motor. The combination of elliptical motion and friction between the tip and the surface of the stage leads to the actuation. A laser vibrometer was used to measure the displacement and velocity of the dynamic part. An image of the motor moving the stage is shown in Figure 3.7.

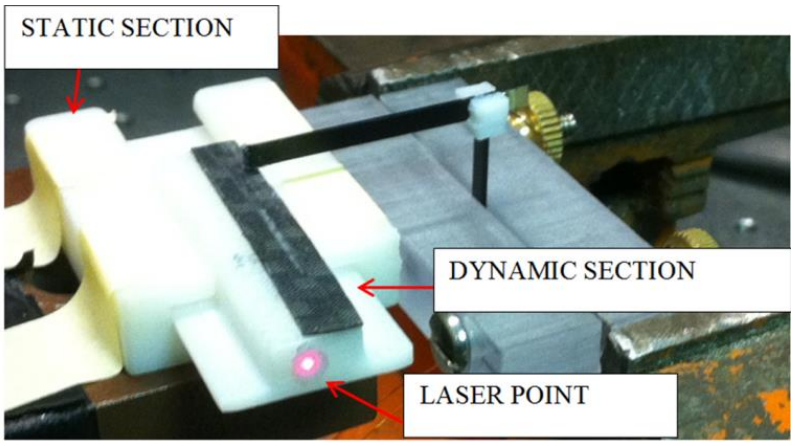

Figure 3.7 Experimental setup for actuating linear stage.

Friction between the tip and the contact surface must exist for the stage to operate. For this reason, three different high friction contact surfaces were used in the experiment to characterize the linear stage: rubber, ABS plastic and sand paper. The measured velocity from the three surfaces is shown in Figure 3.8. It can be seen in this graph that the highest velocity of 12mm/s was achieved when the surface of the stage was covered with sand paper. During this experiment, the mass of the dynamic section was 3 gm. The rubber surface even though resulted in small velocity had a very steady rate and quiet operation. Also, compared to the sand paper and ABS plastic, the rubber did not ware off quickly. The prototype of the stage was not optimized rather it was just used to quantify the performance of the motor. Additional work on the frictional contact surface is required to achieve reliable performance.

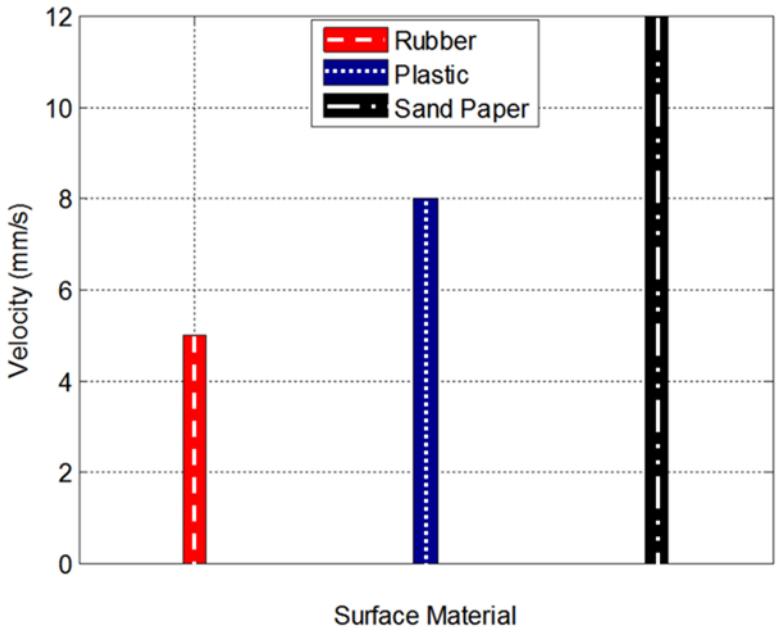

Figure 3.8 Velocity data of linear stage with different surface materials.

In addition to linear stage, a rotational stage was also developed in order to obtain the remaining characteristics for the motor. As in the previous case, the rotational stage was fabricated by using the rapid prototyping machine. The procedure to measure the rotational velocities, torque and efficiency, followed the method reported in References [77] and [78]. Figure 3.9 shows the experimental setup used for rotary stage characterization. There are three main components besides the motor as shown in the image, EM1-1-900 Transmissive Optical Encoder Module with 900 lines (US Digital products), HUBDISK-1-900-118-I (US Digital products), and HIOKI 3193 Power HiTester. In this setup, the tip of the motor generated elliptical motion and therefore was able to turn the HUBDISK whose motion was detected by the optical encoder. The displacement data was then acquired in Labview and analyzed, resulting in angular velocities and torque relationship.

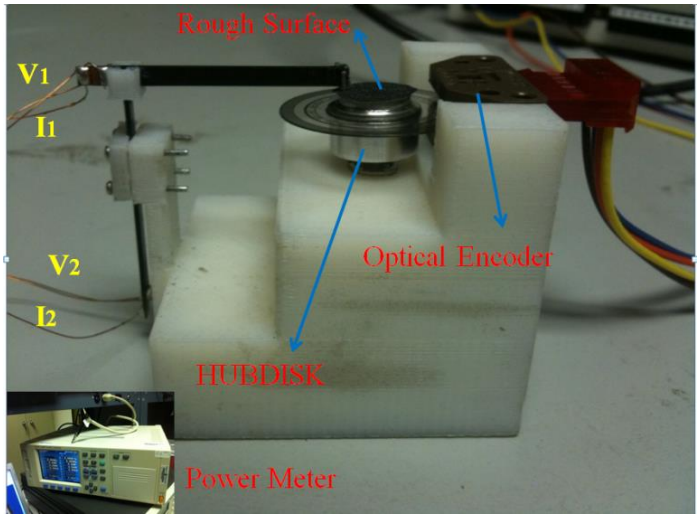

Figure 3.9 Experimental setup for measuring rotational velocity, torque and efficiency.

During this experiment, the RMS current and voltage values were also recorded, so that the efficiency of the motor could be determined. The piezoelectric motor was driven at resonance with a harmonic input of $120V_{pp}$. The torque of the motor was measured following the relationship:

$$\tau = J\frac{d\omega}{dt} \tag{3.2.0}$$

Where τ is the torque generated by the motor, J is the moment of inertia for the hub disk and $\frac{d\omega}{dt}$ is the angular acceleration of the hub disk.

The mass moment of inertia for the hub disk was known, $0.0576\,kgmm^2$. Since the disk was rotating on a small shaft, the mass moment of inertia for the shaft was also added to give a total of $0.06\,kgmm^2$. The only remaining term in Eq. (3.2.0) was the angular acceleration of the disk. The angular acceleration was calculated by using the following method. The encoder measured the angle of rotation in radians for a certain time interval. A plot of the data collected was generated into Matlab and a polynomial fit for the curve was created. For the purpose of this experiment, a 6^{th} order polynomial was selected to represent the position curve. This polynomial was then differentiated and an equation of the angular velocity curve was obtained. Figure 3.10 shows a plot of the position and velocity curves with respect to time. As seen on the figure, the velocity reaches an angular speed of 118 rad/sec and a steady state after 0.3 sec. The equation above the plot defines the velocity curve polynomial. This equation was differentiated so that

acceleration of the disk could be attained. The acceleration of the motor was measured during the transient time, 0.3 sec.

$$Vel = 1e7\left(6(0.0001)t^5 + 5(-0.0047)t^4 + 4(0.0688)t^3 + 3(-0.5401)t^2 + 2(2.3858)t - 5.6197\right)$$

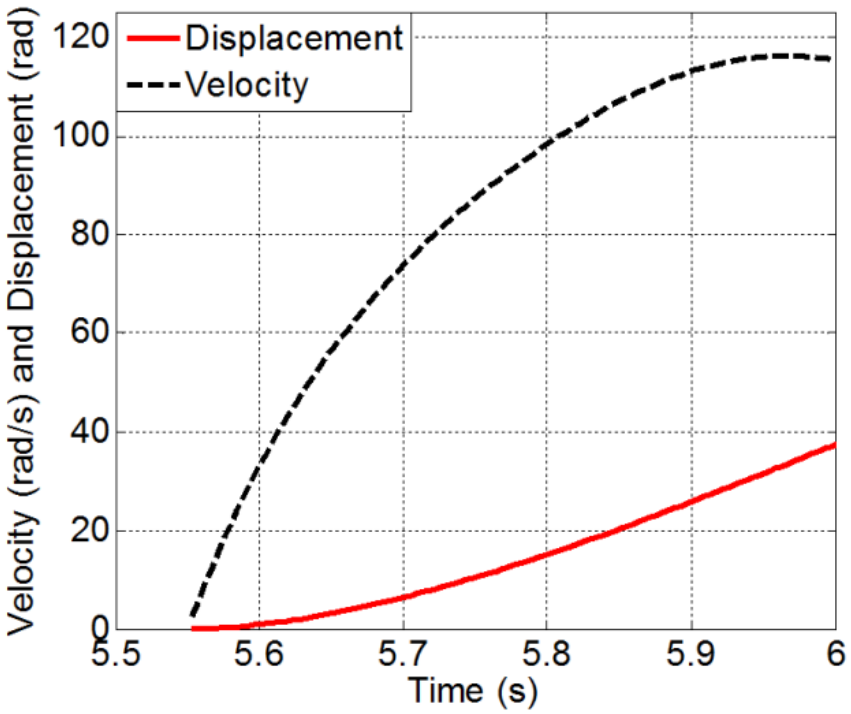

Figure 3.10 Displacement and velocity curves of the L-Shape piezoelectric motor.

The efficiency of a mechanical system is given as:

$$\eta = \frac{P_{out}}{P_{in}} = \frac{\tau(Nm)\cdot\omega(\frac{rad}{s})}{P_1(W)+P_2(W)}\cdot 100 \qquad (3.2.0)$$

where $\tau(Nm)$ is the torque measured using Eq. (3.2.0), $\omega(\frac{rad}{s})$ is the angular velocity of the disk, and $P_1(W)$ and $P_2(W)$ are the average power going into each bimorph measured by HIOKI 3193 Power HiTester. An important note in the efficiency calculations is taking account of the fact that the bimorphs themselves have a very low energy transmission coefficient that is directly related to the k31 value – electromechanical coefficient. Following Wang and Du [79], the relationship between the electromechanical coefficient k31 and an energy transmission coefficient of bimorph under constant external force loading condition $\lambda_{\max}$ is given as:

$$\lambda_{max} = \frac{32}{9k_{31}^{\ 2}}\left(\sqrt{1-\frac{k_{31}^{\ 2}}{4}}-\sqrt{1-\frac{13k_{31}^{\ 2}}{16}}\right)^2 \tag{3.2.0}$$

Using Eq. (3.2.0) and the measured k31 value for the APC international bimorphs of 0.4, the efficiency of the bimorphs was calculated to be 4.92%. In order to focus on the efficiency of the motor as a whole without considering the very low efficiency of the piezoelectric bimorphs, for the results presented, it was assumed that the efficiency of the bimorphs was 100%. Therefore the maximum efficiency of piezoelectric motor was measured to be 8.55%. With this information, the load characteristics for the L-Shape piezoelectric motor are shown in Figure 3.11. The motor reaches velocity of 118 rad/s, torque of 4.7 x 10^{-5} N.m and maximum efficiency of 8.55%.

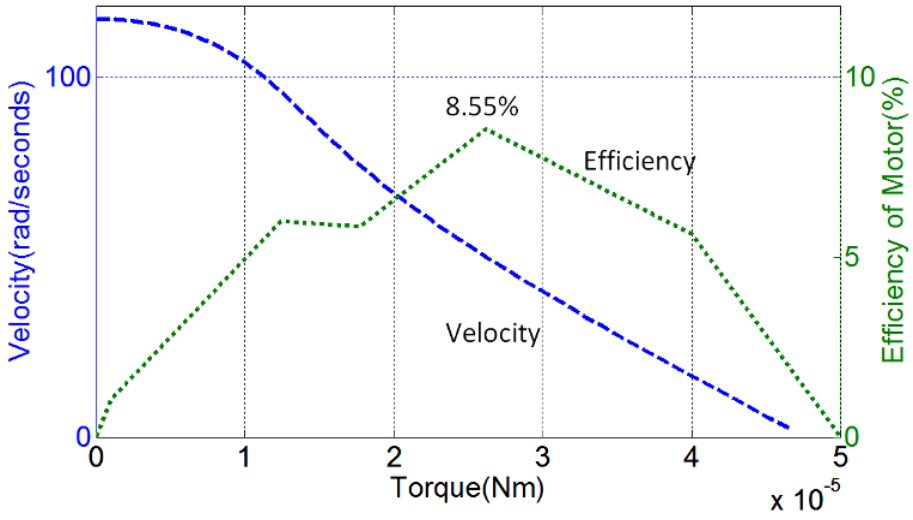

Figure 3.11 Load characteristics of L-Shape piezoelectric motor.

3.2.2 Crawling inspired robot utilizing L-Shape Piezoelectric Actuators

As discussed in the Introduction of this dissertation, the main objective of the work is the development of locomotion mechanisms for wireless capsule endoscopy. Therefore the L-Shape piezoelectric motor was utilized in the development of a legged type mechanism inspired by millipedes and centipedes. The design of the motor is shown once again in Figure 3.12 but now inverted, as it was in this form when integrated onto a milibot.

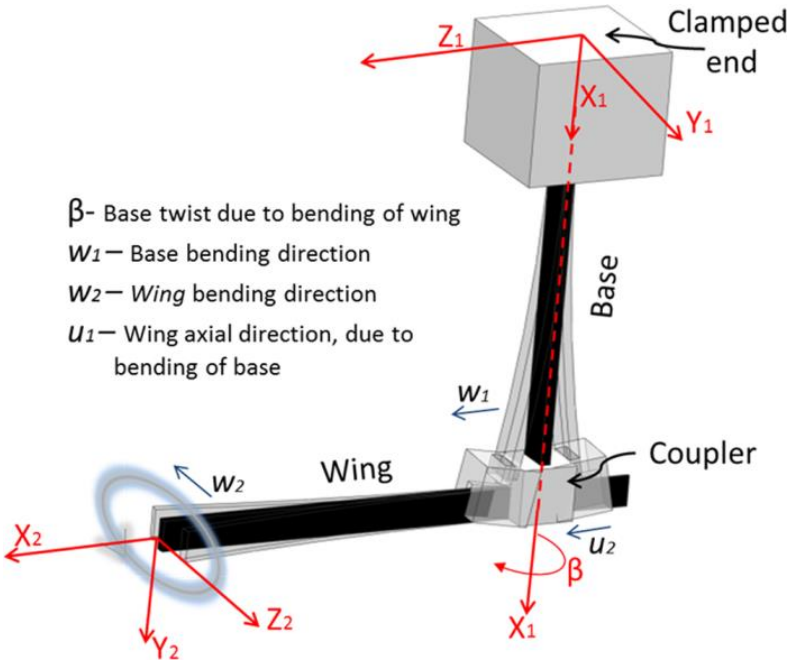

Figure 3.12 L-Shaped piezoelectric motor.

As a result of the design of the L-Shape motor, a 3D prototype design of a prototype is shown in Figure 3.13. Figure 3.13 (a) shows the design and Figure 3.13 (b) the principle of operation of the robot presented in this study. The robot is composed of four L-Shape piezoelectric motors, each representing a leg of a crawling insect. As the motors are actuated, an elliptical motion at the tip of the motor (the point where the end of the wing touches the ground) is generated, which consequently propels the robot. In the laboratory, an experimental setup which drives the robot was developed as shown in Figure 3.13(a). Most common four legged insect propel their body using the gait shown in Figure 3.13(b). This means that two legs that are positioned diagonally from each other move in phase with each other, but together they are 90° out of phase from the other leg pair. The gait of the crawling robot can be described as follows. At its initial step, step 0, all four legs are in contact with the ground. At step 1, FR and RL are actuated. During this state they are no longer in contact with the ground, instead they swing forward in air. Once the swing is completed they come into contact with the ground at step 2. During this intermediate step which is only for a short time period all four legs are in contact with the ground. Following this, in step 3, the FR and RL grab onto the ground surface and pull back to its starting position, therefore propelling the robot forward. During the same time the FL and RR, leave the ground and swing forward in air. Once this is accomplished, in step 4, all four

legs are touching the ground, same as step 2. Finally, in step 5, the inverse of step 3 can be observed. The steps continue to repeat as long as power is supplied to the piezoelectric actuators. Even though four motors, each composed of two piezoelectric elements needed to be actuated, it was possible to obtain the desired gait through the use of basic lab equipment. In the case of our crawling robot, a function generator (Model 650, Wavetek, San Diego) was used to generate two sinusoidal waves that are 90° out of phase from each other. The signals were amplified using high power amplifier (NF HAS 4052). From the amplifier, signals were directed to the piezoelectric beams, according to the flow diagram shown in Figure 3.13.

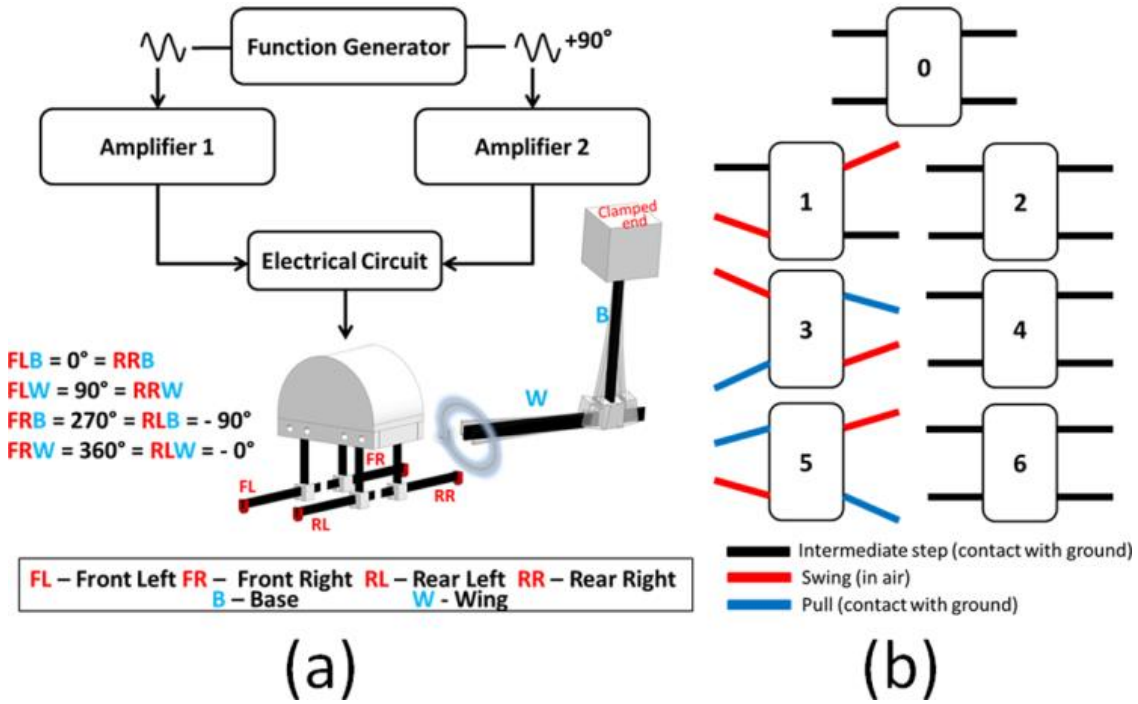

Figure 3.13 Crawling robot principle of operation: a) Actuation setup of piezoelectric motors, b) Schematic diagram representing the gait of the robot

The advantage of using piezoelectric motor over conventional electromagnetic actuators for crawling insects is miniaturization and control. A single electromagnetic motor might have higher torque, however because of its size, only one would be able to fit into an insect size robot and as such it would not be possible to achieve full control over the robot. On the other hand, each piezoelectric bimorph can be controlled independently. By reversing the voltage potential, the robot can move in reverse and by varying the voltage amplitude of one pair of legs over the other one, steering can be achieved in any direction. In addition, by simply changing the

frequency of the signals sent to the piezoelectric bimorphs, control over the speed of the robot can be accomplished. Finally, piezoelectric bimorphs can be reduced in size much easier than electromagnetic motors can as seen in the parametric study shown in Chapter 2.

3.2.2.1 Experimental Characterization

In order to characterize the functionality of the motor, multiple tests were conducted. A key functionality of the endoscopic robots is safe operation inside the human GI tract. Inside the human GI tract, it is imperative that the forces exerted by the robot are minimal. This way damaging and scarring of the tissue can be avoided. In addition, the robot should also be capable of carrying additional weight on board such as: wireless camera, battery, illumination lamp, control chip, biopsy mechanism, diagnostic and location sensors and etc. Two experiments that test this capability of the robot were conducted and the results are presented in Figure 3.14. In Figure 3.14 (a), 3-axis ±6g accelerometer (Newark element14, Eval-ADXL325Z) was placed on the top surface of the robot in order to collect data for accelerations along the three-directions. This data was then multiplied by the mass of the robot (11.6g) to obtain the forces generated by the crawling robot. In Figure 3.14(b), similar test was conducted where the tip of one leg was attached by a string to a load cell (Transducer Techniques, GSO-10). As the piezoelectric motor was actuated, a force generated at the tip of the leg was transmitted to the load cell and then the pull force was measured. The pull force generated by a single L-Shape piezoelectric motor composed of piezoelectric bimorphs (APC international, model 40-2040) and operated at 80V input was around 10 grams for preloads of 5-7grams. The preloads were applied by applying tension in the string that connected the tip of the robot's leg with the load cell. The reason as to why the piezoelectric bimorphs were driven at 50% of the maximum recommended voltage limit was to prevent the fatigue and improve the reliability.

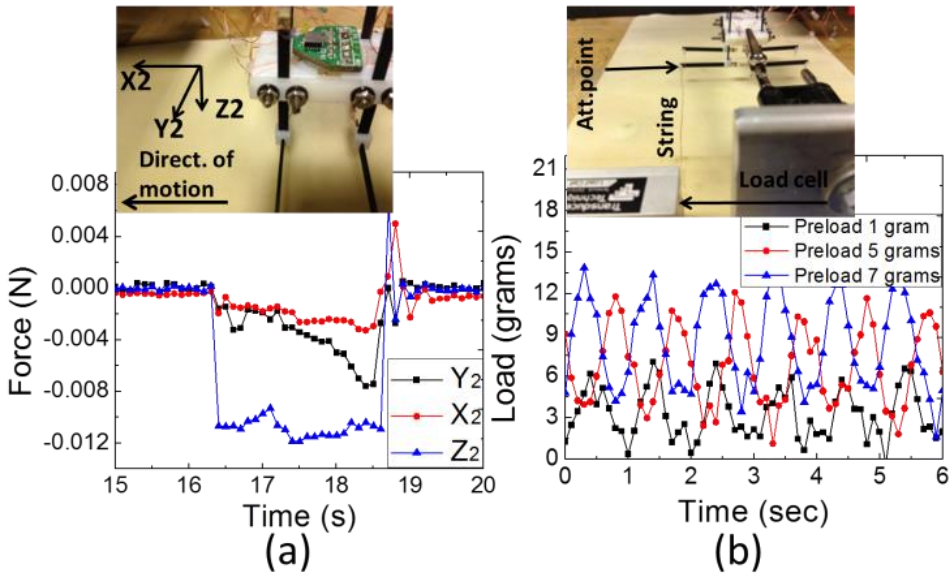

Figure 3.14 Forces produced by robot: a) Forces in x, y and z direction as the robot moves, and b) Pull force exhibited by the robot

Besides measuring the force exerted by the robot, it was possible to obtain results on the motion of the legs at their tip using high speed camera and visual processing software. Figure 3.15 shows the summary of the motion of the legs in a 2-D plane. Figure 3.15 (a) and (b) plot the motion of each leg in the Z_2 and Y_2 direction as a function of time. These results confirm that the desired gait for the motion of the robot has been achieved. The leg pairs, "Front Left and Rear Right" and "Front Right and Rear Left" moved with 90° phase delay with respect to each other. Figure 3.15 shows the motion of each leg in the $Y_2 - Z_2$ plane (side view). As shown on the plot, each leg generates elliptical motion which is essential for the motion of the robot. The slight error between the amplitudes of the legs is partially due to the angle and depth effect at which the high speed camera acquired the images as well as the installation of the legs onto the robot. Nevertheless, even with the slight error, it is clear that the tip movement generated the motion initially desired.

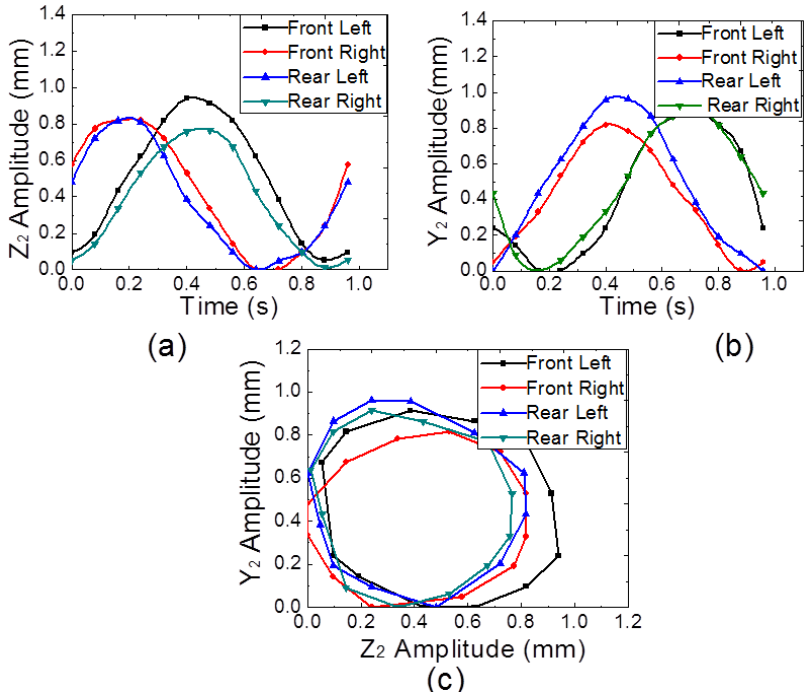

Figure 3.15 Motion of the tip of the legs: a) motion of the legs in the x-direction, b) motion of the legs in the y-direction, c) elliptical motion generated at the tip of each leg

Next, the robot was actuated at 1Hz and 60Hz to quantify the kinematics. Since the motion of the legs at 80V is around 1mm in diameter, we were able to achieve velocities of 1mm/s at 1Hz excitation. At the actuation frequency of 60Hz, the robot achieved speeds up to 65mm/s. The reason why the relationship between the frequency and speed is not linear is because the frequency of 60Hz approached the natural frequency of the L-Shape motor. When actuated at the natural frequency, the elliptical motion that is generated at the tip becomes greater. In addition, payload of 12grams was attached onto the robot and its motion was monitored. No alterations of the motion of the robot were observed. Finally a resistor of 4.7kΩ was introduced in series to measure the current going into the robot. As a result the power delivered to the robot was measured to be 8mW at 80V potential.

3.3 U-Shape Motor Experimental Study

Similarly to the L-Shape piezoelectric motor, the U-Shape piezoelectric motor was both experimentally characterized and then implemented onto a locomotion mechanism platform inspired by a crawling millipede. Figure 3.16 shows the representation of the U-shape

piezoelectric motor and its vibrational characteristics. It was previously discussed that the wing similar to the base acts as a cantilever beam. Actuating a cantilever beam at the 1st resonance frequency, results in generation of the 1st vibrational mode where maximum deflection is exhibited at the free end. This can be seen for both the base (motion in x-direction) and wing (motion in z-direction) in Figure 3.16 (top left). In order to capture the motion at the tip in both axes, two laser vibrometers (PSV400 and OFV350, Polytec, Inc.) were used similar to the L-Shape motor.

In the first set of experiments, the base was the only element excited using a chirp signal input to determine the natural frequency of the system. Following this, the same test was conducted through the actuation of the wing, while the base was kept at rest. It was determined that for specific geometry of the U-Shape piezoelectric motor with base length of 15 mm and wing length of 26.5 mm, the 1st natural frequencies for the base and wing were 139 Hz and 149 Hz respectively. The reason why the free lengths were not the same is due to the fact that the wing had a loading effect on the base. From the relationship shown in Eq. (3.3.0):

$$f = \sqrt{\frac{k}{m}} \tag{3.3.0}$$

frequency is inversely proportional to mass and is directly related to stiffness. By manipulating these two parameters, it was possible to bring the natural frequencies of both beams in close vicinity to each-other. In order to obtain an elliptical motion at the tip, the two piezoelectric bimorphs were excited by a voltage potential at the same frequency, but with a phase difference of 90° as shown in Figure 3.16 (top right). It is important to assure that the 1st natural frequency for both the base and wing either match or remain in vicinity of each other as shown in Figure 3.16 (bottom left). The reason is related to the fact that when the motor is driven at a single frequency, in ideal condition, this frequency needs to correspond to the 1st natural frequency for both the base and wing. In this arrangement, a largest deflection is generated at the tip. As shown in Figure 3.16 (bottom right), the elliptical motion was generated by the piezoelectric tip at different operating frequencies. When the U-shaped motor was actuated at 139 Hz (which corresponds to the resonance frequency of the base) the elliptical motion obtained was larger in the x-direction. Conversely at 149 Hz excitation (which corresponds to the resonance frequency of the wing), the elliptical motion was larger in the z-direction. This is due to the fact that the two frequencies correspond to the natural frequencies of individual bimorphs. As a result, the

largest envelope of deflection would be expected at a frequency between 139 Hz and 149 Hz. Accordingly, 144 Hz was measured as a the optimal point of operation for the U-Shape piezoelectric motor based on its: geometry, boundary conditions, material properties and the lab setup. To note, the motion generated in the y-direction was much smaller when compared to the other two directions and therefore was not included in the analysis.

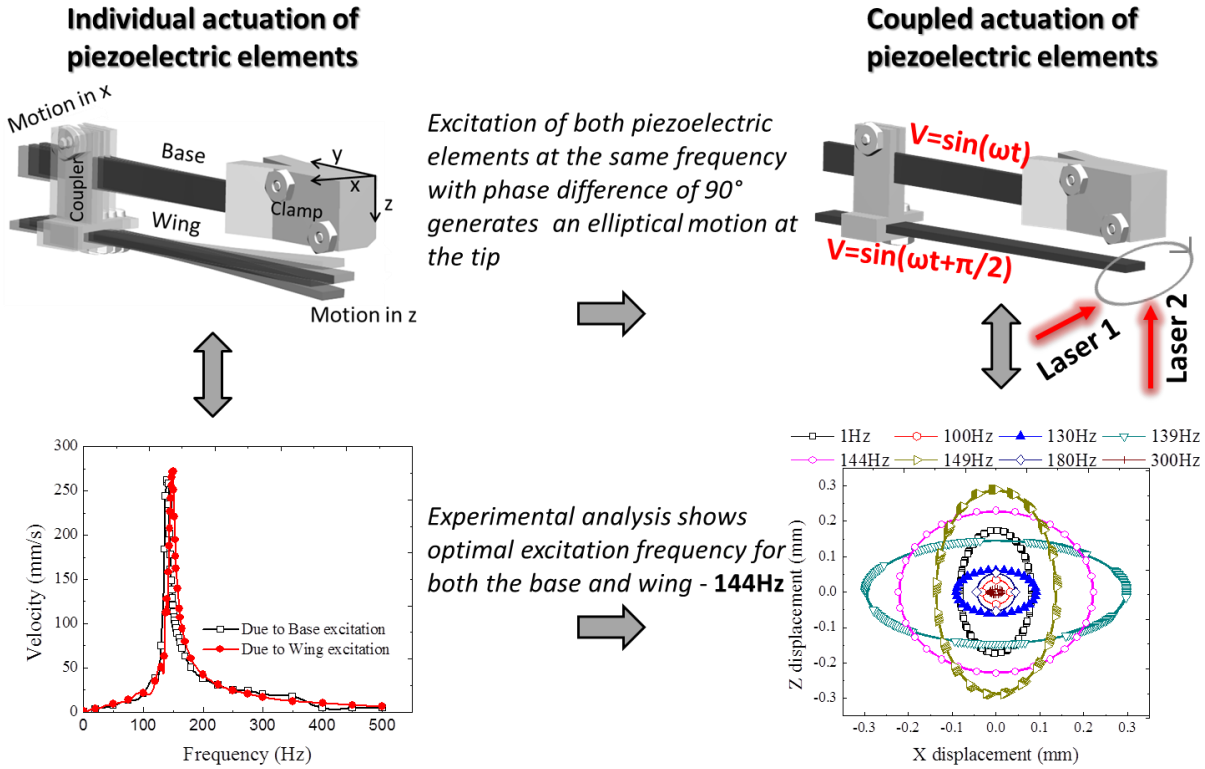

Figure 3.16 Principle of operation of U-shaped piezoelectric motor and its vibrational characteristics

3.3.1 U-Shape Motor Characterization

Next, the performance of the motor was determined using a rotating test platform equipped with an angular displacement encoder. The details of the setup are discussed in section 3.2 in this chapter. Figure 3.17 summarizes the results obtained for the U-Shaped piezoelectric motor. The motor was operated at its natural frequency of 144Hz with a voltage input of 70.7Vrms. As the rotational stage was actuated, the angular displacement was acquired using the optical encoder (DISK-2-2500-1000-IE US digital). A polynomial fit representing the displacement as a function of time acquired by the digital encoder was differentiated to obtain the angular velocity and then differentiated once more to obtain the angular acceleration. Figure

3.17(a) shows the angular displacement and angular velocity as a function of time. The largest velocity achieved at the applied input voltage to the bimorphs was 65rad/s. The torque generated by the motor can be obtained using Eq. (3.3.1):

$$\tau = J_{total}\alpha \tag{3.3.1}$$

where α is the angular acceleration and J_{total} is 1.67E-7 $kg - m^2$. Once the torque is known, the mechanical power can be computed using Eq.((3.3.1)) as illustrated in Figure 3.17 (b).

$$P_{mech} = \tau \times \omega \tag{3.3.1}$$

The maximum mechanical power obtained from the current design was 0.84mW at ω of 42rad/s. By measuring the input power to the system (32mW), the efficiency for the U-shape piezoelectric motor was obtained. Figure 3.17 (c) presents the data for efficiencies and angular velocity as a function of torque. Two different efficiency curves were plotted in this figure, one for the motor as it was experimentally obtained in the laboratory-setting and another by assuming that the piezoelectric bimorphs had 100% electrical to mechanical conversion efficiency.

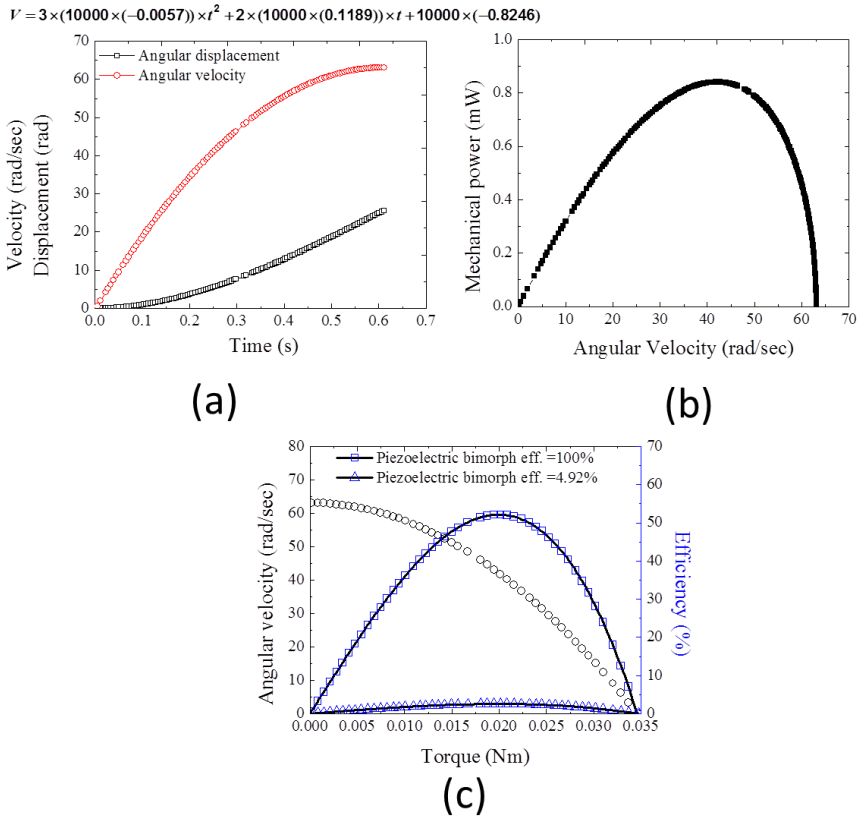

Figure 3.17 Performance characterization curves of U-Shape piezoelectric motor: (a) Angular velocity and angular displacement as a function of time, (b) Mechanical power as a function of angular velocity, (c) Angular velocity and efficiency of motor as a function of torque.

3.3.2 Crawling Inspired Robot

After detailed mechanical characterization of the U-shaped piezoelectric motor, the worked proceeded with the development of millipede-inspired robotic locomotion mechanism (millibot). By utilizing the elliptical/circular motion of the piezoelectric motor and coupling multiple motors in a row as shown in Figure 3.18 (a) a travelling wave was generated similar to that of the millipede as shown in Figure 3.20. Figure 3.18 (b) shows the operation mechanism of the millibot and also illustrates the driving scheme used in a laboratory setting. Since the input signals applied to the individual elements of the motor (base and wing) were 90° out of phase and the motion of one of the U-shape piezoelectric motor was 90° out of phase from the one behind it, the electrical driving became easier. A single function generator and two amplifiers used to amplify the voltage signal going to the piezoelectric elements were used in order to actuate the milibot. The principle of operation of the millibot is illustrated in Figure 3.18 (c) and it is best described as follows: in step 1, all legs are touching the ground surface; in step 2, the FL

and RR leg leave the ground surface and swing forward in air while the FR and RL leg propel the milibot body forward by pulling on the ground surface beneath; in step 3 all four legs are touching the ground surface similarly to step 1; step 4 is the opposite of step 5 where the FL and RR legs are now in contact with the ground and propel the milibot forward by grabbing and then pulling on the ground surface, while the FR and RL legs on the other side swing forward in air; step 5 is equal to step 1 and 3 and finally step 5 represents the beginning of the new cycle, hence it is equal to step 2. The locomotion principle continues as long as there is power delivered to the milibot.

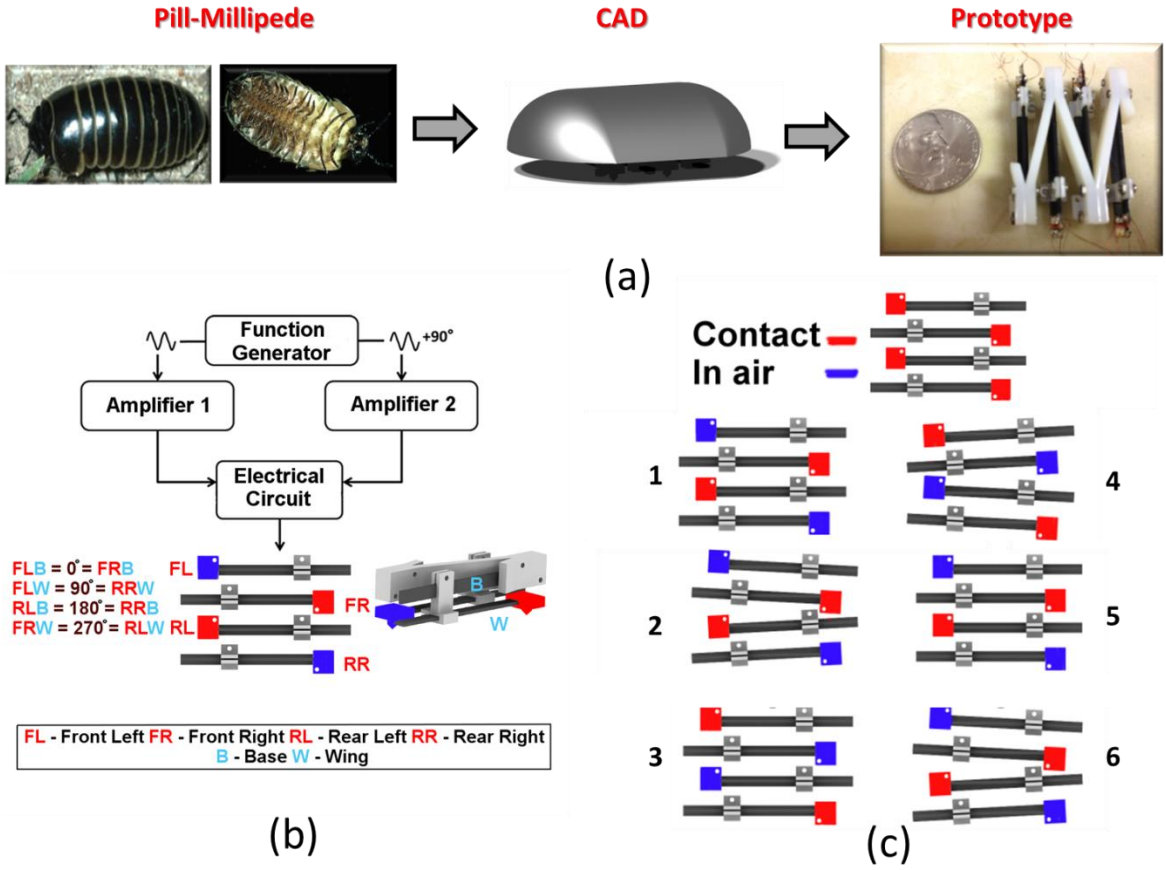

Figure 3.18 Millibot: (a) Millipede inspired mobile robot utilizing U-Shaped piezoelectric motor, (b) Experimental setup, and (c) Gait of millibot

Lastly, the locomotion mechanism of the millibot was characterized using a high-speed camera as shown in Figure 3.19. Image processing was used to obtain the data from the robot as it was actuated with varying driving conditions. Two plots can be seen in Figure 3.19 corresponding to the motion of the legs as a function of time in the x-direction, y-direction and then motion of the legs in the x-y plane. The legs exhibited the elliptical motion as desired to

achieve the walking gait. The millibot was actuated at different frequencies and the power consumption was measured to be 6mW at 1Hz excitation frequency and 70Vrms, which as a reference would translate to around 5-12 hours of operation in a scenario where the robot is powered by a 3V watch battery.

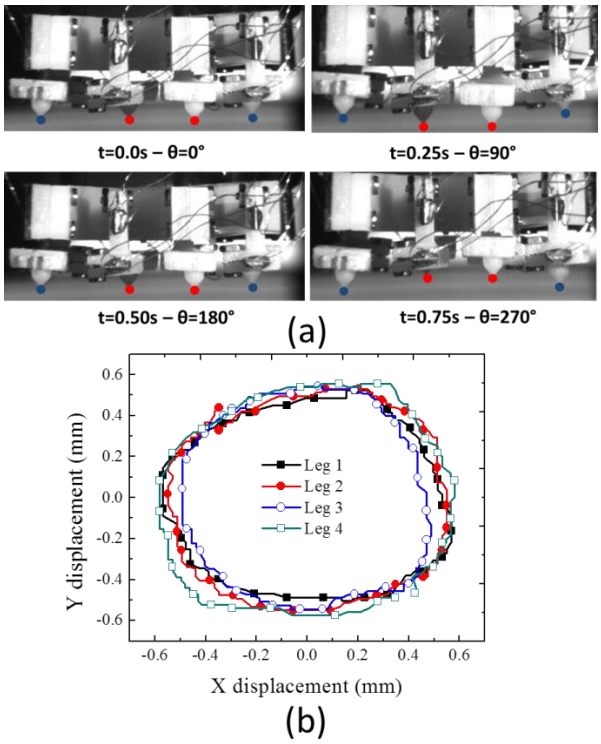

Figure 3.19 Locomotion characterization of the millibot: (a) Four distinct time steps demonstrating the motion of the robotic legs, (b) Elliptical motion generated at the tip of the motor in the x-y plane

3.3.2.1 Modeling the kinematics of the robot

The motions of the legs of the robot take the form of a wave which propagates alongside the body. During forward movement, the motion of one leg pair is 90° out of phase from the other leg pair. A kinematic analysis of robot can be obtained following the methodology presented in [76], where every leg has the walk pattern in common and the tips of the legs trace a circular path as shown in Figure 3.15 (c) and Figure 3.19 (b). To note, the result presented in this study have shown elliptical motion due to the fact that both the base and wing were actuated by the same voltage potential. Circular motion at the tip can easily be achieved, by simply adjusting the voltage potential applied to the wing and base. For simplicity, the floor is assumed to be rigid, therefore the motion of the legs create a semicircle indicated in red, Figure 3.20.

From this analysis the velocities of the wave and robot are defined through (3.3.2) and (3.3.3) as:

$$V_{wave} = \frac{\theta r}{t_T} \tag{3.3.2}$$

$$V_{robot} = \frac{2r\sin\left(\frac{\theta}{2}\right)}{t_p} \tag{3.3.3}$$

where V_{wave} is the velocity of the wave, V_{robot} is the velocity of the robot, r is the radius of the reference circle that the motion of the legs trace, θ is the angle between the point of contact and the radius of the reference circle, t_T is the transference time representing the time it takes for the leg to move in air during the recovery stage and t_P is the time during the propulsive stage while the leg is in contact with the ground.

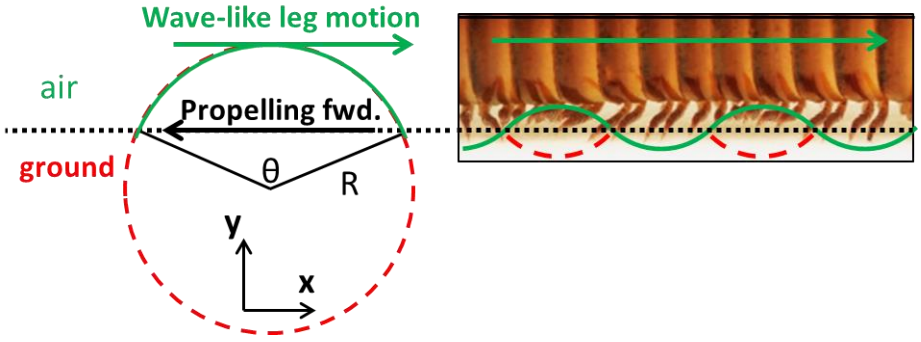

Figure 3.20 Circle reference and variables of the path that the legs trace.

The total time it takes for the robot to execute one step forward is calculated through Eq. (3.3.4):

$$T = t_T + t_p \tag{3.3.4}$$

and by knowing:

$$h = r - r\cos\left(\frac{\theta}{2}\right) \tag{3.3.5}$$

a relationship between the time, velocities, clearance h and the angle can be obtained.

Using all this information a frequency of the traveling wave can be calculated through (3.3.6) as:

$$\omega = \frac{\theta}{t_T} \tag{3.3.6}$$

With the frequency defined, a motion in 2-D can be expressed through cycloid functions in the x, y coordinates as:

$$\begin{aligned} x_i &= r(t - \sin(\omega t - \phi_i)) \\ y_i &= r(1 - \cos(\omega t - \phi_i)) \end{aligned} \tag{3.3.7}$$

where t is time in seconds while the robot is in motion and ϕ is the phase between consecutive legs.

Based on this analysis a model of the motion of the robot can be approximated. Improvements on this model are required for incorporating the effect of different environment that the robot will operate. One such improvement will have to take into account that the surface onto which the robot will be crawling will not be rigid as the ground, but rather soft as to simulate the GI tract environment.

3.4 Conclusion

This chapter encompassed the experimental characterization of the two piezoelectric motors developed: L-shape and U-Shape and their integration onto a legged type WCE. First, the experimental results obtained for the L-Shape motor were compared against the theoretical models discussed in Chapter 2. Once the models were validated, experimental characterizations were conducted for both the L-Shape and the U-Shape piezoelectric motors in terms of their velocities and torques. Finally, both motors were integrated onto a legged locomotion platform inspired by crawling millipedes. The developed prototypes, showed very promising results for swallowable robot applications in terms of the power requirements, velocities of propulsion and simplicity in the design. The L-Shape motor, had a resonance frequency of 247Hz, exhibited torque of 4.7 x 10^{-5} N.m while requiring power input to the milibot of at excitation frequency of 8mW at excitation frequency of 1Hz. Similarly, the U-Shape motor had a resonant frequency of 144Hz and exhibited 0.03mN-m torque while requiring low power input to the milibot of 6mW at excitation frequency of 1Hz.

Chapter 4 – Controlled Locomotion of Wireless Capsule Endoscopes through Traveling Wave Phenomenon

4.1 Introduction

This dissertation covers two locomotion mechanisms for WCEs, legged and body actuated, where both use the principle of traveling waves as propulsion but in a very different way. This chapter explains a novel method for WCE locomotion mechanism using capsule body actuation providing theory and experiment to illustrate the fundamentals. Unlike the legged type mechanism presented in Chapter 3 where multiple actuators in a row create the profile of a traveling wave, the mechanism described here is based upon the vibration excitation that causes the entire capsule to behave as a traveling wave. This implies that a controlled locomotion of WCEs can occur simply by proper vibration of the capsule shell.

As described in Chapter 1, traditional WCE as the one shown on the left in Figure 4.1, is usually composed of electromagnetic motors, linkages, gears, and different type of legs. This type of mechanism even though has been shown to be effective in terms of the propulsion, it has a major downside. Some of the main challenges in WCEs are the power source and limited space available inside the capsule which is used to store the batteries, micro controllers, cameras, various sensors, communication devices, biopsy tools and other components. All of the elements necessary for locomotion as shown in Figure 4.1 are both space consuming and complex. Due to these requirements, a new concept for propulsion of wireless capsule was developed that relies on only two elements: piezoelectric disks and the body of the capsule, Figure 4.1 (RH side). The actuation principle discussed in this chapter will eliminate the need for any of the traditional elements (gears, linkages, electromagnetic motors and legs) and thus provide more storage space and major reduction in design complexity.

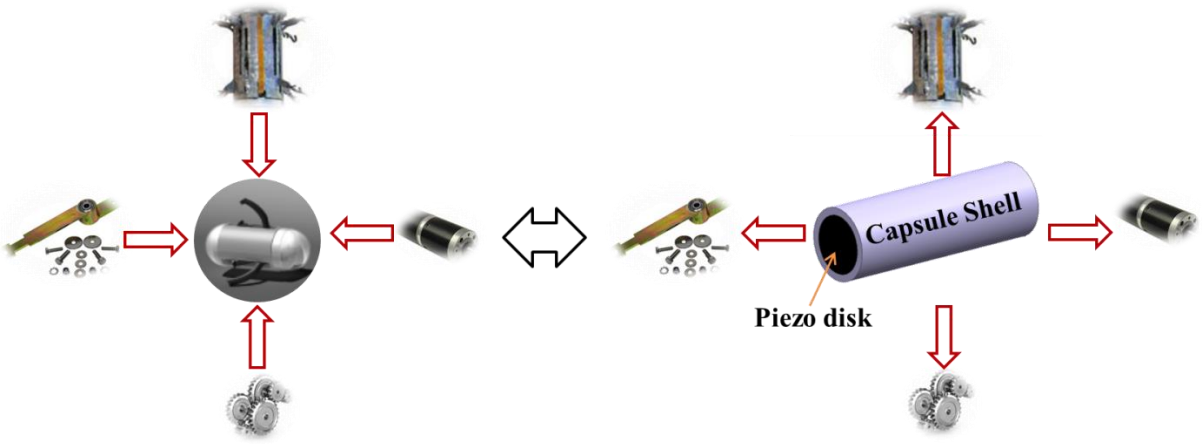

Figure 4.1 Concept of traveling wave based wireless capsule endoscope

In the center of the figure 4.2 is a cylinder that can be assumed to represent the body of the WCE. On the left side of Figure 4.2, a front view of the cylinder with a piezoelectric disk in the middle is shown. The piezoelectric disk represents the actuation element in this locomotion mechanism. It should be noted that there are two piezoelectric disks, each located at both ends of the cylinder. As the piezoelectric disks are actuated, the strain is transferred to the capsule shell, and by following specific excitation sequence, a traveling wave can be generated. This wave is then used as means of propulsion. In order to simplify the problem of modeling and characterization of complex structures such as cylinders, a small cross-section was used. This section is represented by a beam with free-free boundary conditions and piezoelectric elements on the bottom side act as an excitation source. Similar to the cylinder, the free-free beam will also experience traveling wave phenomenon if excited properly. The chapter covers the fundamentals of propagating mechanical waves, their generation through finite mediums such as free-free beams and also experimental characterization.

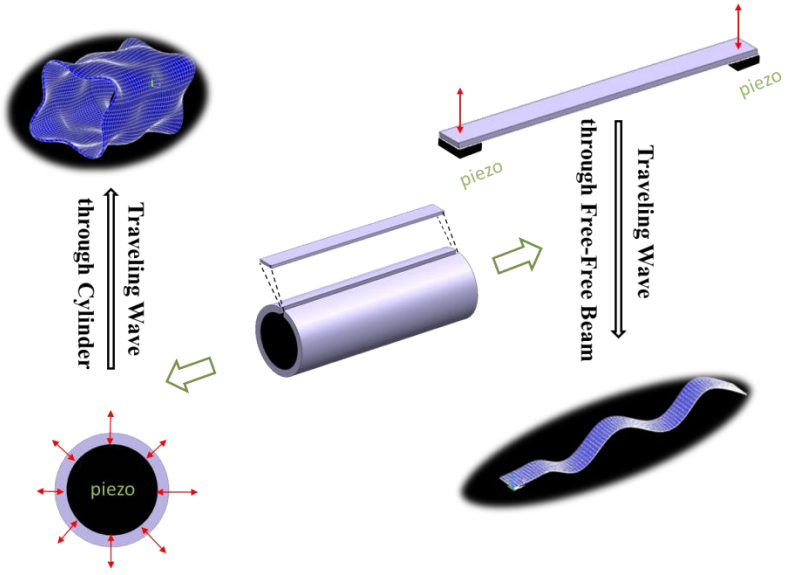

Figure 4.2 Schematic description of the approach used for the analysis of locomotion mechanism inspired by the traveling wave phenomenon

4.2 Traveling Waves Formation

As a result of an oscillation and coupling between the structure and medium, mechanical waves are generated and propagated through the underlying medium. In solids, the motion is accompanied by energy transfer from one point to another and therefore it can be used as a propulsion mechanism. This has been demonstrated in natural micro-organisms where waves propagating through their body (head towards tail) result in propulsion [80, 81]. Through the observation of examples found in nature, the phenomenon of mechanical waves shows great potential towards the development of propulsion mechanisms [82] and biologically engineered structures [83]. Even though in its infant stage, simulated (artificially generated) traveling waves through solid structures have demonstrated propulsion on both biological and mechanical systems. On the biological side, flagella locomotion mechanism has been engineered as a first step towards establishing platform for biological machines[84]. On the mechanical side, the development of traveling waves has been investigated in order to answer the question, "Can carpets fly"[85] [86]. No matter what the real motivations and applications behind traveling wave inspired mechanism are, the first step towards their understanding would be development of basic theory and experiments that illustrate the physics behind the generation and propagation

of waves in controlled manner. This chapter encompasses the theoretical and experimental analysis for the formation of mechanical waves through solid structures such as a free-free beam. This theory can be extended to the development of future cylinder-based WCEs locomotion/propulsion mechanisms.

The principle behind the generation of mechanical waves is related to the vibrational characteristics of structures that are accompanied by corresponding natural frequencies and mode shapes. Structures oscillate as a result of energy input coming from the external sources and by understanding the structural dynamics it is possible to excite them in such a way that will result in generation of mechanical waves. In this study, piezoelectric elements represent the excitation source for the structure of choice. It was observed that when a beam was excited by two sinusoidal forces acting at two different locations, but at a phase difference of 90°, a travelling wave was created. This behavior was experimentally and theoretically analyzed. The schematic diagram, shown in Figure 4.3, illustrates how the first four mode shapes of a free-free beam contribute towards the development of traveling waves. The level of contribution of specific mode shapes is directly dependent on the frequency and location at which a structure is excited. In Figure 4.3 the excitation frequency is between the 2nd and 3rd natural frequency of the beam and the individual signals are at a phase difference of 90°. As a result, the highest contributions of the mechanical wave comes from the neighboring mode shapes, and the phase difference is the factor which dictates whether the traveling wave will occur or not. When a structure is excited with a single force, waves are generated and reflected due to a high impedance change. These waves have equal magnitude but travel in opposite direction and generate standing waves, $w(x,t) = A\sin(\omega t - kx) + B\sin(\omega t + kx)$; in this case the amplitude A and B are equal in magnitude. When a structure is excited at two points at the same frequency, but with phase difference between them, a part of the reflected wave is negated (as A≠B) and correspondingly results in a combination of a stationary wave and a traveling wave. The dominance of the traveling wave over the standing wave behavior depends on two factors: the frequency of excitation and the fixed phase.

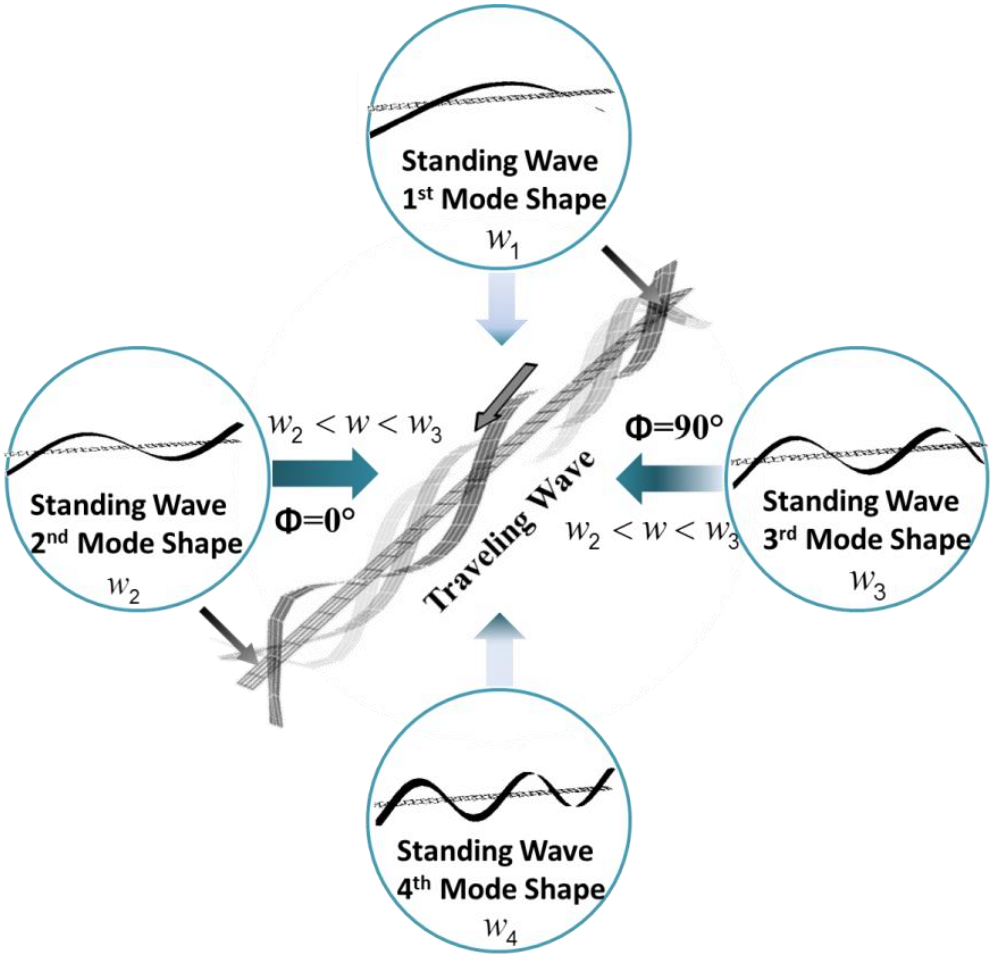

Figure 4.3 Concept description for formation of the traveling waves through finite medium.

4.3 Theoretical modeling

Starting from the fundamentals of mechanical wave excitation, a theory can be developed that can formulate the system dynamics and provide the response of structure as it vibrates resulting in either standing or traveling waves. A diagram describing the parameters used in the model is presented in Figure 4.4. For simplicity, point force excitation was used to model the Euler-Bernoulli distributed parameter beam with free-free boundary conditions.

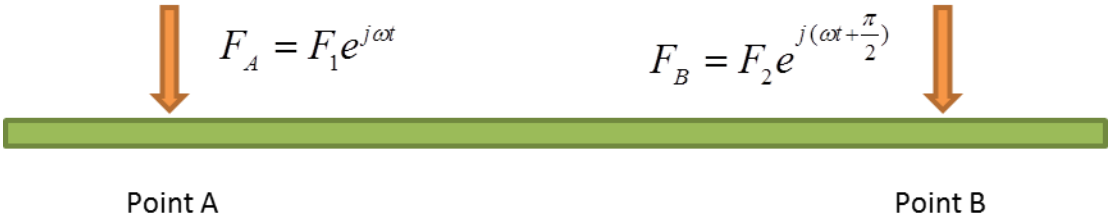

Figure 4.4 Schematic diagram of the beam structure.

The general equation for the distributed parameter model for the system was derived using the equation of motion for a beam shown in Eq.(4.3.1) :

$$\rho A(x)\frac{\partial^2 w(x,t)}{\partial t^2} + \frac{\partial^2}{\partial x^2}\left[EI(x)\frac{\partial^2 w(x,t)}{\partial x^2}\right] = F(x,t) \tag{4.3.1}$$

where ρ is density, A is cross sectional area of the beam, EI is the bending stiffness and F is the excitation force. First, the homogeneous solution for the differential equation was obtained by setting the right hand side to null:

$$\rho A\frac{\partial^2 w(x,t)}{\partial t^2} + EI\frac{\partial^4 w(x,t)}{\partial x^4} = 0 \tag{4.3.2}$$

In order to solve the differential equation, separation of variables solution of the form $w(x,t) = X(x)T(t)$ was assumed, where by substituting it into the general equation of motion, Eq. (4.3.3) and (4.3.4) were obtained:

$$\frac{\partial^2 w(x,t)}{\partial t^2} + c^2\frac{\partial^4 w(x,t)}{\partial x^4} = 0 \tag{4.3.3}$$

$$c^2\frac{X''''(x)}{X(x)} = -\frac{\ddot{T}(t)}{T(t)} = \omega^2 \tag{4.3.4}$$

where $c = \sqrt{\frac{EI}{\rho A}}$ and ω is the natural frequency of the system. Note that from Eq. (4.3.4), two equations are obtained: spatial and temporal. In the spatial domain Eq. (4.3.4) becomes:

$$X''''(x) - \left(\frac{\omega}{c}\right)^2 X(x) = 0 \tag{4.3.5}$$

and in the temporal domain Eq. (4.3.4) becomes:

$$\ddot{T}(t) + \omega^2 T(t) = 0 \tag{4.3.6}$$

where general solutions for the spatial and temporal equations are assumed to be:

$$X(x) = a_1 Sin\beta x + a_2 Cos\beta x + a_3 Sinh\beta x + a_4 Cosh\beta x \tag{4.3.7}$$

$$T(t) = A\sin(wt) + B\cos(wt) \tag{4.3.8}$$

where the coefficients $a_1 - a_4$ are obtained from the boundary conditions and A and B from the initial conditions.

For free-free boundary conditions, the bending moment and shear force on each end of the beam are null, therefore $EI\frac{\partial^2 w}{\partial x^2} = 0$ and $\frac{\partial}{\partial x}\left[EI\frac{\partial^2 w}{\partial x^2}\right] = 0$ respectively. As a result, the characteristic equation is described through Eq. (4.3.9) and the mode shape through Eq. (4.3.10):

$$Cos\beta L \times Cosh\beta L = 1 \tag{4.3.9}$$

$$\Phi_n(x) = Cosh\beta_n x + Cos\beta_n x - \sigma_n(Sinh\beta_n x + Sin\beta_n x) \tag{4.3.10}$$

where $\sigma_n = \frac{Cosh\beta_n L - Cos\beta_n L}{Sinh\beta_n L - Sin\beta_n L}$ and L is the length of the beam.

Once an expression for the temporal and spatial equations was obtained, the step that followed was to use them in the EOM. As a result the steady state solution for a forced input can be expressed through Eq. (4.3.11)

$$X(x)\ddot{T}(t) + c^2 X''''(x)T(t) = f(x,t) \tag{4.3.11}$$

Substituting Eq. (4.3.4) results in Eq.(4.3.12):

$$X(x)\left[\ddot{T}(t) + \omega^2 T(t)\right] = f \times e^{j(\omega t+\phi)} \times \delta(x-l) \tag{4.3.12}$$

where $\delta(x-l)$ is the Dirac delta function indicating the location at which the unit force is applied. Substituting the homogeneous solution of the spatial part $X(x)$, the following expression is obtained:

$$\Phi_n(x)\left[\ddot{T}_n(t) + \omega_n{}^2 T_n(t)\right] = f \times e^{(j\omega t+\phi)} \times \delta(x-l) \tag{4.3.13}$$

where $\omega_n = \beta_n{}^2\sqrt{\frac{EI}{\rho A}}$. The orthogonality conditions can be described through Eq. (4.3.14) as:

$$\int_0^L \Phi_m(x)\Phi_n(x) = \begin{cases} 0, & m \neq n \\ L, & m = n \end{cases} \tag{4.3.14}$$

The orthogonality condition are applied in Eq. (4.3.13) which is then integrated across the length of the beam as shown in Eq. (4.3.15)

$$\left[\int_0^L \Phi_n(x)\times\Phi_n(x)dx\right]\times\left[\ddot{T}_n(t)+{\omega_n}^2T_n(t)\right]=f\times e^{(j\omega t+\phi)}\times\int_0^L\Phi_n(x)\times\delta(x-l)dx \tag{4.3.15}$$

Next an expression in the time domain can be obtained which resembles a single degree of system without damping Eq. (4.3.16) and with damping Eq. (4.3.17):

$$\ddot{T}_n(t)+{\omega_n}^2T_n(t)=\frac{f}{L}\times e^{(j\omega t+\phi)}\times\Phi_n(l) \tag{4.3.16}$$

$$\ddot{T}_n(t)+2\zeta\omega_n\dot{T}_n(t)+{\omega_n}^2T_n(t)=\frac{f}{L}\times e^{(j\omega t+\phi)}\times\Phi_n(l) \tag{4.3.17}$$

In order to obtain the frequency response function (FRF) between the input and the output, the following steps were utilized. First the Laplace transform was applied while setting the initial conditions to zero:

$$let\qquad \tilde{\omega}_{ij}=\begin{cases}\omega_n & i=j\\ 0 & i\neq j\end{cases} \tag{4.3.18}$$

As a result Eq.(4.3.17) becomes:

$$(s^2+2\zeta\tilde{\omega}s+\tilde{\omega}^2)T(s)=\frac{F(s)}{L}\times\Phi(l) \tag{4.3.19}$$

The FRF for a single degree 2nd order system was then represented by Eq. (4.3.20) and Eq. (4.3.21) in the frequency domain, $s=j\omega$ as:

$$\frac{T(s)}{F(s)}=\frac{\Phi(l)}{L\times(s^2+2\zeta\tilde{\omega}s+\tilde{\omega}^2)} \tag{4.3.20}$$

$$H(j\omega)=\frac{T(j\omega)}{F(j\omega)}=\frac{\Phi(l)}{L\times(\tilde{\omega}^2-I\omega^2+j\times2\zeta\tilde{\omega}\omega)} \tag{4.3.21}$$

Finally the temporal solution was presented as follows:

$$\begin{aligned}T_1(j\omega)&=F_1(j\omega)\cdot H(j\omega)=\frac{\Phi(l_1)\cdot fe^{j\omega t}}{L\times(\tilde{\omega}^2-I\omega^2+j\times2\zeta\tilde{\omega}\omega)}\\ T_2(j\omega)&=F_2(j\omega)\cdot H(j\omega)=\frac{\Phi(l_2)\cdot fe^{j(\omega t+\phi)}}{L\times(\tilde{\omega}^2-I\omega^2+j\times2\zeta\tilde{\omega}\omega)}\end{aligned} \tag{4.3.22}$$

By the principle of mode summation, the final result was obtained as shown in (4.3.23):

$$w(x,t)=X(x)T(t)=\sum_{n=1}^{\infty}\Phi_n(x)\left(T_1(t)+T_2(t)\right) \tag{4.3.23}$$

4.4 Experimental Characterization

An experimental setup under the laboratory condition was conducted in order to verify the theoretical model discussed in Section 4.3. Figure 4.5 (a) shows the experimental setup. A brass beam with length=0.305m, width=0.0195m and thickness=0.000832m was suspended on elastic bands in order to simulate the free-free boundary conditions. The response of the vibrating system was experimentally measured using a laser scanning vibrometer and data acquisition system (PSV400, Polytec Inc.). The results as a function of the frequency and the corresponding mode shapes are shown in Figure 4.5 (b) and the first seven natural frequencies are compared against the theory in Table 4-1. In Figure 4.5, an illustration of the traveling wave obtained from the experimental characterization is presented in order to confirm the hypothesis that mechanical waves can be induced onto a structure as long as there is a phase difference between the signals and the excitation frequency is between the two bending modes.

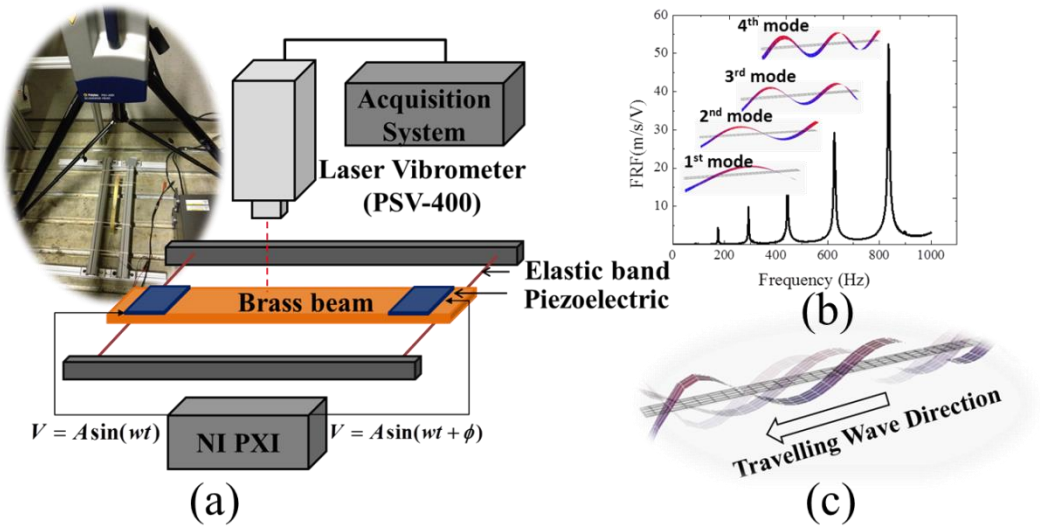

Figure 4.5 Experimental analysis of traveling waves generated on a free-free beam. (a) Experimental Setup, (b) Modal Analysis, (c) Traveling wave through free-free beam

Table 4-1 Experimental and theoretical results for the natural frequency of free-free beam

Frequency	Experiment (Hz)	Point Force D.P. (Hz)	Error (%)
1	35	31.69	10.4
2	89.69	87.37	2.66
3	175.9	171.1	2.81
4	293.4	282.9	3.71
5	444.4	422.5	5.18
6	625.3	590.2	5.94
7	835.3	785.6	6.32

A comparison of the traveling wave behavior was conducted at a frequency which was half way between the third and fourth mode shape. The phase difference was kept at 90° between the two excitation signals. This comparison for the free-free case is presented in Figure 4.6. Figure 4.6 (a) displays the results from the simulated model while the respective experimental results are shown in Figure 4.6 (b). The figure shows the response of the vibrating beam as a function of time with both the XY and YZ planes projected. These projections were used to illustrate the existence of the traveling wave and its profile respectively. The blue area on the XZ plane represents the total space covered by the beam during its motion in time. Similarly, the projection on the XY plane represents the beam amplitude as it changes with time.

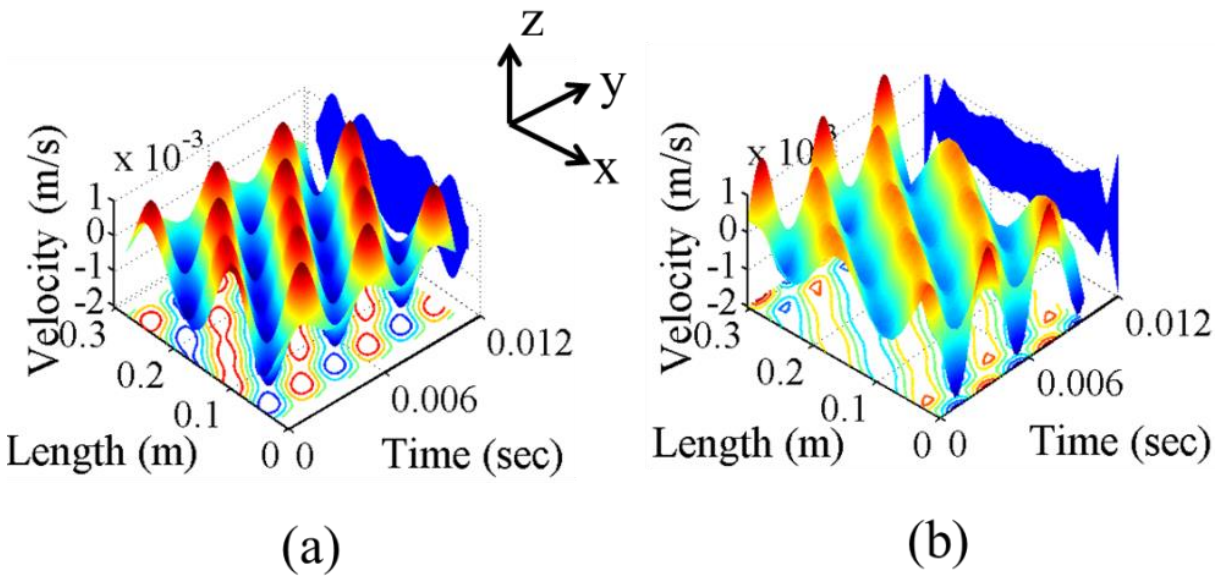

Figure 4.6 3D representation of traveling waves obtained (a) theoretically and (b) experimentally.

Once the simulated models were verified for the specific case, additional analysis were conducted in order to better understand the behavior of the structure as it deformed. The results of this analysis are presented in Figure 4.7, where the response of the beam was calculated and then simulated for the given boundary conditions. Correspondingly, the frequency response function (FRF) for each structure was obtained and the resonance frequencies were identified. The insets above the FRF curve correspond to the profile of the waves generated at the resonance frequency and the insets below the FRF curve, to the ones generated at a frequency, which is between two resonant frequencies. A clear distinction between the traveling waves and standing waves can be identified from the insets. The profiles (XZ plane projection) allure to the fact that standing waves (above the FRF curve) are associated with nodal points and traveling waves (below the FRF curve) are not, which is expected from the nature of the two waves. In addition, the contour plots associated with each profile compliments the analysis and describes the behavior in further details. As presented, the contours for standing and the traveling waves are clearly distinct from each other for any frequency or boundary condition. The standing wave contours are discontinuous and the ones for traveling waves are continuous, which suggests the presence or absence of nodal points respectively. In addition, for the traveling waves, the figures can be used to identify not only the presence of the wave, but also the traveling direction and the

corresponding speed. If the slopes are negative, the wave moves from left to right and conversely if the slopes are positive, the direction is from right to left. The reason why the direction of travel alternates as the excitation frequency moves, for example from $w \in (w_1, w_2)$ to $w \in (w_2, w_3)$ to $w \in (w_3, w_4)$, is due to the existence of even and odd mode shapes which are coupled with the phase difference between the excitation signals.

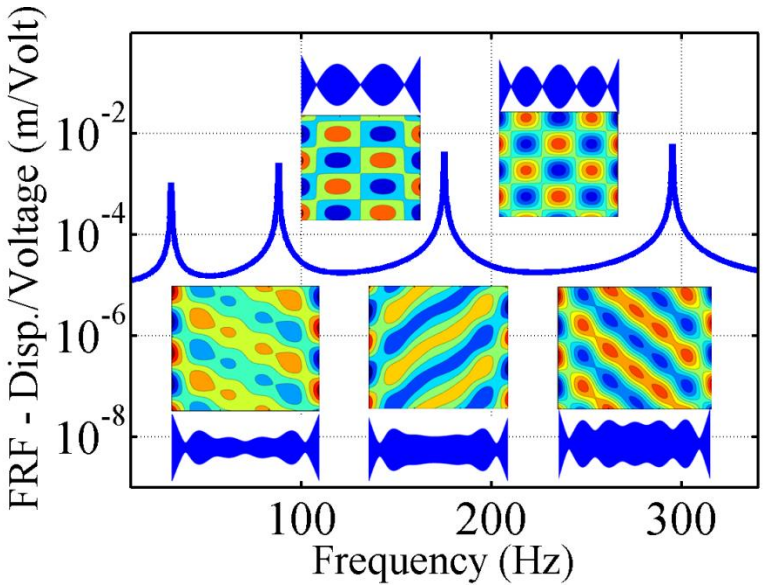

Figure 4.7 Complete analysis of the traveling waves through finite medium and their behavior on a free-free beam

Previous results have achieved only a partial validation of the dynamical model, which is presented in Figure 4.6. In order to answer the question, "How well does the theoretical model predicts the wave profile of a traveling wave seen experimentally?", additional study was conducted. The results are presented for a specific frequency $w \in (w_3, w_4)$, 241Hz, which resulted in generation of traveling waves. The theoretical model showed a close match with the experimental data. The profile of the traveling wave corresponds with the projection of the XZ plane in Figure 4.6.

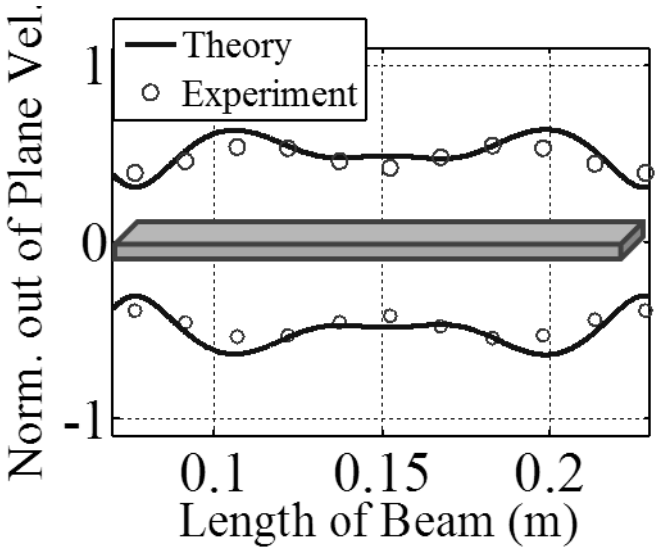

Figure 4.8 Traveling wave envelope obtained experimentally and theoretically. Actuation was conducted at a frequency between two mode shapes with phase difference of 90° and frequency of 241Hz

4.5 Mechanical Wave Characterization

In addition to the theoretical model that describes the dynamics of mechanical wave through free-free beam, additional work on characterization is required to explain the parameters governing the generation and propagation behavior. A study by Bucher et al. focused on the mechanical wave characterization and identification [87] demonstrated that when a structure is excited at two points at the same frequency but with phase difference of 90° a propagating wave occurs. This is due to the fact that part of the reflected wave which normally occurs during impedance changes, is negated (as A≠B in $w(x,t) = A(kx - wt) + B(kx + wt)$) and correspondingly results in a combination of a stationary wave and a traveling wave.

As mentioned earlier, piezoelectric elements were used as the excitation source. Piezoelectric plates are an alternative to vibration shakers and provide more practical solution in the design of propulsion mechanism. This study shows that each frequency has a corresponding phase which contributes towards wave formation and it is not fixed to 90° as previously reported. Hence, two different approaches that are used to measure the quality of the generated waves are presented: Hilbert's and Fourier's approach. There two approaches were validated through experimental work and then compared for a free-free beam.

As stated previously, mechanical waves form as a function of frequency and phase difference, and based on their behavior they can be classified as either standing, traveling or

hybrid (combination of standing and traveling). A schematic representation of the waveforms for each of these types of waves is shown in Figure 4.9. Noticeable difference between the three can be identified in this figure. The pure standing wave is associated with nodal points and only transverse harmonic deflection while the pure traveling wave does not contain any nodal points and propagates with non-varying amplitude. The special case is the hybrid wave which is a combination of standing and traveling waves where the amplitude of the wave propagates while oscillating transversely. The dominance of the traveling wave over the standing wave behavior is directly related to two factors corresponding to frequency and phase difference between the two excitation signals. It is precisely these parameters that are being investigated in the wave analysis through Hilbert's and Fourier's approach in order to obtain the quality of the wave and its direction of travel.

Hilbert's approach is achieved in the time domain where the response of any structure such as the free-free beam is represented in the complex plane. Through experiments, using a laser scanning vibrometer or accelerometers, the response of the system is a real quantity. In order to obtain its orthogonal counterpart, i.e. the imaginary component, the signal goes through a transformation, hence Hilbert's transform described through equation Eq. (4.5.1)

$$w_h(x,t) = w(x,t) + iH(w(x,t)) \tag{4.5.1}$$

where w_h is the analytical response. Following this approach, the response of an individual point on the structure as a function of time will result in a circle. This is achieved as follows. In Hilbert's transform, the trajectory of each point can be represented by a sinusoidal signal ($w(x,t)$) and its Hilbert transformed signal ($iH(w(x,t))$ also a sinusoidal wave, but with phase difference of 90 degrees. When the analytical signal is plotted in the complex plane the response is represented as a circle with radius equal to the amplitude of vibration. Therefore, in a scenario where pure traveling wave exists, the amplitude of all the points across the structure are the same, hence result is shown with multiple circles characterized with equal radiuses (all lie on top of each other). Unlike pure traveling waves, pure standing waves have points with zero displacements (nodal points), maximum displacements and points with amplitudes in between. This corresponding results appear with a filled circle when presented in the complex plane. Finally, in the case for hybrid waves, the minimum amplitude is never zero since nodal points do not exist, hence doughnut shape circle is observed.

The Fourier's represents the response of the system also in the complex plane but in the frequency domain. Since all the points are excited at one frequency, the phase and the magnitude of the Fast Fourier Transform (FFT) peak of individual points is of interest. Unlike the Hilbert's approach where single point traces a circle as a function of time, here, the phase and magnitude of vibration of a point is recorded and plotted as a single value in the complex plane. Accordingly, when a pure traveling wave occurs, the amplitudes and phase differences between the consecutive points along the structure form a circle. This is due to the fact that there exists phase difference between the consecutive points, hence there is a propagating wave and since their amplitudes are identical the points lie on a circle. When standing wave is generated, the phase is either 0° or 180°, and the FFT magnitudes are different which results in a straight line in the complex plane. Finally, for the hybrid wave case, the existent phase difference and different magnitudes of the FFT result will result in a response that is represented by an ellipse. Due to the phase change, the points in the complex plane will not lie along a straight line, but rather on an ellipse. If the effect of traveling wave is dominating, the ellipse will resemble more to a circle, conversely if standing wave is dominating, the ellipse will transform to a straight line.

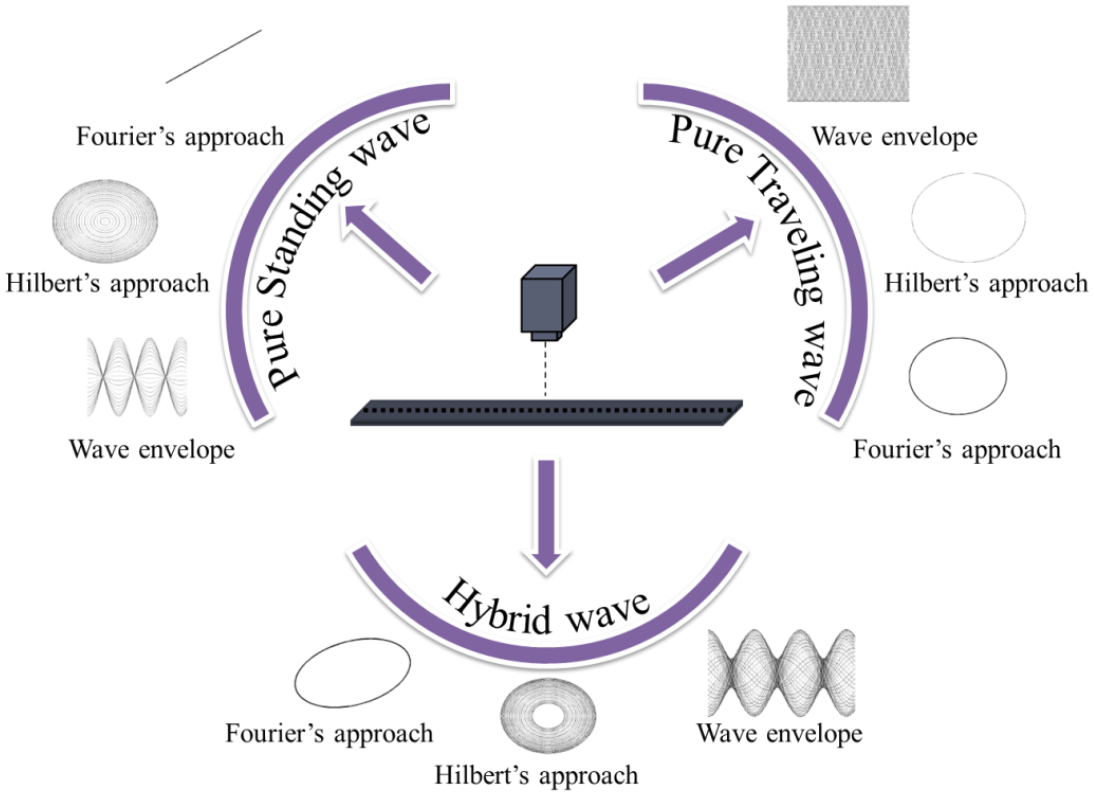

Figure 4.9 Conceptual illustration of standing, traveling and hybrid waves and the different methods of their classification

The theoretical model developed in Section 4.3 was used along with an electro-mechanical model utilizing piezoelectric actuation. It has been observed that when a beam is excited with two input signals with phase difference between them than a traveling wave is generated. A full study on this observation has been conducted for different frequency inputs. An example of these results is presented for a frequency of 243Hz (equal to the arithmetic mean of the 3rd and 4th natural frequency) and phase difference of 90°. Accordingly, Figure 4.10 presents the results obtained theoretically and experimentally for the disclosed parameters (phase and frequency). Since hybrid wave was observed, it was intuitive that the waveform would not indicate any nodal points, Figure 4.10 (a). As a result of the previous discussion, two results were expected, a doughnut shape circle representing the Hilbert's approach shown in Figure 4.10 (b) and an ellipse obtained using the Fourier's approach shown in Figure 4.10 (c). The comparison between the experimental and theoretical results for each case revealed very close match, showing the accuracy of the model in predicting the wave response. To note in Figure 4.10 (b), two experimental points (obtained from a smaller window along the length of the beam) were

selected (the maxima and minima point on the waveform) in order to present the response. This was done for more convenient visual representation of the results. As seen, the responses for the two points trace a circle (dashed red line) where the inner radius and outer radius equal the values of their vibration amplitudes. On the other side, using Fourier's approach, the phase and magnitude of the FFT response for multiple points across the length of the beam for the specified window, was first calculated and then plotted in complex domain. Accordingly, due to the nature of the waves, the points lie on an ellipse.

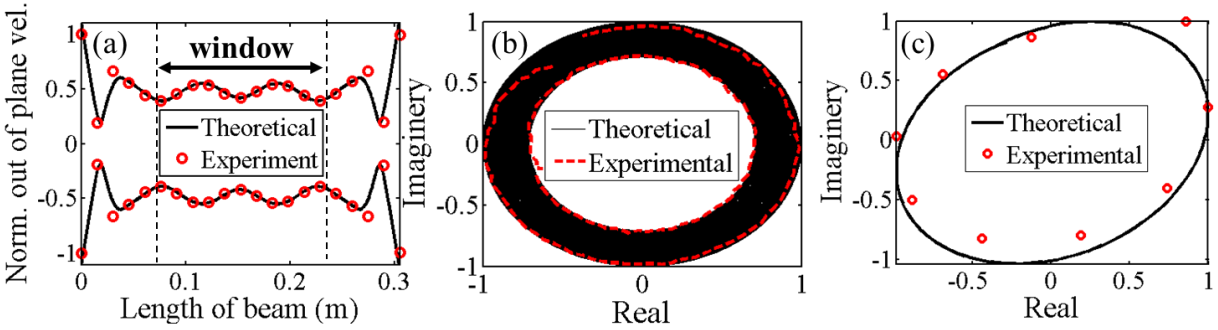

Figure 4.10 Comparison of mechanical waves obtained experimentally and theoretically at 243Hz and phase difference of 90° between the two excitation signals: (a) traveling wave waveform, (b) response of the wave according to the Hilbert's approach, (c) response of the wave according to the Fourier's method

Once the theoretical model was validated against the experimental one, the step that followed was to use any of the two approaches in order to classify and quantify the waves. This was achieved by obtaining their cost function (CF), Eq. (4.5.2).

$$CF = \frac{r_{\max} - r_{\min}}{r_{\max} + r_{\min}} \tag{4.5.2}$$

where $r_{\max}$ corresponds to the outside radius of circle in the Hilbert's approach and the major radius of an ellipse in the Fourier's approach, and $r_{\min}$ corresponds to the inside radius of a circle and minor radius in the two approaches respectively, Figure 4.10 (b-c). In this study, Hilbert's approach was used to define the CF for a free-free beam. Consequently, presented in Figure 4.11 are the results obtained through simulations for the CF which was attained by varying the frequency (0Hz-650Hz) and phase angle (-180° – 180°). The results clearly indicate that phase angle of 90° is not the only possible phase required to obtain the traveling waves. Instead, it can be observed that each frequency has a corresponding phase which affects the cost of the wave

being formed. According to Eq.(4.5.2), CF=1 corresponding to pure standing wave, CF=0 for pure traveling wave, and 0<CF<1 for hybrid waves. The lighter color region that resembles a straight line connects two corners diagonally for each frequency range ($\omega \in (\omega_1, \omega_2)$, $\omega \in (\omega_2, \omega_3)$ or $\omega \in (\omega_3, \omega_4)$) corresponds to the lowest CF, i.e. region at which highest quality traveling waves are formed.

Besides the CF calculation, this study also demonstrates the ability of the theoretical model to predict the direction in which the waves travel. The blue color (negative CF) indicates the direction of the waves traveling from right towards left, and conversely the red color (positive CF) shows the direction of the waves traveling from left to right. As a consequence, it has been observed that when passing from ($\omega \in (\omega_1, \omega_2)$ to $\omega \in (\omega_2, \omega_3)$ to $\omega \in (\omega_n, \omega_{n+1})$), direction of the traveling waves alternate. Accordingly in the $\omega \in (\omega_1, \omega_2)$ region, the wave travels from right to left and in the $\omega \in (\omega_2, \omega_3)$ region, the wave moves left to right.

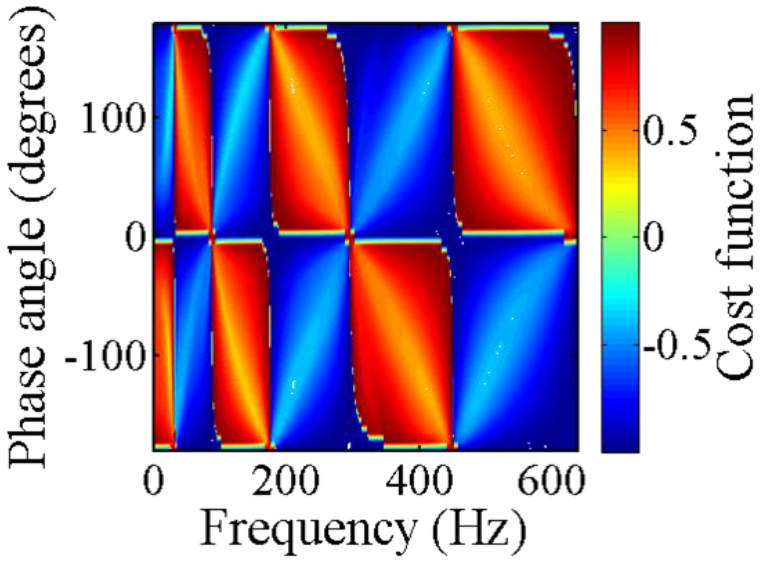

Figure 4.11 Parametric study and cost function analysis Red color – wave travels from right to left, blue color – wave travels from left to right**.**

In order to describe in detail the CF and its outcome as a result of the two parameters: frequency and phase, attention should be paid to the $\omega \in (\omega_2, \omega_3)$ and $\phi \in (0,180)$ region, Figure 4.12 (a). The results clearly indicate the affect the phase has over the CF. These results were validated experimentally and are shown in Figure 4.12 (b), where the phase was kept constant at 90° and the frequency was varied. As noted, 90° phase difference establishes a V-shaped

relationship with frequency. What this means is that for a free-free beam, the 90° phase gives lowest CF at approximately half way between two mode shapes, but at any other region before or after, the CF increases proportionally. This can also be seen by the insets representing the responses of the waves for each point along the curve using Hilbert's approach. At a frequency of 130Hz the ratio between the outer and inner radius is minimal, alluring to the fact that the CF is lowest, hence highest quality traveling wave is obtained. As the excitation frequency approaches the natural frequencies (ω_2 or ω_3), the ratio between the radiuses increases and correspondingly the quality of the traveling wave is reduced. Besides the 90° case, another validation presented in Figure 4.12 (c) was conducted in order to demonstrate that the most effective traveling wave in terms of the CF will occur on the linear slope line (shown in dark blue). This illustrates direct proportionality between the frequency and phase and the color bar indicates how close the experimental results compare with the theoretical prediction along this line. The results shown in this study support the previously made claim that both the frequency and phase play a crucial role in the quality of traveling waves.

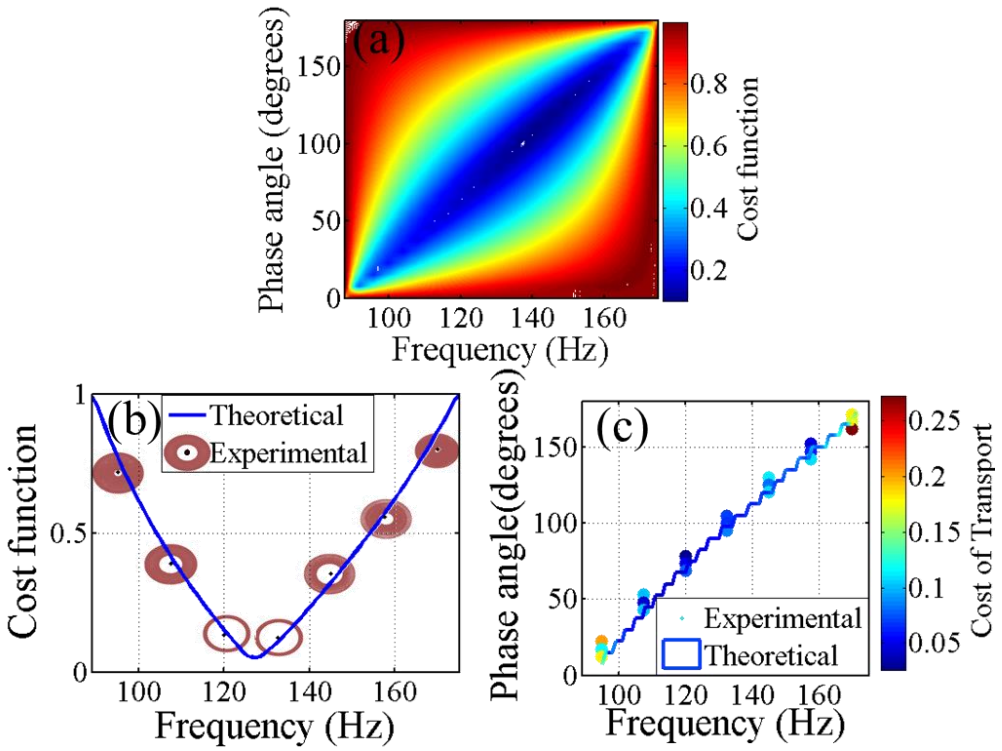

Figure 4.12 Theoretical and experimental results of the cost function between the 2nd and 3rd mode shape. (a) Cost Function window between the two mode shapes, (b) Theoretical and experimental results of the CF as a function of frequency and phase angle 90°, (c) Theoretical and experimental results of the minimal CF

Once the relationship between the phase and frequency was established through the calculation of the CF, the final investigation conducted was to compare the Hilbert's approach to Fourier's approach in order to show the effectiveness of the two methods. The comparisons of the results are shown in Figure 4.13 for two different frequencies, 243Hz ($\omega \in (\omega_3, \omega_4)$)in Figure 4.13 (a-c) and 720Hz ($\omega \in (\omega_6, \omega_7)$) in Figure 4.13 (d-f). Points corresponding to the maxima, minima and arbitrary location in between the two extremes are presented on the wave envelope in Figure 4.13 ((a) and (d)). In Figure 4.13 (b and e) the amplitude and phase of these points is shown in the complex plane, while in Figure 4.13 (c and f), the amplitude of these points as a function of time is illustrated by their rotation around a circle with radius equal to their amplitudes.

The results of this analysis show that the Fourier's approach (Figure 4.13 (b) and (e)) is a more robust method for defining the CF experimentally since it requires less number of points to fit an ellipse. In order to demonstrate this, evenly distributed points were selected across a

window of interest along the beam and their number increased as to monitor the convergence of the CF. Nevertheless, the total number of points needed to obtain an accurate value for the CF is dependent on the frequency at which the wave propagates. Intuitively, lower frequencies correspond to lower number of points and higher frequencies to higher number of points, Figure 4.13 (b and e). Similarly, Hilbert's approach also has a proportional relationship between the frequency of excitation and number of points used to measure the CF, Figure 4.13 (c and f). However, Hilbert's approach requires somewhat higher number of points since accurate measurements can only be achieved if the points selected are placed directly on top of minima and maxima of the waves. Because of the fact that Hilbert's approach requires accurate placements of sensors experimentally, and Fourier's approach uses ellipse fitting method to demonstrate the CF, it is more affordable to use the latter one. Theoretically, however both approaches can be used. In fact the Hilbert's approach for theoretical analysis might be the better choice due to the fact that no curve fitting method is required for approximating the CF, rather straight forward implementation of the selected points is used to define the circle.

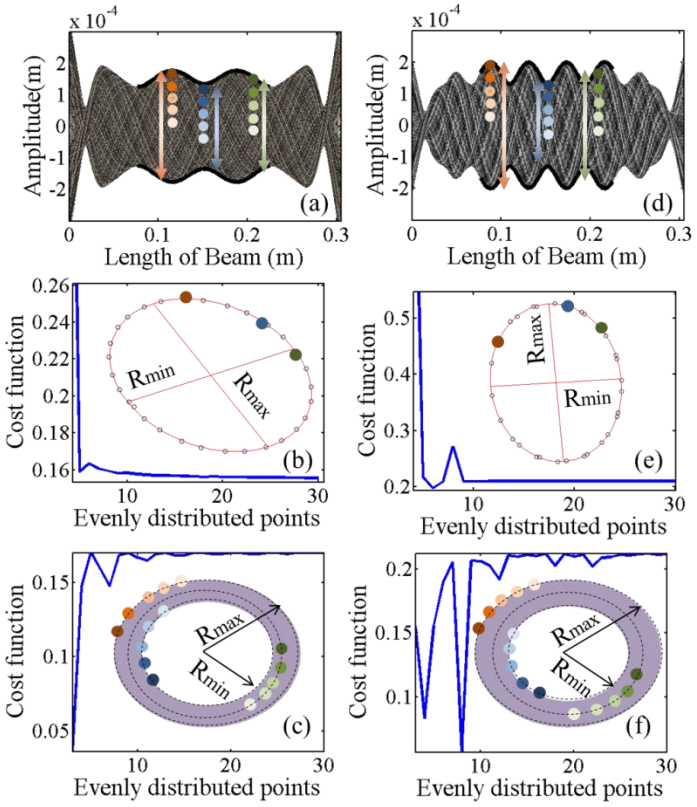

Figure 4.13 Comparison between the Hilbert's and Fourier's approach at 243Hz (a-c) and 720Hz (c-d) : (a and d) Hybrid wave waveform, (b and e) CF as a function of points taken across the structure, Points corresponding to the maxima, minima and arbitrary in between the two are

presented. Fourier's approach, (c and f) CF as a function of points taken across the structure, Hilbert's approach

4.6 Conclusion

In conclusion, this study provides comprehensive investigation on the structural dynamics of beam activated by the piezoelectrics. It provides mathematical foundation towards the generation and propagation of the mechanical waves. A distributed parameter model was developed and validated using the experimental results. The results presented in this chapter were found to accurately predict the dynamics of the traveling waves. Moreover the study demonstrates the capabilities of two approaches, Hilbert's and Fourier's approach, to accurately predict and represent the quality of the mechanical waves being generated. The theory was compared against the experiment for multiple scenarios by varying both the frequency and phase. Accordingly, the results demonstrated that the quality of traveling waves at their occurrence at specific frequencies is highly dependent on the phase angle between the excitation signals used. A comparative analysis was conducted on the Hilbert's and Fourier's approach in use of these methods towards representing the nature of traveling waves. The chapter describes a methodology that will serve as a guideline in the development of WCEs locomotion mechanisms using traveling wave phenomenon.

Chapter 5 – Complementary Technology for the Intelligent Healthcare Environment

This chapter presents the design and characterization of three components required to implement the intelligent healthcare environment. These three components are: multifunctional image guided surgical platform (MIGS), thermal energy harvesters and thermo-acoustic sonars. The MIGS platform is a diagnostic and surgical tool that will assist with the automated ex-vivo skin imaging and treatment. It is an image guided platform consisting of three key elements: three axes scanning and positioning stage, optical coherence tomography probe and a laser scalpel. All three combined together allow construction of a medical device that can be used for delicate and intricate surgical procedures within limited distance underneath the skin. The second component is power source for the sensors embedded within the room that provide feedback for the closed loop control of the various systems. This is important in order to implement the control algorithms and design automation that is holistic. Wiring all the sensors is not an option and batteries have limited lifetime. Thus, an power source based upon the locally available environmental energy is desired. It is a miniature shape memory alloy heat engine that uses the heat wasted from sources such as hot water/steam pipes and converts it into electrical energy required to power wireless sensor nodes.

Finally, the third technology which will complement the healthcare environment is the development and characterization of thermo-acoustic speakers. Due to the flexibility of the device and the miniaturization capabilities, it can be integrated onto the WCEs and can be used as a mobile communication device which will either communicate with outside receivers or multiple other fixed implantable sonars inside the body. This is because nased on the human body topology, acoustic waves represent more promising communication method, than radio frequency waves.

5.1 Multifunctional Image Guided Surgical Platform (MIGS)[3]

This study proposes a novel concept for a three-axis positioning and scanning platform that overcomes the existing gap in technology towards meeting the requirements for displacements, resolution, weight carrying capacity and velocity at small dimensions. The novelty of this work stems from the fact that the three-axis stage design utilizes only two actuators. This system was developed to meet the specific requirements needed for implementation of Multifunctional Image Guided Surgical (MIGS) platform. Mathematical model accounting for the open and closed loop operation of the stage was developed. The stage can provide displacements between 10-20mm in each axis, resolution of less than 10μm and scanning velocity in the range of 10-40mm/s. It can carry weights up to 10grams while meeting the desired requirements. Additionally, the stage has small footprint (50mm x 50mm x 34mm), modular design and extremely cost-effective fabrication. Integration of computer controlled three-axis stage with MIGS platform will provide the opportunity for conducting intricate surgical procedures using remote control or joystick. Finally, demonstration of novel applications is presented that have become possible due to the development of this stage.

5.1.1 Introduction

This research is inspired by the need for a three-axis stage in a surgical tool that will be able to provide fast and accurate analysis of biological tissues at small skin-depths eliminating the need for certain invasive procedures [88]. Many diseased states alter the tissue structure in the vicinity of skin. Thus, detection of these changes and analyzing it at an early stage is of great importance in prevention complexity. One way to detect these changes is by using optical coherence tomography (OCT) based probes [89] that allow imaging at micrometer scale. OCT can provide cross-sectional imaging of tissue structure by focusing a beam of light and then measuring the echo delay time for the light reflected from the microstructural features in the tissue. Compared to the conventional methods for non-invasive procedures such as X-ray radiography, magnetic resonance imaging (MRI), magnetic resonance spectroscopy (MRS), and ultrasound and confocal microscopy, the OCT system is advantageous due to superior depth

[3] Some of the work presented in this section was published in SPIE Smart Structures/NDE conference. The citation are below:
Avirovik, D., Dave, D., Priya, S., "Miniature multifunctional high-performance three-axis positioning and scanning platform," SPIE Smart Structures/NDE, San Diego, Ca, (2013).

resolution (millimeter scale penetration depth) [90]. With its capability to serve as optical biopsy tool, OCT can be used as regular diagnostic imaging tool in ophthalmology, oral and maxillofacial tumors, thermally damaged tissue, and detection of skin cancer.

Building upon the progress made in OCT, we have been developing multifunction image guided surgical platform (MIGS) that integrates all the components required for automated imaging and surgery. The MIGS platform consists of three fundamental components: scanning and positioning stage, OCT probe and laser scalpel. With these three elements integrated onto a single platform, the device transforms to both diagnostic and surgical tool. The stage itself is image guided using the optical probe and therefore it is able to pin point any location requiring a laser scalpel incision. In this study, a description of the success in development of the three-axis positioning stage required for the MIGS platform. Initially, several commercialized three-axis stages from wide variety of manufacturers were investigated such as: ThorLabs, Newscale Technologies, Newport and etc. However, none of them were found to be able to satisfy the requirements of the stage while being affordable. Due to this fact, a design of new stage with cost-effective fabrication methods was found to be necessary to realize the vision of MIGS platform. The outline of the work presented in this paper is the following: literature review of existing platforms available commercially, design and development of the three-axis positioning and scanning platform, control system development for operation of the stage, characterization of the prototype and demonstration of various other potential applications.

5.1.2 Design and Development

The scanning and positioning stage utilizes the principle of lead screw mechanism. An example of a linear stage that uses such setup is shown in Figure 5.1 (a). The mechanism requires five fundamental components: lead screw, nut, two sliders, fixed base and dynamic base, which should be combined in a mathematically controlled fashion to establish required dynamic performance. The sliders were used to constrain the motion of the dynamic base to a single degree of motion in the x-direction while the lead screw and the nut were used to convert rotational motion into linear motion. As the lead screw rotated, the dynamic base moved linearly. The three-axis stage uses two stepper motors whose function was to move the stage in the x and y direction in the horizontal plane and by combining the operation of both motors, z-axis motion was also achieved. Prior literature outlines the lead screw theory for a load moving in the vertical

plane, however, in our knowledge this is the first study on implementing two actuators to achieve three-dimensional controlled motion.

The torque required to lift or lower a load using lead screw mechanism which is directly applicable to the z-axis motion of the stage can be predicted through Eq. (5.1.1) and (5.1.2) given as [91] :

$$T_{Raised} = \frac{Fd_m}{2}\left(\frac{l + \pi f d_m}{\pi d_m - fl}\right) \tag{5.1.1}$$

$$T_{Lowered} = \frac{Fd_m}{2}\left(\frac{\pi f d_m - l}{\pi d_m + fl}\right) \tag{5.1.2}$$

through the force balance presented in the free body diagram (FBD) in Figure 5.1 (b).

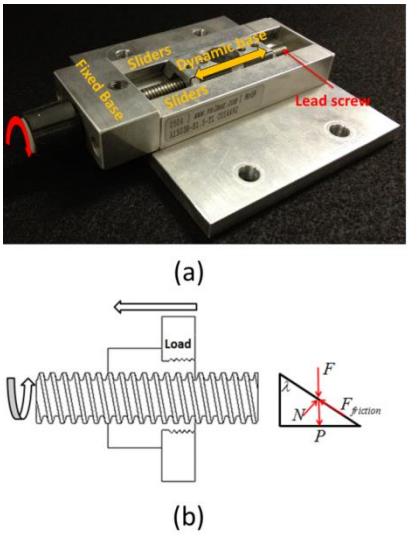

Figure 5.1 (a) Linear stage using lead screw mechanism, (b) Free body diagram (FBD) of translational motion using lead screw mechanism

From the FBD, force balance in the horizontal and vertical plane can be established through Eq. (5.1.3) and Eq.(5.1.4):

$$\sum F_H = fN\sin\lambda - N\cos\lambda = 0 \tag{5.1.3}$$

$$\sum F_V = -F - P + N\sin\lambda + fN\cos\lambda = 0 \tag{5.1.4}$$

where N is the normal force and λ is the lead angle. From these expressions, the force required to push the load and the corresponding torque required by the stepper motor are given by Eq.'s (5.1.4) and (5.1.5) respectively:

$$F = P = mg \tag{5.1.4}$$

$$\tau = \frac{Fd_m}{2} \tag{5.1.5}$$

With this torque prediction, stepper motor actuators AM0820 and AM1020 from Micromo Inc. were selected to drive the stage in x and y direction. Based on the motor selection, lead screw mechanism, scanning area requirements and z axis positioning, a design of the compact stage was developed using NX Unigraphics. Slightly complex geometry of the stage was developed and eliminated the need for CNC approach to fabricate the device. Instead a rapid prototyping machine, EDEN 260v was used (BMDL Lab, Virginia Tech) to manufacture the stage for cost-effectiveness and modularity. Images of the 3D computer aided design (CAD) along with the actual prototype are shown in Figure 5.2(a) and (b). The final completed prototype was found to have the dimensions of 50mm x 50mm x 34mm with mass of 65 grams. mm^2

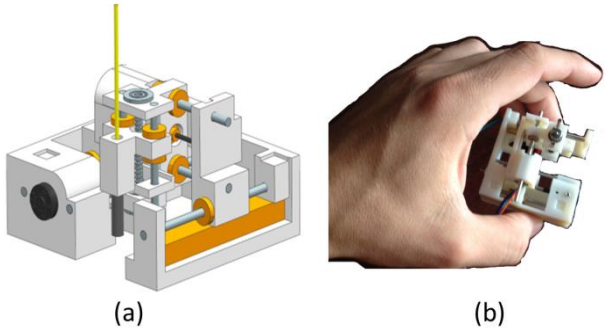

Figure 5.2 Three axis scanning and positioning stage: (a) CAD design, (b) Prototype

5.1.3 Three-axis positioning and scanning stage design using only two actuators

Three axis motorized stages have been around for many years, and their design and principle of operation has not changed. One characteristic that has influenced their design is that due to advances in actuator design, the stages have continuously improved their resolution and speed. In many motorized or non-motorized stages, single axis linear stages represent the

foundation of the three axis stages. This is because three single axis linear stages can be assembled together to provide motion in 3-D. The upside of this scenario is that independent stages can easily be assembled together to provide three-axis motion however the downside is that the size of this system will almost always be greater than a system which is specifically designed to provide three axes motion. This is of importance in this study since our stage has to be designed to have very small footprint. In addition, most systems either use lead screw mechanism where rotational motion is translated to linear or simply use linear actuators to move the axes.

When compared to all of the other motorized stages on the market and published in literature, the novelty of our design comes from the fact that the stage uses only two stepper motor actuators to provide positioning in x, y and z direction. By utilizing the combined motion of the two actuators and a coupling mechanism, positioning in the z-direction was achieved. Figure 5.3 (a) shows an image of the miniature stage developed at Virginia Tech. Stepper motor 1 is responsible for moving the stage in the x direction and stepper motor 2 in the y direction. Both used lead screw mechanisms. The remaining mechanism which is essential for the z axis motion is composed of a pinion and rack gear. The pinion gear is only allowed to rotate along its axis of rotation as shown in Figure 5.3 (a). On the other side, the rack gear is fixed and its motion is constrained in every direction. In order for positioning in the z direction to be achieved, an example is presented which requires displacement of 0.6mm, Figure 5.3(b). The theory of motion for the stage is discussed in the next section of this study. The positioning begins at the initial state at x=0mm, y=0mm. In step 1, motor 2 actuates the stage 10mm in the y direction, aligning the pinion gear to the rack gear. Following this, in step 2, motor 1 moves the pinion gear 2mm in the x direction thus achieving contact between the pinion and rack gear. It then moves 8mm in the positive x direction which due to the interaction between the two gears results in rotation of the pinion gear at a certain angle. This rotation translates to 0.4mm linear motion in the z axis (The relationship between pinion gear rotation and z axis linear motion is discussed in the following section). In step 3, the pinion gear disengages by moving to -2mm relative displacement in the y direction. Since the primary task was to achieve 0.6mm displacement in the z direction, this procedure will have to be repeated in order to obtain the additional 0.2mm. In step 4, motor 1 brings the pinion gear to -10mm relative displacement in x and then in step 5, the pinion gear is positioned to the same location as it previously was in step 1. In step 6, motor 1

moves the pinion gear additional 6mm which translates to total of 0.6mm in the z axis. Finally, the pinion gear returns to the initial position at absolute positing x=0mm, y=0mm as described through step 7. The novelty of the design has been of great importance in decreasing the size of the system. Since less weight is on the stage, the velocities and acceleration are higher as well, leading to shorter scan time.

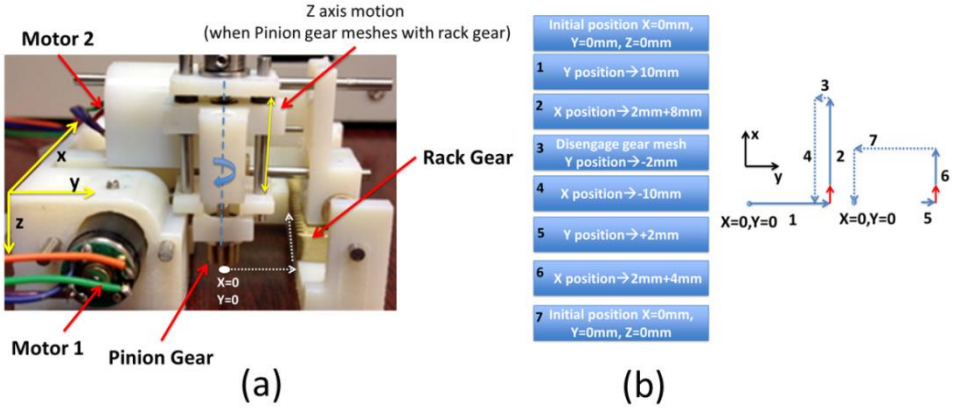

Figure 5.3 (a) Z-axis mechanism, (b) Diagram of translational mechanism in the z-axis example problem)

5.1.3.1 Dynamics of stage

Two stepper motors with lead screws were used to actuate the stage. Direct drive mechanism was used for the motion in the x and y-direction. The advantage of a direct drive mechanism when compared to a mechanism that uses gears is size and resolution. Adding gears to the mechanism would result in a larger footprint of the stage. In addition, backlash is very common when gears are used and therefore resolution as well as precision and accuracy of the stage can be altered. With the stepper motor resolution of 20°, a correlation with the resolution of the stage itself can be established as a function of the lead screw specifications. Lead of 0.4mm was used for motion in the x and z-direction and lead of 0.25mm was used for motion in the y-direction. The resolution in x-direction for a lead of 0.4mm translates to 22 μm. However with the introduction of an EZ4axis stepper motor controller and driver (Allmotion Co.), the resolution of the motor can be increased. The controller can drive the stepper motors at a resolution of $1/8^{th}$ of a step which translates to 2.77 μm linear displacement. Since the commands to the stepper motors are in steps, a relationship for motion in X-direction is shown through Eq. (5.1.5) and (5.1.5):

$$360° = 0.4mm = 160steps \tag{5.1.5}$$

$$\#steps_x = 400 \times \left(x_{\text{distance}}(mm) \right) \tag{5.1.5}$$

Similarly the relationship between the number of steps and the linear motion for the y-axis with lead screw of 0.25mm lead is given as:

$$\#steps_y = 640 \times \left(y_{\text{distance}}(mm) \right) \tag{5.1.5}$$

Finally a slightly more complex approach is required to determine an expression for the number of steps needed for the z-axis to move to a certain distance. This is due to the fact, that once the two gears mesh, a relationship between the displacement caused by motor1 and the rotation of the pinion gear needs to be established. For a specific displacement in the z-axis, the pinion gear rotates by an angle, θ:

$$\theta = \frac{z_{\text{distance}}}{\left(\frac{0.4mm}{360°} \right)} \tag{5.1.5}$$

Now that an expression of θ is obtained, the next step was to determine the displacement in the x-direction which stepper motor 1 needs to provide while both pinion and rack gears are in contact. This relationship is shown through Eq. (5.1.5)

$$x_{\text{distance}} = radius_{gear} \left(\frac{\theta}{90°} \right) \tag{5.1.5}$$

or number of steps:

$$\#steps = radius_{gear} \left(\frac{\theta}{90°} \right) \times 400 \tag{5.1.5}$$

With this analysis, the specification of the stage is shown in Table 5.1-1. With impressively miniature size, the stage can achieve high velocities of above 40mm/s and resolution in all three directions of <10 μm.

Table 5.1-1 Three-axis positioning and scanning stage specifications

Size	50 *mm* x 50 *mm* x 34 *mm*
Scanning and positioning range in X direction	12 *mm*
Scanning and positioning range in Y direction	10 *mm*
Positioning range in Z direction	10 *mm*
Velocity	< 70 *mm / s*
Repeatability	Excellent $\pm 3 \mu m$
Resolution in x direction	2.7 μm
Resolution in y direction	1.7 μm
Resolution in z direction	0.05 μm
Mass	65g

5.1.3.2 Kinematic study

Besides the dynamic analysis of the stage, kinematic study was conducted to analyze the dynamic performance. The stage can also be referred as Cartesian manipulator due to the fact that all of its joints are prismatic (they allow linear relative displacement between two links). Our stage is composed of three prismatic joints, thus having three degrees of freedom (DOF). The reason behind using prismatic joints over revolute is because high resolutions were required. Another characteristic of the Cartesian manipulator is the size of its workspace, Figure 5.4(a). The ratio between the workspace and the size of the stage due to the novelty of the design has shown to be superior to any commercially available platform (discussed in the Comparative study section).

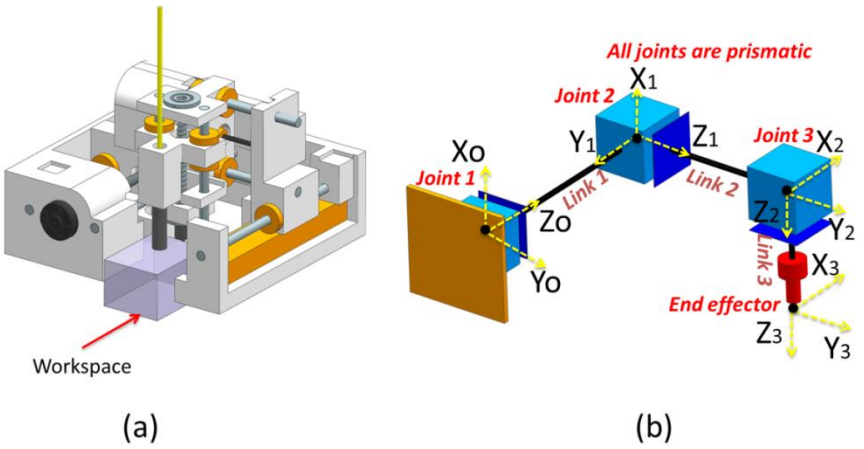

Figure 5.4 (a) Workspace representation of the three-axis scanning and positioning stage, (b) Diagram describing the Cartesian manipulator composed of prismatic joints and links

The kinematic study was conducted using the known dynamic analysis algorithm [92]. Forward kinematic study, following the Denavit-Hartenberg (D-H) convention was established in order to obtain relationship between the individual joints of the three-axis positioning and scanning stage and the end effector, which is represented by either the OCT probe or the laser scalpel. By conducting this analysis the orientation and position of the end effector as function of reference frame was obtained. Figure 5.4 (b) was used as a graphical representation of the (D-H) convention. Following this method, each homogeneous transformation is represented by Eq.(5.1.6) as:

$$A_i = \begin{bmatrix} \cos(\theta_i) & -\sin(\theta_i)\cos(\alpha_i) & \sin(\theta_i)\sin(\alpha_i) & a_i\cos(\theta_i) \\ \sin(\theta_i) & \cos(\theta_i)\cos(\alpha_i) & -\cos(\theta_i)\sin(\alpha_i) & a_i\sin(\theta_i) \\ 0 & \sin(\alpha_i) & \cos(\alpha_i) & d_i \\ 0 & 0 & 0 & 1 \end{bmatrix} \tag{5.1.6}$$

where $a_i, \alpha_i, \theta,$ and d_i are the D-H parameters for each link as listed in Table 5.1-2.

Table 5.1-2 D-H Parameters for three-axis positioning and scanning stage

	Link 1	Link 2	Link 3
a_i - the distance from z_{i-1} to z_i, measured along x_i	0	0	0
α_i - the skew angle from z_{i-1} to z_i, measured about x_i	$-\pi/2$	$\pi/2$	0
d_i -distance from x_{i-1} to x_i as measured along z_{i-1}	d_1	d_2	d_3
θ_i - angle from x_{i-1} to x_i, measured about z_{i-1}	0	$-\pi/2$	0

Using the parameters obtained from the D-H Convention, the transformation matrices between the three links can be calculated through Eq. (5.1.7):

$$\begin{aligned} T_1^{\,0} &= A_1 \\ T_2^{\,0} &= A_1 A_2 \\ T_3^{\,0} &= A_1 A_2 A_3 \end{aligned} \tag{5.1.7}$$

From here, the transformation matrix, that expresses the position and orientation of the end effector with respect to the initial frame is expressed through $T_3^{\,0}$. For example, if an end effector orientation is presented in vector form, $m = \begin{bmatrix} 0 \\ 1 \\ 0 \\ 1 \end{bmatrix}$, with coordinates $x = 0, y = 1, z = 0$, the position and orientation of the end effector in the inertial frame is calculated through Eq. (5.1.8). This analysis is conducted using the parameters listed in Table 5.1-2, with $d_1 = 0, d_2 = 0$ and $d_3 = 1$.

$$I.F.Orientation = T_3^{\,0} \cdot m = \begin{bmatrix} -1 \\ 1 \\ 0 \\ 1 \end{bmatrix} \tag{5.1.8}$$

To notice the last entry of the vector m is always 1 since it has to be a 4x1 matrix in order to be multiplied by the 4x4 D-H transformation matrix. In the $I.F.Orientation$ matrix the last entry is always going to be 1 as well.

5.1.3.3 Control System

Controlling the motion of the three–axis scanning and positioning stage required developing an algorithm which will control the stepper motor and with that the motion of the stage. EZ 4-axis stepper motor controller and driver (Allmotion Inc.) was used to perform this task. The algorithm was developed using NI Labview, outlined by the diagram illustrated in Figure 5.5. USB serial interface between the control station and the controller was used. Once the program starts, automatic initialization of the stage is conducted. This is achieved by moving the motors to their absolute position and bringing the stage to its initial state. Following this step, the algorithm allows the user to make a decision on the action he/she would like the stage to perform. Some examples allowed by the present algorithm is positioning the stage in x, y and z direction or any combined variation of the three, scanning in single axis or conducting a planar raster scan. For each event, the user can specify the displacement, velocity and acceleration. Once selected, the corresponding commands are sent to the controller which amplifies the signal and delivers it to the respective motor. At a point when the event is completed, the program allows the user to go back and select the next action or to terminate the program and end the control procedure.

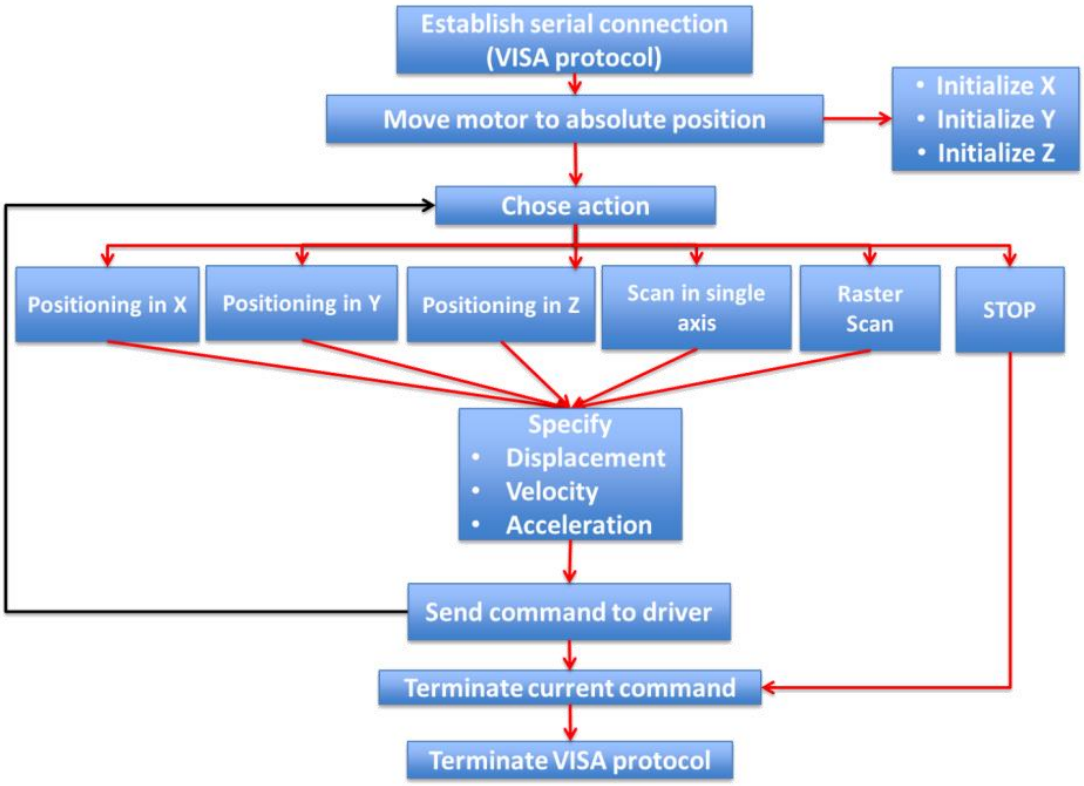

Figure 5.5 Diagram of the control system for the three-axis positioning and scanning stage

The algorithm developed for the stage allows manual control using predetermined parameters. Similar program was developed using joystick to use the stage as a manipulator which allows control on the go. The raster scan speed can be controlled by controlling the speed of the stepper motor and positioning to a desired point can be achieved in all three-axes by specifying coordinates. Since the stage uses stepper motors, open loop control was used for the system rather than closed loop. The resolution, reliability and design of the stepper motor allows the use of open loop control unlike servo motors and piezoelectric motors which require encoders to measure the displacement or angle of rotation and establish a feedback loop which minimizes the error between the desired input and the measured output.

The stepper motors used in the three-axis positioning and scanning stage are two phase motors (n=2) with five magnetic pole pairs (m=5). The step angle of the motor is defined by Eq. (5.1.9) and (5.1.10) as:

$$\Delta\alpha = \frac{360^\circ}{s} \tag{5.1.9}$$

$$S = 2 \cdot n \cdot m \tag{5.1.10}$$

A voltage signal was applied to a pulse generator which sends pulses to the windings associated with the two phases. By controlling the pulse time, the velocity of the stepper motor was controlled. Since the actuation principle i.e. steps per revolution was directly related to the number of pulses, these motors were usually driven in an open loop and therefore do not require encoders thus making the system simple, low cost and small in size. As discussed in [93], the value of the pulse at each phase was defined through Eq. (5.1.11) as:

$$p_j = \sin(\alpha_{i+1} n + \phi_0) \tag{5.1.11}$$

where α_{i+1} is the desired position, and ϕ_0 is the location of the winding of the phase where the pulse is being sent. The time dependency of the pulse sequence is described by:

$$\Delta t = \frac{|fUt|}{m} \tag{5.1.12}$$

where f f is scaling factor used to tune the system and t is a time step for generated pulse in the related phase.

Finally, an important characteristic of any stepper motor control is the torque required to accelerate a specific load. As discussed in [93], the magnetic field generated inside the stepper motor due to a voltage input can be assumed to be sinusoidal. As such, each phase contributes certain torque towards the total motor torque, Eq. (5.1.13):

$$T_{Mj} = \sin\left[n\alpha(t) + \phi_{oj} \right] I_j(t) k_m \tag{5.1.13}$$

where the subscript j refers to the winding of interest, $\alpha_j(t)$ is the angular position of the rotor, ϕ_{oj} the angular position of the corresponding winding, $I_j(t)$ the current running through the winding and k_m is the motor constant. Because voltage is being applied to the stepper motor, current inside the motor is induced as well and the relationship between the two is expressed through Eq. (5.1.14) as:

$$\begin{aligned} U_j &= emf_i + RI(t) + L\frac{dI}{dt} \\ emf_j &= k_m \sin(n\alpha(t) + \phi_{0j})\omega \end{aligned} \tag{5.1.14}$$

where emf_i is the electromotive force i.e. the voltage generated by magnetic force, R is the resistance of the winding, L the inductance in the winding and ω is the angular velocity. The total torque of the motor is then defined as:

$$T_A = \sum_{j=1}^{m=2} T_{Mj} - D\omega - T_f \qquad (5.1.15)$$

where D is viscous damping and T_f is the frictional torque obtained from Eq. . Based on this analysis a dynamic model of a stepper motor was created which can be used for further analysis in improving the design, efficiency and characteristics of the design as well as towards development of a more sophisticated control system for the complex platforms.

5.1.3.4 Experimental Analysis

The three-axis positioning and scanning platform was tested on a vibration isolation table due to the sensitivity of the experiments that required micrometer resolution. An illustration of the experimental setup is shown in Figure 5.6. The main components of the setup included: laser vibrometer (Polytec PSV-400), power supply (BK Precision 9110 DC Power supply), acquisition system, controller and a computer running NI Labview (not shown in image).

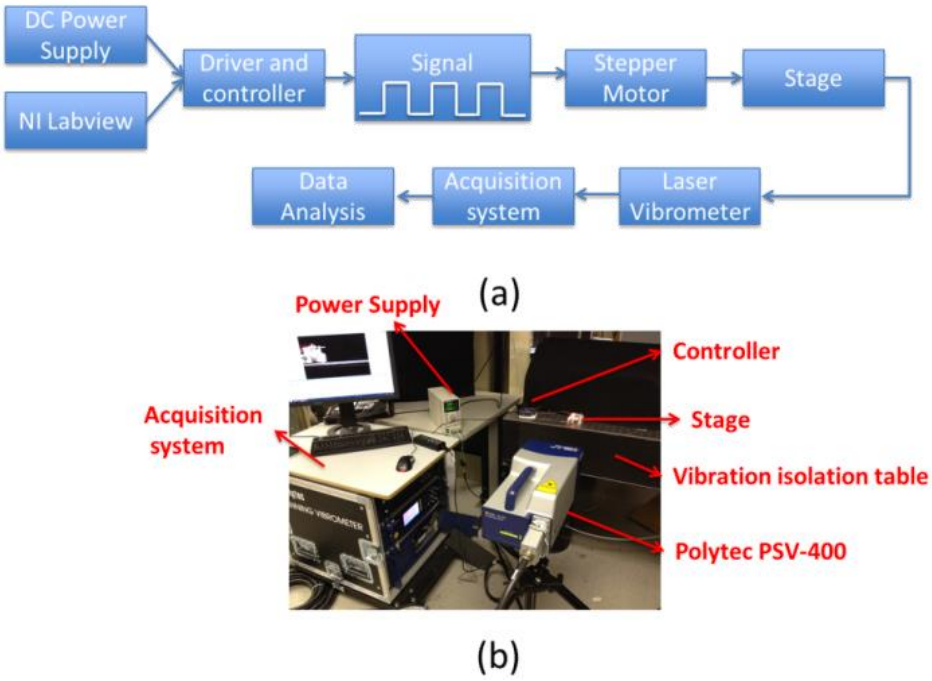

Figure 5.6 (a) Experimental setup diagram, (b) Experimental setup

Two fundamental tests were conducted in order to characterize the stage: velocity and rigid motion analysis. The velocity test was conducted for stage displacements in the x and y directions of 1mm. The stage was first actuated in an oscillatory motion for 10 seconds in the x-direction and then in the y-direction. As noticed on the plot shown in Figure 5.7 the average

velocity in the x-direction was 69mm/s and in the y-direction, 48mm/s. Since the stage was able to move at this speed for displacements of only 1mm, the same velocities would also apply for displacements >1mm as well. The reason why the velocity in the x-direction is higher than the one in the y-direction is due to the fact that the actuator in the x-direction is a more powerful motor with a lead screw M1x0.4. On the other side the actuator responsible for moving the y-axis of the stage is a slightly less powerful motor with lead screw M1.2x0.25.

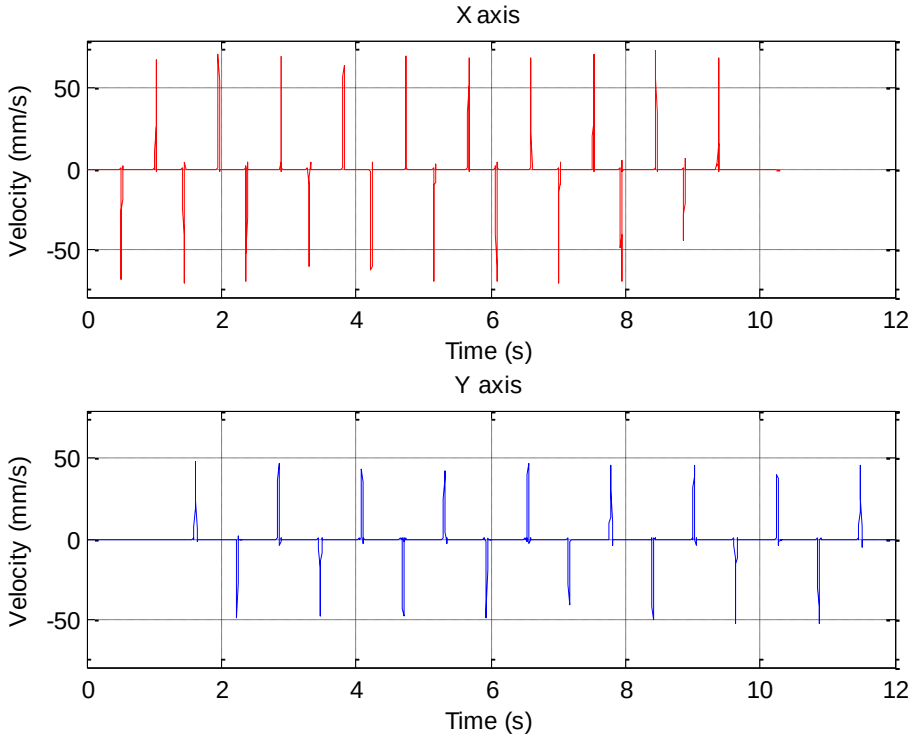

Figure 5.7 Velocity measurements in the X and Y direction

Using the same experimental setup, rigid motion study was explored. For both x and y-axis actuations, three-sections over the range of the entire body were selected and the motion was then analyzed. First, the stage was actuated at a distance of 4mm. The laser was then used to obtain frequency response function (FRF) of the vibration of the platform. It was determined that the frequency of oscillation was around 2Hz. As such, "Fast Scan" was performed using the Polytec Scanning Vibrometer at a 2Hz setting. Each section was defined by 28 points. The stage was actuated at a frequency of 2Hz for a longer period of time and data of the vibration of each point was acquired. The rigid motion was then visually inspected as shown in Figure 5.8. Figure 5.8(a) and (b) correspond to the vibration of the structure out of the page and into the page along the x-axis, and Figure 5.8(c) and (d) correspond to the vibration out of the page and into the page

along the y-axis. For example, looking at Figure 5.8 (a), one can notice the three sections 1, 2 and 3 representing the stage in motion. The (-) sign in front represents the motion of the section in the negative x-direction, i.e. -4mm and the (---) sign represents the mid relative position x=2mm. In Figure 5.8(b) sections 1, 2 and 3 have a sign (+) which corresponds to motion of that section in the positive x-direction, +0mm. Similarly explanation is applied for Figure 5.8(c) and (d), where the only difference is motion of the stage in the y-axis.

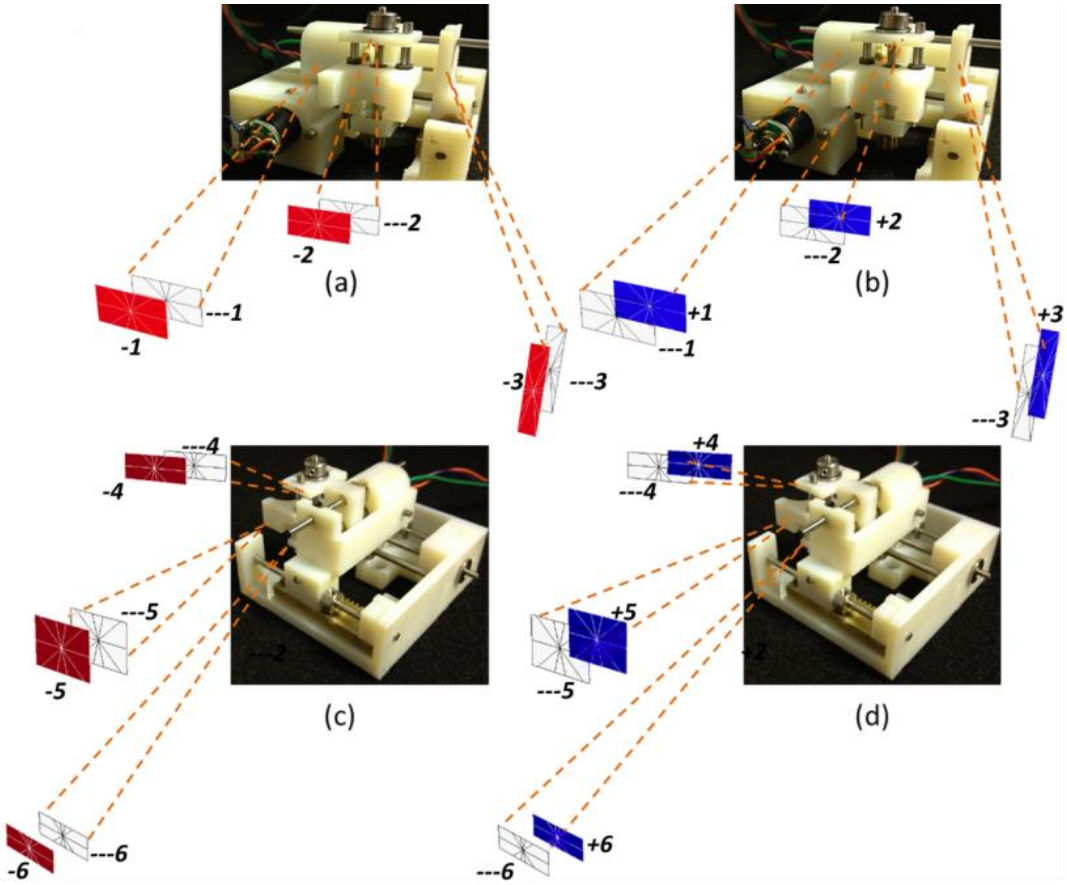

Figure 5.8 Rigid motion study: (a) x-axis out of the page, (b) x-axis into the page, (c) y-axis out of the page, (d) y-axis into the page. 1, 2, 3 are the sections representing the x-axis and 4, 5, 6 the sections representing the y-axis. Each section is defined by 28 individual points. The symbols before each number: " – ", " --- " and " + ", represent motion in the negative direction, mid position and motion in the positive direction respectively

The scanning laser vibrometer recorded the velocities of each individual point from each section, 1, 2, 3 and consequently provided the results of the mode shape of the stage. From the results shown in Figure 5.8, all of the 28 points from each section moved at the same frequency in the same plane. This concludes that the motion of the stage in the x and y-direction is in fact rigid. If this was not the case, than the shape of each section would not be a flat rectangle as

shown. In addition, the motion of all three sections was synchronized because all of the sections pass through the relative location at x=2mm or y=2mm at the same time, thereby confirming the expected results.

Resolution and repeatability test of the stage were also conducted using a laser displacement sensor (MTI Instruments). The stage was actuated 6 times backward and forward for three different lengths: 10 μm, 1mm and 5mm. The experimental results were obtained digitally and it was determined that the stage had repeatability with error of $\pm$ 4 μm. Similarly, the laser was used to measure the resolution of the stage, which has shown that the experimental resolution was around 3 μm in the x and y-direction. A test was conducted to identify the writing resolution of the device as described below. An ultra-fine pen with a nib diameter of around 300 micron was used as a mock-up OCT probe for proof-of-concept experiment. The stage was positioned above a blank sheet of paper at the origin of the local coordinate system. An algorithm in Labview was developed to control the stepper motors to recreate the different patterns. The output of this experiment for different sample patterns is shown in Figure 5.9 taken using an optical microscope (Omano OM99T-V7 - 6.5x-45x). The least count shown as a scale reference is 0.5mm. For both the maze and the raster scan, Figure 5.9 (a) and (b) correspondingly, the spacing between two consecutive lines was 100 µm. This figure clearly demonstrates the ability of the system to provide micro-scale surgical scanning and cutting in complex pattern with high degree of resolution. In real systems, one can easily scale the dimensions of the stage to match the dynamic parameters required for scanning through an optical source or for cutting through a laser source.

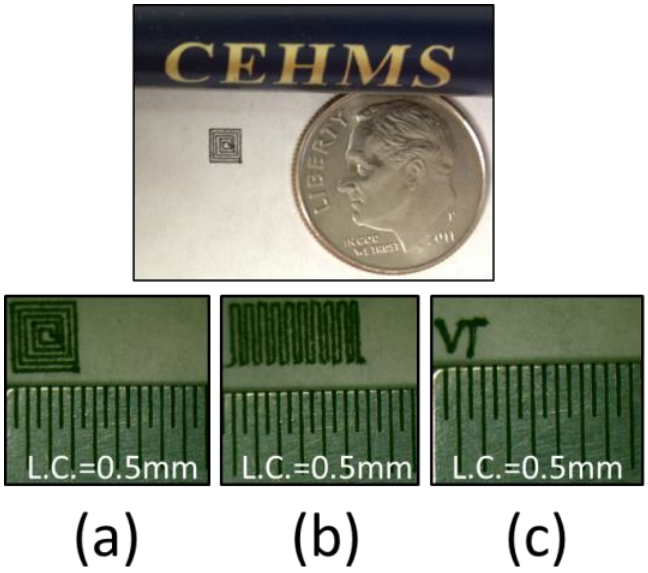

Figure 5.9 Complex geometrical patterns written using the 3-axis stage: (a) Maze, (b) Raster Scan, (c) Virginia Tech logo

5.1.4 Comparative research study

Linear stages, whether they are single or multi-axes have been commercialized for various applications. However, finding a motorized stage which will be able to satisfy the requirements of complex systems such as MIGS platform discussed in Ref. [88] was not possible based on the literature and market search. Due to these reasons a new type of stage was designed and developed. Since the capability of a specific stage is mainly dependent on the actuator it uses, research on different type of actuators was conducted to guide the selection. The research was mainly focused towards the smallest actuators available commercially which can also meet the required speed, resolution and torque. Most promising actuators were found from manufacturers such as: Micromo, Nanomotion, Anaheim Automation, New Scale Technologies and Physik Instrumente. Comparative study of actuators for the MIGS platform is presented in Figure 5.10. As noticed on the plot, eight different actuators contributed to the list. The actuators presented are of the following type: stepper motors (SPM1) and (SPM4), servo motor, (SM2) and piezoelectric motors, (PM3), (PM5), (PM6), (PM7), (PM8), Table 5.1-3. All of the motors with the exception of (PM3) were characterized with force output >1N which was considered to be suitable for a miniature three-axis system. The most important characteristics with the exception of the force were: velocity, resolution and size. The chart shown in Figure 5.11 allows

a visual representation of the most important characteristics for the three-axis positioning and scanning stage and the specifications are shown in Table 5.1-4. Since our objective was to make the smallest possible stage which can achieve velocities between 10-40mm/s, and resolution of <10microns, the most promising actuators were (SPM1), (PM3) and (PM5).

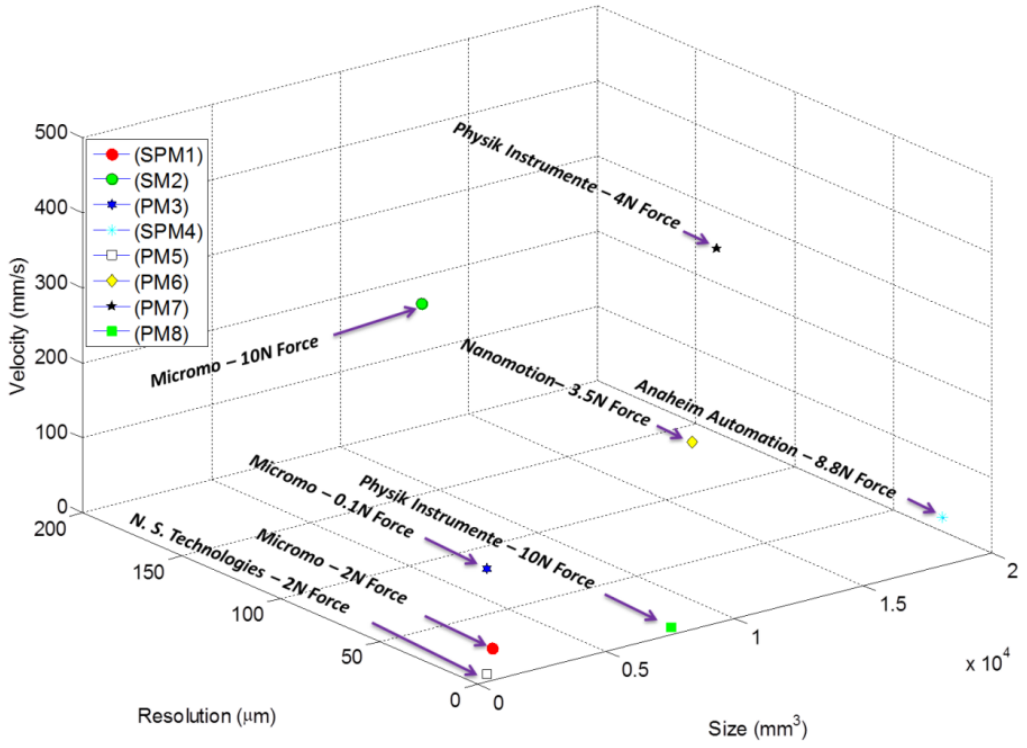

Figure 5.10 Actuator comparison chart

Table 5.1-3 Actuator specifications

Actuator (make/model)	**Force Output** (N)	**Velocity** $\left(\frac{mm}{s}\right)$	**Resolution** (μm)	**Size** (mm^3)
(1) Micromo - Stepper motor with lead screw M1.2x0.25 [94]	2	40-50	1.7	693
(2) Micromo - Linear DC-servomotor [95]	10	200	180	11641
(3) Micromo - Piezowave Motor [96]	0.1	150	1	443.52
(4) Anaheim Automation – High torque stepper motor with lead screw M4x1.27 [97]	8.8	60	0.7	18119
(5) New Scale Technologies – Piezoelectric Motor Squiggle [98]	2	10	0.5	403
(6) Nanomotion – HR1 series [99]	3.5	250	0.1	8326
(7) Physik Instrumente – Piezoelectric motor U-164 [100]	4	500	0.05	9306
(8) Physik Instrumente – Piezoelectric Motor N-310 Nexact [101]	10	10	0.05	7500

The stepper motors used a lead screw mechanism which transformed the rotational motion into linear motion. Based on the combined specifications between the lead screw and the motor itself a comparison could be obtained with the linear piezoelectric motors. Micromo's (PM3) was the smallest motor, however due to the very small force it produces it was eliminated from the selection process. Between the Micromo's stepper motor (SM1) and the Squiggle motor (PM5), the stepper motor was selected as the main actuator in the three-axis positioning and scanning platform. The main reasons behind this decision were: higher velocities, lower price, simplicity of the control system and greater robustness. The remaining motors even though

characterized with impressive resolution and very high velocities, were simply much larger than (PM1) and therefore were not selected in the final design.

The three-axis scanning and positioning stage using Micromo's stepper motor satisfied all of the requirements while maintaining miniature design. Our stage was compared to other available stages on the market which share similar displacement range, 10mm-20mm. Stages from leading precision manufacturers (Zaber, ThorLabs, New Scale Technologies, Newport and Physik Instrumente) were compared to our stage. The results are shown in Figure 5.11 supported by the specifications listed in Table 5.1-4. The comparison study was based on three categories: velocity, resolution and size. To note, due to the shape of the stage, the size was defined as a volume of a cube enclosing the stage, and was based on the available information on the corresponding websites. From Figure 5.11 it can be seen that the stage presented in this chapter outperforms the referenced stages in the velocity and miniature size category, but not in the resolution. Even though in the resolution category, the other stages outscored, this was not of great importance since the initial resolution requirement was <10 µm which we achieved.

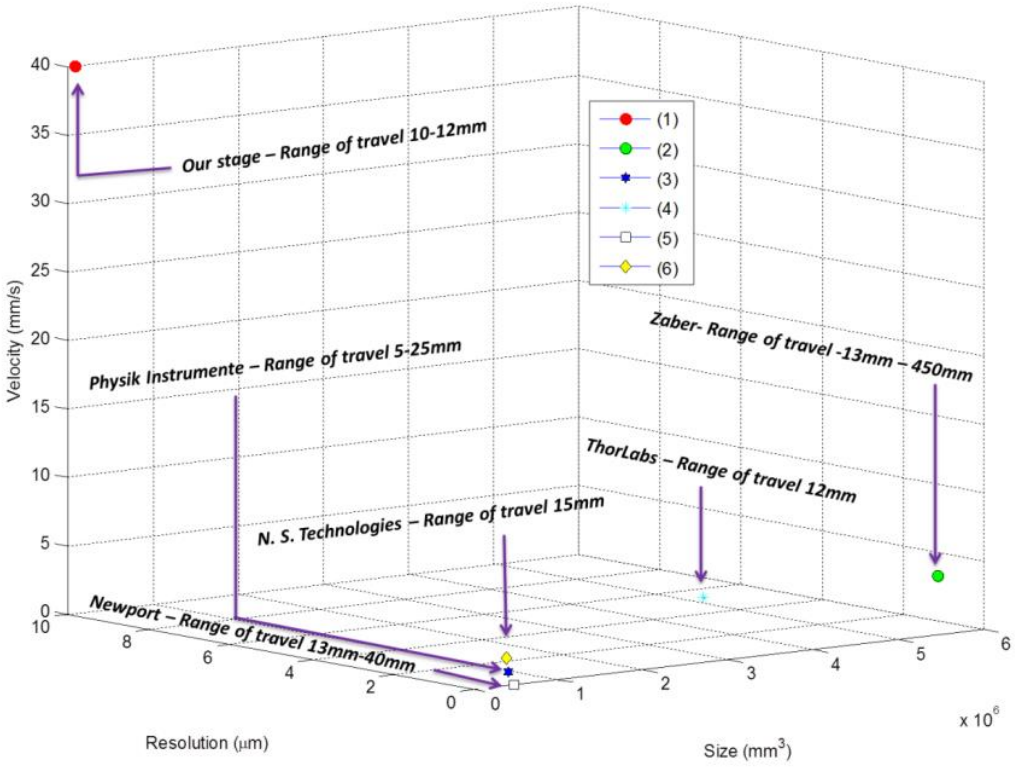

Figure 5.11 Three axis motorized stage comparison chart

Table 5.1-4 Three axis motorized stage specifications

Stage (make/model)	Velocity $\left(\frac{mm}{s}\right)$	Resolution (μm)	Size (mm^3)
(1) Our stage	40-50	<10	85000
(2) ZABER - XYZ series [102]	4	0.4	5644621
(3) Physik Instrumente – M110 [103]	1	0.05	430528
(4) ThorLabs – MT3-Z8 - XYZ Motorized 1/2" Translation Stage [104]	3	2	3647257
(5) Newport - Motorized Gothic-Arch Bearing Stage [105]	0.02	0.03	478973
(6) New Scale Technologies - Motorized stage Squiggle [106]	2	0.02	393144

Please note that this section was presented just to assist the readers with the literature review of the precision stages and actuator available commercially. The comparative analysis conducted using the information available in open literature was focused on specific set of parameters that were important towards our stage. The hope is that readers will continue to revise and add more information to this table which will make the list exhaustive and help towards the design of better performing systems.

5.1.5 Applications of three-axis positioning and scanning platform

The platform presented in this study can be used as a tool in many different applications besides meeting the requirements for MIGS platform briefly mentioned earlier. In this study two promising applications where the stage opens up new opportunity are presented.

5.1.5.1 Laser based micro-machining

The stage can be integrated with a laser which can be used for engraving, dissecting biological tissues, precise machining through different materials etc. An experimental setup for this type of application is shown in Figure 5.12. Some of the key elements in the setup are a power supply required by the EZ4axis controller responsible for controlling and driving the stepper motors integrated into the platform. A control station running NI Labview was used to develop an algorithm which sends commands to the controller and therefore guides the motion of the stage. Several different patterns in 2-D such as squares, spirals, circles can be programmed in NI Labview and then sent to the EZ4 axis controller which can drive the stepper motors and generate the desired pattern. LabView NI SoftMotion module allows design of custom motion control applications using graphical tools. It takes a CAD drawing, converts it in to a coordinate system and accordingly achieves control over the motors.

In Figure 5.12, the laser was composed of a laser diode, heat sink and a lens all housed into one module. The platform was not limited to this laser only, but can be modified to accommodate any type of laser using fiber optic coupling between the laser diode and the lens. Fiber optic cables allow for more flexible operation due to high efficiency in guiding light. In such scenario, one end of the fiber optic cable would be coupled with the laser diode away from the stage. This allows for a more powerful laser and better heat sink which are generally much larger in size than the laser shown in Figure 5.12. The other end of the fiber optic cable will integrate a collimator and a lens which with today's technology can house both in a module with diameter of 2-3mm and length of up to 8mm.Some of the advantages of this type of setup over other conventional laser cutters is that it is much smaller in size and will focus only in applications requiring small micro level precision. The system as proposed will be more modular since the stage can be moved to the specimen itself instead of the other way around. Finally the system is much more affordable due to its design, simplicity and ease of handling.

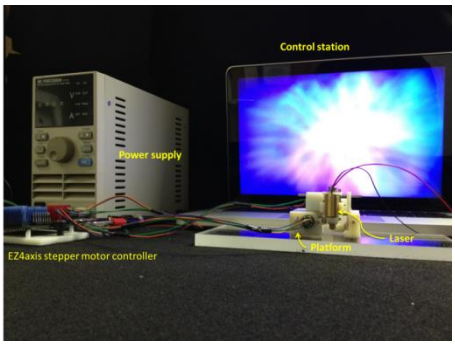

Figure 5.12 Setup for a laser-based micromachining

Some aspects of this applications that need to be considered in order for the setup to provide the desired results such as achieving a certain resolution and specifying the right material and operation conditions. The resolution of the laser cutting platform is limited to the resolution of the stage and the diameter of the laser beam. The resolution of the stage is dependent on the combined resolution of the actuators and lead screw, and the size of the spot can be written as:

$$Spot\ diam = \frac{4M^2 \lambda f}{\pi D} \tag{5.1.15}$$

where λ is the wavelength of the laser beam, M is the beam mode parameter, f is the focal length and D is the laser beam diameter as it comes out from the collimator. The laser diode generates high intensity of light which is focused to a single spot size using a collimator and a lens. The energy is focused to a point which is great enough to break the atomic bonds of the material thus melting it. The higher the absorbance coefficient and the lower the reflecting coefficient of the material, the more efficient will be laser machining [107]. Based on the thermodynamic theory proposed in literature [20], the power required to melt a specific volume is defined by:

$$P_{FC} = \frac{E_{FC}}{t} = \rho w_K t_C v_C \Delta h_m \tag{5.1.15}$$

where E_{FC} is the energy, t is time, ρ is density of the material, Δh_m is the enthalpy increase needed to melt the material and w_K, t_C and v_C are the width, thickness and cutting speed. In addition, the cutting speed is defined as:

$$v_c = \frac{P_L}{2t_c r_0 \rho \Delta h_m} \tag{5.1.16}$$

where P_L is the available laser power and r_0 is the radius of the laser beam.

5.1.5.2 Mask-less lithography

Another promising application for the stage is in photo-lithography patterning. In photo-lithography, the process begins with a clean silicon wafer which is then thermally oxidized. The SiO_2 layer created on the silicon wafer is mainly used as insulation or sacrificial layer depending upon the application. Once the thermal oxidation procedure is complete a photoresist is spun on the silicon wafer. Depending on the angular velocity of the spin coater, thickness of the photo resist can be regulated. Next, the silicon wafer is placed on an oven to be soft baked. An illustration of the steps in photolithography is shown in Figure 5.13(a). This figure compares the traditional photolithography process with the proposed new approach. In the conventional procedure after the photoresist has been spun, a mask is required for etching the pattern. Once mask has been positioned on the silicon wafer, UV light exposes the photo resist. Soon afterwards the wafer is hard baked and the result is shown in the bottom of Figure 5.13(a). Using the modified process proposed here, there will be no need for the mask. Instead, the platform is used to guide a UV light beam over a silicon wafer. Following this method, the photo-resist exposure is controlled by controlling the motion of the three-axis positioning and scanning stage. In this application the UV light was focused to a micrometer diameter spot size which exposed the photo-resist as the stage moved it along a desired path. An image of the experimental setup inside the Virginia Tech clean room is shown in Figure 5.13(b). Once more a control station was used to develop the algorithm required for moving the UV light beam. Similar to the laser tool application, the system proposed was fiber coupled. Fiber optic cable on one side was connected to a UV Light source and on the other side to a collimator and a lens. In our clean room, the photoresist was mostly sensitive to 365nm and 405nm wavelengths and light intensity $> 8 \frac{mW}{cm^2}$ and $18 \frac{mW}{cm^2}$ respectively. Depending on the power delivered to the photoresist, the speed of the stage varied as well. The exposure time was dependent on the exposure dose which varied with different photo-resist. The lens and collimators were placed inside a housing module in the stage dictating the focal length and spot size, i.e. the resolution of the MEMS fabrication platform.

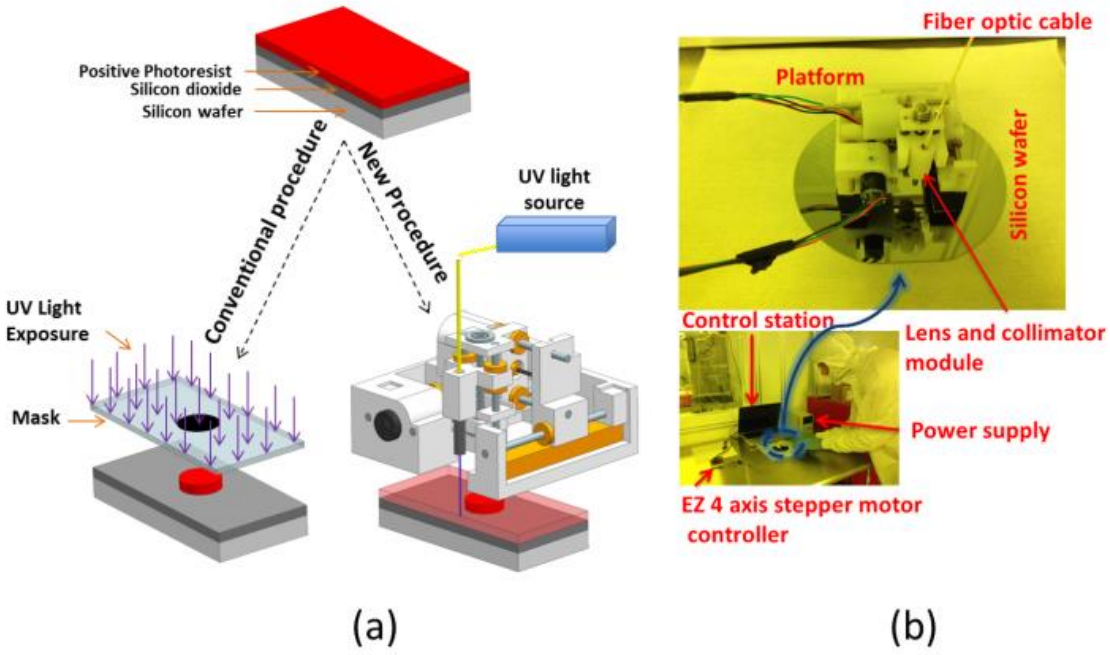

Figure 5.13 MEMS Fabrication procedure. (a) Conventional vs. Proposed, (b) mask-less photolithography setup in the clean room

The main advantage of our approach over the conventional process is exclusion of the mask design from the photolithography procedure. Since masks are mostly outsourced, they are usually accompanied by a time delay and costs. In addition once a mask is build, changes on it cannot be made, but a new one has to be created. With our system, any pattern which is desired can be directly transferred to the wafer itself, making the procedure less time consuming and more affordable. Further, any changes or modifications to desired patterns can be updated on the demand. Also in the clean room our setup is much more modular due to its size and fiber–optic cable coupling and can be conducted with ease. In comparison, the conventional method requires mask aligner and large equipment which limits the mobility.

5.1.6 Conclusion

In this study three-axis positioning and scanning stage with miniature size and competitive performance characteristics was successfully conducted. The necessary parameters and specifications for affordable/applicable actuators were also established. The design was developed in NX Unigraphics and then manufactured using rapid prototyping techniques. The

size of stage was 50mm x 50mm x 34mm achieving 12mm x 10mm scan area and 10mm z-axis motion. Multiple experiments were conducted on the stage to verify the predicted capability. We were able to show that resolutions of less than 10μm can be achieved along with excellent repeatability and velocities of greater than 40mm/s. For the first time a novel concept of a stage was demonstrated, which can achieve three-axis positioning using only two actuators. Finally different applications of the stage were analyzed including laser based micro-machining and mask-less lithography.

5.2 Miniature Shape Memory Alloy Heat Engine for Powering Wireless Sensor Nodes[4]

Shape Memory Alloys (SMAs) exhibit temperature dependent cyclic deformation. SMAs undergo reversible phase transformation with heating that generates strain which can be used to develop heat engine. This study is based on the emphasis that environmental heat can first be converted into mechanical energy through SMA deformation and then into electrical energy using a micro turbine. The presented SMA heat engine was tailored to function as a miniature energy harvesting device for wireless sensor nodes applications in medical institutions. This is due to the great desire for improved monitoring system in intelligent healthcare environments. As a result of this push, sensor deployment which will be able to measure just about anything will be inevitable. Accordingly, powering these sensors becomes a challenging issue, since wiring is not an option. A proposed solution to this existent problem is covered in this section.

5.2.1 Introduction

Wireless sensing nodes are becoming ubiquitous addressing the requirements of smart healthcare system, in order to provide continuous monitoring and automated system. As discussed in Chapter 1, sensor networks are going to represent essential elements in establishing

[4] Some of the work discussed in this section was published in the Energy Harvesting and Structures journal. The citation is below. "The final publication is available at http://www.degruyter.com/view/j/ehs.2014.1.issue-1-2/ehs-2013-0003/ehs-2013-0003.xml"

- Avirovik, D., Kishore, R., Vuckovic, D., Priya, S., "Miniature Shape Memory Alloy Heat Engine for Powering Wireless Sensor Nodes", Energy Harvesting and Systems,De Gryter,0,1-6 (2014)

closed loop system which will continuously acquire data, analyze, interpret and then respond accordingly. The challenge with the implementation of wireless nodes lies in powering them over a long period of time, in most cases greater than 5 years. The obvious powering options are wires and/or batteries. These unfortunately are not the optimal solutions. Wires are expensive to maintain and install, and their use for powering large number of sensors will be quite disruptive and wearisome for both the medical staff and patients. On the other side, batteries require recharging or replacing and then there exist the problem of their disposal. In addition maintenance of sensors, especially those integrated inside the walls will be very troublesome. This need has driven research on the energy harvesters that can convert the locally available energy into electricity and replenish the storage media. Since the objective is targeting sensors integrated inside medical institutions, only vibration and thermal become obvious choices. Vibration would mainly come from a larger equipment such as a generator, however due to the fact that such equipment is only located at few places around hospitals, the one realistic alternative remaining is thermal. This is due to the presence of many hot sources inside buildings, specifically hot water/steam pipes. Along this line of thought, it was demonstrated here a thermal energy harvesting concept that has significant promise in the constant temperature environment.

Conventional methods for low power energy harvesting from heat are mainly based upon the thermoelectric or pyroelectric effect. Thermoelectric (TE) devices convert temperature gradient across the device into electricity. Pyroelectric devices generate electricity in response to the alternating temperature variations. Pyroelectric materials have been reported to possess higher efficiencies compared to other thermal harvesters approaching up to 50% Sebald, Pruvost [108]. Results have shown that power densities of 12.9μW/cm^2 can be obtained for Pb(Zr,Ti)O_3 and 100-169μW/cm^2 for piezoelectric relaxor single crystals Sebald, Guyomar [109]. However, the requirement of cyclic temperature variations, rarely found in nature, limits the use of pyroelectric effect for energy harvesting applications. Unlike pyroelectrics, thermoelectric devices are most commonly used as heat recovery agents. TEs can reach power density of 200 μW/cm^3 for dimensions on the order of 0.25cm^{3}Roundy, Steingart [110]. However, thermoelectric devices require an effective heat sink which adds to the size, cost and complexity of the device. In addition, the efficiency for these devices at temperatures below 200°C is below

5% and at temperatures below 100°C efficiency drops to much less than 1% Ismail and Ahmed [111].

This study focuses on an alternative heat energy recovery mechanism for applications where temperatures are less than 100°C. The mechanism is based on the shape memory alloy (SMA) that exhibit memory effect which translates into a mechanical force when driven beyond the austenite finish temperature. SMAs have been utilized in numerous actuations and sensing applications [112], [113],[114], [115], [116]. They have also been explored for heat engine applications, where the first one was developed more than half a century ago [117]. Since then, several researchers have utilized the SMAs for converting heat energy into mechanical energy Wakjira [118], Wang [119], Johnson [120], Pachter [121], but none of these designs are commercially available for thermal energy harvesting. Further, prior research has mainly targeted large scale conversion of thermal energy into mechanical energy and has not been able to provide complete solution for continuous harvesting and storing the generated electricity. Sato et al. have demonstrated a functional SMA heat engine Sato, Yoshida [122] that produced 1.16W using five SMA belts and the size of system without generator was on the order of 1850mm x 550mm x 500mm.

An optimum solution for the SMA heat engine suitable for implementation at miniature scale that could lead to new generation of power sources for wireless sensor nodes is provided. The fundamental challenge at smaller dimensions lies in the fact that the torque generated by the SMA wire should be sufficient to overcome the cogging torque of the electro-magnetic generator. It has been demonstrate that this challenge can be overcome by designing generator that is able to self-start. Three basic measurements were conducted to evaluate the capability of the system: angular speed as a function of temperature, mechanical power as a function of angular velocity, and electrical power as a function of the mechanical power generated. Using the miniature SMA heat engine, a fully functional self-powered wireless sensor node was developed.

5.2.2 Experimental Setup and Principle of Operation

The design of a small scale heat generator is based on the concept proposed by [123] almost 30 years ago. The design of the “Heatmobile” as it has been referred to in the literature is composed of three main components: hot water reservoir, pulley system and an SMA wire. Figure 5.14 shows the description of the experimental setup as well as a diagram outlining the

operation principle of the device. The key components of the device are SMA loop wire of 300μm diameter (Grand Illusions Inc.) and two pulleys offset from each other at a specified distance limited by the length of the SMA loop wire. Cold pulley is attached to an electromagnetic generator developed in our laboratory and hot pulley is submerged in a hot water reservoir. The temperature of the hot water is regulated by a hot plate and was measured using a thermocouple. Just besides cold pulley, a propeller from a micro wind turbine is used to cool the SMA wire through forced convection of room temperature airflow. A tachometer was used to measure the angular velocity of the blades i.e. the electro-mechanical generator.

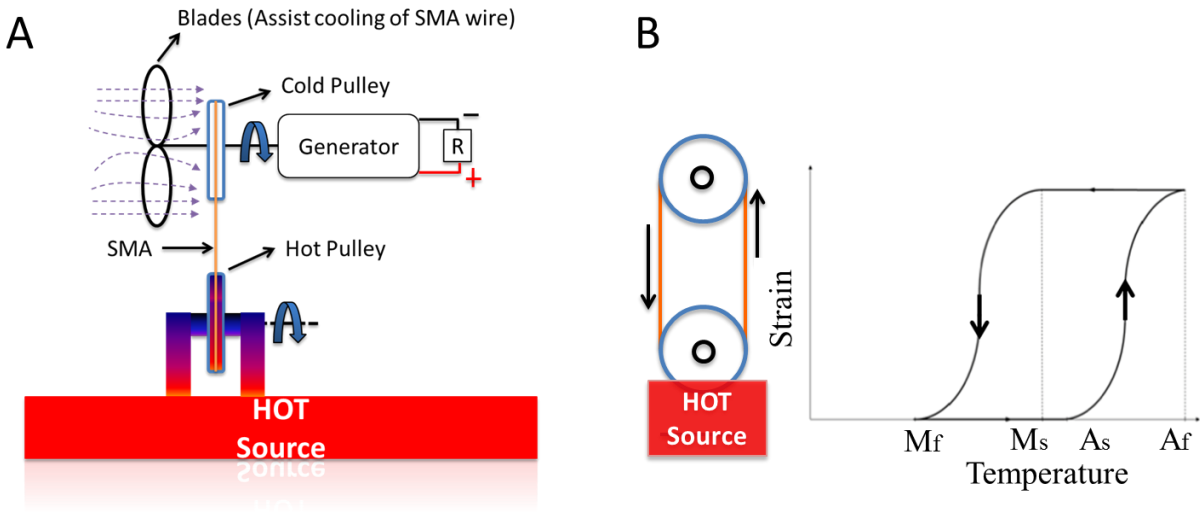

Figure 5.14 Measurement technique: (A) Illustrative diagram of experimental setup, (B) Experimental setup used for characterization

Due to the shape memory effect, as the SMA loop wire comes in contact with the hot water, it transforms from the martensite to austenite phase as shown in Figure 5.14(b), therefore causing the wire to return to its original shape (which was initially straight). As the SMA wire strains, torque is generated around hot pulley, causing the pulley to rotate. Since the pulleys are connected via the SMA wire, cold pulley rotates as well and consequently turns the generator. The SMA wires have very low heat capacitance which allows the SMA part that was submerged under water to cool-off almost immediately after it leaves the hot water medium. The part of the loop wire that follows next, comes in contact with the hot water, heats up and as a result strains, thus repeating the process all over again. The system can run continuously as long as the

temperature of the hot water is maintained above the transition temperature. In addition to the strain created at the bottom of the hot pulley, during operation, vibration in the SMA wire is another factor that aids the continuous rotation of the SMA turbine.

5.2.3 Experimental Characterization of Device

By regulating the temperature of the water reservoir and monitoring the angular speed, a derivation of the relationship between the angular speed and temperature in both the heating and cooling stage was obtained. Figure 5.15 illustrates how the temperature affected the angular velocity in both the heating and cooling stage. As seen here, the highest angular speed was achieved at 71°C, corresponding to 480rev/min. A small hysteresis of about 1.5°C was also observed. The generator started spinning at 65.5°C during the heating phase and then came to a halt at a temperature of 64°C towards the end of the cooling phase. The hysteresis was expected since additional energy (higher temperature) was initially required in order to overcome the cogging torque of the generator.

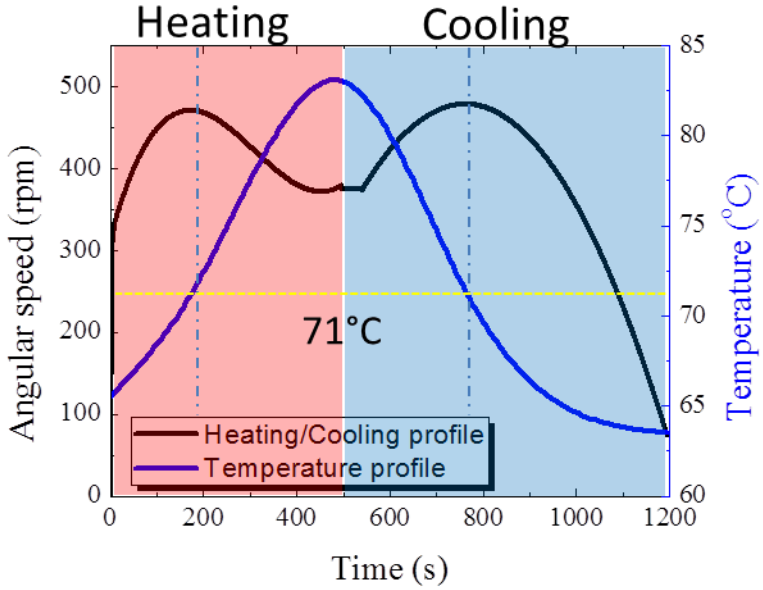

Figure 5.15 Angular speed of the generator as a function of temperature

Once it was identified that highest angular speed occurred at 71°C, the temperature of the water reservoir was fixed and the mechanical power of the device was measured. Figure 5.16 shows the angular speed measured as a function of time. The experimental results of the angular speed are represented by a 6^{th} order polynomial shown in Figure 5.16(a). The torque was

calculated following the methodology described elsewhere [124]. The angular speed reached steady state in a very short time period; therefore, in order to obtain the torque generated by the device, the focus was mainly on the transient response of the speed curve. By differentiating the speed expressed as a 6th order polynomial, angular acceleration was obtained. The torque generated by the device was calculated using eq.(5.1.17):

$$\tau = J_{total} \times \alpha \tag{5.1.17}$$

where α is the angular acceleration and J_{total} is described through eq. (5.1.18) as:

$$J_{total} = J_{pulley} + J_{blades} + J_{generator} \tag{5.1.18}$$

where J_{pulley} is 4.71E-7 $kg-m^2$, J_{blades} is 8.74E-7 $kg-m^2$ and $J_{generator}$ is 6.046E-6 $kg-m^2$. Lastly, the mechanical power curve illustrated in Figure 5.16(b) was calculated using eq. (5.1.19) :

$$P_{mech.} = \tau \times \omega \tag{5.1.19}$$

From these results, the maximum mechanical power from the current design was calculated to be 2.57mW at the angular speed of 226rev/min as shown in Figure 5.16(b).

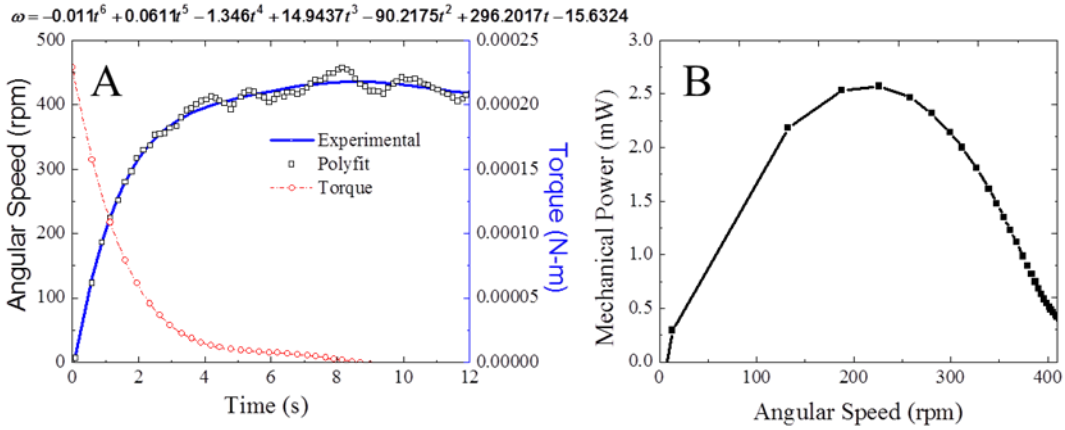

Figure 5.16 Mechanical characterization of SMA turbine: (A) Angular velocity and Torque curves, (B) Mechanical power as a function of angular speed

The next step was converting the mechanical energy to electrical energy through the utilization of the micro electro-magnetic generator. In this experiment, the device was run at its optimal condition, i.e. 71°C. A resistor sweep study was conducted where the voltage was measured across different load resistances ranging from 1Ω-1000 Ω as shown in Figure 5.17(a).

Figure 5.17(b) represents the electrical power generated by the system at different resistance values. The maximum electrical power measured was 1.76mW at 80Ω load resistance.

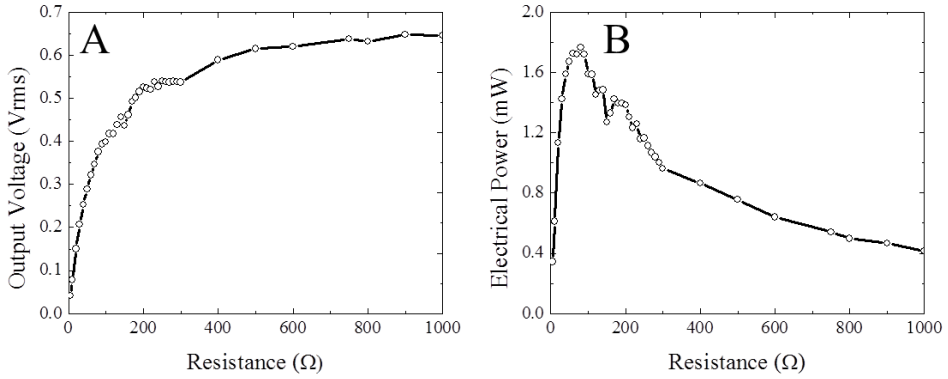

Figure 5.17 Electrical characterization of SMA turbine: (A) Output voltage as a function of resistance, (B) Electrical power as a function of resistance

5.2.4 Demonstration study

A wireless sensor network was powered by the SMA heat engine as a demonstration. In this system, the SMA powered generator was charging a buffer storage, which once filled, provided energy to a wireless sensor node, that in turn, transmitted the measured ambient temperature to a nearby base station, which displayed the data on a computer screen. Figure 5.18 shows the block diagram of the electrical system. The first step in utilizing the available power generated was converting the alternating current output of the generator into direct current. Due to low currents on the order of mA, voltage drop over the diodes in the rectifier introduced significant power losses. In order to provide higher efficiency, a voltage doubler was chosen as a rectifier circuit bringing the efficiency to 56%. The power management unit consisted of a BQ25504 circuit (Texas Instruments Inc.) which had an integrated DC/DC step up converter on the input together with a power management module that controlled the connection between the load and the storage. By doubling the input voltage, as stated previously, the relative difference between input and output voltage was reduced allowing the DC/DC converter to operate at higher efficiency compared to the efficiency in case of a standard diode bridge. BQ25504 circuit has integrated power management features that allowed for the load to be disconnected from the storage until the storage reached predefined voltage level. Our application had this threshold

level set to 3.1V. Once active, load drained the energy stored until the voltage on the storage reached 2.2V. Storage used was a 2.2mF aluminum electrolytic capacitor. This storage was chosen based on the load of the system, which in our application was a wireless sensor platform ez430 (Texas Instruments). This platform consisted of a low power MSP430 microcontroller with onboard temperature sensor and an attached 2.4 GHz CC2500 radio module.

The network was set up in a way that once active, the microcontroller performed a set of measurements and transmitted the data over radio to the base station. Microcontroller measured ambient temperature and storage voltage. Following transmission, the microcontroller put the radio module to sleep, disabled the temperature sensor and entered a low power sleep mode for duration of one second. After the sleep time expired, the microcontroller would wake up and the cycle would repeat itself. The cycle of sleeping-waking up-measuring-transmitting-sleeping continued as long as there was sufficient energy in the storage. In case, where there was not enough energy, the power management module would power down the microcontroller and wait until the storage voltage level reached predefined value. The storage was being actively charged as long as there was power coming from the SMA generator and the charging process was not affected by microcontroller operation.

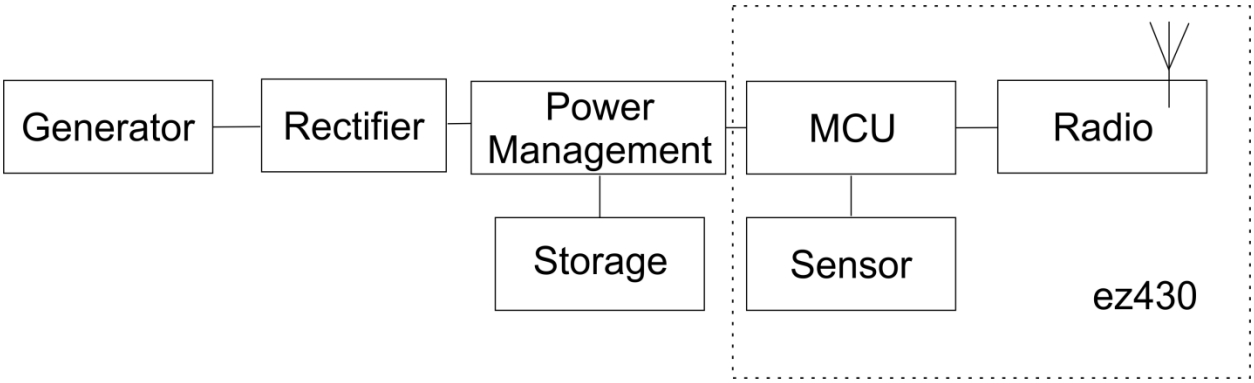

Figure 5.18 Block diagram of the wireless node

5.2.5 Discussion

Unlike all the previous studies, this study focuses on the development of a miniature heat recovery system which can be integrated in healthcare, as well as residential and industrial environments. Different scenarios for providing the heat to the miniature SMA heat engine can be designed. One of the alternative ways is to deliver the heat wirelessly through microwaves or

laser light (See Appendix A) and then converting the light energy into electrical energy in order to power wireless sensor nodes. The objective is to heat a small section of the SMA wire to a specific temperature. Figure 5.19 shows the practical scenario that can be built using the SMA heat engine concept. The proposed solution allows integration of the SMA thermal energy harvester onto hot water pipes which run throughout hospitals in order to take the heat and convert it into usable electrical energy for powering numerous sensors such as: RFID, temperature, humidity, motion and occupancy, accelerometers and etc.

By simply replacing the hot water source with a hot pipe source and attaching the SMA heat engine onto the outer shell of the pipe, electrical energy can be continuously generated.

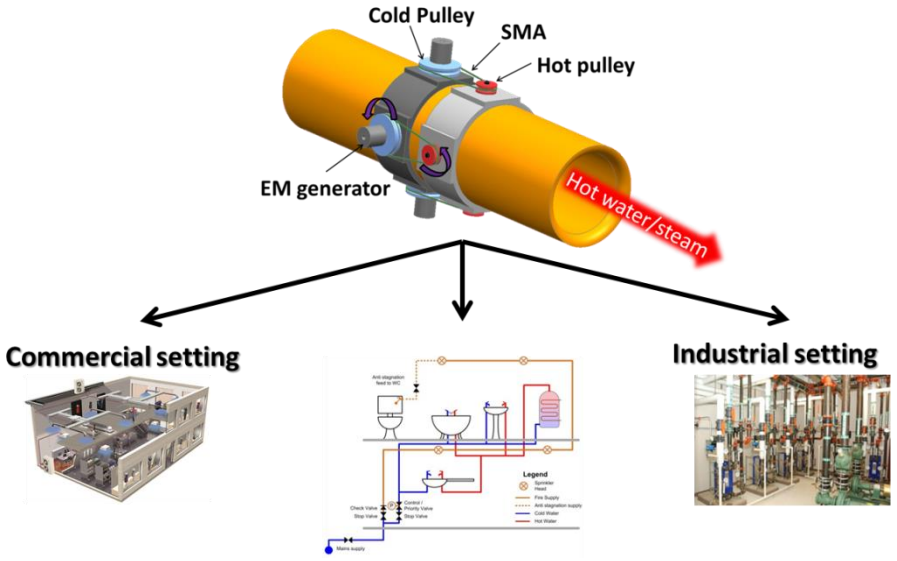

Figure 5.19 Conceptual illustrations for implementation of miniature SMA heat energy harvester

Most SMAs operate at temperatures of 70°C or 90°C depending on their classifications Low Temperature (LT) or High temperature (HT) SMAs respectively. These temperatures are high for the outside environment; however temperatures greater than 40 C° are very realistic in variety of scenarios. [125]have shown the potential for lowering the martensite to austentite transition temperature by changing the composition of the SMA. The results showed that increased Ni content in conjunction with Cu doping results in significant shift of the transition temperature. The power generation capability is highly dependent on the electro-magnetic generator characteristics. The electromagnetic generator used in this study can produce up to 257mW power at angular velocities of 4200 RPM. Introducing gear system will allow the increase of the RPM while sacrificing the torque. The torque can be increased to by adding more

SMA wires to the system. At present 4:1 gear ratio with a single wire was achieved, but future studies will include even higher gear ratios in order to maximize the output power.

5.2.6 Conclusion

In summary, this study presented a concept of a miniature heat engine utilizing a 300μm SMA wire that generated enough torque required for turning an electromagnetic generator. Characterization of the mechanical and electrical component of the device was conducted and a complete wireless sensor system where a hot water reservoir was used as a heat source and the SMA device as a heat recovery generator was developed. The generator was able to produce 1.7mW of electrical power which was more than enough to charge a wireless sensor node, thus demonstrating the potential for this harvester to be used as primary source of energy for wireless sensor networks.

5.3 Carbon Nanotube Thermo-Acoustic Projector

With new implantable sensors being developed and their integration inside the human body for health monitoring, there will be a need for a system where communication occurs between the sensors without wires. Imagine a scenario where many implantable sensors communicate between each other and a control system makes real time decision on whether implantable drug delivery devices should be activated or not or whether the patient should be warned of an imminent threat to his/her life. It is well known that RF signals are the main means in sensor communications in air medium, but in water it is quite the opposite, their operation is very poor. Since the human body is almost 65% water, different means of communication are necessary and the most promising solution are acoustic waves. A new research initiative has recently been started by the WiNES Lab at the University of Buffalo, claiming that acoustics can be used as means of communication inside the human body. The diagram shown in Figure 5.20 presents such a scenario. In addition, a wireless capsule such as those discussed in Chapters 3 and 4 can also be equipped with thermo acoustic sonars and can effectively communicate with sensors already implantable inside the body. This will allow continuous communication and operation not just between the fixed sensor nodes but also the mobile sensors as in the case for WCEs. The sound generated from the thermo-acoustic sonars need not only be used as a communication device between implantable sensors. They could be used in recovery rooms providing sound medical therapy. The emphasis in this chapter is to present first describe the

concept and then analyze the thermo-acoustic projectors using the carbon-nanotube sheet technology.

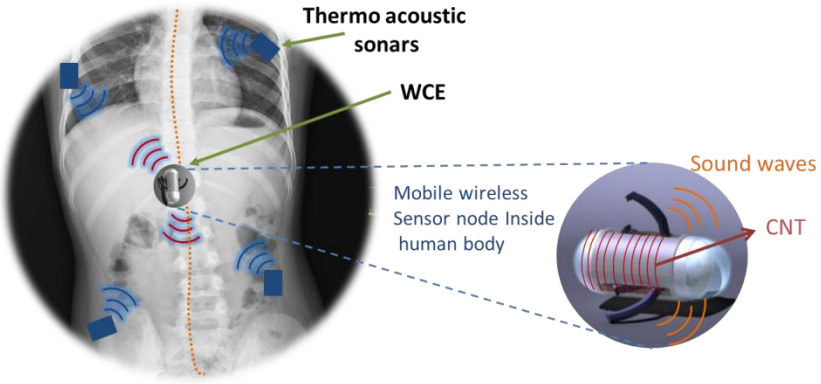

Figure 5.20 Thermo-acoustic sound projectors inside the human body

5.3.1 Introduction

Carbon Nano Tubes (CNT) are cylindrically aligned nanostructures which have shown to have extraordinary properties, such as mechanical, electrical and also thermal. Due to their thermal-conductive properties, CNTs are able to generate smooth-spectra sound over a wide frequency range (1-10^5 Hz) through means of thermo-acoustics. Aliev et al. [126] have developed a CNT device for underwater applications, where a sheet of CNTs was suspended over two electrodes. Due to the very low heat capacity of the CNTs, the sheet temperature can synchronize with electrical current running through it. As a result, by supplying alternating current, thermal pressure is being generated across the sheet, which translates into acoustic waves in the audible range (20Hz-20kHz). As described in Ref [126], the underwater thermo-acoustic projector is simply composed of CNT sheet and two electrodes.

According to the model developed in Ref [127], the sound generation efficiency for open CNT sheets increases proportionally to f^2:

$$\eta=\frac{\pi f^2}{4\rho_g v_g C_p{}^2 T_0{}^2}P_h \tag{5.1.20}$$

where $\boldsymbol{f}$ is frequency, $\boldsymbol{\rho_g}$ is density of inert gas, $\boldsymbol{v_g}$ is the sound wave speed in the inert gas, $\boldsymbol{C_p}$ is the heat capacity of the gas, $\boldsymbol{T_0}$ is the temperature of the surrounding ambient gas and $\boldsymbol{P_h}$ is the

applied AC power. This equation describes that the efficiency of the device decreases in high frequency regions and it essential to seal the (CNT) sheets as they are sensitive to the environment due to their nano-scale thickness and high surface temperature. The device reported in study was encapsulated between rigid plates in inert gas. In this case, the efficiency of the device is inversely proportional to f^2, therefore contributing to higher efficiency at low frequency operations.

$$\eta = \frac{(\gamma - 1)^2 \rho_{air} Q^2}{2 f^2 V^2 v_g} P_h \tag{5.1.21}$$

where γ is the heat capacity ratio and Q is the quality factor of vibrating plates. Since the device is enclosed, mechanical dynamics are introduced to the system which requires studying the structural dynamics. The thermo-acoustic sonar generates thermal pressure that translates into an acoustic pressure which acts on the walls of the device and consequently induces vibration. This vibration influences the dynamics in the system and changes the performance characteristics. The higher the power delivered to the projector, the higher the pressure generated and accordingly the higher is the amplitude of vibration. The resonance of the device is in this case is highly dependent on the material properties of the plate, the inert gas used, boundary conditions and stiffness properties.

In order to obtain efficient and compact sound projector, a comprehensive set of experimental characterization were necessary in conjunction with the modification to the structure and materials. The functionality of the thermo-acoustic projectors is a function of many design and operation parameters: boundary conditions, dimensions, number of material layers, operation frequency, power inputs, temperature and etc. Accordingly, different experimental setups were developed to understand the effect of these parameters. The content discussed in this chapter was mainly focused on the dynamic characterization and vibration properties of the acoustic projector as well as thermal characterization following the experimental setup defined in Figure 5.21.

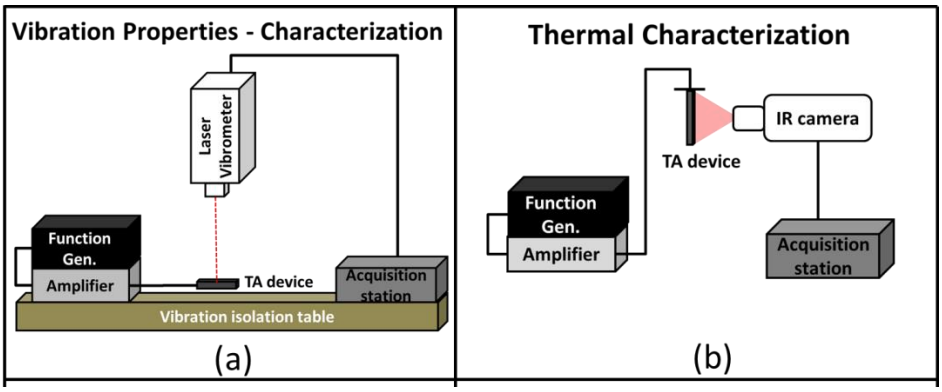

Figure 5.21 Experimental setup for characterizing MWCNT sheets

5.3.2 Modeling

In order to provide a mathematical approximation of the response of the CNT projector as it vibrates due to the harmonic thermal pressure generated inside the encapsulated device, a lumped element model was developed. This model is respectively shown in Figure 5.22. The plates used to encapsulate the device are represented by: spring, mass, damper elements, and the boundary conditions (B.C.) which are result of the silicon spacers placed between the two plates represented by spring and damper elements. The harmonic pressure generated is a function of the thermal expansion and acoustic pressure generated inside the CNT projector, and is represented by $F_1\cos(\omega t)$ and $F_2\cos(\omega t)$.

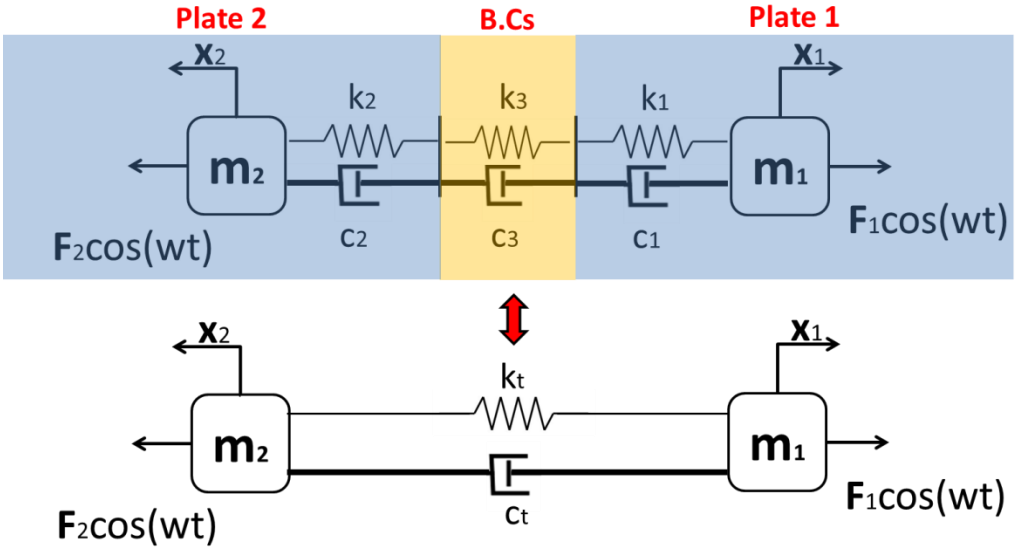

Figure 5.22 Lumped element mechanical model representation of the CNT projector

Additional springs and damper elements can be used to represent the system more accurately, however, the principle of modeling will remain the same. The effective stiffness and damping will finally be expressed by a single damper and single spring element, simply by adding them in series as shown in eq.'s below:

$$\frac{1}{k_t}=\frac{1}{k_1}+\frac{1}{k_2}+\frac{1}{k_3}\Leftrightarrow\frac{1}{c_t}=\frac{1}{c_1}+\frac{1}{c_2}+\frac{1}{c_3} \tag{5.2.1}$$

$$k_t=\frac{k_1k_2k_3}{k_2k_3+k_1k_2+k_1k_2} \tag{5.2.2}$$

$$c_t=\frac{c_1c_2c_3}{c_2c_3+c_1c_2+c_1c_2} \tag{5.2.3}$$

Once the effective stiffness and damping is determined, the equation of motion for the system is expressed as:

$$\begin{aligned}\ddot{m}_1\ddot{x}_1&=F_1-k_t(x_1+x_2)-c_t(\dot{x}_1+\dot{x}_2)\\ \ddot{m}_2\ddot{x}_2&=F_2-k_t(x_1+x_2)-c_t(\dot{x}_1+\dot{x}_2)\end{aligned} \tag{5.2.4}$$

Finally, one way to determine the response of the system is through state space representation of the model and numerically calculating the response using Matlab. The procedure of obtaining the state space matrix for the equations of motion obtained in eq.(5.2.4) is shown below:

$$\begin{bmatrix}x_1\\ \dot{x}_1\\ x_2\\ \dot{x}_2\end{bmatrix}=\begin{bmatrix}x_1\\ x_2\\ x_3\\ x_4\end{bmatrix} \tag{5.2.5}$$

$$\begin{aligned}\dot{x}_1&=x_2\\ \dot{x}_2&=\frac{F_1}{m_1}-\frac{k_t}{m_1}\left(x_1+x_3\right)-\frac{c_t}{m_1}(x_2+x_4)\\ \dot{x}_3&=x_4\\ \dot{x}_4&=\frac{F_2}{m_2}-\frac{k_t}{m_2}\left(x_1+x_3\right)-\frac{c_t}{m_2}(x_2+x_4)\end{aligned} \tag{5.2.6}$$

$$\begin{bmatrix} x_1 \\ \dot{x}_1 \\ x_2 \\ \dot{x}_2 \end{bmatrix} = \begin{bmatrix} 0 & 1 & 0 & 0 \\ -\frac{k_t}{m_1} & -\frac{c_t}{m_1} & -\frac{k_t}{m_1} & -\frac{c_t}{m_1} \\ 0 & 0 & 0 & 1 \\ -\frac{k_t}{m_1} & -\frac{c_t}{m_1} & -\frac{k_t}{m_1} & -\frac{c_t}{m_1} \end{bmatrix} \begin{bmatrix} x_1 \\ x_2 \\ x_3 \\ x_4 \end{bmatrix} + \begin{bmatrix} 0 \\ F_1 \\ 0 \\ F_2 \end{bmatrix} \cos(\omega t) \qquad (5.2.7)$$

An example of the system illustrated in Figure 5.22 for the given values below is shown in Figure 5.23.

$$m_1 = 1kg$$
$$m_2 = 1kg$$
$$k_t = 100N/m$$
$$c_t = 0.7N/m/s$$
$$F_1 = F_2 = 120N$$
$$\omega = \omega_n$$

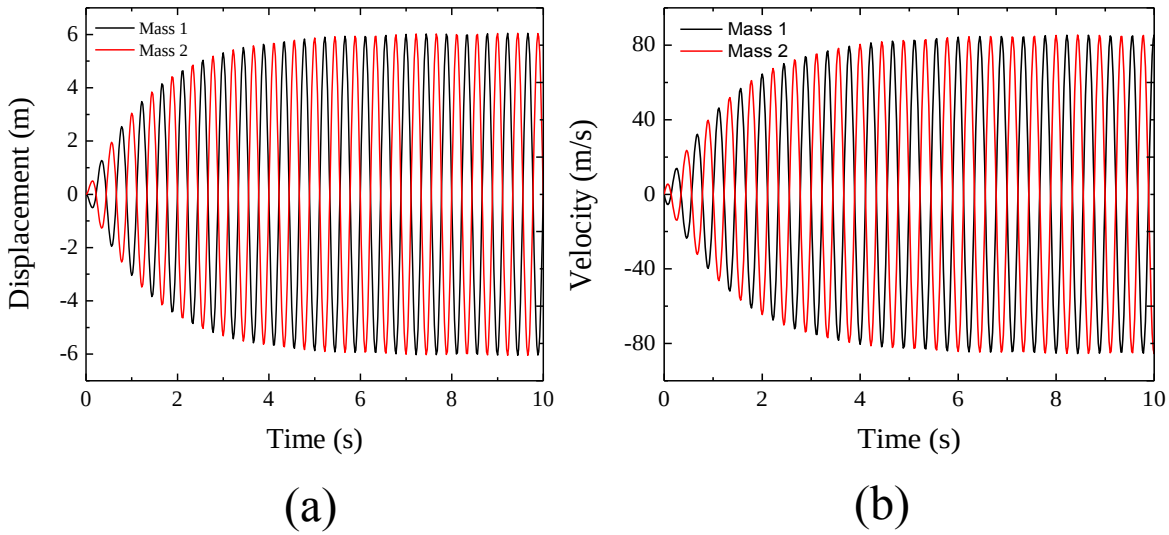

Figure 5.23 Displacement and Velocity as a function of time

.

In addition, parameterization study of the system represented by Figure 5.22 was also conducted in order to determine the response of the system as a function of stiffness. The relationship between the natural frequency and stiffness and amplitude of vibration and natural

frequency are shown in Figure 5.24. In the parameterization study, initial conditions $\begin{bmatrix} x_1 \\ \dot{x}_1 \\ x_2 \\ \dot{x}_2 \end{bmatrix} = \begin{bmatrix} 1 \\ 0 \\ 0 \\ 0 \end{bmatrix}$ were used.

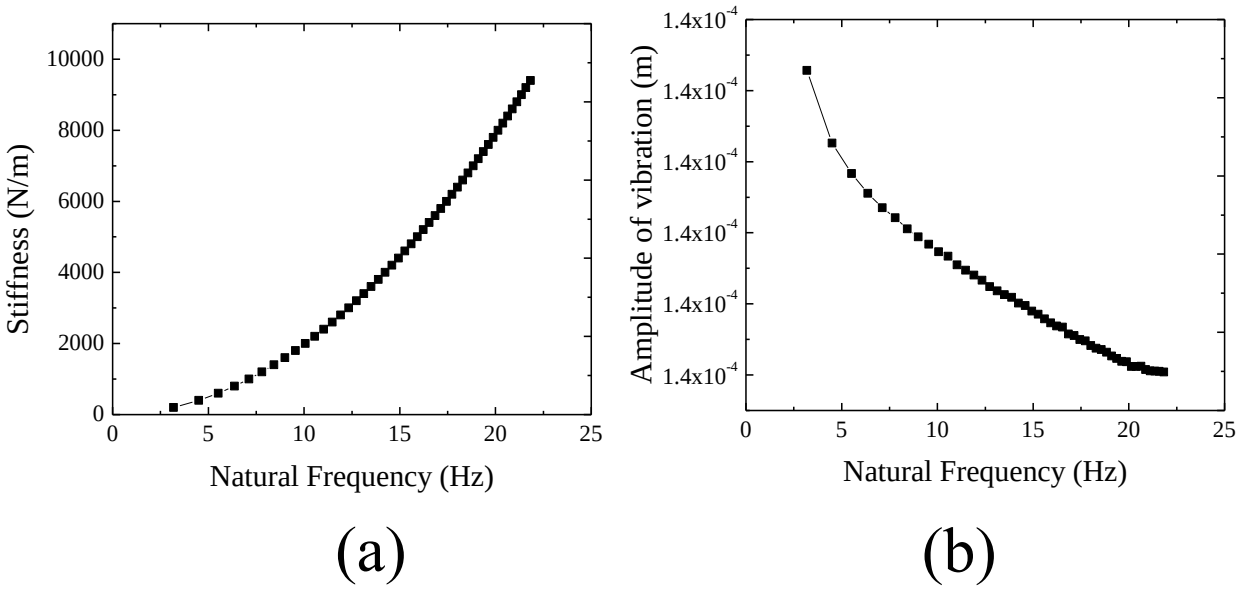

Figure 5.24 (a) Natural frequency as a function of stiffness, (b) Amplitude of vibration as a function of natural frequency

5.3.3 Results and Discussion

One sample device developed by the NanoTech Institute - University of Texas, Dallas is shown in Figure 5.25. The device is composed of three strips of superimposed MWNT sheets suspended between two glass plates (75 x 50x 1mm microscope slides). Elastic silicon rubber strips were used to separate the MWNT sheet from the glass plates. Figure 5.25 presents the overview of devices subjected to different boundary conditions (B.C.). Analysis of the vibration of this device for various B.C. was conducted using a scanning laser vibrometer, Polytec PSV400 (VAST Lab, Virginia Tech).

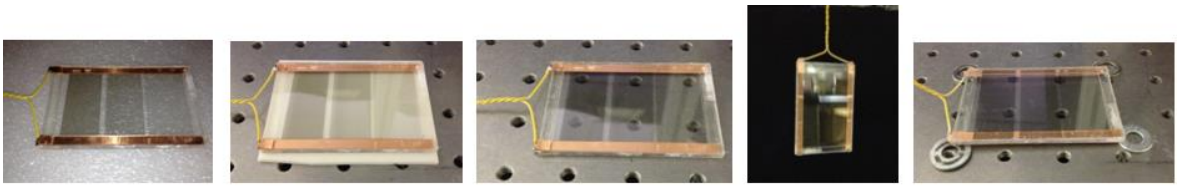

Figure 5.25 Free-Free boundary conditions for vibrational characterization of variable MWNT sheets TA device: a) Soft mat, b) stiff mat, c) table top, d) hanging, e) suspended

Shown in Figure 5.26 is the frequency spectrum (1000Hz – 10000Hz) of the vibrating TA device for different external boundary conditions. The frequencies between the different cases were only slightly different and their magnitudes also varied due to the different damping introduced to the system. As seen in Figure 5.26 (a), the largest amplitudes were derived from the suspended and hanging boundary conditions with fundamental frequencies of 2262.5Hz and 2276.5Hz respectively. Besides the fundamental frequency, the spectrum includes two other resonance frequencies for the device at different boundary conditions. In the case for the suspended boundary condition, these frequencies were found to be 3743Hz and 4945Hz respectively. In addition to the frequency spectrum, Figure 5.26 (b), (c) and (d) show the experimentally observed deflection shapes at these three resonance frequencies.

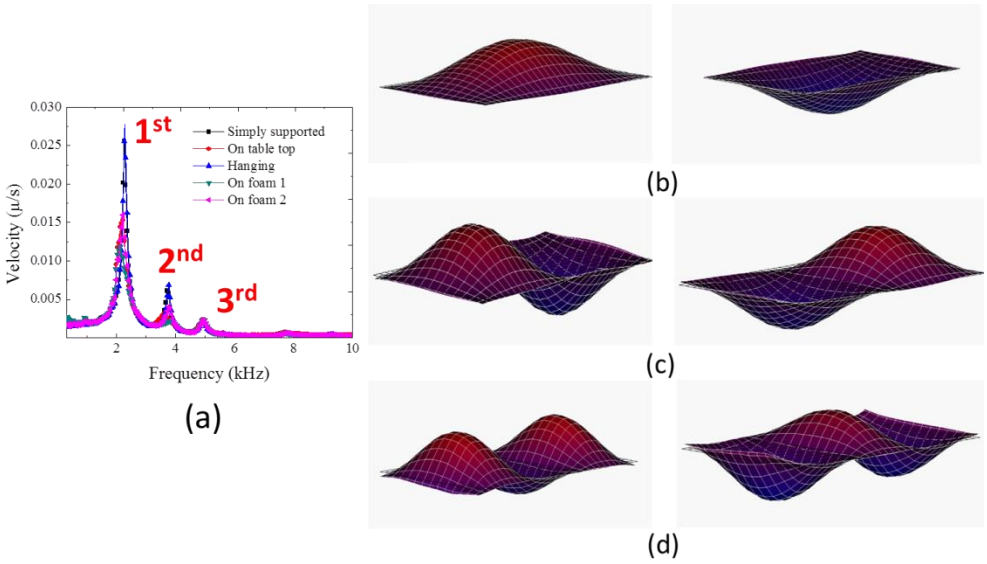

Figure 5.26 Vibration characterization study: a) Frequency response spectrum of TA device based on different free-free boundary conditions, b) 1st Mode Shape, c) 2nd Mode Shape, and d) 3rd Mode Shape.

Through excitation of the TA device at the 1st natural frequency and using the laser vibrometer, it was possible to obtain the velocity of the plate at specific points across the surface, Figure 5.27. By integrating the velocity profile, displacement profile of the TA sample was also obtained. The results presented are for power inputs of 3.7W, while the device was actuated at the 1st resonance frequency.

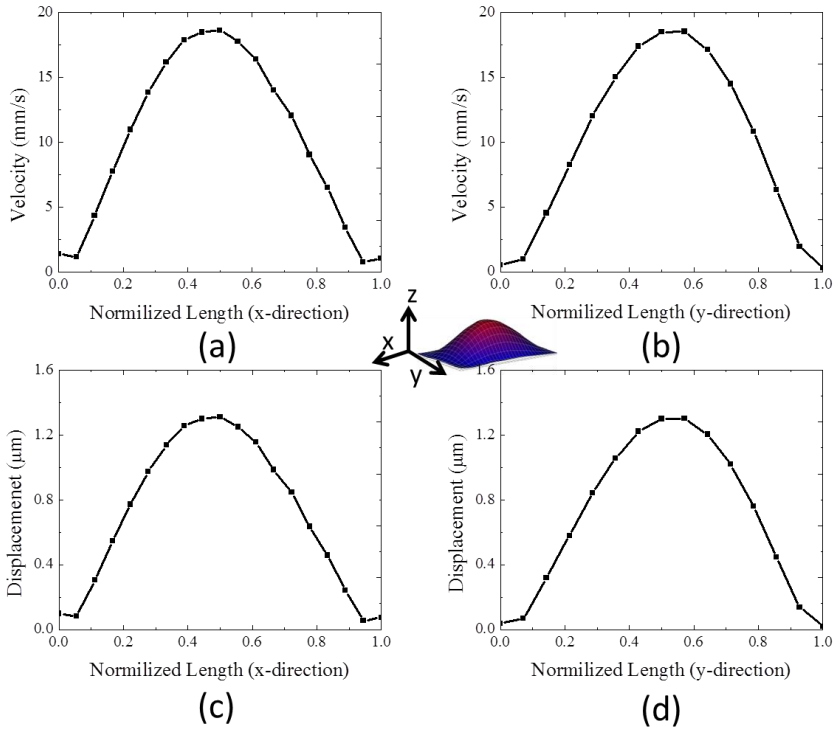

Figure 5.27 Velocities and displacement of TA devices at 1st natural frequency: a) Velocity through the centerline in x direction, b) Velocity through the centerline in y direction, c) Displacement through the centerline in x direction, and b) Displacement through the centerline in y direction.

The results obtained from the experimentail setup in Figure 5.21 are significant because it allows observation of the mode shapes of the different TA projectors. By understanding the mode shapes, at different frequencies an explanation for the intensity of sound can be observed. Actuating the device at the 1st natural frequency, corresponding to the 1st mode shape, would generate the largest sound pressure since the surface being actuated is much larger when compared to the other modeshapes. For example the second modeshape implies that pressure is only generated by ½ of the plate surface. The other ½ is generating sound pressure in the

opposite direction. Since it was found that the 1st mode shape generates the largest sound pressure, the following step was optimization of the structure through amplification of the bending mode of the walls of the TA. Accordingly, the interior boundary conditions were altered by changing the compliance of the device.

Five rectangular TA projectors consititng of a single CNT sheet layer were developed by (University of Texas, Dallas). The only difference between the samples were that each had different compliance properties. The schematic diagram of the projector is shown in Figure 5.28 (a). To control the distance between CNT sheet and the glass plates, elastic rubber strips (spacers) were used with varying width. This allowed variation in the compliance, where the compliance is inversely proportional to the width of the spacers. For symmetry the same elastic strips were attached to the opposite glass as well.

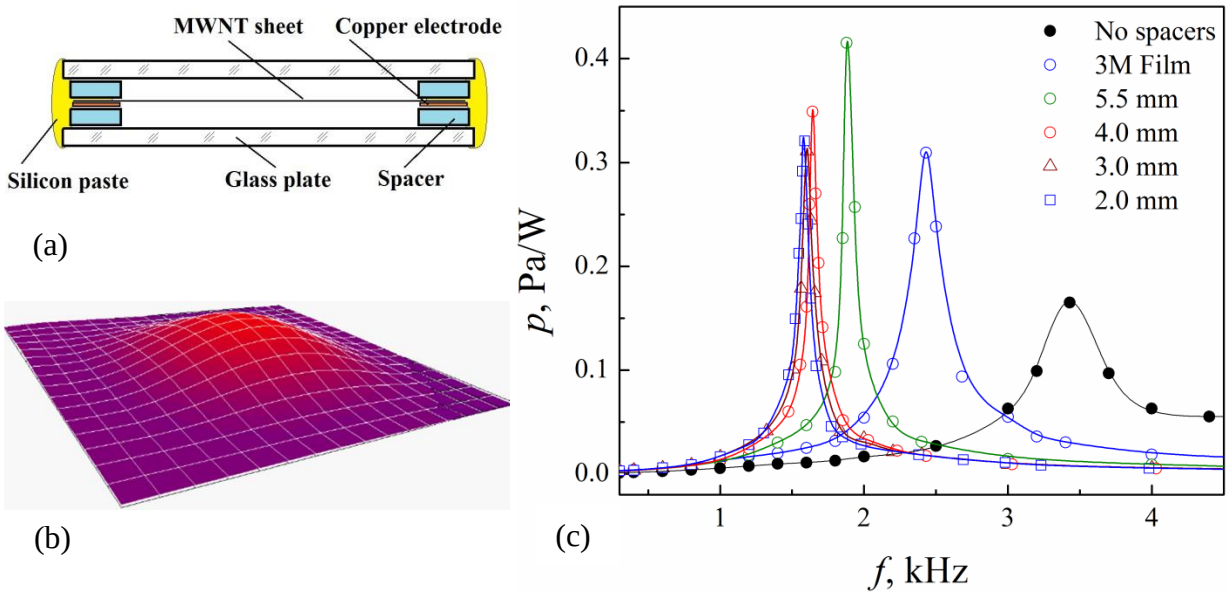

Figure 5.28 (a) Schematic diagram of the TA projector comprising free-standing MWNT sheet suspended between two soda-lime glass plates (1x50x75 cm3 Corning microscope slides). (b) The typical image of the plate displacement at first harmonic taken by scanning laser vibrometer Polytec PSV400. (c) The sound pressure spectra of several TA projector comprising single MWNT sheet suspended between two glass plates. The spectra were taken in the near field (r=3 cm) in air.

Accordingly, the device were characterized using the laser vibrometer experiment setup previously discussed. The results are shown in Figure 5.29 where the velocity and displacement profiles for the different samples are presented. As can be seen in Figure 5.29 (e) the internal

boundary conditions changed from C-C-C-C (No spacers) to S-S-S-S (3mm). As a result the displacement and velocity curves were much larger for the S-S-S-S boundary conditions.

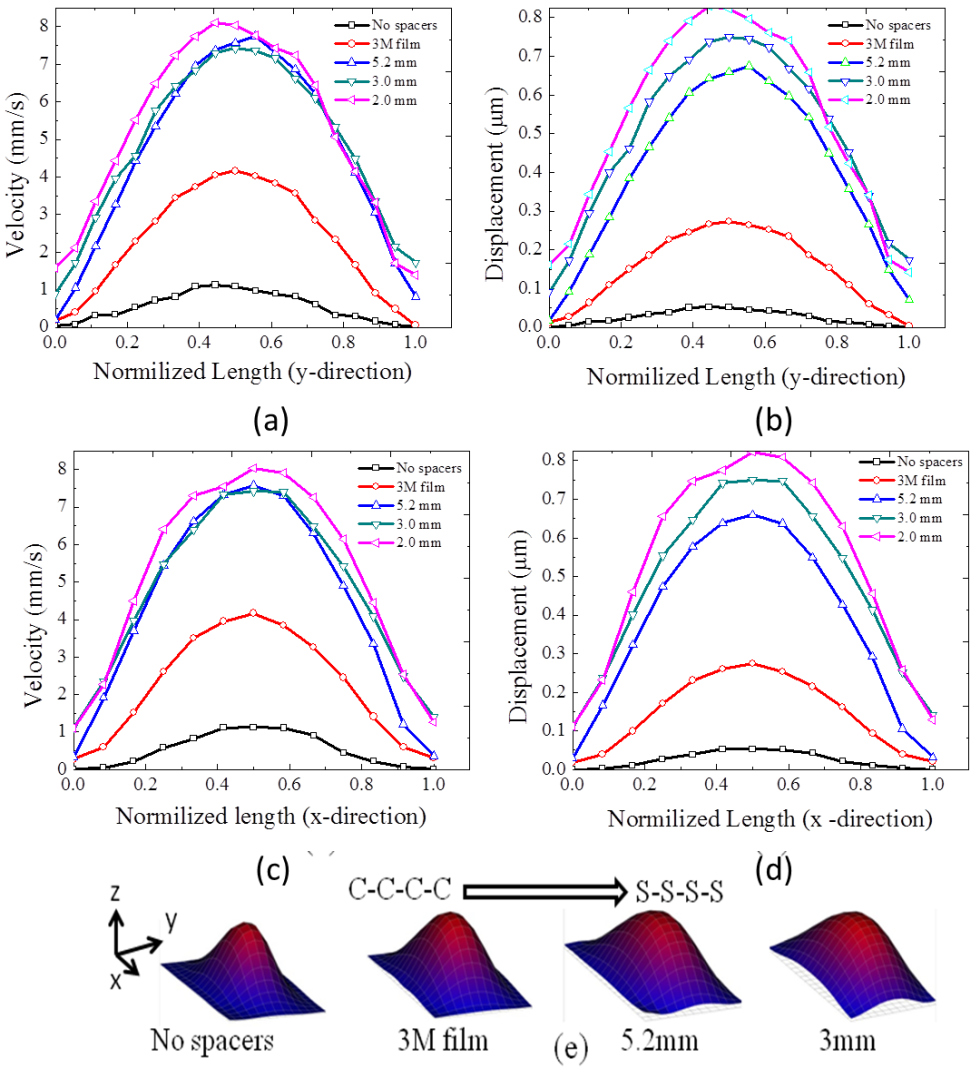

Figure 5.29 Vibration summary results of TA device with different compliance: (a) velocity profile in x direction, (b) velocity profile in y direction (c) displacement profile in x - direction, (d) displacement profile in y direction, (e) 3-D profile for different compliance designs. (C-C-C-C corresponds to clamped conditions around the four edges, S-S-S-S corresponds to simply supported conditions around the four edges)

Besides dynamical characterization, thermal test on the TA device was also conducted using IR camera. The device used in this experiment and the temperature profiles are presented in Figure 5.30. Moreover a representation of the temperature distribution across the plate at different applied powers and time steps is presented in Figure 5.31 (a) and (b). The clear distinction between the temperature profile across the three layers, two layer and single layer

segment is evident. These results are quite interesting and useful, because the data obtained shows the evident distinction between the layers which in reality is not due to temperature, but rather black body emissivity. The emissivity is a function of density which is a function of number of MWNT sheets. Therefore it is possible in future studies to estimate the emissivity of the CNT sheets and by doing that to estimate the real temperature of the carbon nanotubes. Nevertheless the Figure 5.31 (a) and (b) clearly illustrates that the temperature increases proportional with power and time. On the other side Figure 5.31(c) shows the cooling profile of the TA device due to the free convection at room temperature. The device was heated until it reached a stable temperature of 75°C, followed by a period of cooling which was 6 min. In addition to this study, expanding this experiment in order to obtain data which will extract fundamental information on the heat transfer, temperature distribution, device thermal failure and other relevant coefficients will be conducted in future study.

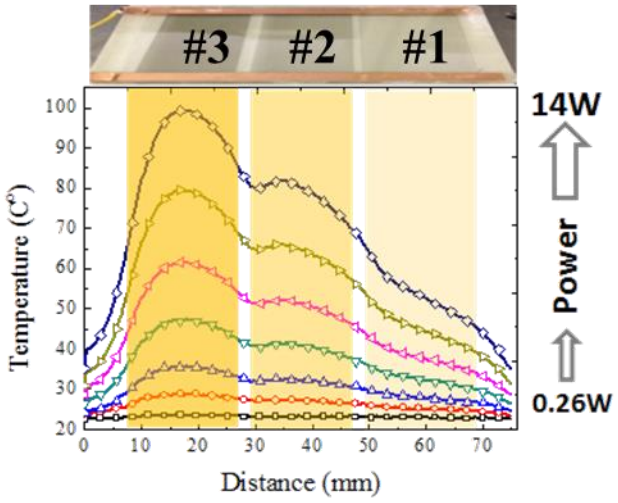

Figure 5.30 Temperature profile of TA device with three different sections, three layers, two layers and single layer of CNT sheets

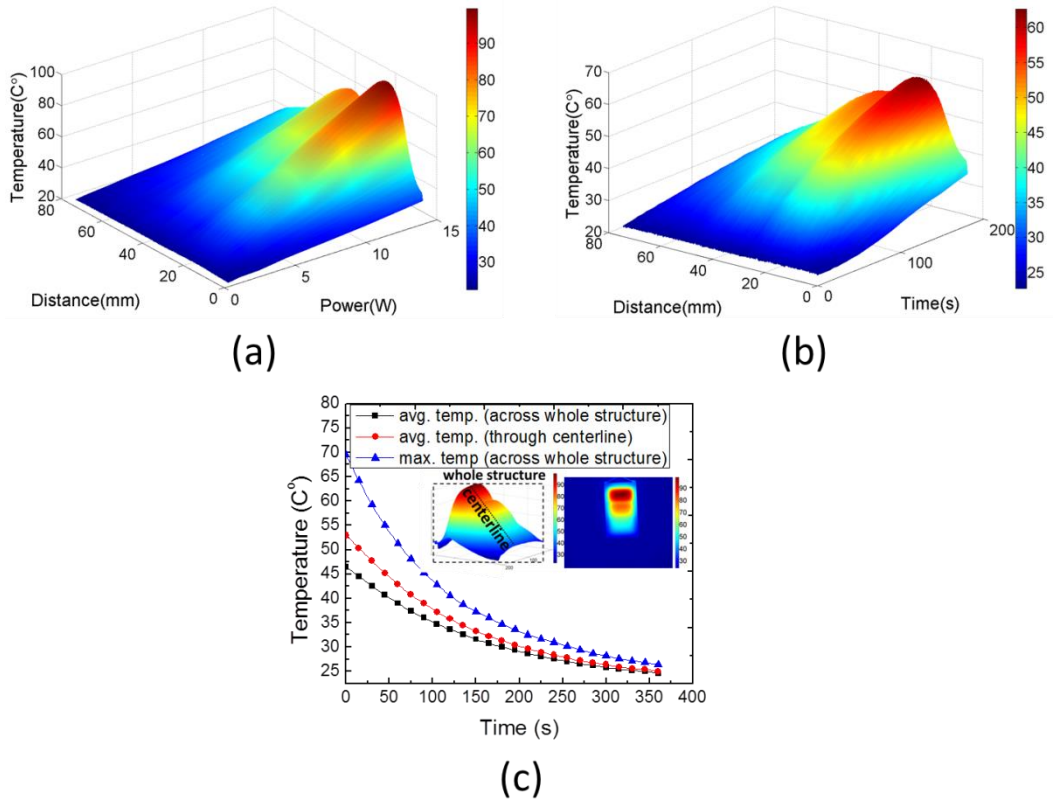

Figure 5.31 Experimental results on the thermal characteristics of TA device: a) Temperature profile through the center line over TA device for different power levels at 60sec time interval, b) Temperature profile through the center line of TA device as a function of time at 3.7W power input, and c) Cooling profile of TA device

5.3.4 Conclusion

The vibration of plates which is due to the alternating thermal pressure is desirable for effective acoustical waves. This can be achieved if the resonance frequency of the vibrating plate is exhibiting the first mode shape as it resembles a piston-like parallel motion. In order to achieve this motion, spacers with different widths were integrated in the device in order to change the boundary conditions from CCCC to SSSS. By having SSSS, higher quality factor and larger velocities could be obtained which are directly proportional to the acoustic power out. A detailed vibrational study has been conducted on these devices and the results have been presented in this dissertation. Moreover, the thermal dependence as a function of both power and time has been investigated. Even through the work on the CNT thermo-acoustic sonar is preliminary, the study has demonstrated the capabilities of these devices to produce sound.

Chapter 6 –Conclusions and Future Studies

6.1 Summary and Conclusion

This work has resulted in technological advances that will facilitate the development of an intelligent healthcare environment. The focus areas of the research were locomotion mechanisms for wireless capsule endoscopes, multifunctional image guided surgical platform (MIGS), miniature shape memory alloy heat engine for powering wireless sensor nodes and thermo acoustic projectors using CNT sheets. Two different categories of locomotion mechanisms for WCEs were developed, legged and body type, both influenced by the traveling wave phenomenon. Chapters 2 and 3, described the locomotion mechanism and details of the study conducted on the characterization of the L-Shape and U-Shape piezoelectric actuators used in the legged type mechanisms. In-depth theoretical analysis was conducted on the L-Shape piezoelectric motor that also applied towards the U-Shape piezoelectric motor. The theoretical analysis guided the experimental work and the results were used to validate the distributed parameter and FEM models. The characterization of the L-Shape and U-Shape piezoelectric motor was conducted in terms of the torques, velocities and efficiencies. Lastly, the actuators were integrated in a pattern that represented the first step towards the development of a legged locomotion mechanism for WCEs. Millipede-inspired crawling robots whose leg motion exhibits propagating wave motion were developed and the locomotion characteristics were quantified. The study presented the potential for the milibots to be used in the future locomotion mechanisms for medical applications. Besides the legged type locomotion mechanism, non-legged type locomotion mechanism was also pursued and details were discussed in Chapter 4. Chapter 4 included the fundamental analysis on the development of a novel WCE propulsion mechanism that utilizes the traveling wave phenomenon. By inducing traveling waves onto a beam structure, a concept for a future WCEs design was developed. In this dissertation, study on the free-free beam was used as a model to understand the traveling wave formation and their classifications. A theoretical study using distributed parameter model was conducted along with the experimental validation that provides insight in the dynamics of the traveling waves on a free-free beam.

Chapter 5 provides the description of the other critical components required for the implementation of the intelligent health care environment. These components include the MIGS

platform, the thermal energy harvester and the thermo-acoustic sonars. The MIGS platform required the scanning and positioning stage that had desired resolution, scanning velocities and dimensions. In order to meet the requirements of the three axis scanning and positioning stage, a novel design was developed that utilized only two actuators to achieve the three axis positioning. The capability of the stage was demonstrated by developing a scanning system that created the high precision patterns. Energy harvesting capabilities are required for powering the sensor nodes that are embedded in the nursing room. These sensors provide important feedback for the automation control algorithms. A miniature shape memory alloy heat engine was proposed and developed for powering the wireless sensor nodes since hot water pipes are part of the infrastructure. It was demonstrated that the harvester can wirelessly power a temperature sensor node. Lastly, a thermo-acoustic device was developed with the potential to be used as a communication element between the implantable sensors. Two parameters: vibration and temperature play an important role in maturing the acoustics. Correspondingly vibration and thermal studies were conducted in order to characterize the device and establish a baseline for future design of CNT inspired thermo-acoustic sonars.

6.2 Future Studies

Legged locomotion mechanism –L-Shape or U-Shape based locomotion mechanisms require miniaturization of the actuators in order to fit on the capsule size platform. Since a detailed theoretical and parametric study has already been conducted and the vibrational characteristics and geometrical requirement are already known, the next step would be to develop fabrication approaches for miniature piezoelectric bimorphs and their assembly within the given fixture. One question that remains open is whether the legged mechanism can anchor itself inside the GI tract in order to resist the peristaltic force.

The inside of the GI tract from the esophagus to the rectum represents a very challenging area in terms of maneuverability. The channels vary in size and shape across the length. Further, surface roughness, elasticity and softness also vary along the length. The difficulty in having a generic solution for a WCE lies in anchoring of the device to a particular section inside the GI tract. Internally guided capsules using crawling motion to propel through the GI tract have not had much success with the exception of one particular study reported in Ref. [44],[43]. In that study, authors were able to integrate the Gecko inspired technology of dry micro patterned

adhesives to the legs of a wireless capsule. Because of the presence of the micro patterned adhesives, the authors were able to demonstrate anchoring capabilities on porcine small intestines.

An alternative approach to the previously mentioned anchoring mechanism was also explored and this method can be integrated directly onto the legs of the WCE robot. It works on the same principle as a common syringe.Figure 6.1 shows an illustration of a syringe that is used to create suction and lift an object. Through small volume change inside the tube a vacuum is created that is strong enough to hold the piece of Dragon skin. Similar idea can be used on a small scale where multiple syringes like elements are integrated onto the WCE robot presented in this dissertation, Figure 6.2. They can be used to grab onto the walls of the GI tract through suction. Since the development of the robot is on a millimeter scale, these suction elements will be developed using MEMS fabrication procedures. As illustrated in the figure, the plunger will be moved by a piezoelectric element with the indicated clamping conditions. When voltage is applied to the piezoelectric element, strain is generated which pulls the plunger upward, as shown in the figure. This motion contributes to a volume change inside the tube which translates to a vacuum being created at an instant when the legs of the WCE are in contact with the walls of the GI tract. Having generated suction, higher friction between the legs of the robot and the GI tract walls can be achieved which will normally happen if the piezoelectric element is actuated in correlation with the L-Shaped piezoelectric motor. As long as voltage is being supplied to the piezoelectric element, the vacuum will be present and the capsule will remain anchored. When compared to other methods, suction can potentially create an efficient, coordinated and safe way to anchor the capsule without scarring the GI lumen.

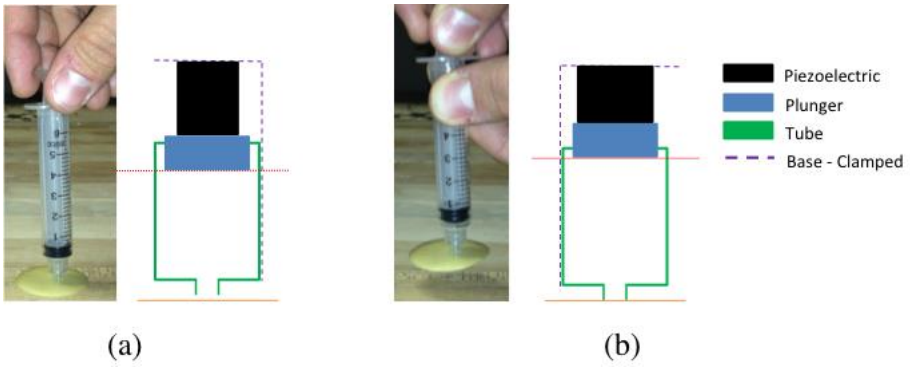

Figure 6.1 Suction mechanism: (a) Initial state, (b) Suction

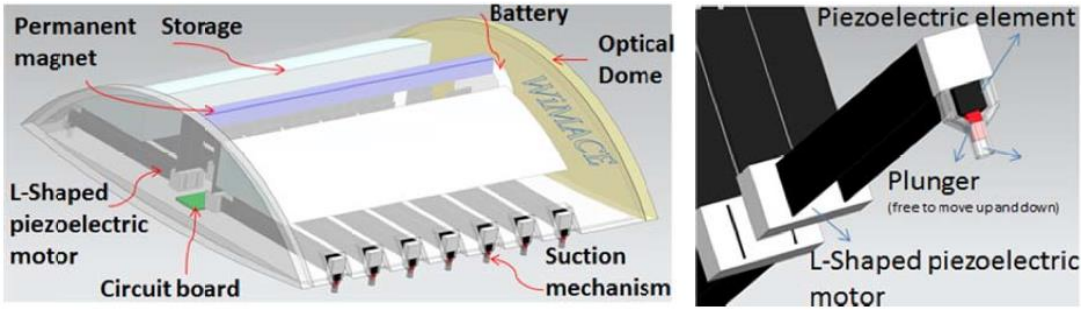

Figure 6.2 Design of a L-Shape actuator driven capsule with a suction mechanism

In case of the legged locomotion mechanisms (Chapters 2,3), the main challenge is to truly understand the biology behind the millipedes and/or centipedes and use that as advantage in development of a future locomotion mechanism for WCE. Understanding the muscle activity and corresponding motion of the millipede tentacles is a promising approach towards achieving this goal. Once the muscle activity is understood, actuators can be developed and implemented onto a locomotion mechanism.

Traveling wave (TW) inspired locomotion mechanism: Since the guideline for TW generation has already been established and detailed work on TW characterization has been achieved (Chapter 4), moving forward with a cylindrical design requires only reusing the existing FEM model with appropriate parameters. An experimental setup similar to the one shown in Chapter 4 can be used to validate the results. One question that might arise is whether the deflection of the structure as the traveling waves propagate is sufficient to achieve propulsion inside the GI tract.

Utilizing the already developed modeling technique developed both through FEM and distributed parameter, it is possible to conduct parametric study based on the geometrical constraints and material properties. Correspondingly, low thickness, high flexibility material will allow larger amplitudes. Moreover, the velocity of the capsule is highly dependent on the frequency of excitation, where higher the frequency higher is the velocity. This is because the traveling wave generated at higher frequencies results with larger contact surface areas which contributes towards faster motion.

Since steering inside the GI tract is desired capability and it can allow camera to focus on to specific areas of interest, the concept of the WCE presented in Chapter 4, would need to be modified. The concept described in Figure 4.2, uses piezoelectric disks placed at both ends of the cylinder. Due to the radial straining of the piezoelectric disks, equal force is distributed along the

circumference of the cylinder. This would correspondingly generate traveling waves with equal amplitudes around the circumference and thus allow propulsion in either forward or reverse direction. A prototype of the concept has already been developed and tests are going to be conducted in immediate future. Shown in Figure 6.3 are experimental prototypes of the locomotion mechanism. Preliminary results on the free-free beam have indicated propulsion using the TW phenomenon. The piezoelectric beam in Figure 6.3 (a) was excited at a frequency which was between two natural frequencies with a phase difference of 90°. The result was forward propulsion with velocities ≈5cm/s without any optimization of the contact surface interaction, geometry and/or material properties of the beam. In future studies, similar analysis to the one conducted and presented here will be obtained for a cylinder shape device (30mmx12mm).

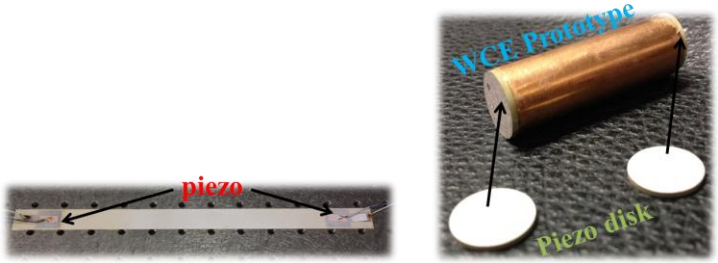

Figure 6.3 Prototypes of traveling wave inspired locomotion mechanisms: (a) free-free beam, (b) wireless capsule endoscope

In order to achieve steering, a slightly different version of the WCE design is necessary. The concept described in Figure 6.4 shows that instead of piezoelectric disks, piezo patches positioned along the circumference of the WCE will produce traveling waves if actuated according to the guidelines specified in Chapter 4. Micro fiber composite (MFC) patches can be used as actuation elements due to their flexibility and large strain output compared to traditional ceramic PZTs. It should be noted that there are two sets of four piezoelectric elements. Each set is located at one end of the cylinder, where the patches are evenly distributed around the circumference of the cylinder. As the piezoelectric elements are actuated, the strain is transferred to the capsule shell, and by following specific excitation sequence, a traveling wave is generated. Steering for this concept can be achieved by simply delivering higher voltage potential to one set of piezoelectric elements over the others. This is because control over the traveling waves along

the cylinder can be obtained through selective frequency and voltage inputs to individual piezo elements.

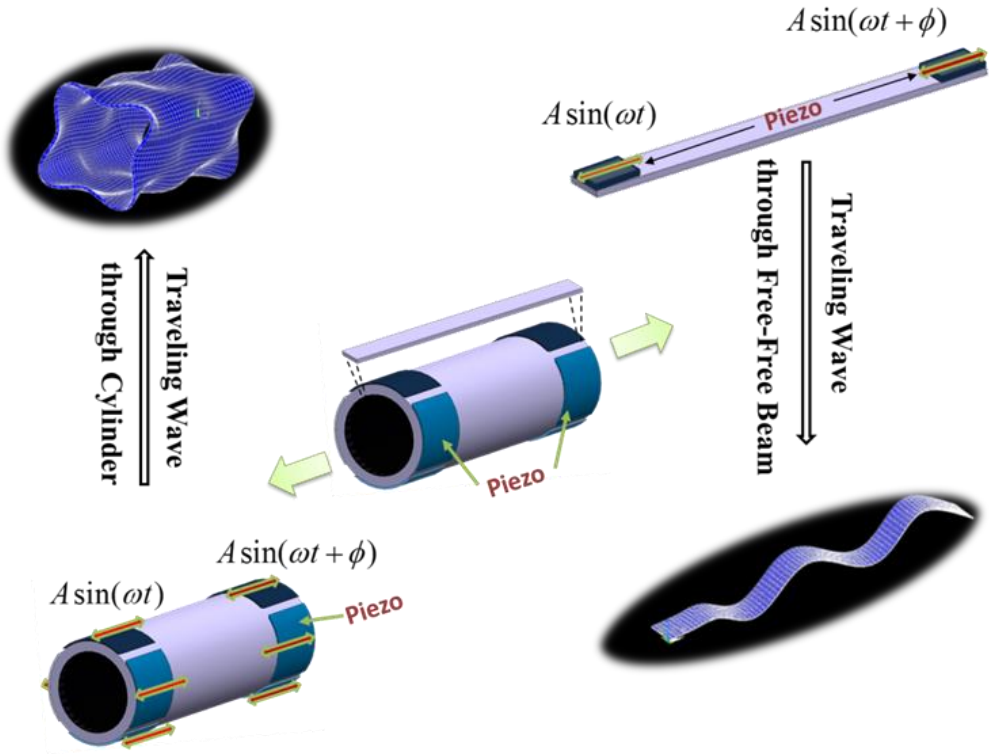

Figure 6.4 Alternative concept of the one presented in Figure 4.2, Chapter 4.

Multifunctional Image Guided Surgical Platform (Chapter 5.1) **-** The initial requirements for the development of a high precision platform with resolution<5μm, velocities greater than 40mm/s and scanning area in the range of 10x10x10mm were rather challenging tasks. There are many three axis scanning and positioning stages on the market that can meet these requirement, nevertheless their size is simply too large for the intended applications. Accordingly, as described in Chapter 5.1, platform that met all the requirements was developed from a concept and 3-d design in NX Unigraphics, to fully operational prototype. The size of the device even though very competitive, when compared to commercial products, still requires scaling. With the development of the L-Shape and U-Shape piezoelectric actuators and the traveling wave inspired mechanisms, the potential to bring the size down while meeting all the key requirements is quite possible.

One important task that remains unsolved and is the first immediate future step for the scanning stage is conducting tests on biological tissue. So far only a mock-up OCT probe has

been used to validate the operational characteristics of the platform. Testing will be conducted once the OCT probe and the laser scalpel are fully developed and operational (Collaborators from University of Texas – Arlington are addressing these aspects). By simply placing the OCT and laser scalpel at the designated place on the three axis scanning and positioning stage presented in Chapter 5.1 and controlling the motion of the stage (already accomplished), 3-D image of the tissue topography will be identified. This remaining test will complete the MIGS device and demonstrate the capability and advantages of this ex-vivo imaging medical technology.

Thermal energy harvester (Chapter 5.2) has demonstrated the capability to extract heat and generate enough electrical energy to power the wireless sensor node. Nevertheless the demand for power is much greater than a single sensor. As discussed in Chapter 1, wireless sensor networks are going to become essential in intelligent health care environment. Numerous networks will be required to provide the continuous monitoring of the medical environment, and this will require significant amounts of power. As a result there are few future steps that are necessary to be investigated before the thermal energy harvester can be integrated in hospitals.

The first step towards this objective is identifying the strain/force relationship of market available SMA wires and their integration onto a pulley design. Understanding the kinematics of the pulley design as a function of force and strain is the first step in optimization of the SMA energy harvester. The more challenging aspect is creating a model that will take into account the thermal input, which is required to strain the SMA wire and correspondingly actuate the pulley mechanism. In trying to determine how temperature affects the system and how much heat is actually required for the system to operate, efficiency of the system can be calculated. This approach will require a coupled thermo-mechanical model of the shape memory alloy which needs to be addressed. The study presented in Chapter 5.2 demonstrated the capability of the energy harvesting device for water as a source of heat. An alternative and a more realistic application is to have the harvester attached directly to a hot water pipe from which it will absorb the wasted heat and convert it to electrical energy. Achieving actuation of the SMA mechanism through solid-solid conduction has already been achieved in the lab. Nevertheless, characterization of the system for its performance in terms of velocity, temperature and power generation needs to be next pursued. It is important that a heat transfer conduction model is developed in order to assist with the future design. The results for the SMA thermal engine

presented in Chapter 5.2 used a micro-electrical generator which was not optimized for the velocity at which the pulley mechanism operated. In the case of the micro-generator the operation velocities could go up to 4000 rev/min. At this rotational velocity, the power generated by the generator was 257mW, while at only 400RPM this power was as low as 1.7mW.

In order to increase the power output by the thermal generator, the velocity at which the generator turns has to increase. Correspondingly, planetary gear set, with appropriate gear ratio can be integrated to achieve such speeds. Since increase in velocity through gear train requires higher torque, multiple SMA wires can be integrated onto the pulley mechanism, which will contribute towards this objective. Finally, improving the capabilities of the SMA wire can also be achieved, and its temperature dependence fixed accordingly. For an equiatomic Ni-Ti alloy, replacing nickel with 10 at% copper reduces the thermal hysteresis by 50% or more, [125]. For Ni- Ti alloys with nickel content greater than 50 at%, transition temperature decreases linearly at a rate of 100 °C/Ni at%. What this means is that, if Cu is added, than the hysteresis loop of the SMA wire will reduce or increase and respectively will make the actuation response of the SMA either faster or slower, respectively. On the other side if the Ni content is greater than the phase temperature of the SMA reduces and correspondingly the operation temperature drops, which will allow the system to run not only at temperatures around 70°C, but much lower temperatures as well.

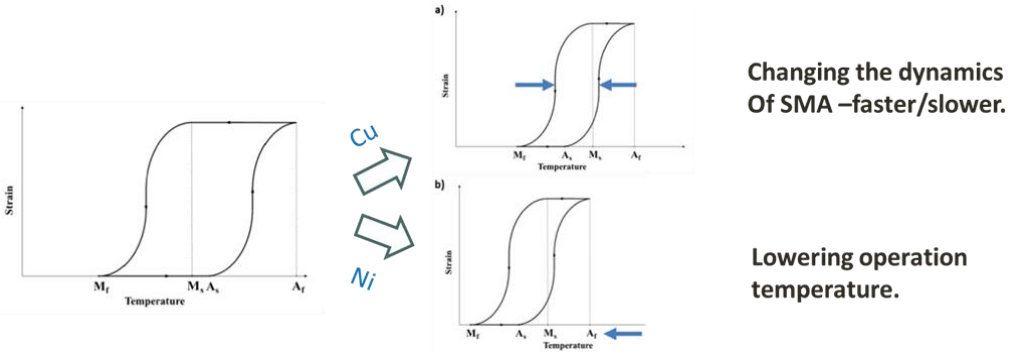

Figure 6.5 Altering the properties of SMA in order to change the dynamics of the system

Thermo-acoustic projectors-In future the CNT thermo-acoustic sonar can further be miniaturized in order to be implanted inside the body and act as a communication device between sensors. Accordingly, it is first necessary that acoustic wave propagation through human body and/or human body to outside body environment is addressed and understood. Some

immediate steps scheduled to take place near future is further testing and characterization of the CNT projector in water environment. Since the pressure increases with water depth, loading effects will have an impact on the response of the device. This will affect both the resonance frequency of the system as well as sound propagation. That is why it is important that both theoretical and experimental model of the CNT is generated and validated. Accordingly, measurement of sound pressure underwater at different depths (0-2m) in a water tank at the BMDL lab at Virginia Tech will be conducted. Both the loading effect for different plate thicknesses: the frequency shift and quality factor under water will be measured. The tests will be conducted at different power levels. Laser scanning vibrometer similar to the setup presented in Chapter 5.3 will be used in order to obtain the response of the system (velocity).

Particle Image Velicometry (PIV) and Particle Image Thermography (PIT) will be performed in air in order to understand the dynamics of the argon particles (medium of enclosed CNT sheets) as a function of the thermal pressure generated. Knowing this, better understanding of the thermal characteristics of the projector will be established, which will contribute to a more compliant, higher efficient device. Once this is achieved an equivalent circuit model, which will couple the electrical, thermal and mechanical theoretical models will be established in order to represent the complete CNT projector. This will be achieved after developing individual, thermal, electrical and mechanical models.

Finally, one area worth investigating would be to use the thermo-acoustic speakers as a replacement to the piezoelectric disks in the traveling wave inspired WCE (Chapter 4). Due to the thermal → vibration→ sound capability of the thermo acoustic device, the potential to generate traveling waves through the body of the capsule while emitting sound is definitely possible.

Appendix A. Remote light energy harvesting and actuation using shape memory alloy – piezoelectric hybrid transducer[5]

Shape Memory Alloys (SMAs) exhibit memory effect which causes the alloy to return to its original shape when heated beyond the transformation temperature. In this study, it is shown that SMA can be heated remotely by laser and the resulting deformation can be converted into electricity through piezoelectric bimorph. In addition, the laser actuated SMA deformation can also be used to provide controlled actuation. Experimental results were provided demonstrating both the power harvesting and actuation behavior as a function of laser pulse rate. SMA used in this study exhibited higher absorption in the ultra violet region which progressively decreased as the absorption wavelength increased. Raman analysis revealed TiO_2 formation on the surface of SMA, whose concentration increased irreversibly with temperature. Negligible changes in the surface oxidation were detected in the working temperature range (<150 ^{o}C).

A.1 Introduction

Shape Memory Alloys (SMAs) have the ability to recover their shape when heated that results in transformation from the martensite to austenite phase. The work conducted by the SMA during transformation upon heating has been utilized in many actuators and sensing applications including robotics, aircraft wing morphing, medical devices etc.[112, 113, 115, 116, 128-130]. Conventionally, heating of SMAs has been achieved by resistive joule heating. However, this method could be cumbersome in certain actuation applications as it requires extensive wiring and electronics to achieve the nonlinear control of deformation. In applications where large power supplies cannot be incorporated on-board, the requirement of high current flow becomes a limitation for SMA. An effective alternative to resistive heating will be a non-contact method such as a light beam to heat the SMA. The light intensity and wavelength can be tailored from a remote location to modulate the temperature distribution and hence actuation characteristics of SMA. In this study a description of a breakthrough in this direction as well as laser actuation characterization of SMA is provided. A limited number of studies on laser

[5] Some of the work discussed in Appendix A was published in IOP Smart Materials and Structures. The citation is below:

- Avirovik, D., Kumar, A., Bodnar, R. J., Priya S., "Remote light energy harvesting and actuation using shape memory alloy—piezoelectric hybrid transducer," Smart Materials and Structures, 22, 052001, (2013)

actuated SMA have been reported in literature,[46, 131] and none have proposed the structure that couples SMA with piezoelectric bimorph in a hybrid configuration. This hybrid configuration opens the possibility of designing remote light energy harvesting and actuation systems.

A.2 Design concept and experimental setup

Presented in Figure A.1 (a) is a schematic description of the remote light energy harvesting and actuation hybrid system. It is composed of a piezoelectric bimorph in cantilever beam configuration, SMA wire attached to the beam at three different locations, and a laser. Depending on the attachment location, the response of the system was found to vary. Figure A.1 (b) and (c) illustrate three distinct relationships used to characterize the system. The typical hysteresis loop (Figure A.1 (b)) describes the relationship between strain and temperature, where temperature is a function of time over which the wire was exposed to laser light. As the temperature of the SMA wire increases, strain in the SMA is generated and consequently transferred to the piezoelectric bimorph. This transfer of energy can be seen through the time dependent displacement plot (Figure A.1 (c)). The deflection of the piezoelectric bimorph results in generation of electrical charge which can be harvested and stored.

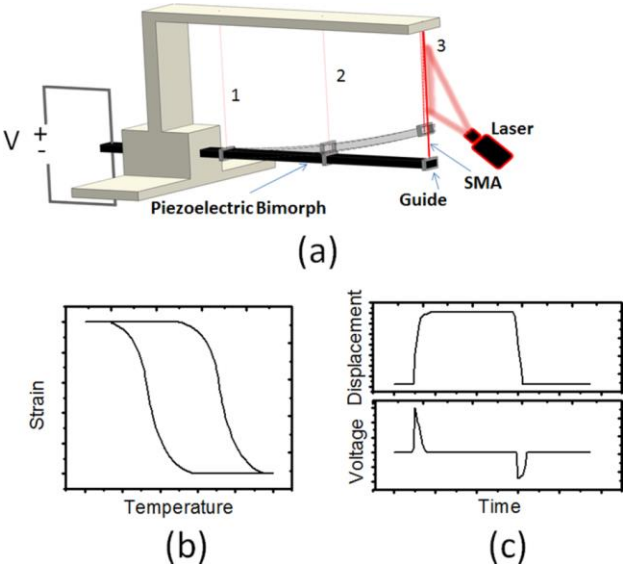

Figure A.1 Schematic representation of system: (a) Piezoelectric bimorph in a cantilever beam configuration in non-deformed and deformed shape as a result of SMA wire actuation, (b) Hysteresis loop of SMA, (c) Voltage generated by the piezoelectric bimorph and tip deflection of cantilever beam.

The hybrid system was characterized using the experimental setup shown in Figure A.2. A piezoelectric bimorph (APC International, 40-2030) arranged in a cantilever configuration as illustrated in Figure A.1 was coupled with a SMA wire of diameter 100 µm. In order to control the pre-load, the SMA wire was directly attached to a load cell (Transducer Techniques, GSO-100) which was then attached to a positioning stage. As the stage translated, the preload on the SMA changed. The input to the system was provided through an 808 nm laser diode. Because the laser diode was continuous, a shutter mechanism was constructed to pulse the laser beam directed onto the SMA. The following output signals were acquired: temperature of SMA wire measured using a K-type thermocouple (Omega Engineering Inc., CHAL-002), force generated by SMA wire using the load cell, displacement of piezoelectric bimorph at the tip measured using a laser displacement sensor (MTI Instruments, LTC-050-20) and voltage measured across varying resistance. All the data were acquired using the adequate modules (NI9219, NI9215, NI9211and cRIO9074) and processed in Labview.

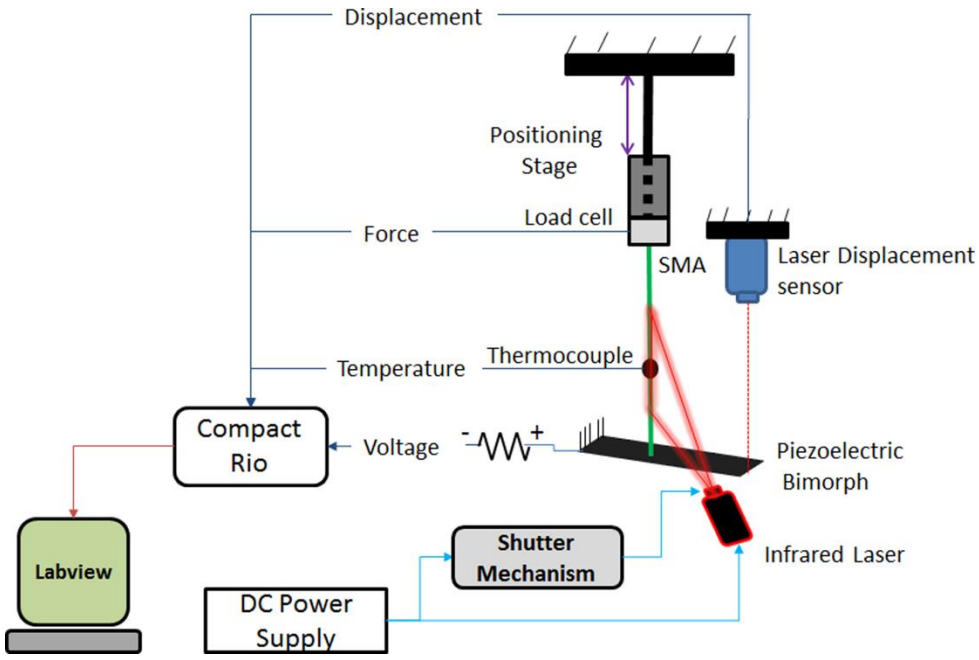

Figure A.2 Experimental setup used in this study

A.3 Hybrid system characterization study

By focusing the laser beam onto the SMA wire, the direct relationship between temperature and displacement, and temperature and force can be achieved. As discussed previously, these relationships can be represented by hysteresis loops shown in Figure A.3(a). The data shown in this figure correspond to inner hysteresis loops due to the fact that SMA wire was only heated to

110°C. If higher temperature along the SMA wire was achieved as well as forced convection cooling was applied, the hysteresis loop would have resembled Figure A.1 (b). To note it was assumed that only the portion of the wire exposed to the laser beam (≈ 50% of the SMA wire total length) was at 110°C. The temperature distribution along the remaining portion of the wire is dependent on the heat transfer coefficient which was obtained through a lumped capacitance model, [132] as shown in Figure A.3(b). The experimental value was compared to the lumped capacitance model using the heat transfer equation[133] given by Eq. (B.7):

$$\dot{T} = hA_s\left(T - T_\infty\right) / \rho vc \tag{B.7}$$

where h is the heat transfer coefficient, A_s is the surface area of the SMA wire, T is the temperature of the SMA wire, T_∞ is the ambient/room temperature, ρ is the density of the SMA wire, v is volume and c is the heat capacity. In our case, a constant convective heat transfer was assumed which simplifies Eq. (1) to Eq. (B.7):

$$T = T_\infty + (T_i - T_\infty)e^{-\lambda t} \tag{B.7}$$

where T_i is the initial temperature of the SMA wire, t is time, and λ is expressed through Eq. (B.7) as:

$$\lambda = \frac{A_s h}{\rho vc} \tag{B.7}$$

Figure A.3(c) shows the output signals for temperature, tip displacement, voltage and load as a function of time. All of the data presented in this figure were obtained at 0.05Hz pulsating signal and SMA attachment point at location 1 after eight cycles (Figure A.1 (a)). The performance characteristics of SMA are related to the preload, however the performance of our system is related to the location where the SMA is attached to the piezoelectric bimorph.

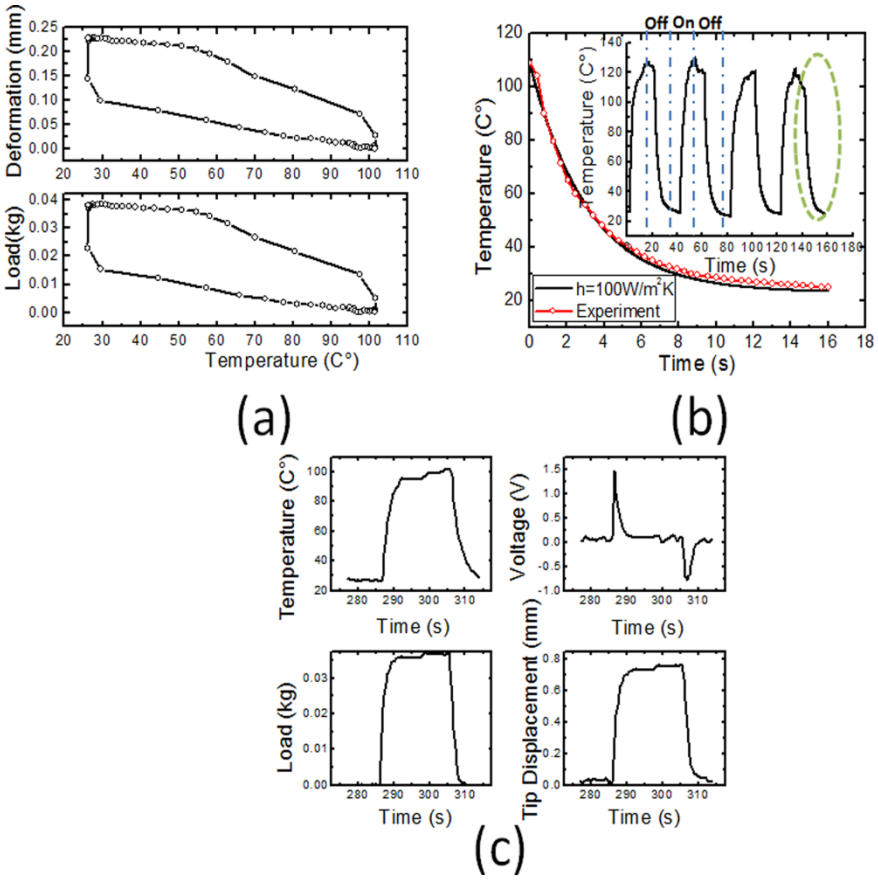

Figure A.3 (a) Experimentally obtained hysteresis loops of SMA wire, (b) Experimental and numerical model of temperature as a function of time to determine heat transfer coefficient, (c) Outputs of the system as a function of time

Multiple tests were conducted, where the resistance, frequency, preload and SMA attachment location were varied. The preload was controlled by adjusting the positioning stage and the frequency of actuation by utilizing the shutter mechanism. Figure A.4 shows the relationship between RMS power and frequency of actuation for different preload values and SMA attachment locations. It was observed that the maximum power, ~0.05μW, was achieved for preload of 15-35 gm in the frequency range of 0.6-0.8Hz, while SMA wire was attached at location 1 (Figure A.1 (a)).

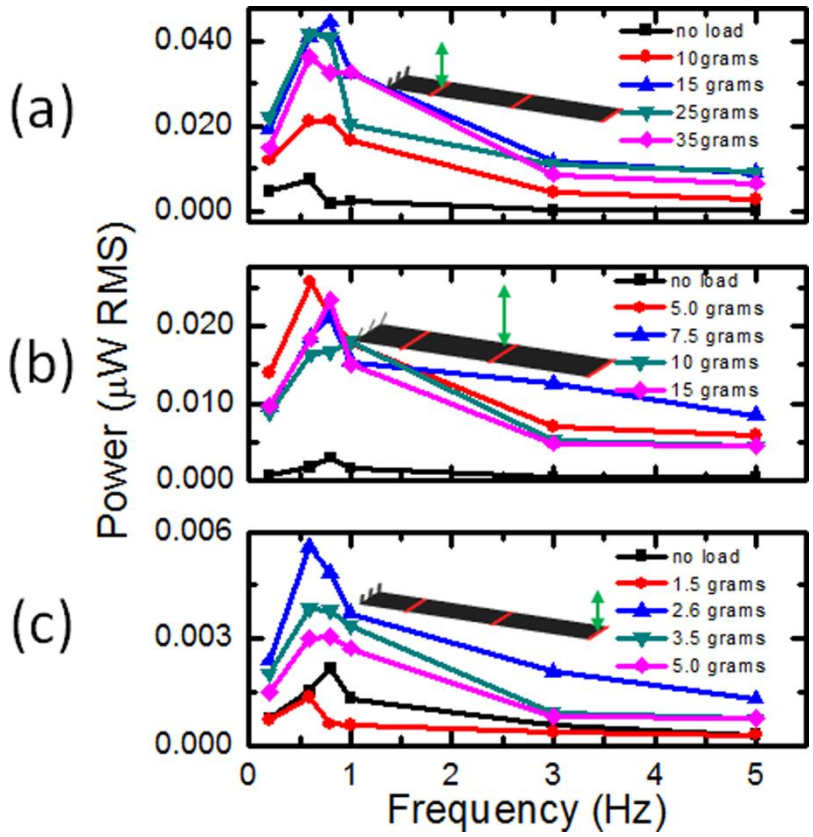

Figure A.4 Power generated by the piezoelectric bimorph as a function of frequency for different preloads and SMA attachment locations

Further analysis was performed to characterize the actuation capabilitites of the system. Primarily, different pre-loads were used at a frequency of 0.2Hz to determine the highest force and deflections (Figure A.5(a)). It can be seen that the highest response appears at preload of 25 gm. Next, at the optimal preload of 25 gm, tip displacement as a function of force generated by the SMA at different frequencies of excitation (Figure A.5(b)) was obtained. It can be observed that the performace area decreases with increase in the frequency of excitation. This was expected due to the fact that the SMA was not given enough time to lower its temperature and therefore not allowing it to go back to its initial state, thus achieving lower displacements and force.

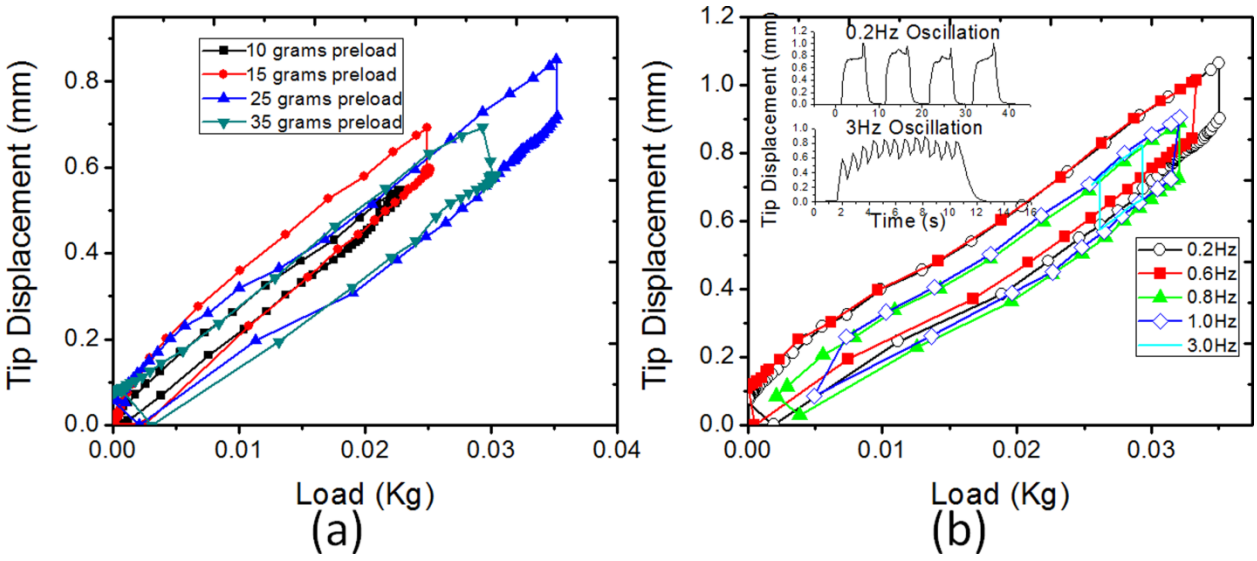

Figure A.5 Actuation characteristics of system: (a) Tip displacement as a function of different preloads, (b) Tip displacement as a function of load at different frequencies of excitation

A.4 Material analysis and optical properties of SMA wire

In order to explain the laser actuation of SMA, material analysis was conducted to understand the structure, absorbance behavior and surface stability as a function of temperature. The SMA wire was characterized using X-ray diffractometer (PANalytical X'Pert, CuKα; Philips, Almelo, the Netherlands), 193 nm ArF Excimer laser combined with an inductively coupled plasma mass spectrometer (LA-ICPMS; Agilent Technologies 7500cs), UV-Vis-NIR spectrophotometer (Hitachi, U4100, Japan) and Raman Spectrometer (JY Horbia LabRam HR 800, Horiba Ltd., Japan). Figure A.6(a) shows X-ray diffraction patterns of as-received and annealed (600^{o}C for 2 h) SMA wire. On annealing, the peak at 2θ = 44.0^{o} becomes narrower and shifts towards lower Bragg angle (2θ = 42.7^{o}), indicating increased crystallization. These patterns correspond to cubic crystal structure of NiTi (space group Pm3m, Z = 1; JCPDS # 19-0850). The elemental analysis of the wire conducted using LA-ICPMS system revealed the presence of Ti and Ni as the major elements, with the amounts as 44.22 and 54.75 wt%, respectively, with 0.01 wt% each of Al, Cr and Fe as trace elements. The data collected from six different regions exhibited negligible variation in composition. The atomic proportions of Ti:Ni in the SMA wire is 51:49, with traces of Al, Cr and Fe. Figure A.6(b) shows the UV-Vis-NIR absorbance of the SMA. It can be seen that highest absorbance occurs in the UV region, and absorbance decreases as the absorption wavelength increases.

The average input power to the SMA will depend on the product of absorbance, diameter of the wire, diameter of the laser beam and average output power from the laser. The parameters other than the absorbance are invariables, and therefore the temperature rise is expected to be proportional to the absorbance. Also, it is know that if shining the SMA with the laser wavelength of λ the surface reflection coefficient r can be represented as:

$$r = (n-1)/(n+1) \tag{B.8}$$

where n, the refractive index can be defined as $n = \sqrt{\varepsilon}$, and using Drude model ε is expressed as below:

$$\varepsilon = 1 - \omega_p^2/(\omega^2 + i\omega\omega_\tau) \tag{B.9}$$

where plasma frequency (ω_p) and collision frequency ω_τ are given as $\omega_p^2 = n_e e^2/m\varepsilon_o$ and $\omega_\tau = n_e e^2/m\sigma(T)$, respectively; $n_e \sim 3.1\text{x}10^{23}$ cm^{-3} for bulk Ni-Ti alloy and σ(T) (room temperature values being ~$0.5\text{x}10^{-6}$ Ωm) is temperature dependent conductivity[134, 135] and m is effective mass of electron. Using energy conservation, the flux (F_d) in SMA can be expressed as:

$$F_d = (1 - |r|^2) I_o \tag{B.10}$$

where I_o is the laser irradiance. For the frequency $\omega_\tau \le \omega \le \omega_p$, i.e., 0.124 μm $\le \lambda \le$ 88.369 μm, the Drude models gives the flux (F_d) as: $F_d \sim 2\omega_\tau I_o/\omega_p$. This indicates that same temperature rise (T_m) can be achieved at varying laser wavelengths; the only difference will be in the rise time.

In Figure A.6(c), Raman spectrum of a fresh cross-section of SMA wire show a characteristic air band in low wavenumber range[136][4]. No other bands were observed in the fresh cross-section of the SMA wire. However, as-received SMA wire exhibits Raman bands at 238, 446 and 613 cm^{-1}. These correspond to Ti-O related Raman modes and reflect formation of TiO_2 as a result of oxidation of the metal. The heat of formation of TiO_2 and NiO are given as follows [137]:

$$Ti(s) + O_2(g) \rightarrow TiO_2\left(-956\ kJ\ mol^{-1}\right) \tag{B.11}$$

$$Ni(s) + O_2(g) \rightarrow NiO\left(-241\ kJ\ mol^{-1}\right) \tag{B.12}$$

The heat of formation of TiO_2 is about four times higher than that of NiO. For this reason chemisorption of oxygen mainly takes place on Ti sites. On heating the SMA wire, the TiO_2

bands become progressively more intense with increasing temperature, and these bands become even stronger on subsequent cooling (Figure A.6(d)). However, negligible change is observed below 150 ^{o}C.

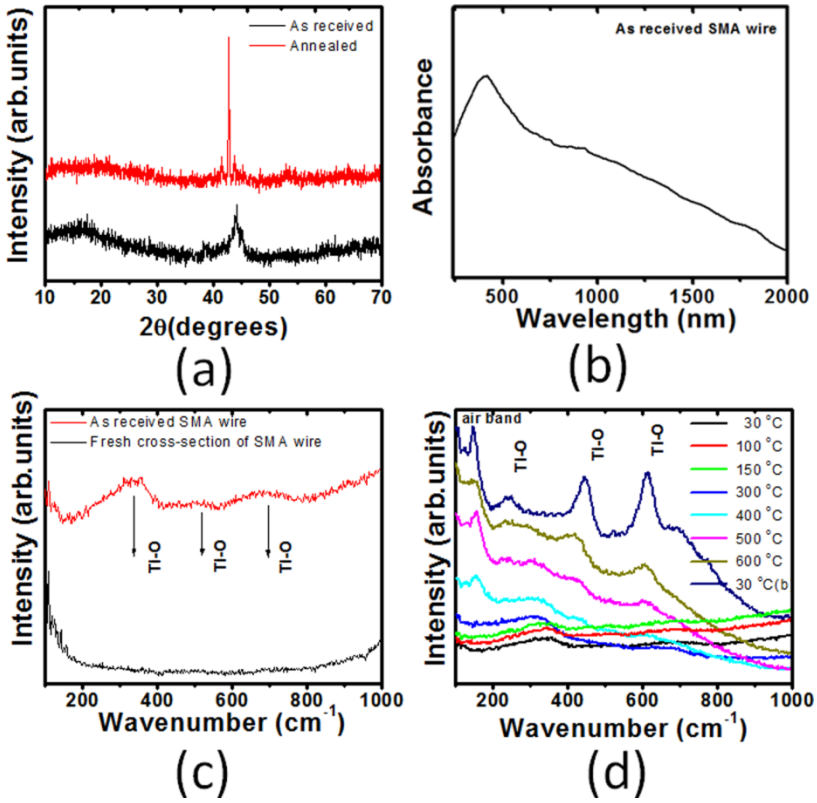

Figure A.6 (a) X-ray diffraction pattern, (b) absorbance, and (c) and (d) Raman spectra of the SMA

A.5 Conclusion

In conclusion, a novel system for remote energy harvesting and actuation by coupling SMA with a piezoelectric element was developed. The non-contact actuation of the SMA was accomplished by heating with a laser located at a remote location. Experimental analysis of the hybrid system was conducted to obtain: force, deflection, voltage and temperature. Material characterization on the SMA wire was conducted to determine optical properties of the wire, as well as the effect of heating on the composition of the wire.

Publications that have resulted from this dissertation

Journal Articles:

A. E. Aliev, N. K. Mayo, R. H. Baughman, **D. Avirovik**, S. Priya, M. R. Zarnetske, J. B. Blottman, " Thermal Management of Thermoacoustic Sound Projectors Usinga Free-Standing Carbon Nanotube Aerogel Sheet as Heat Source", Nanotechnology, (under review)

A. E. Aliev, N. K. Mayo, R. H. Baughman, **D. Avirovik**, S. Priya, M. R. Zarnetske, J. B. Blottman, "Thermoacoustic excitation of sonar projector plates by free-standing carbon nanotube sheets", Journal of Physics D: Applied Physics, (under review)

Avirovik, D., Butenhoff, B., Priya S., "Millipede-inspired Locomotion through Novel U-Shaped Piezoelectric Motors", Smart Materials and Structures, (2014)

Avirovik, D., Kishore, R., Vuckovic, D., Priya, S., "Miniature Shape Memory Alloy Heat Engine for Powering Wireless Sensor Nodes",Energy Harvesting and Systems, (2014)

Avirovik, D., Kumar, A., Bodnar, R. J., Priya S., "Remote light energy harvesting and actuation using shape memory alloy—piezoelectric hybrid transducer," Smart Materials and Structures, 22, 052001, (2013)

Avirovik D., Priya S., "L-shaped piezoelectric motor-Part I: Design and experimental analysis", Ultrasonics, Ferroelectrics and Frequency Control, IEEE Transactions on;59:98-107,(2012)

Avirovik D., Karami M.A., Inman D., Priya S., "L-shaped piezoelectric motor-part II: Analytical modeling", Ultrasonics, Ferroelectrics and Frequency Control, IEEE Transactions on;59:108-20,(2012)

Conference Proceedings:

Avirovik, D., Priya, S., "Crawling-inspired robot utilized L-Shape Piezoelectric actuators," IEEE/ASME Inter. Conf. on Advanced Intelligent Mechatronics Wollongong, Australia, (2013).

Avirovik, D., Dave, D., Priya, S., "Miniature multifunctional high-performance three-axis positioning and scanning platform," SPIE Smart Structures/NDE, San Diego, Ca, (2013).

Avirovik D., Digant D., Priya S., "Miniature image guided three-axis scanning and positioning system", SPIE Smart Structures/NDE, San Diego, Ca, (2012)

References

[1] Grush, L., "Diagnostic errors more common -and more deadly - than other treatment errors," Fox News, (2013).
[2] John Bonifield, Cohen, E., "10 shocking medical mistakes," CNN Health, (2012).
[3] Wheeler, J., "GE Healthcare's Smart Patient Room to Begin Data Collection," GE Healthcare, (2010).
[4] Klevens, R. M., Edwards, J. R., Richards, C. L., et al., "Estimating health care-associated infections and deaths in US hospitals, 2002," Public health reports, 122, 160, (2007).
[5] Edelman, R. R., Warach, S., "Magnetic resonance imaging," New England Journal of Medicine, 328, 708-716, (1993).
[6] Pauls, S., Fischer, A.-C., Brambs, H.-J., et al., "Use of magnetic resonance imaging to detect neoplastic meningitis: Limited use in leukemia and lymphoma but convincing results in solid tumors," European journal of radiology, 81, 974-978, (2012).
[7] Houssami, N., Turner, R., Morrow, M., "Preoperative magnetic resonance imaging in breast cancer: meta-analysis of surgical outcomes," Annals of surgery, 257, 249-255, (2013).
[8] Berquist, T. H., [MRI of the Musculoskeletal System], Wolters Kluwer Health, (2012).
[9] Roy, S., Bandyopadhyay, S. K., "Detection and Quantification of Brain Tumor from MRI of Brain and it's Symmetric Analysis," International Journal of Information and Communication Technology Research, 2, (2012).
[10] Gurker, N., [X-Ray Imaging], Advances in X-Ray Analysis, Springer, pp. 263-272, (1980).
[11] Xu, M., Wang, L. V., "Photoacoustic imaging in biomedicine," Review of scientific instruments, 77, 041101-041101-041122, (2006).
[12] Huang, D., Swanson, E. A., Lin, C. P., et al., "Optical coherence tomography," Science, 254, 1178-1181, (1991).
[13] Fujimoto, J., "Optical coherence tomography," Conference on Lasers and Electro-Optics, Optical Society of America, (2006).
[14] Ring, E., Ammer, K., "The technique of infrared imaging in medicine," Thermology international, 10, 7-14, (2000).
[15] Duck, F. A., Baker, A. C., Starritt, H. C., [Ultrasound in medicine], CRC Press, (2002).
[16] Fuhrer, P., Guinard, D., "Building a Smart Hospital using RFID Technologies," ECEH, 91, 131-142, (2006).
[17] Healthcare, G., "Adventure Series." http://www.gehealthcare.com/usen/accessories/adventure.html, (2013).
[18] Salamon, E., Kim, M., Beaulieu, J., et al., "Sound therapy induced relaxation: down regulating stress processes and pathologies," Medical Science Monitor, 9, RA96-RA101, (2003).
[19] McEwen, B. S., "Stress, adaptation, and disease: Allostasis and allostatic load," Annals of the New York Academy of Sciences, 840, 33-44, (1998).
[20] Despot E.J., Fraser C., "Small bowel endoscopy in inflamatory bowel disease," Best Pract Res Clin Gastroenterol, 26(23): 279-291, (2012, Jun).
[21] Schoen R.E., Pinsky P.F., Weissfeld J.L., et al., "Colorectal-cancer incidence and mortality with screening flexible sigmoidoscopy ", N Engl J Med 366(325):2345-2357, (2012).
[22] Wilkins T., Khan N., Nabh A., et al., "Diagnosis and management of upper gastrointestinal bleeding. Am Fam Physician," Review PubMed PMID: 22534226, 85(85):469-476, (2012).
[23] Chen T., Wu H.F., Shi Q., et al., "Endoscopic management of impacted esophageal foreign bodies. Dis Esophagus," doi: 101111/j1442-2050201201401x, (2012).

[24] Urso G., Interlandi D., Puglisi M., et al., "The combined endoscopic therapy (band ligation and sclerosis) in the eradication

of the esophageal varices in the cirrhotic patient: our experience," Minerva Gastroenterol Dietol, 52(53):309-316, (2006).
[25] Hirdes M.M., Siersema P.D., van Boeckel P.G., et al., "Single and sequential biodegradable stent placement for refractory benign

esophageal strictures: a prospective follow-up study," Endoscopy, 44(47):649-654, (2012).
[26] Pigò F., Bertani H., Manno M., et al., "i-Scan high-definition white light endoscopy and colorectal polyps: prediction of histology, interobserver and intraobserver agreement," Int J Colorectal Dis (2012).
[27] Toennies, J. L., Tortora, G., Simi, M., et al., "Swallowable medical devices for diagnosis and surgery: the state of the art," Proceedings of the Institution of Mechanical Engineers, Part C: Journal of Mechanical Engineering Science, 224, 1397-1414, (2010).
[28] Htwe, T. M., Poh, C. K., Li, L., et al., "Vision-based techniques for efficient Wireless Capsule Endoscopy examination," Defense Science Research Conference and Expo (DSR), 2011, IEEE, pp. 1-4, (2011).
[29] Turgis, D., Puers, R., "Image compression in video radio transmission for capsule endoscopy," Sensors and Actuators A: Physical, 123, 129-136, (2005).
[30] Van Gossum, A., Munoz-Navas, M., Fernandez-Urien, I., et al., "Capsule endoscopy versus colonoscopy for the detection of polyps and cancer," New England Journal of Medicine, 361, 264-270, (2009).
[31] Bhuvanan, K., Krishna, A. S., Golla, G., et al., "A Multi-camera Wireless Capsule Endoscopic System," India Educators' Conference (TIIEC), 2013 Texas Instruments, IEEE, pp. 65-68, (2013).
[32] J. L. Toennies, G. T., M. Simi, P. Valdastri, R. J. Webster III, "Swallowable medical devices for diagnosis and surgery: the state of the art," Proc IMechE 224 Part C: J. Mechanical Engineering Science, (2009).
[33] Chino, M., "Researchers Transmit 10mbps Broadband Data Through Human Arm," (2010).
[34] Dittrich, T., "High Powered Medicine," (2011).
[35] Carta, R., Tortora, G., Thoné, J., et al., "Wireless powering for a self-propelled and steerable endoscopic capsule for stomach inspection," Biosensors and Bioelectronics, 25, 845-851, (2009).
[36] Kim, T. S., Song, S. Y., Jung, H., et al., "Micro capsule endoscope for gastro intestinal tract," Engineering in Medicine and Biology Society, 2007 EMBS 2007 29th Annual International Conference of the IEEE, IEEE, pp. 2823-2826, (2007).
[37] Gonzalez-Guillaumin, J. L., Sadowski, D. C., Kaler, K. V., et al., "Ingestible capsule for impedance and pH monitoring in the esophagus," Biomedical Engineering, IEEE Transactions on, 54, 2231-2236, (2007).
[38] Valdastri, P., Simi, M., Webster III, R. J., "Advanced technologies for gastrointestinal endoscopy," Annual review of biomedical engineering, 14, 397-429, (2012).
[39] Kong, K.-c., Cha, J., Jeon, D., et al., "A rotational micro biopsy device for the capsule endoscope," Intelligent Robots and Systems, 2005(IROS 2005) 2005 IEEE/RSJ International Conference on, IEEE, pp. 1839-1843, (2005).
[40] Park, S., Koo, K.-i., Bang, S. M., et al., "A novel microactuator for microbiopsy in capsular endoscopes," Journal of Micromechanics and Microengineering, 18, 025032, (2008).

[41] Quirini, M., Webster, R., Menciassi, A., et al., "Design of a pill-sized 12-legged endoscopic capsule robot," Robotics and Automation, 2007 IEEE International Conference on, IEEE, pp. 1856-1862, (2007).
[42] Quaglia, C., Buselli, E., Webster, R. J., et al., "An endoscopic capsule robot: a meso-scale engineering case study," Journal of Micromechanics and Microengineering, 19, 105007, (2009).
[43] Glass, P., Cheung, E., Sitti, M., "A legged anchoring mechanism for capsule endoscopes using micropatterned adhesives," Biomedical Engineering, IEEE Transactions on, 55, 2759-2767, (2008).
[44] Karagozler, M. E., Cheung, E., Kwon, J., et al., "Miniature endoscopic capsule robot using biomimetic micro-patterned adhesives," Biomedical Robotics and Biomechatronics, 2006. BioRob 2006. The First IEEE/RAS-EMBS International Conference, pp. 105-111, (2006).
[45] Kim, B., Park, S., Jee, C. Y., et al., "An earthworm-like locomotive mechanism for capsule endoscopes," IEEE, pp. 2997-3002, (2005).
[46] Kim, B., Lee, M. G., Lee, Y. P., et al., "An earthworm-like micro robot using shape memory alloy actuator," Sensors and Actuators A: Physical, 125, 429-437, (2006).
[47] Kim, B., Lee, S., Park, J. H., et al., "Inchworm-like microrobot for capsule endoscope," Robotics and Biomimetics, 2004 ROBIO 2004 IEEE International Conference on, IEEE, pp. 458-463, (2004).
[48] Li, W., Guo, W., Li, M., et al., "A novel locomotion principle for endoscopic robot," IEEE, pp. 1658-1662, (2006).
[49] Park, H., Park, S., Yoon, E., et al., "Paddling based microrobot for capsule endoscopes," Robotics and Automation, 2007 IEEE International Conference, pp. 3377-3382, (2007).
[50] Liang, H., Guan, Y., Xiao, Z., et al., "A screw propelling capsule robot," Information and Automation (ICIA), IEEE International Conference pp. 786-791, (2011).
[51] Spanner, K., "Survey of the Various Operating Principles of Ultrasonic Piezomotors," Physik Instrumente GmbH& Co., Karlsruhe, Germany, (2006).
[52] http://www.konicaminolta.com/about/research/core_technology/picture/antiblur.html, "Supersonic Linear Actuator."
[53] Zhao, C., [Ultrasonic Motors Technologies and Applications], Science Press, Bejijing, (2010).
[54] M K Kurosawa, O. K., Y Tsuchitoi, et al., "Transducer for high speed and large thrust ultrasonic linear motor using two sandwich-type vibrators ", IEEE Transactions on Ultrasonics, Ferroelectrics and Frequency Control, (1998).
[55] Y Tomikawa, T. O., T Takano, "Ultrasonic motors-constructions/characteristics /applications," Ferroelectrics, (1989).
[56] M K Kurosawa, S. U., "Hybrid transducer type ultrasonic motor," IEEE Transactions on Ultrasonics, Ferroelectrics and Frequency Control, (1991).
[57] S Ueha, Y. T., [Ultrasonic Motors-Theory and Applications], Oxford University Press, (1994).
[58] M K Kurosawa, K. N., T Okamoto, "An ultrasonic motor using bending vibrations of a short cylinder," IEEE Transactions on Ultrasonics, Ferroelectrics and Frequency Control, (1989).
[59] T Sashida, T. K., [An Introduction to Ultrasonic Motors], Oxford:Clarendon Press, (1993).
[60] Henderson, D. A., "Simple Ceramic Motor...Inspiring Smaller Products," presented at the 10th International Conference on New Actuators, (2006).
[61] Zumeris, J., European Patent Application EP 0 663 616 A2, (1994).

[62] S. Johanson, M. B., P. O. Lithel, "Fine Walking Actuator " in: 6337532B1 USP (Ed.), U.S. Patent 6337532B1, (2002).
[63] Leo, D., [Engineering Analysis of Smart Material Systems], (2007).
[64] T. Morita, M. K., T. Higuchi, "A cylindrical shaped micro ultrasonic motor utilizing PZT thin film 1.4 mm in diameter and 5.0 mm long stator transducer," Elsevier Sensors and Actuators, (1999).
[65] Uchino, K., [FEM and Micromechatronics with ATILA Software], Taylor and Francis Group,LLc, Boca Raton, Fl, (2008).
[66] P. Hagedorn, J. W., "Traveling Wave Ultrasonic Motors, Part I: Working Principle and Mathematical Modelling of the Stator," Journal of Sound and Vibration, (1991).
[67] M. Tsai, C. H. L., S.H. Hwang, "Dynamic Modeling and Analysis of a Bimodal Ultrasonic Motor," IEEE Transactions on Ultrasonics, Ferroelectrics and Frequency Control, (2003).
[68] N. Hagood IV, A. M., "Modeling of a Piezoelectric Rotary Ultrasonic Motor," IEEE Transactions on Ultrasonics, Ferroelectrics and Frequency Control, (1995).
[69] A. Erturk, D. J. I., "An experimentally validated bimorph cantilever model for piezoelectric energy harvesting from base excitations," IOP Science, (2008).
[70] Inman, D. J., [Engineering Vibration], 3 ed., Pearson Education, Inc., Upper Saddle River, New Jersey, pp. 465-525, (2008).
[71] A. Erturk, D. J. I., [Piezoelectric Energy Harvesting Chapter 2], Wiley, (2010).
[72] Hoover, A. M., Steltz, E., Fearing, R. S., "RoACH: An autonomous 2.4 g crawling hexapod robot," Intelligent Robots and Systems, 2008 IROS 2008 IEEE/RSJ International Conference on, IEEE, pp. 26-33, (2008).
[73] Bergbreiter, S., Pister, K. S., "Design of an autonomous jumping microrobot," Robotics and Automation, 2007 IEEE International Conference on, IEEE, pp. 447-453, (2007).
[74] Hoffman, K. L., Wood, R. J., "Myriapod-like ambulation of a segmented microrobot," Autonomous Robots, 31, 103-114, (2011).
[75] Katie L. Hoffman, Wood, R. J., "Towards a multi-segment ambulatory microrobot," IEEE International Conference on Robotics and Automation, Anchorage, Alaska, (2010).
[76] J. Sathirapongsasuti, N. Punnanithi, Wimonkittiwat, P., "A mathematical explanation of millipede's walk: Walking with a Millipede," Intel ISEF, (Bangkok, Thailand, 2004).
[77] Kentaro Nakamura, M. K., Hisayuki Kurebayashi, and Sadayuki Ueha, "An Estimation of Load Characteristics of an Ultrasonic Motor by Measuring Transient Responses," IEEE, (1991).
[78] Burhanettin Koc, S. C. a. K. U., "A Piezoelectric Motor Using Two Orthogonal Bending Modes of a Hollow Cylinder," IEEE, (2002).
[79] Qing-Ming Wang, X.-H. D., "Electromechanical Coupling and Output Efficiency of Piezoelectric Bending Actuators," IEEE, (1999).
[80] Dreyfus, R., Baudry, J., Roper, M. L., et al., "Microscopic artificial swimmers," Nature, 437, 862-865, (2005).
[81] Machin, K., "Wave propagation along flagella," J exp Biol, 35, 796-806, (1958).
[82] Chen, L., Ma, S., Wang, Y., et al., "Design and modelling of a snake robot in traveling wave locomotion," Mechanism and Machine Theory, 42, 1632-1642, (2007).
[83] Kim, S., Song, W. J., Jang, J., et al., "Mechanical frequency selectivity of an artificial basilar membrane using a beam array with narrow supports," Journal of Micromechanics and Microengineering, 23, 095018, (2013).
[84] Williams, B. J., Anand, S. V., Rajagopalan, J., et al., "A self-propelled biohybrid swimmer at low Reynolds number," Nature communications, 5, (2014).

[85] Argentina, M., Skotheim, J., Mahadevan, L., "Settling and swimming of flexible fluid-lubricated foils," Physical review letters, 99, 224503, (2007).
[86] Jafferis, N. T., "The flying carpet and other tales," (2012).
[87] Bucher, I., "Estimating the ratio between travelling and standing vibration waves under non-stationary conditions," Journal of sound and vibration, 270, 341-359, (2004).
[88] Avirovik, D., Dave, D., Priya, S., "Miniature image guided three-axis scanning and positioning system," SPIE - Smart Structures/NDE, pp. 83430H, (2012).
[89] Fujimoto, J. G., Brezinski, M. E., Tearney, G. J., et al., "Optical biopsy and imaging using optical coherence tomography," Nature Medicine, 1, 970-972, (1995).
[90] Feldchtein, F., Gelikonov, V., Iksanov, R., et al., "In vivo OCT imaging of hard and soft tissue of the oral cavity," Optics Express, 3, 239-250, (1998).
[91] Richard G. Budynas, Nisbett, J. K., [Shigley's Mechanical Engineering Design], 8th ed., (2008).
[92] Mark W. Spong, Seth Hutchinson, Vidyasagar, M., [Robot Modeling and Control], John Wiley & Sons, Inc, (2006).
[93] Morar, A., "Stepper motor model for dynamic simulation," Acta Electrotehnica, 44, 117-122, (2003).
[94] Micromo, "Miniature Stepper Motor Drive Systems." http://www.micromo.com/stepper-motors-datasheets.aspx, (2012).
[95] Micromo, "Linear Motors." http://www.micromo.com/linear-motors.aspx, (2012).
[96] Micromo, "Piezo Motors - PiezoWave Motor." http://www.micromo.com/piezo-motors.aspx, (2012).
[97] Automation, A., "08Y - High Torque (Square) Stepper Motors ". http://www.anaheimautomation.com/products/stepper/stepper-motor-item.php?sID=8&pt=i&tID=75&cID=19, (2012).
[98] Technologies, N. S., "SQL-3.4 SQUIGGLE Micro Motors for OEMs." http://www.newscaletech.com/motorsforoem-SQL34.html, (2012).
[99] Nanomotion, "Nanomotion's HR1 Motor." http://www.nanomotion.com/index.aspx?id=2574&itemID=1440, (2012).
[100] Instrumente, P., "PILine Ultrasonic Motor U-164." http://www.physikinstrumente.com/en/products/prdetail.php?sortnr=1000210, (2012).
[101] Instrumente, P., "PiezoWalk Motors N-310." http://www.physikinstrumente.com/en/products/prdetail.php?sortnr=1000700, (2012).
[102] Zaber, "Three-Axis Stages with Built-in Controllers." http://www.zaber.com/products/product_group.php?group=XYZ, (2012).
[103] Instrumente, P., "M-110 · M-111 · M-112 Compact Micro-Translation Stage." http://www.physikinstrumente.com/en/products/primages.php?sortnr=701650&picview=1#gallery, (2012).
[104] ThorLabs, "MT3-Z8 - XYZ Motorized 1/2" Translation Stage." http://www.thorlabs.com/thorproduct.cfm?partnumber=MT3-Z8, (2012).
[105] Newport, "Motorized Gothic-Arch Bearing Stage, 40x40 mm, 13 mm XYZ Travel, M4 and M6." http://search.newport.com/?q=*&x2=sku&q2=9062-XYZ-PPP-M, (2012).
[106] Technologies, N. S., "Motorized Positioning Stages." http://www.newscaletech.com/motorized_stages.html, (2012).
[107] Mahrle, A., Beyer, E., "Theoretical aspects of fibre laser cutting," Journal of Physics D: Applied Physics, 42, 175507, (2009).

[108] Sebald, G., Pruvost, S., Guyomar, D., "Energy harvesting based on Ericsson pyroelectric cycles in a relaxor ferroelectric ceramic," Smart Materials and Structures, 17, 015012, (2008).
[109] Sebald, G., Guyomar, D., Agbossou, A., "On thermoelectric and pyroelectric energy harvesting," Smart Materials and Structures, 18, 125006, (2009).
[110] Roundy, S., Steingart, D., Frechette, L., et al., [Power sources for wireless sensor networks], Wireless sensor networks, Springer, pp. 1-17, (2004).
[111] Ismail, B. I., Ahmed, W. H., "Thermoelectric Power Generation Using Waste-Heat Energy as an Alternative Green Technology," Recent Patents on Electrical Engineering, 2, 27-39, (2009).
[112] Kudva, J., "Overview of the DARPA smart wing project," Journal of Intelligent Material Systems and Structures, 15, 261-267, (2004).
[113] Morgan, N., "Medical shape memory alloy applications—the market and its products," Materials Science and Engineering: A, 378, 16-23, (2004).
[114] Villanueva, A., Joshi, K., Blottman, J., et al., "A bio-inspired shape memory alloy composite (BISMAC)," Smart Mater Struct 19, 025013, (2010).
[115] Villanueva, A., Smith, C., Priya, S., "A biomimetic robotic jellyfish (Robojelly) actuated by shape memory alloy composite actuators," Bioinspiration & Biomimetics, 6, 036004, (2011).
[116] Tadesse, Y., Villanueva, A., Haines, C., et al., "Hydrogen-fuel-powered bell segments of biomimetic jellyfish," Smart Materials and Structures, 21, 045013, (2012).
[117] Banks, R. M., "Energy conversion system," Google Patents, (1975).
[118] Wakjira, J. F. "The VT1 shape memory alloy heat engine design": Virginia Polytechnic Institute and State University; (2001).
[119] Wang, F., "Energy conversion system," (1981).
[120] Johnson, A. D., "Memory alloy heat engine and method of operation," Google Patents, (1977).
[121] Pachter, J. J., "Engine," Google Patents, (1979).
[122] Sato, Y., Yoshida, N., Tanabe, Y., et al., "Characteristics of a new power generation system with application of a Shape Memory Alloy Engine," Electrical Engineering in Japan, 165, 8-15, (2008).
[123] Wang, F. E., "Energy conversion system," Google Patents, (1981).
[124] Avirovik, D., Priya, S., "L-shaped piezoelectric motor-Part I: Design and experimental analysis," Ultrasonics, Ferroelectrics and Frequency Control, IEEE Transactions on, 59, 98-107, (2012).
[125] Villanueva, A., Gupta, S., Priya, S., "Lowering the power consumption of Ni-Ti shape memory alloy," SPIE Smart Structures and Materials+ Nondestructive Evaluation and Health Monitoring, International Society for Optics and Photonics, pp. 83421I-83421I-83412, (2012).
[126] Aliev, A. E., Lima, M. D., Fang, S., et al., "Underwater sound generation using carbon nanotube projectors," Nano letters, 10, 2374-2380, (2010).
[127] Aliev, A. E., Gartstein, Y. N., Baughman, R. H., "Increasing the efficiency of thermoacoustic carbon nanotube sound projectors," Nanotechnology, 24, 235501, (2013).
[128] Tadesse, Y., Hong, D., Priya, S., "Twelve degree of freedom baby humanoid head using shape memory alloy actuators," Journal of mechanisms and robotics, 3, (2011).
[129] Andreasen, G. F., Hilleman, T. B., "An evaluation of 55 cobalt substituted Nitinol wire for use in orthodontics," The Journal of the American Dental Association, 82, 1373-1375, (1971).
[130] Lagoudas, D. C., [Shape Memory Alloys - Modeling and Engineering Applications], Springer, (2007).

[131] Zaidi, S., Lamarque, F., Favergeon, J., et al., "Wavelength selective shape memory alloy for wireless micro-actuation of a bistable curved-beam," Industrial Electronics, IEEE Transactions on, 1-1, (2011).
[132] Tadesse, Y., Thayer, N., Priya, S., "Tailoring the Response Time of Shape Memory Alloy Wires through Active Cooling and Pre-stress," Journal of Intelligent Material Systems and Structures, 21, 19-40, (2010).
[133] Frank P. Incropera, David P. Dewitt, Bergman, T. L., et al., [Fundamentals of Heat and Mass Transfer], 6th ed., John Wiley and Sons, (2007).
[134] Hu, Y. F., Deng, W., YUE, L., et al., "Microdefects and electron densities in NiTi shape memory alloys studied by positron annihilation," Transactions of Nonferrous Metals Society of China, 16, 1259-1262, (2006).
[135] K. Worden, W. A. Bullough, Haywood, J., [Smart Technologies], World Scientific, Singapore, (2003).
[136] Pérez del Pino, A., Serra, P., Morenza, J., "Coloring of titanium by pulsed laser processing in air," Thin solid films, 415, 201-205, (2002).
[137] R.C. Weast, Astle, M. J., [CRC Handbook of Chemistry and Physics], CRC Press, Boca Raton, Florida, (1982).